



HAL
open science

Analysis of the stress gradient effect in Fretting-Fatigue through a description based on nonlocal intensity factors

Claudio Montebello

► To cite this version:

Claudio Montebello. Analysis of the stress gradient effect in Fretting-Fatigue through a description based on nonlocal intensity factors. Solid mechanics [physics.class-ph]. Université Paris Saclay (CO-mUE), 2015. English. NNT: 2015SACLN019 . tel-01238905

HAL Id: tel-01238905

<https://theses.hal.science/tel-01238905>

Submitted on 7 Dec 2015

HAL is a multi-disciplinary open access archive for the deposit and dissemination of scientific research documents, whether they are published or not. The documents may come from teaching and research institutions in France or abroad, or from public or private research centers.

L'archive ouverte pluridisciplinaire **HAL**, est destinée au dépôt et à la diffusion de documents scientifiques de niveau recherche, publiés ou non, émanant des établissements d'enseignement et de recherche français ou étrangers, des laboratoires publics ou privés.

NNT : 2015SACLN019

THESE DE DOCTORAT
DE L'UNIVERSITE PARIS-SACLAY,
préparée à l'École Normale Supérieure de Cachan

ÉCOLE DOCTORALE N° 579
Sciences mécaniques et énergétiques, matériaux et géosciences (SMEMAG)

Spécialité de doctorat : Mécanique

Par

M. Claudio Montebello

Analysis of the stress gradient effect in Fretting-Fatigue through a description
based on nonlocal intensity factors

Thèse présentée et soutenue à Cachan, le 26 novembre 2015 :

Composition du Jury :

M. Yves Nadot, Professeur, ENSMA Poitiers, Président du jury
M. Daniel Nelias, Professeur, INSA Lyon, Rapporteur
Mme Marie-Christine Baietto, Directrice de Recherche - CNRS, INSA Lyon,
Rapporteur
M. David Hills, Professeur, University of Oxford, Examineur
M. Yoann Guilhem, Maître de Conférences, ENS Cachan, Examineur
Mme S. Pommier, Professeure, ENS Cachan, Directrice de thèse





Acknowledgements

I would like to take this opportunity to sincerely thank all the people with whom I had the opportunity to work at the LMT-ENS Cachan and at SNECMA Villaroche. I spent a great time there, in a challenging environment, working on a project that passionates me. When I decided to pursue a PhD I knew that the road would have been long and arduous. Luckily, in these three years, I encountered a lot of amazing people that contribute to make my research work much easier.

I would like to sincerely thank all the members of the jury for the interest showed in my work. Their questions and remarks undoubtedly contribute to increase the quality of the manuscript.

My sincere thanks need to be addressed to Sylvie Pommier, my PhD advisor. Her support, her suggestions and her always positive attitude have been extremely important to perform my work in the best possible conditions.

Similarly, I have really appreciated the possibility to have a constant interaction with my industrial advisors at Snecma. A special thanks goes to Jean Meriaux; he is at the origin of the project on which I worked, but more than that, he has always been ready to help me whenever I had a problem. I cannot forget Julien Leroux, Karim Demmou and Nathalie Serres; all of them have been really kind and helpful.

I would like to thank all of my present and former colleagues at the LMT-ENS Cachan: Amaury, Matteo, Enrico, Andrea, Ionut, Maxime and all the others for the great times we had.

Last but not least, a big thanks to Manon and my family for unconditionally supporting me during these three years.

Claudio Montebello

Contents

List of Figures	v
List of Tables	xi
Nomenclature	xiii
Introduction	1
1 Industrial Context and State of the Art	5
1.1 Industrial context	7
1.1.1 Turbofan	8
1.1.2 Connection between disk and blade root	10
1.1.3 In-flight loading condition experienced at contact interfaces . .	12
1.1.4 Snecma dimensioning process	13
1.1.5 Industrial objectives	14
1.2 Fretting-fatigue modeling	16
1.2.1 Historical review	16
1.2.2 Fretting-fatigue test geometries	20
1.2.3 Fretting-fatigue test apparatus	22
1.2.4 Slip quantification for transition criteria	25
1.3 Damaging mechanisms in fretting-fatigue	27
1.3.1 Fretting map	28
1.3.2 Crack initiation	28
1.3.3 Crack propagation	32
1.3.4 Crack arrest	35
1.3.5 Fretting-fatigue peculiarities	37
1.4 Life prediction criteria	40
1.4.1 Crack initiation prediction criteria	41
1.4.2 Life prediction criteria	45
1.5 Scientific challenges	47
2 Nonlocal description of the fretting-fatigue problem	51
2.1 Background	53
2.2 Mechanical field partitioning technique	55

2.3	Contact mechanics and FE computation	57
2.3.1	Stick-slip evolution for plain fretting	58
2.3.2	Stick-slip evolution for fretting-fatigue	61
2.3.3	Stress field computation in the substrate	62
2.3.4	FE model details	64
2.4	Nonlocal stress intensity factor computation	65
2.4.1	Selection of the reference fields	66
2.4.2	Normalization of the reference fields	67
2.4.3	Nonlocal intensity factor computation	69
2.4.4	Evolution of the intensity factors during fretting-fatigue	71
2.5	Influence of the contact geometry on the reference functions	74
2.6	Sensitivity analysis	76
2.6.1	Influence of the size of the extraction zone	78
2.6.2	Influence of the mesh size	81
2.6.3	Influence of the mesh type	84
2.7	Chapter highlights	85
3	Application of the approach to fretting-fatigue test data	89
3.1	Application strategy	91
3.2	Experimental data	92
3.2.1	Test apparatus	93
3.2.2	Ti-6Al-4V	93
3.2.3	Inconel 718	95
3.2.4	35NiCrMo16 low-alloyed steel	96
3.3	Application of the approach	98
3.3.1	Gross slip frontier	99
3.3.2	Plain fretting	102
3.3.3	Fretting-fatigue	104
3.4	Influence of the friction coefficient variation	107
3.5	Chapter highlights	110
4	Crack initiation prediction criteria	111
4.1	Crack initiation frontier prediction strategy	113
4.2	Multiaxial fatigue criteria	113
4.2.1	From velocity field to stress field	113
4.2.2	Reference field interpolation	114
4.2.3	Computation of the strain and stress field	118
4.2.4	Application of the multiaxial fatigue criteria	123
4.3	Fracture mechanics approach	139
4.4	Chapter highlights	142
	Conclusion and perspectives	145
A	Karhunen-Loeve transform	151

Contents

Bibliography

157

List of Figures

1.1	(a) LEAP; (b) SaM146.	8
1.2	Turbofan schematic.	9
1.3	(a) Disc-blade dovetail type joint; (b) disc-blade fir-tree type joint.	10
1.4	(a) CFM56-7B fan blade hub; (b) disc-blade connection load components.	11
1.5	(a) Airbus A380-842 disc failure; (b) section of the IP turbine disc; (c) damages resultant from disc failure, [ATSB, 2010].	12
1.6	In-flight relative displacement at the contact interface, [Mary, 2009].	12
1.7	Evolution of the stress tensor at the contact surface and far from it as a function of the contact status, i.e. stick or stick-slip.	13
1.8	FE model of the blade root attachment.	14
1.9	Stress distribution at the blade root / disc contact surface, [Ferré et al., 2013].	15
1.10	Effect of relative slip on fretting-fatigue strength, [Nishioka and Hirakawa, 1969a].	18
1.11	(a) Fretting-fatigue S-N curves for aluminium alloy 2014A in the fully aged condition; (b) fretting-fatigue S-N curves for stainless steel EN58A in the annealed condition, [Waterhouse et al., 1983].	19
1.12	(a) Schematic of the dog bone specimen/cylindrical pad configuration; (b) fretting-fatigue apparatus, [Araújo and Castro, 2012].	21
1.13	(a) Schematic representation of the loading at the interface disc/blade root; (b) dovetail blade root test apparatus [Rajasekaran and Nowell, 2006].	22
1.14	(a) Fretting-fatigue single actuator machine; (b) Fretting-fatigue double actuator machine, [Lee and Mall, 2004].	23
1.15	Geometrical and load simplifications in fretting-fatigue tests.	24
1.16	Transition between fretting regime and reciprocal sliding, [Meriaux, 2010, Mary, 2009].	25
1.17	Transition criteria in fretting regimes, [Fouvry et al., 1996].	26
1.18	Loading conditions described by the term fretting-fatigue, [Hills and Nowell, 1994].	27

List of Figures

1.19	(a) Relation between slip amplitude and wear rate, [Vingsbo and Söderberg, 1988]; (b) material response fretting map, [Fouvry et al., 1996].	29
1.20	(a) Stress concentration at the contact surface; (b) fretting scar and crack initiation, [Proudhon et al., 2006].	30
1.21	Different crack propagation stages under plain fretting.	30
1.22	Quantitative analysis of a 3D fretting crack morphology by X-ray tomography: evolution of the nucleation and propagation angles ϑ_i , ϑ_p and ϑ_s measured inside the material along the specimen thickness, [Proudhon et al., 2007].	31
1.23	Crack loading modes.	32
1.24	Typical fracture mechanics fatigue crack propagation behavior.	34
1.25	Kitagawa-Takahashi diagram, [Miller, 1993b].	35
1.26	(a) Crack length evolution in function of the number of cycles under plain fretting, $P_{0,max} = 700$ MPa, $Q_{max} = 280$ N/mm; (b) maximum crack length in function of Q_{max} , [Kubiak, 2006].	36
1.27	Short crack arrest schematic representation [Kubiak, 2006].	37
1.28	Different crack propagation stages under fretting-fatigue.	38
1.29	Illustration of the fretting-fatigue mapping concept defined for partial slip condition, [Fouvry and Kubiak, 2009].	39
1.30	Fretting-fatigue Map, ($P = 227$ N/mm, $p_0 = 450$ MPa (a): AISI 1034/52100 (Radius pad = 40 mm); (b) Ti-6Al-4V/52100 (Radius pad = 30 mm), [Fouvry and Kubiak, 2009].	40
1.31	Experimental crack initiation boundaries in term of maximum local quantities for Inconel 718 in plain fretting as a function of the pad radius [Amargier et al., 2010].	44
1.32	Schematic representation of the radial shape process volume, [Proudhon et al., 2005].	45
1.33	Evolution of the crack tip stress intensity factors for plain fretting and fretting-fatigue, [de Pannemaecker et al., 2015].	46
1.34	(a) Typical fretting-fatigue mark on an unbroken specimen, [Bellecave et al., 2014]; (b) stress gradient evolution for two plain fretting test with different pad radii.	48
1.35	(a) Wear on the internal part of a CFM56-3A fan root; (b) fretting-fatigue scar; (c) cracks initiation sites.	49
2.1	Crack analogue approach (flat punch over planar surface), [Giannakopoulos et al., 1998].	53
2.2	(a) Illustration of the different scales in fracture mechanics ;(b) reference frame attached to the crack tip T, [Fremy et al., 2012].	55
2.3	Reference frame (R') attached to the contact tip in which the velocity field (Equation 2.8) is defined.	56

List of Figures

2.4	Schematic representation of cylinder-plane contact configuration under fretting-fatigue.	59
2.5	Evolution of the stick-slip zone as a function of the tangential force for cylinder plane configuration in plain fretting.	60
2.6	Illustration of Mindlin surface shear distributions generated in partial slip cylinder/plane contact under plain fretting and fretting-fatigue loading conditions, [Fouvry et al., 2014].	62
2.7	(a) Von Mises stress distribution in the substrate; (b) Stress tensor evolution as a function of the normalized depth.	64
2.8	FEM parameters and loading evolution used.	65
2.9	Extraction of the velocity field over a circular zone centered at the contact edge.	66
2.10	Different steps in the FE computation to extract the reference fields.	67
2.11	(a) Comparison between radial evolution of \underline{d}^s and radial evolution of the displacement field at the crack tip (mode I); (b) Comparison between tangential evolution of \underline{d}^s and tangential evolution of the displacement field at the crack tip (mode I).	68
2.12	(a) Comparison between radial evolution of \underline{d}^a and radial evolution of the displacement field at the crack tip (mode II); (b) Comparison between tangential evolution of \underline{d}^a and tangential evolution of the displacement field at the crack tip (mode II).	69
2.13	(a) Error evolution introduced by the approximation; (b) evolution of the stick-slip region during fretting-fatigue cycle; (c) cyclic tangential load, Q	70
2.14	(a) Radial evolution of \underline{d}^c ; (b) $(++)$ evolution of $\underline{g}^c(\vartheta)$ applied on a circle around the contact tip.	72
2.15	Evolution of I^a and I^s during a plain fretting FE simulation.	73
2.16	Evolution of I^a and I^c during a plain fretting FE simulation.	73
2.17	Schematic representations of the steps of the algorithm: (\rightarrow) classic path, (\dashrightarrow) the re-computation of the reference fields is skipped.	75
2.18	Comparison of $\underline{g}^a(\vartheta)$ for different geometries characterize by a change in pad radius.	76
2.19	Comparison of $\underline{g}^s(\vartheta)$ for different geometries characterize by a change in pad radius.	77
2.20	Comparison of $\underline{g}^c(\vartheta)$ for different geometries characterize by a change in pad radius.	77
2.21	Plane/plane contact configuration with rounded edges.	78
2.22	Schematic representation of the sensitivity analysis concerning the effect of the variation of the size of the extraction zone, Ω	79
2.23	Nonlocal intensity factor as a function of radius.	80
2.24	Error evolution as a function of radius.	80
2.25	Mesh employed in the FE computations.	81
2.26	Nonlocal intensity factor as a function of the mesh size.	83

List of Figures

2.27	Error evolution as a function of the mesh size.	84
2.28	Nonlocal intensity factor as a function of the mesh size and element type: CPE3 (linear triangular element), CPE4R (linear quadrilateral element), CPE6M (quadratic triangular element) CPE8R (quadratic quadrilateral element).	85
2.29	Error evolution as a function of the mesh size and element type: CPE3 (linear triangular element), CPE4R (linear quadrilateral element), CPE6M (quadratic triangular element) CPE8R (quadratic quadrilateral element). Example of triangular and quadrilateral meshes for a configuration corresponding to 10 elements for half-contact width.	86
3.1	Different steps in the application of the methodology developed in Chapter 2.	92
3.2	(a) Plain fretting; (b) fretting-fatigue test apparatus.	93
3.3	(a) Crack initiation frontiers in plain fretting for different contact configurations; (b) evolution of the crack initiation frontiers in fretting-fatigue for two different radii ($\sigma_B(R = 0.01)$), Ti-6Al-4V.	94
3.4	(a) Crack initiation frontiers in plain fretting for different contact configurations , Inconel 718.	95
3.5	(a) Crack initiation frontiers in plain fretting for different contact configurations; (b) evolution of the crack initiation frontiers in fretting-fatigue for two different radii, 35NiCrMo16 low-alloyed steel.	97
3.6	(a) Evolution of the gross slip limit in nonlocal coordinates for different Coulomb's friction coefficients and different geometries (Table 3.5); (b) relation between local and nonlocal friction coefficient (35NiCrMo16 low-alloyed steel).	101
3.7	(a) Evolution of the gross slip limit in nonlocal coordinates for different Coulomb's friction coefficients and different geometries; (b) relation between local and nonlocal friction coefficient (Ti-6Al-4V).	101
3.8	(a) Evolution of the gross slip limit in nonlocal coordinates for different Coulomb's friction coefficients and different geometries; (b) relation between local and nonlocal friction coefficient (Inconel 718).	102
3.9	Nonlocal crack initiation boundaries for Inconel 718 in plain fretting.	103
3.10	Nonlocal crack initiation boundaries for Ti-6Al-4V in plain fretting. .	103
3.11	Nonlocal crack initiation boundaries for 35NiCrMo16 low-alloyed steel in plain fretting.	104
3.12	Nonlocal crack initiation boundaries evolution with the introduction of a cyclic bulk load, σ_B , for 35NiCrMo16 low-alloyed steel in fretting-fatigue.	105
3.13	Nonlocal crack initiation boundaries evolution with the introduction of a cyclic bulk load, σ_B , for Ti-6Al-4V in fretting-fatigue.	106
3.14	Nonlocal crack initiation frontier in fretting-fatigue for Ti-6Al-4V. . .	106

List of Figures

3.15	(a) Variable displacement method to compute the friction coefficient (b) evolution of the friction coefficient as a function of contact radius and maximum Hertzian pressure, [Fouvry et al., 2014].	108
3.16	Variation of the crack initiation frontiers as a function of the friction coefficient for Ti-6Al-4V.	109
4.1	Crack analogue approach, $0 \leq \vartheta \leq 2\pi$	115
4.2	(a) Comparison between radial evolution of \underline{d}^s and radial evolution of the displacement field at the crack tip (mode I); (b) Comparison between tangential evolution of \underline{d}^s and tangential evolution of the displacement field at the crack tip (mode I).	116
4.3	(a) Comparison between radial evolution of \underline{d}^a and radial evolution of the displacement field at the crack tip (mode II); (b) Comparison between tangential evolution of \underline{d}^a and tangential evolution of the displacement field at the crack tip (mode II).	116
4.4	Interpolation of $\underline{g}^s(\vartheta)$	119
4.5	Interpolation of $\underline{g}^a(\vartheta)$	119
4.6	Comparison between the evolution of $\sigma_{xx,FF}$ at the contact front and $\sigma_{xx,CT}$ at the crack tip (FF: fretting fatigue, CT: crack tip).	121
4.7	Stress field re-construction by using the nonlocal intensity factors (FE parameters: plain-fretting analysis, Pad radius = 20 mm, friction coefficient = 1.0, Young's modulus = 119 400 MPa, Poisson's ratio = 0.3, $P = 347 \text{ N mm}^{-1}$ and $Q^* = 237 \text{ N mm}^{-1}$), IF: intensity factors, FE: finite elements.	122
4.8	Schematic view of the different steps in the application of the modified Wöhler Curve Method, [Araújo et al., 2007].	125
4.9	(a) Material plane and normal and tangential components of the stress tensor projection; (b) rectangular hull with orientation bounding the shear stress path ψ , [Araújo et al., 2011].	128
4.10	Crack initiation frontier obtained by applying the modified Wöhler curve method to the nonlocal crack initiation map for Ti-6Al-4V.	130
4.11	Crack initiation frontier obtained by applying the modified Wöhler curve method to the nonlocal crack initiation map for Inconel 718.	131
4.12	Crack initiation frontier obtained by applying the modified Wöhler curve method to the nonlocal crack initiation map for 35NiCrMo16 low-alloyed steel.	131
4.13	Crack initiation frontier obtained by applying the Crossland criterion to the nonlocal crack initiation map for Ti-6Al-4V.	134
4.14	Crack initiation frontier obtained by applying the Crossland criterion to the nonlocal crack initiation map for Inconel 718.	134
4.15	Crack initiation frontier obtained by applying the Crossland criterion to the nonlocal crack initiation map for 35NiCrMo16 low-alloyed steel.	135

List of Figures

4.16	Schematic representation of the assumption made to decouple the effect of the plain fretting loading to the cyclic bulk force.	136
4.17	(a) Evolution of I_{max}^a as a function of σ_B in a situation where no tangential force, Q , is applied as described in Figure 4.16b; (b) Prediction of the experimental data by applying the assumption presented in Equation 4.86.	137
4.18	Tridimensional crack initiation frontier obtained by applying the modified Wöhler curve method to the nonlocal crack initiation map for Ti-6Al-4V.	138
4.19	Tridimensional crack initiation frontier obtained by applying the Crossland criterion to the nonlocal crack initiation map for Ti-6Al-4V. . .	139
4.20	(a) Kinked crack; (b) Fretting-fatigue analogue problem.	140
4.21	Comparison between different strategies to predict the crack initiation frontier location.	142
5.1	Details of a 3D cylinder-plane contact FE model, used to extract the nonlocal intensity factors.	148
5.2	(a) Triaxiality variation as a function of the specimen width, d ; (b) Nonlocal intensity factor variation as a function of the specimen width.	149
5.3	Schematic representation of the nonlocal intensity factor extraction process applied to an industrial component.	150
A.1	Example of the utilization of the POD technique to reduce the image size.	154
A.2	Evolution of the error in the POD approximation as a function of the number of terms used.	155

List of Tables

3.1	Mechanical properties of Ti-6Al-4V used in [Ferré et al., 2013].	94
3.2	Mechanical properties of Inconel 718 used in [Amargier et al., 2010].	96
3.3	Mechanical properties of 35NiCrMo16 low-alloyed steel.	96
3.4	Test data for 35NiCrMo16 low-alloyed steel presented in [Fouvry et al., 2014] (PF: plain fretting, FF: fretting-fatigue), number of cycles = 10^6	97
3.5	Gross slip frontier evolution in nonlocal quantities for 35NiCrMo16 low-alloyed steel.	100
3.6	Variation of the ratio between local and nonlocal friction coefficient as a function of the material considered.	100
4.1	Coefficient values allowing to interpolate $\underline{g}^s(\vartheta)$ and $\underline{g}^a(\vartheta)$ and the ones obtained for crack-tip displacement field in mode I and mode II.	118
4.2	Percentage relative error between the stress tensor at the contact edge and at the crack tip for $\vartheta = 3/2\pi$	122
4.3	Calibration values used for the modified Wöhler curve method and the Crossland criterion, l_{ref} : normalization length for confidentiality issue.	133
4.4	Location of the initiation frontier following a fracture mechanics approach.	141

Nomenclature

Abbreviations:

LEFM	Linear Elastic Fracture Mechanics
Y_s	Yield Strength
UTS	Ultimate Tensile Strength

Symbols:

$\underline{d}^s(\underline{x})$	Symmetric spatial reference field
$\underline{d}^a(\underline{x})$	Antisymmetric spatial reference field
$\underline{d}^c(\underline{x})$	Complementary spatial reference field
$I^s(t)$	Intensity factor (symmetric part)
$I^a(t)$	Intensity factor (antisymmetric part)
$I^c(t)$	Intensity factor (complementary part)
I_{max}^s	Maximum value of the intensity factor (symmetric part) over a cycle
I_{max}^a	Maximum value of the intensity factor (antisymmetric part) over a cycle
I_{max}^c	Maximum value of the intensity factor (complementary part) over a cycle
$\underline{v}(\underline{x}, t)$	Velocity field expressed in the reference frame attached to the contact edge
q_{max}	Maximum tangential shear stress at the contact surface
p_0	Maximum normal pressure at the contact surface
P	Linear normal force applied to the cylinder pad
Q	Fretting linear tangential force applied to the cylinder pad
Q*	Fretting linear tangential amplitude

Nomenclature

δ	Fretting displacement
σ_B	Maximum fatigue stress amplitude
ΔK	Stress intensity factor range
$f(r)$	Radial evolution of the spatial reference field
\underline{g}	Tangential evolution of the spatial reference field
$\xi_e(t)$	Error of the elastic approximation
$\xi_{tot}(t)$	Error of the total approximation
μ	Coulomb friction coefficient
$\tilde{\mu}$	Nonlocal Coulomb friction coefficient

Introduction

Aerospace structures are usually designed to operate for a long period of time (30-40 years and sometimes even more) assuring the same level of safety all lifelong. In this context, fatigue problems are the most common way of failure, as shown by the rare accidents occurred in the past.

The aircraft engines do not escape this fact. In the case of Snecma, among the different research area where the company is currently active, one in particular is becoming more and more important which is fretting-fatigue.

This phenomenon concerns all the engineering assemblies subjected to vibrational loading. Microsliding is experienced over part of the contact interface, which will damage the surface, leading to crack initiation very early in the life of the components. The disc-blade root attachment of the turbofan engine is the perfect spot for observing fretting-fatigue related damage. This is the reason why Snecma has funded an important research campaign intending to improve the understanding of fretting-fatigue with a direct consequence on the company procedures in terms of dimensioning rules and methodologies.

The main challenges from a scientific and industrial standpoint are the following ones:

- Ameliorate the existent numerical methods capable to predict the knockdown factor introduced by fretting-fatigue.

One of the reasons why this phenomenon is particularly difficult to handle is the fact that the contact between the bodies introduces an important stress gradient in the components. The latter has to be taken into account in order to have a good prediction of damaging process.

On the other hand, fretting-fatigue is a highly multiscale phenomenon. For instance, considering the example of the disc-root attachment, its size is some centimeters, the fretting scar observed at the interfaces is limited to some micrometers while the variation of the stress magnitude is already evident some micrometers far from the surface.

Furthermore, the evolution of the stress gradient depends on the geometry of the contact, which makes the results obtained through experimental tests, difficult to transpose to different geometries.

- Be able to handle the different scales introduced by the fretting-fatigue problem

through some kind of model reduction techniques in order to conceive new algorithms that can be used in industrial applications.

In this manuscript a practical solution to overcome the aforementioned challenges is proposed.

A new method to describe the stress gradient effect in fretting-fatigue through nonlocal intensity factors is developed. The interest of the approach comes from the geometry independent nature of the nonlocal intensity factors. Therefore, they can be used to characterize the stress field around the contact edges for any given geometry and represent an objective way to compare experimental results coming from different test campaigns. This description is obtained through nonintrusive post-processing of FE computations and is conceived in order to be easily implementable in an industrial context.

The manuscript is divided into four main chapters:

- **Chapter 1.** The fretting-fatigue phenomenon is introduced by describing its effects on the industrial applications. Then a focus is done on the turbofan engine, explaining in detail its functioning which allows the reader to understand why some components are particularly sensitive to fretting-fatigue damage.

In the second part of the chapter, a bibliographic review is presented which has the function to introduce some important concepts. The following topics are addressed: damage mechanism in plain fretting and fretting-fatigue, the different fatigue criteria available in the literature and the effect of the stress gradient.

The chapter ends with a discussion on how the research work presented here is intended to add some new knowledge to the fretting-fatigue research community.

- **Chapter 2.** A new method to describe the stress gradient effect in fretting-fatigue is presented. By analyzing the mechanical fields in the proximity of the contact edges, it has been possible to extract nonlocal intensity factors that take into account the stress gradient evolution. For this purpose, the kinetic field around the contact ends is partitioned into a summation of multiple terms, each one expressed as the product between nonlocal intensity factors, I^s , I^a , I^c , depending on the macroscopic loads applied to the mechanical assembly, and spatial reference fields, \underline{d}^s , \underline{d}^a , \underline{d}^c , depending on the local geometry of the part.

A sensitivity analysis is performed in order to understand the impact that some key parameters have on the algorithm outcome.

- **Chapter 3.** The procedure presented in Chapter 2 is applied to fretting-fatigue test data.

In particular, it is shown that is possible to describe the crack initiation mechanism taking into account the gradient effect, by using the nonlocal intensity factors as reference quantities.

- **Chapter 4.** Several multiaxial fatigue criteria are coupled to the description of fretting-fatigue through nonlocal intensity factors to obtain an analytical crack initiation frontier, function of common material data such us the pure torsion and the push-pull fatigue limit. By exploiting the description developed to partition the velocity field, the associated stress field is computed which is used as input for the multiaxial fatigue criteria.

Chapter 1

Industrial Context and State of the Art

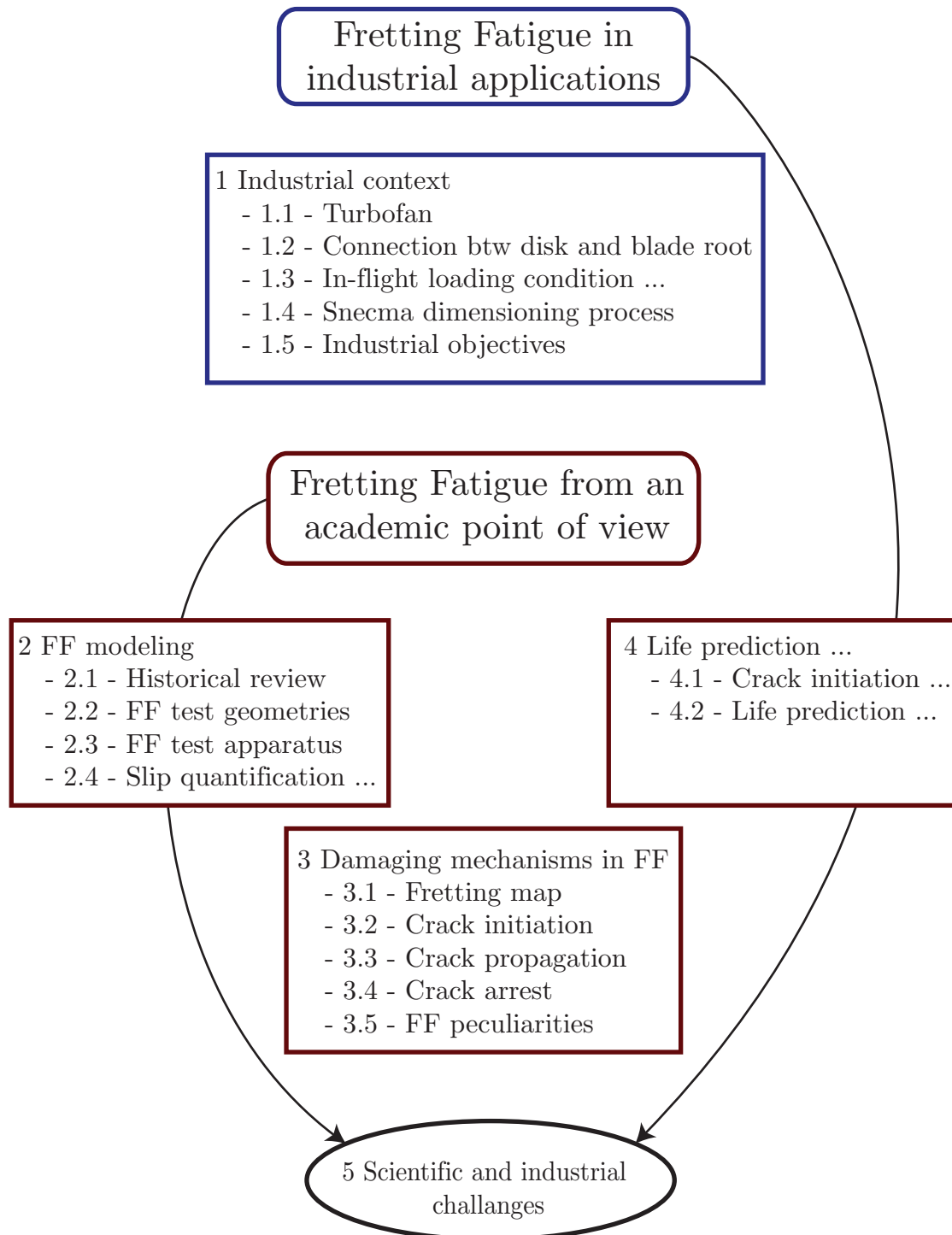
Fretting occurs every time a junction between components is subjected to oscillating forces or vibrations. At the contact surface a micro relative tangential displacement over part of the interface is experienced. Combined with cyclic bulk fatigue loading, the so-called fretting-fatigue is a frequent source of failure constituting a major concern in safety-critical industries such as aerospace or nuclear power generation.

In the first part of this chapter the industrial framework, in which this research has been performed, is presented. Then, the principle of functioning of a modern turbofan is introduced, focusing in particular on the reasons why some components may suffer fretting-fatigue problems during the engine lifespan.

In the second part, a more academical description of fretting-fatigue is presented, articulated around a brief review of the major scientific breakthroughs in the comprehension of this phenomenon during the last century. The attention is focused on the damaging process; the crack initiation phase is analyzed as well as the propagation stage which can end with the arrest of the crack or continue until the failure of the part depending on the fretting-fatigue load magnitude. The main fatigue criteria used to predict crack initiation or crack arrest are then listed.

The chapter concludes with a discussion on how the research presented in this manuscript may ameliorate the way in which fretting-fatigue is described in relation with the limitations of the existent approaches.

Chapter 1 - Table of Contents Flowchart



1.1 Industrial context

Aircraft are among the most complex engineering systems that have been developed. Since the first flight of the Wright brothers in 1903, enormous technological breakthroughs have transformed the initial pioneering experience of flight in the safest way to travel.

Despite this “idyllic” portrait of the aviation industry, in-flight failures still occur. In particular, a recent study [Findlay and Harrison, 2002] shows that fatigue-related problems are the cause of almost 60% of the total in-service failures. The most famous ones are probably the two Comet crashes in 1954, both of them caused by explosive cabin decompression. Scrupulous investigations proved that the failure of the pressurized cabin was due to fatigue crack growth initiated at windows caused by square corners that generate a severe stress concentration, [Withey, 1997]. Although serious fatigue failures had occurred before, as discussed in [Williams, 1965], these two accidents clearly demonstrated for the first time the negative impact that fatigue could have on the aviation industry. Since then, fatigue in aircraft structures has been a well-recognized problem with significant implications for transportation safety.

In the last twenty years the attention has been focused on turbofan engines that due to their complexity are the perfect candidates for fatigue failure. A massive research project, *National Turbine Engine High Cycle Fatigue (HCF) Science and Technology (S&T) Program*, funded by the Air Force, the Navy, and NASA, has started in 1994, aiming at reducing the negative impact that high cycle fatigue has on engine safety, reliability and readiness. An economic quantification of this impact, [Garrison, 2000], shows that it can exceed \$400 million per year.

Looking more closely at the reasons of failures in aircraft engines, one in six of all accidents are caused by fretting, [Thomson, 1998]. Fretting occurs every time two contacting bodies are subjected to oscillating forces or vibrations, which give rise to micro relative tangential displacement over part of the interface. Combined with high cycle fatigue loading, the so-called fretting-fatigue has a negative effect on the material fatigue limit [Lindley, 1997], and represents a major concern for engine makers. In this context, Snecma, part of SAFRAN group, has designed and funded an important research campaign, the COGNAC project (**C**OMpetition between the **G**radient effect and the scale effect in **N**otch fatigue **A**nd **C**ontact fatigue), intending to improve the understanding of fretting-fatigue with a direct consequence on the company procedures in terms of dimensioning rules and methodologies. This PhD thesis has been performed as a part of this research framework.

In the next section the principle of functioning of a turbofan engine is presented which is followed by a deeper analysis of the mechanism that makes some of the engine components the perfect spot for failures caused by fretting-fatigue.

1.1.1 Turbofan

The turbofan is an air-breathing jet engine widely used in commercial aircraft and business jets due to the high thrust combined with good fuel efficiency. As its name suggests (“turbo” + “fan”), it is composed by a gas turbine which generates mechanical energy from combustion, and a ducted fan that exploits this energy to accelerate the airflow rearwards.

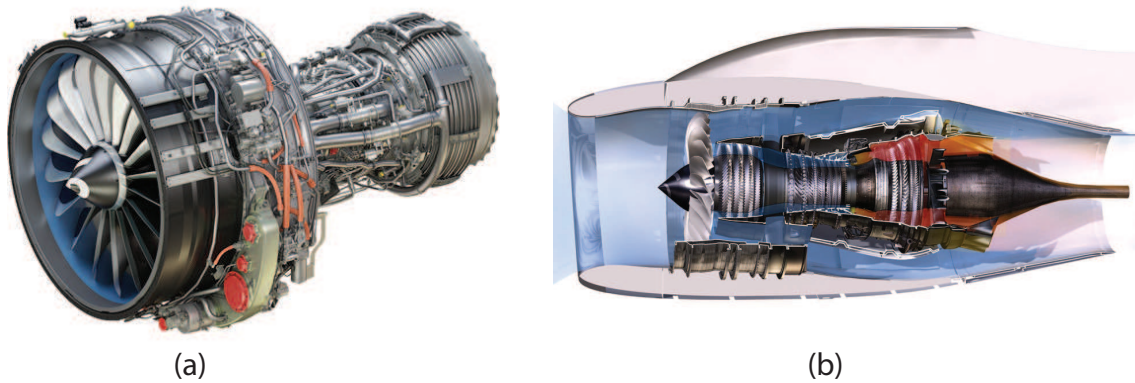


Figure 1.1: (a) LEAP; (b) SaM146.

The first and the most characteristic component in the engine is the fan, which purpose is to suck air from the outside accelerating it. The amount of air that the fan can handle is enormous considering that at takeoff this value can overcome a ton per second of air. Passing through the fan, the air separates into two streams; only 15/20 per cent of it flows into the internal core of the engine (hot stream) while the remaining 80/85 per cent (cold stream) is ducted along the outside of the core and is forced through a narrowing space which increases its speed (Figure 1.2). The ratio of the air bypassing the core to the air passing through it, is called bypass ratio. Because of its huge volume, the bypass air only needs to accelerate by a small amount in order to develop huge thrust.

The hot stream enters the internal core where two compressor stages, the low-pressure compressor (LPC) and high-pressure compressor (HPC), force its temperature and pressure to rise. Here the air passes through several smaller stages, each consisting of a set of rotating blades in between a set of stationary blades. Then the air enters the combustion chamber where its energy level is greatly increased by adding fuel through a series of injectors and igniting it. The higher is the pressure of the air the more energy will be added during combustion and the more efficient the process becomes. This is why the compressor stages are so important.

At the exit of the combustion chamber the super heated (the air at this stage can reach 1700 °C) and compressed air enters the high-pressure turbine, which has the purpose to extract enough energy from the air to turn the high-pressure compressor. Then, the hot stream flows into the low-pressure turbine that has the task to power

the low-pressure compressor as well as the large fan thanks to the remaining energy absorbed from the airflow.

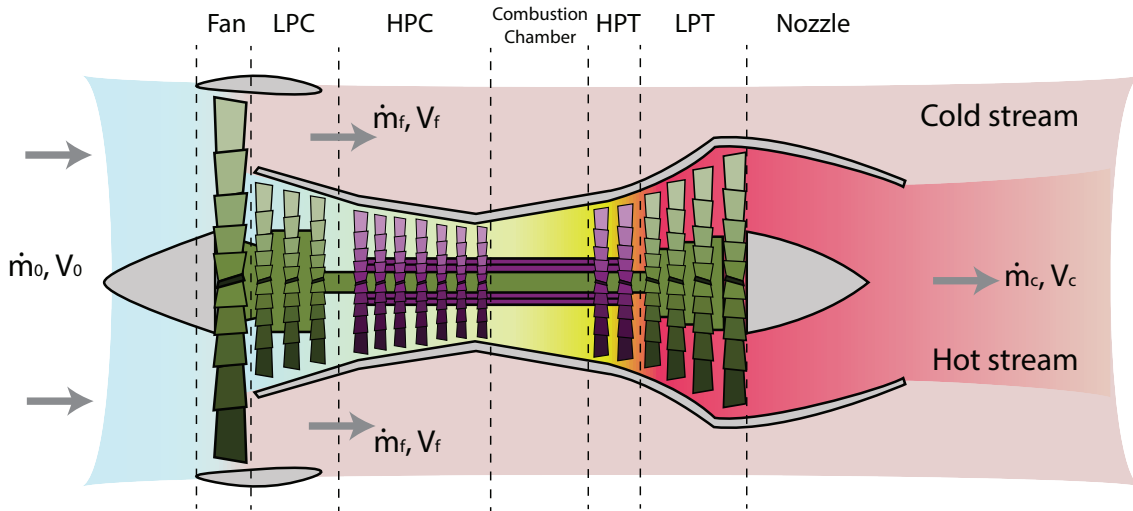


Figure 1.2: Turbofan schematic.

Finally the combusted air races out through the exhausted nozzle at the back of the engine to be accelerated one last time. This exhausted stream produces only 20 percent of the engine total thrust. The remaining 80 percent is produced by the large volume of accelerated bypass air exiting the fan duct.

The description of the principle of functioning of the turbofan helps to realize the complexity of this engineering system. A small amelioration in one of the steps listed above can have a huge impact on the performance. Engine makers like Snecma, are challenged to continuously increase the overall efficiency of their products, in order to remain competitive: a little reduction in the fuel consumption means a considerable saving for airline companies. This optimization can be obtained in different ways:

- a better understanding of the aerodynamics inside the rotating parts can increase the performance of the compressor and turbine stages;
- new materials able to withstand higher temperatures have a positive effect on the thrust and fuel consumption;
- the use of composite materials, as it is the case for the fan of the LEAP engine, allows to reduce the weight of the structure;
- a better comprehension of the material deterioration due to fatigue will reduce maintenance costs.

The last point is the one debated in the research work, presented here, aiming at bringing new knowledge to ameliorate the understanding of fretting-fatigue, reducing in this way the maintenance cost and optimizing the design of the parts concerned by this phenomenon.

1.1.2 Connection between disk and blade root

In the previous section the principle of functioning of a modern turbofan engine has been presented. To sum up, the turbine stages extract the energy from the airflow, exiting the combustion chamber, to turn the compressor and the fan. It is clear, therefore, that the rotating parts play a major role. They usually share a common design configuration: a set of blades attached to a disk that is fitted onto the shaft which is responsible for the transmission of the power from one stage to another.

Concerning the attachment between blade root and disk, different choices can be made to ensure the connection. In Figure 1.3, the most common configurations are shown. The blades are fitted into the disk via a dovetail or a fir-tree connections, that ensure the radial retention of the blade, transmitting at the same time the tangential force to the disk. In addition, they allow the easy insertion and removal of the blades, which represents a fundamental requirement since in case of failure only the damaged blade is replaced with positive consequences in terms of maintenance cost and reliability.

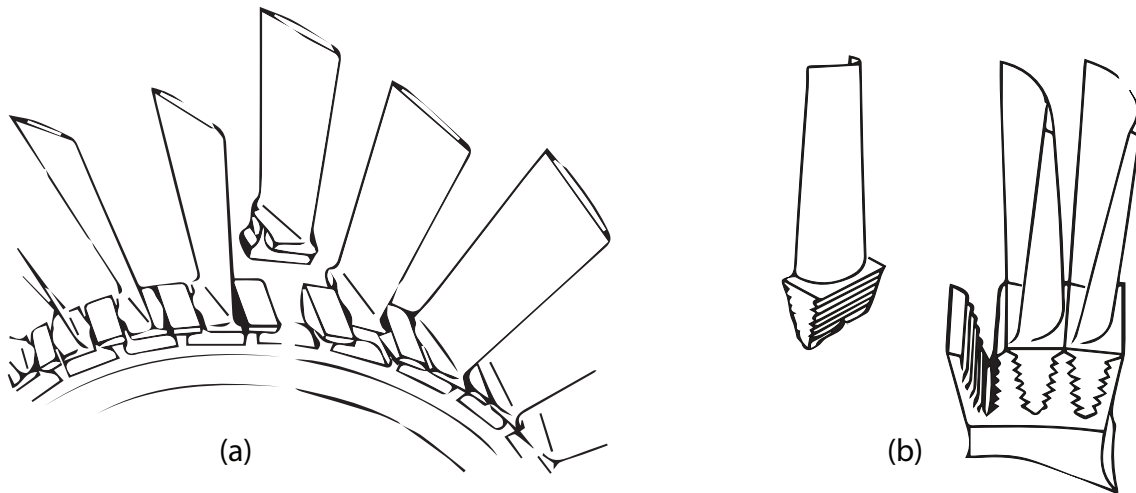


Figure 1.3: (a) Disc-blade dovetail type joint; (b) disc-blade fir-tree type joint.

The strength of this type of connection represents also its weakness. The easy insertion and removal capability requires a small clearance between the dovetail blade root and the corresponding disc surface. Once the engine is switched on the centrifugal force tends to pull apart the joint, generating a normal load that presses the two bodies one against the other while the interaction between the airflow and the blades causes vibrations that propagate up to the contact surface where a relative displacement (δ) is experienced, (Figure 1.4).

The micro-slip is the cause of surface damage which leads to the initiation of embryo cracks very early in life. The initiated cracks can then propagate either in the blade root or in the disc due to the cyclic bulk fatigue loading generated by the centrifugal force. The design of the turbofan is such that the failure of a blade root

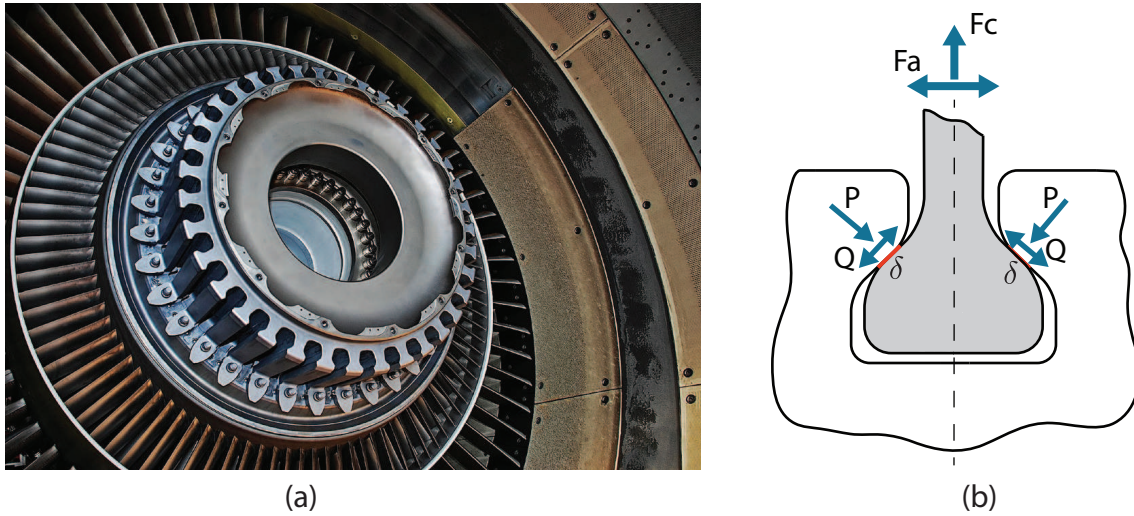


Figure 1.4: (a) CFM56-7B fan blade hub; (b) disc-blade connection load components.

with consequent detachment of the part can be absorbed entirely by the external structure of the engine, as it was the case for the accident reported in [ATSB, 2002]. On the contrary, the disc failure will inevitably have more serious consequences since its mass coupled with the high rotational speed gives it enough energy to pass through the engine case. The crash of a DC-10 in Sioux City, Iowa, in 1989 or the most recent uncontained engine failure experienced by an A380 in Singapore (Figure 1.5) show the results that this type of malfunctioning can have.

In order to limit the damage at the contact interface between the blade root and the disk some solutions can be adopted:

- the modification of the surface properties through the introduction of a compressive residual stress can stop or at least slow down the crack propagation process, [Liu and Hill, 2009, Mall et al., 2011];
- the intercalation of a thin layer of softer material between the contacting bodies works as a shelter preventing the propagation of the damage into the substrate [Fridrici et al., 2003].

The analysis presented in the following sections does not take into account the aforementioned techniques to mitigate the damage at the contact surface. With that said, there are no particular limitations for the introduction of the effects of these palliative techniques inside the methodology developed and this could be the object of future works.

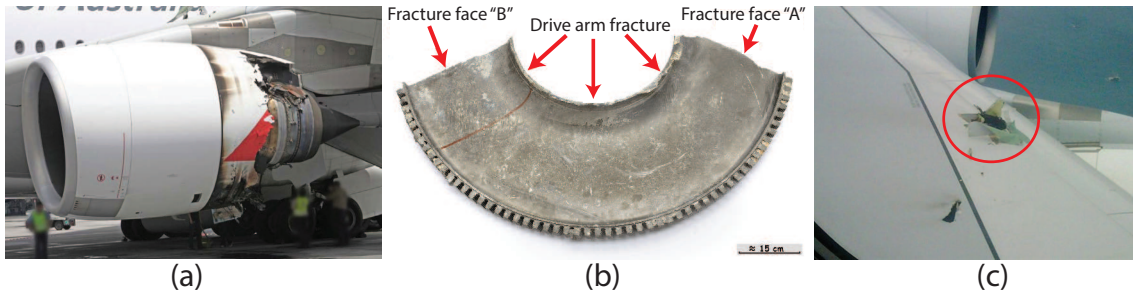


Figure 1.5: (a) Airbus A380-842 disc failure; (b) section of the IP turbine disc; (c) damages resultant from disc failure, [ATSB, 2010].

1.1.3 In-flight loading condition experienced at contact interfaces

The first step in the process of preventing catastrophic failure of the blade root/disc attachment is the knowledge of the exact load spectrum that this part will experience. An accurate estimation, however, is hard to obtain since it is almost impossible to perform in-situ measurements during in-flight service. A first evaluation can be done by simplifying the classic flight mission in three different phases: take off, cruise and landing (Figure 1.6).

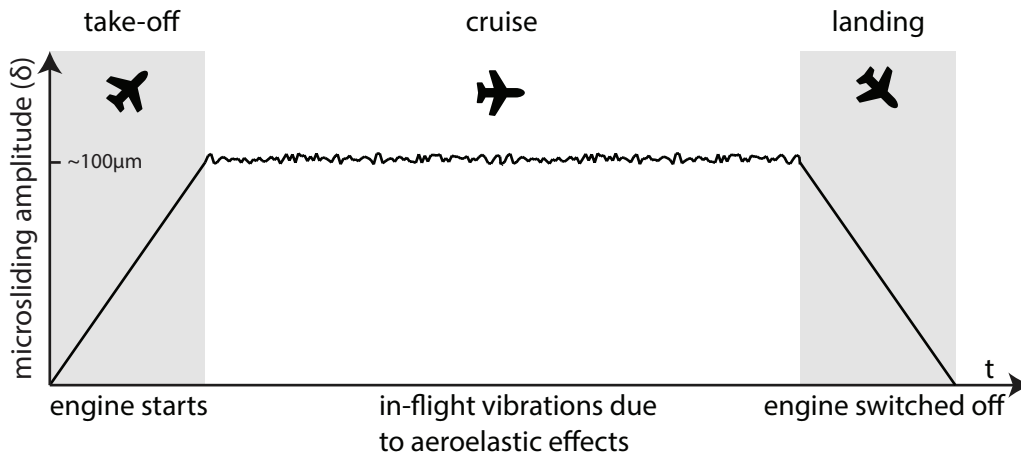


Figure 1.6: In-flight relative displacement at the contact interface, [Mary, 2009].

During the take-off phase the engine starts and the centrifugal force, experienced by the blades, attains its maximum. As a consequence an important displacement is observed at contact interface (50 - 100 μm). Once the aircraft reaches its cruise altitude the rotational speed of the turbofan remains almost constant as well as the centrifugal force. This phase of the flight is characterized by high frequency vibrations caused by the interaction between the airflow and the blades resulting in

micro-displacement over part of the contact interface ($\simeq 10\ \mu\text{m}$). Finally at the end of the landing phase, the engine is switched off and the loads fall to zero.

To sum up, the connection between blade root and disc experiences two types of fatigue loading:

- i) low cycle fatigue (LCF) loads that characterize take-off and landing;
- ii) high-cycle fatigue (HCF) loads caused by high frequency vibrations that are predominant during cruise.

Fretting-fatigue is generated by the coupling between this two type of loading; the high frequency vibrations produce micro-displacements over part of the contact interfaces damaging the surface and promoting the initiation of cracks (fretting) while the fatigue loads, generated by the cyclic variation of the centrifugal force, play an important role in the crack propagation.

A more detailed analysis of the contact status at the interface between the disk and the blade root, highlights the presence of a central zone where the two bodies are in stick condition, surrounded by a second zone in the proximity of the contact edges where slip is experienced (Figures 1.7). The discontinuity at the transition between stick and partial slip zone creates a strong stress concentration. Furthermore, the influence of the contact rapidly vanishes as soon as we move away from the surface, thus a steep stress gradient is observed.

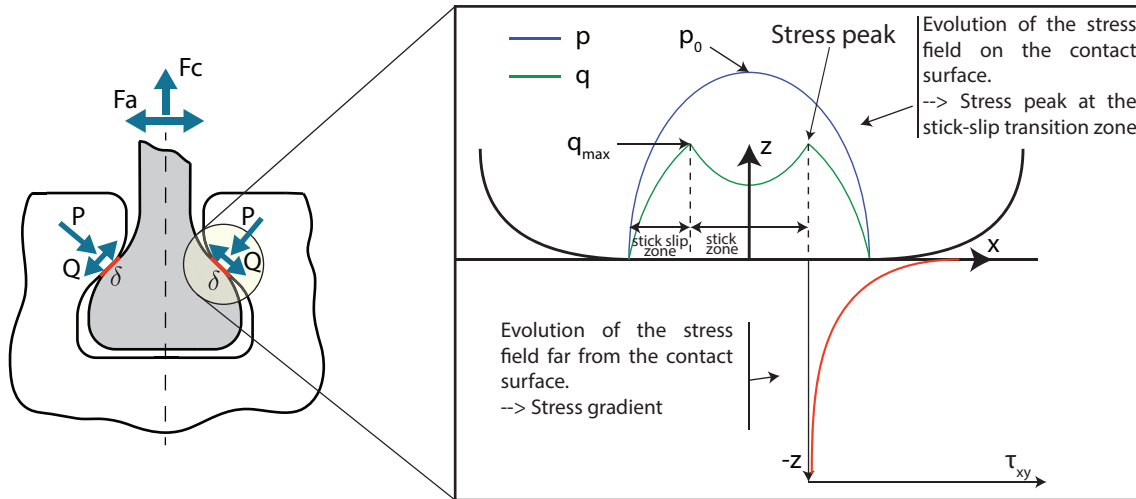


Figure 1.7: Evolution of the stress tensor at the contact surface and far from it as a function of the contact status, i.e. stick or stick-slip.

1.1.4 Snecma dimensioning process

As previously mentioned, it is difficult to obtain the exact load distribution and evolution experienced by the blade root/disc connection during flight. Numerical

computations are therefore employed to enrich the data obtained through experimental tests. For this purpose, finite element models are extensively used to compute the quantities - stress, strain or displacement - used for the dimensioning process of the part as well as for its optimization. By simulating the aerodynamic interaction between the blades and the airflow and the effects of the centrifugal force, it is possible to estimate the mechanical loads arising in the structure. For instance, this type of computation permits to compute the relative displacement between the contacting bodies.

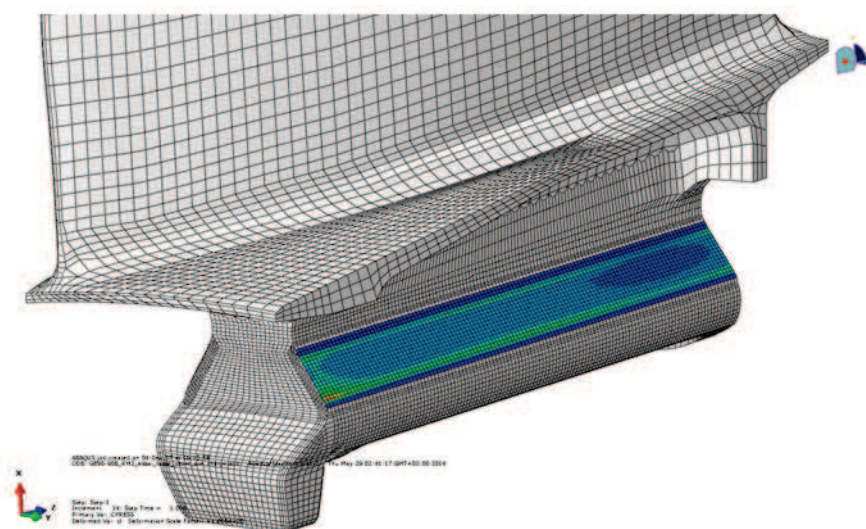


Figure 1.8: FE model of the blade root attachment.

The drawback of this procedure relies on the sensitivity of the results obtained to the level of mesh refinement. A fine mesh (few micrometers) is needed to obtain a convergent solution of the stress distribution at the contact interface (Figure 1.9). This requirement, however, is in conflict with the need of fast computations that can be used for dimensioning purposes. A compromise is therefore reached in order to obtain a sufficiently precise result, minimizing the computational cost.

To ensure the robustness of the procedure a safety factor is applied to the results obtained.

One of the objects of the work presented here is to provide a solution at the “precision vs computational cost” problem. This is possible through a multiscale description of fretting-fatigue that will be presented in the next chapter.

1.1.5 Industrial objectives

The work presented in this manuscript is part of a research framework started by Snecma in 2010, the COGNAC project (**C**ompetition between the **G**radient effect

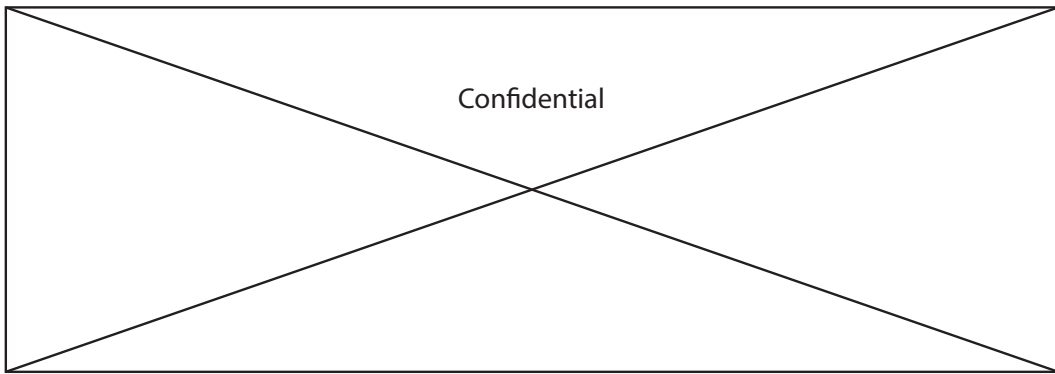


Figure 1.9: Stress distribution at the blade root / disc contact surface, [Ferré et al., 2013].

and the scale effect in **Notch fatigue** And **Contact fatigue**), aiming at better understanding the gradient effect with respect to crack initiation and propagation in fretting-fatigue. Several questions on how to deal with this phenomenon remain open and need to be answered:

- For a contact condition characterized by the presence of a partial slip zone over part of the surface, the discontinuity between the stick and the slip zone introduces a singularity at the origin of a strong stress concentration (Figure 1.7).

For industrial applications, usually, a 3D FE model is employed to compute the stress distribution at the contact surface. However, due to the presence of the stress concentration factor, to obtain a convergent solution a fine mesh is needed (few micrometers) close to the transition zone. For industrial applications, this requirement is difficult to respect since the computational cost would be too high .

It is therefore important to develop prediction tools which use as input quantities that are easier to obtain than the local stresses. This is particularly true for applications characterized by complicate geometries.

- The influence of the contact rapidly vanishes far from the surface. The microcracks, initiated at the interface can therefore stop as a result of the decreasing stress tensor value which is no more sufficient to promote crack growth.

In addition, for the same stress value at the contact surface, different geometries generate different stress gradient evolutions with a direct effect on the fatigue life of the part. Therefore, an analysis based on local quantities (maximum contact pressure, p_0 , and shear stress amplitude, q_{max}) will produce outcomes depending not only on the material of the contacting bodies but also on the geometry of the experimental setup.

This is a major problem for Snecma, because it makes the experimental data obtained on laboratory test machines almost unusable for dimensioning purposes since the scale of these specimens are usually very different from the real industrial part.

A local approach is not sufficient to describe properly the effect of the stress gradient.

- The material volume interested by a stress level able to cause fatigue damage is low and comparable to the grain size. As a consequence fatigue life scatter and size effect are observed which are linked to the probability of encountering a favorable site for crack initiation.

Regarding the research framework in which this work has been performed, three other PhD thesis have been funded on complementary subjects with the aim to achieve a breakthrough in the understanding of fretting-fatigue. In particular, Johan Bellecave, and Barabara Ferry are performing their research in collaboration between the LMT laboratory in Cachan and the university of Brasilia under the supervision of Sylvie Pommier and Alex Araújo. Their works focus on the experimental investigation of the competition between gradient effect and size effect in fretting-fatigue. The fourth PhD thesis is performed at Pprime, by Julien Simon and supervised by Yves Nadot. The aim in this case is to study the effect of the stress gradient in v-notch specimens focusing on the similarities with fretting-fatigue.

The 4 thesis are linked by the challenge to reproduce accurate results concerning initiation, propagation or fatigue life prediction in fretting-fatigue just by using data coming from experimental tests performed on v-notch specimens. These tests are relatively simple and cheap compared to the ones needed for fretting-fatigue. If this possibility is confirmed, it will represents an important result.

1.2 Fretting-fatigue modeling

1.2.1 Historical review

Historically, the first authors reporting fretting related effects were Eden, Rose and Cunningham in a scientific article published in 1911, [Eden et al., 1911]. Despite the initial object of their research was to determine the effect of rotational speed on the Wölher curve of a steel specimen using a rotating beam apparatus, they observed the formation of oxide debris in the steel grips of the testing machine. This curious phenomenon was the object of further investigations in the work of Tomlinson, [Tomlinson, 1927], who designated a test apparatus to produce small amplitude relative movement between two contacting bodies. He concluded that the resultant “brown stain” appearing on the surfaces was related to the tangential motion between the two parts.

Meanwhile fretting side effects started to be observed in industrial applications. Almen [Almen, 1937] performed some research at General Motors on false brinelling as a response to severe wheel bearing damage observed in automobiles that were transported by ship or train before to be delivered. The conclusion was that the vibrations caused during the transportation were at the origin of the damage.

The first big step forward in the understanding of fretting is accomplished thanks to the work of Tomlinson and his colleagues [Tomlinson et al., 1939] that in 1939 published a paper that introduced some fundamental concepts. In particular it is shown that the corrosion observed has mechanical origins rather than chemical ones, and in addition it is recognized that slip - the tangential relative motion over part of the contacting surfaces - is the *sine qua non* of surface damage appearance. Furthermore, the authors suspected a relation between the fretting damage spot and the crack initiation site. Lastly, it is in this paper that the term “fretting corrosion” was employed for the first time.

The appreciable loss in fatigue properties caused by fretting was confirmed in [Warlow-Davies, 1941]. The author performed a series of tests where the specimens experienced first a fretting load in order to create the classic fretting scar on the surfaces, and later the same specimens were inserted in a fatigue machine. By this means, the negative effect of fretting can be quantified by measuring the percentage loss in fatigue strength with respect to the unfretted specimen. The tests were performed for a medium carbon steel and for a nickel-chromium-molybdenum alloy steel showing a fatigue strength reduction of around 13 and 18 per cent, respectively.

Similar results were obtained by [McDowell, 1952, Fenner and Field, 1958]. The first showed that the conjunction of fretting and fatigue produce fatigue strength reduction factors up to 5, while the second proved that fretting works as a catalyst for the crack initiation process observing that the reduction effect was related to the slip magnitude. Fenner showed that the fatigue strength of an aluminum alloy decreases progressively with the increase of the size of the partial slip zone up to 10 μm .

Despite the first scientific and technical breakthroughs, at that time, fretting was still an obscure subjects for engineers. I find amusing what (Sir) Stanley Hooker (assistant chief engineer of Rolls-Royce Ltd) said about Warlow-Davies, [Sharman, 2002], who works under his direction from 1942 to 1946:

“No scratch or frettage was too microscopic to escape his attention, and he possessed the sixth sense of being able instantly to recognize whether such a mark would lead to a dangerous failure”.

Be able to recognize whether a fretting scar was dangerous or not for the mechanical integrity of the part was seen as a magical sixth sense capability!

In the last 50 years an increasing interest on fretting-fatigue has driven a lot of researchers towards important advancements in the discipline. Among the most relevant works, it is worth mentioning the series of papers published by Nishioka and Hirakawa, [Nishioka et al., 1968, Nishioka and Hirakawa, 1969a, Nishioka and Hirakawa, 1969b, Nishioka and Hirakawa, 1969c, Nishioka and Hirakawa, 1969d,

Nishioka and Hirakawa, 1972]. The authors recognized the importance of the slip magnitude in the determination of the damage caused by fretting-fatigue. They focused their attention on press-fitted axles assemblies analyzing the effect of various factors such as size, shape, clamping pressure, magnitude of nominal stresses, on the amplitudes of the relative slip.

They noticed that the damage produced was not proportional to the slip magnitude, in particular, when the relative slip becomes larger than a certain value (in their case 25 microns) the alternating tangential stress to apply in order to observe crack initiation increases. Once the micro-cracks initiate they are soon worn out. This observation will be confirmed and validated some years later by Vingsbo and Söderberg, [Vingsbo and Söderberg, 1988], who defined three regimes: stick regime, mixed stick-slip regime and gross slip regime, as a function of the damage produced. Furthermore, they observed that the cracks usually started in the zone where the stress concentration due to contact is the highest one, (at the contact edges) with an angle inclined towards the center of the contact zone, which is found to be the direction which maximizes the shear stress.

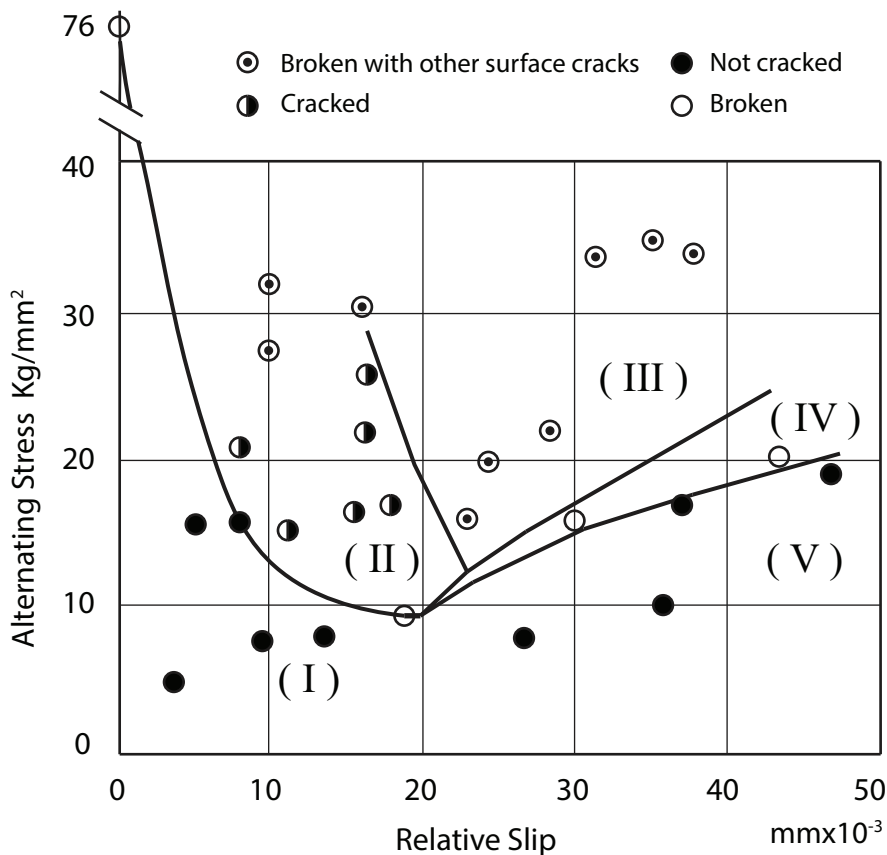


Figure 1.10: Effect of relative slip on fretting-fatigue strength, [Nishioka and Hirakawa, 1969a].

During the Seventies, on the one hand, an increasing number of papers are published focusing on better understanding the fretting-fatigue damage mechanisms, on the other hand, some researchers start addressing the problem of how to efficiently design against fretting-fatigue. It is the case of the papers published by Waterhouse in 1976, [Waterhouse, 1976] and by Hoepfner and Gates in 1981, [Hoepfner and Gates, 1981], where the authors try to give some practical advice in order to avoid fretting-fatigue damage. For instance, the use of lubricant decreases the friction coefficient diminishing the damage at the contact interface. The careful selection of compatible materials, the reduction of the vibrations at the interface in order to limit the slip magnitude, an intelligent design aiming to reduce the stress concentration factors at the contact borders, are some of the advice given by the authors. Furthermore, surface treatments appeared to be one of the best way to avoid or at least to slow down the negative effect of fretting-fatigue as it is proved by the numerous papers that start to be published in those years analyzing this technique, [Waterhouse et al., 1962, Taylor and Waterhouse, 1972, Waterhouse et al., 1983]. In [Waterhouse et al., 1962] the influence of electrodeposited metals on the mechanical response of a mild steel is investigated concluding that the overall effect depends on the balance between the reduction of fretting damage and the negative effect of plating on the fatigue strength of the material. In [Taylor and Waterhouse, 1972] the same type of analysis is carried out, focusing on the effect of sprayed molybdenum coatings. Similar results were obtained. Another possibility to reduce the fretting-fatigue negative effects is to introduce compressive stress on the surface of the part by the use of shoot-peening, [Waterhouse et al., 1983] (Figure 1.11). This last techniques is still used nowadays.

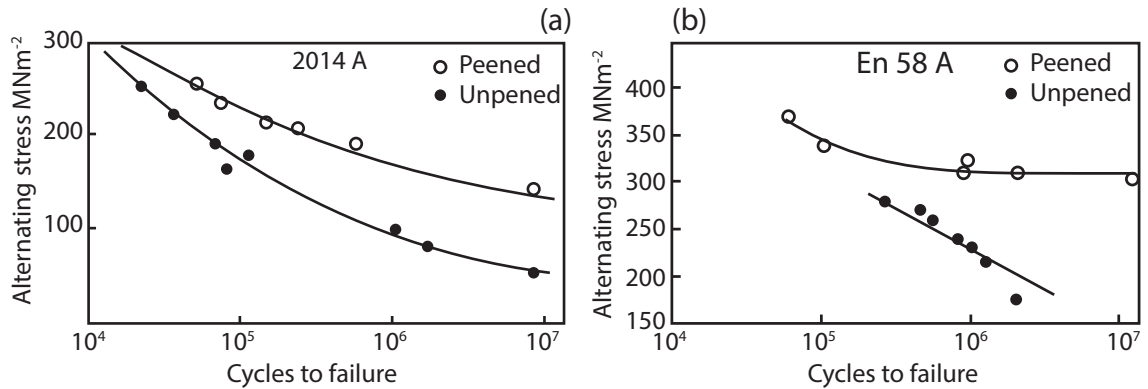


Figure 1.11: (a) Fretting-fatigue S-N curves for aluminium alloy 2014A in the fully aged condition; (b) fretting-fatigue S-N curves for stainless steel EN58A in the annealed condition, [Waterhouse et al., 1983].

With the publication of Johnson’s monograph on contact mechanics, [Johnson, 1985], another improvement in the understand of fretting-fatigue mechanism is achieved. Some interesting analytical results concerning stress and strain at the interface between two contacting bodies are derived, enriching the existent solu-

tions presented some decades before in [Hertz, 1882, Cattaneo, 1938, Muskhelishvili, 1953]. Together with this new information on the mechanical fields arising at the contact surface, some authors started to apply fracture mechanics tools to predict fretting-fatigue endurance. In [Edwards, 1984], the life estimation is done using stress intensity factors that take into account the bulk stress and the forces introduced by fretting. Today, this approach remains very promising as it is proven by a recent article published by Hills and his colleagues, [Hills et al., 2012], who use a similar approach to predict the fatigue life of the specimen.

In the last years the number of articles on fretting-fatigue is increased exponentially. A rapid search on ScienceDirect shows that the number of papers related to fretting-fatigue published in the last twenty years (5122) is more than 3 times the total number of articles published before 1990 (1591). This is the reason why, even if I tried to be exhaustive, I would inevitably miss some important papers. With that said, I would like to spend some words on the work of Hills and Nowell, [Hills and Nowell, 1994] and the one of Giannakopoulos and his colleagues, [Giannakopoulos et al., 1998, Giannakopoulos et al., 2000]. With “Mechanics of Fretting Fatigue”, Hills and Nowell have written a book that is now a bestseller of the fretting-fatigue literature in which a state of the art description of this phenomenon is presented. Giannakopoulos and his colleague, instead, are among the first to demonstrate a quantitative equivalence between contact and fracture mechanics. These two works have had an important influence on the research performed and presented in this manuscript.

1.2.2 Fretting-fatigue test geometries

Fretting-fatigue is considered a plague for the modern industry and its negative effects on mechanical assemblies have been experienced in many different sectors such as automotive, aerospace, train, construct equipment, wire ropes, etc. No matter which industry is concerned, all of them share the need to certify the components to ensure that are riskless for the users. For this purpose experimental test campaigns are usually needed and, considering the wide range of contact configurations existing in the industrial components, a simplification is required. Experimental tests are standardized around three different reference contact configurations: sphere/plane contact, cylinder/plane contact, plane/plane contact.

1.2.2.1 Sphere/plane contact

Sphere/plane contact, is a uni-dimensional configuration for which analytical results obtained by Hertz, [Hertz, 1882], for frictionless normal contact, and by Cattaneo and Mindlin, [Cattaneo, 1938, Mindlin, 1949], are available. This configuration has the advantage to be relatively easily to setup from an experimental point of view since there is no problem related to the alignment of the sphere with respect to the plane being the contact surface a point. On the other hand a 3D computation of the mechanical fields is required whenever the loads are not axisymmetric or the crack

propagation phase is studied; in these cases the computations become heavily time consuming.

1.2.2.2 Cylinder/plane contact

In this case the contact is bidimensional. This statement is true for a value of the ratio, b/a higher than 5, where b is the thickness of the pad, and a is the contact semi-width as it is proven in [Fellows et al., 1995]. In other words, if this condition is respected, the highest stresses will be reached at the center of the specimen (Figure 1.12a), and they will correspond to a plane strain condition. Therefore, the problem can be represented as if it was bidimensional. Due to this important characteristic, this configuration is the one commonly used in fretting-fatigue test campaign; first, the experimental setup is well mastered, secondly, a fast comparison between experimental and computational results is possible.

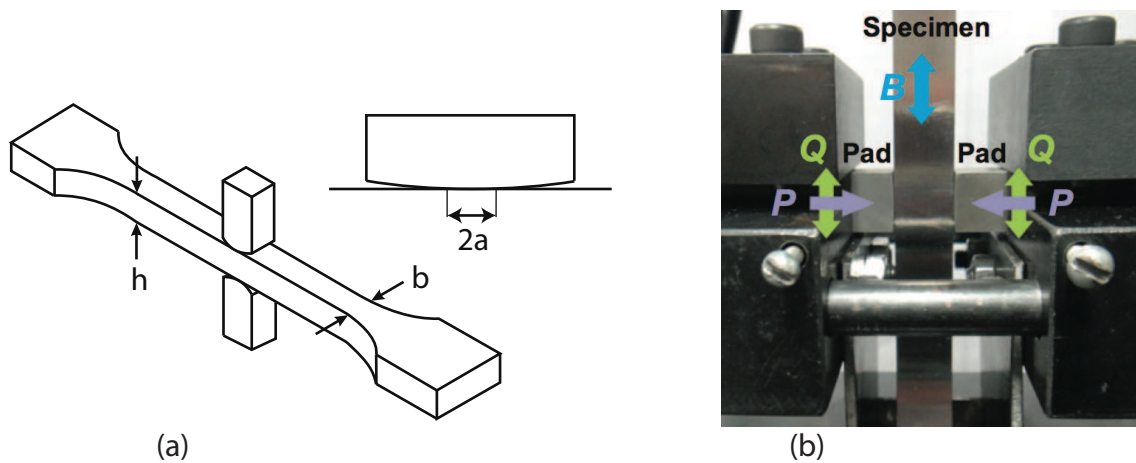


Figure 1.12: (a) Schematic of the dog bone specimen/cylindrical pad configuration; (b) fretting-fatigue apparatus, [Araújo and Castro, 2012].

1.2.2.3 Plane/plane contact

This configuration leads to a tridimensional contact characterized by a stress distribution that, close to the contact borders becomes discontinuous. Some important difficulties in the experimental setup, such as the alignment of the pad, and the need to perform tridimensional FE computations, limit its application. It is worth mentioning that in the last years some analytical solutions concerning the stress distribution have been obtained, [Ciavarella and Macina, 2003].

1.2.2.4 Dovetail/blade root contact

In an article published in 2006, [Rajasekaran and Nowell, 2006], the authors conceived an experimental apparatus to reproduce the loading experienced by a dovetail blade root in an aircraft gas turbine. Certainly, this setup allows to well represents the industrial attachment but, at the same time, it applies to only a specific geometry and is far more difficult to put in place with respect to the aforementioned contact configurations. For this reason this type of test machines represents a niche among the fretting-fatigue test apparatus.

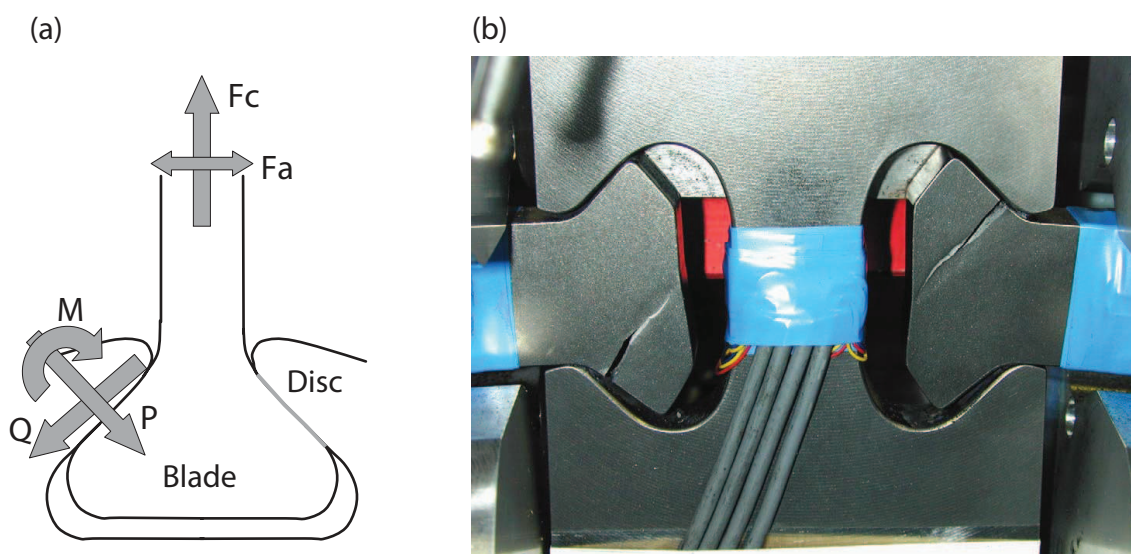


Figure 1.13: (a) Schematic representation of the loading at the interface disc/blade root; (b) dovetail blade root test apparatus [Rajasekaran and Nowell, 2006].

1.2.3 Fretting-fatigue test apparatus

In the previous section the different contact configuration used to simulate fretting-fatigue have been described. Here a detailed description of the whole apparatus employed in the test campaigns is presented. With the exception of the dovetail/blade root contact configuration the other ones share more or less the same setup. In Figure 1.12b, the fretting-fatigue apparatus used by Araújo and his colleagues at the university of Brasilia is shown while in Figure 1.14 a schematic representation of a single actuator test machine and a double actuator one are presented.

Concerning the double actuator test machine (Figure 1.14b), two clamps hold the specimen in the right position. The first one is fixed while the second one is connected to an hydraulic actuator, (actuator 2) that is free to move in the axial direction controlling the bulk tension in the specimen. A second actuator, (actuator 1) is connected to a cradle, carrying the fretting pad arrangement. The two pads

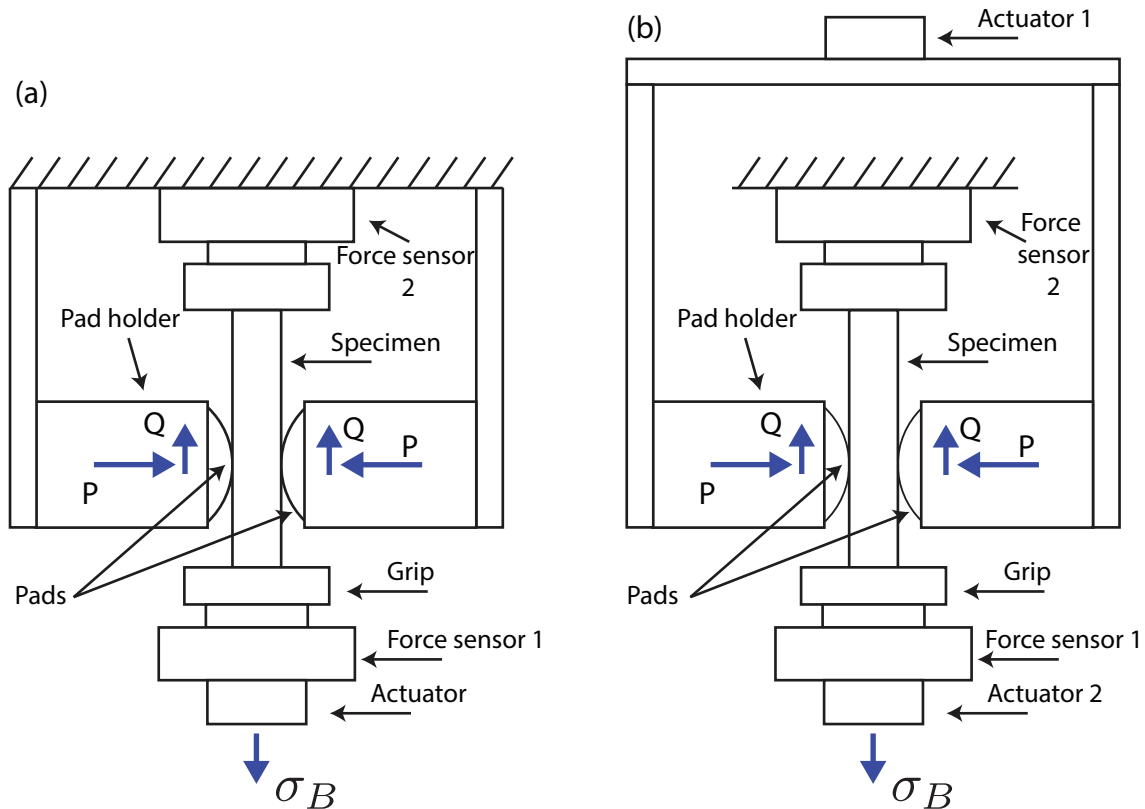


Figure 1.14: (a) Fretting-fatigue single actuator machine; (b) Fretting-fatigue double actuator machine, [Lee and Mall, 2004].

are pressed onto the specimen surface to create the normal force, P , while the tangential force, Q , is regulated by the displacement of the actuator, (actuator 1). The displacement between the specimen and the pads is then recorded, for instance, through the use of laser sensors.

In the case of a single actuator test machine (Figure 1.14a), as its name suggests, there is a single actuator which control the bulk tension in the specimen, σ_B . The fretting pad arrangement is attached to the fatigue test frame and works as a spring that reacts to the motion of the pads pressed against a “dog bone” fatigue specimen. The reaction of the spring results in the cyclic tangential load, Q , whose value is half of the difference between the forces measured at the lower and upper load cells of the servo-hydraulic system.

To sum up, fretting-fatigue is a complex phenomenon that can provoke the failure of the assembly and therefore laboratory tests are needed to understand the damage mechanisms. Since the geometry of the industrial parts are usually extremely complex, a first simplification is made in order to develop a reasonable complex fretting-fatigue test bench. This means that usually one of the following contact configurations - plane/plane, cylinder/plane, sphere/plane - shown in Figure 1.15, is retained.

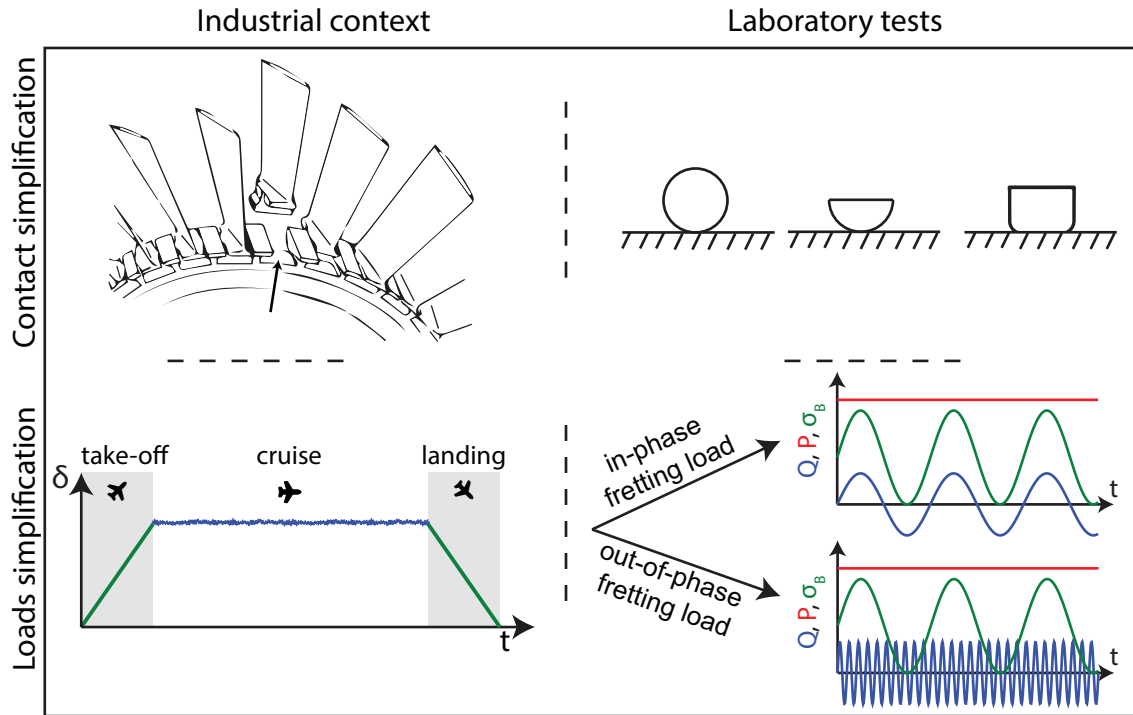


Figure 1.15: Geometrical and load simplifications in fretting-fatigue tests.

A second simplification is done on the load evolution experienced at the disc/blade root connection. Considering that the aeroelastic vibrations can reach frequencies close to 400 Hertz, it is clear that the ratio between the number of fatigue cycles (centrifugal force due to engine switch-on and switch-off) and the fretting ones (generated by the vibrations due to the interaction with the airflow) is really low. In other words, for each flight, just one fatigue cycle is registered while millions of fretting cycles are experienced by the part. This is something to bear in mind since during test campaigns this condition is usually not respected.

The possible test scenarios (with some exceptions) are therefore two: in the case in which a single actuator fretting-fatigue apparatus is the only available, the fatigue load and the fretting ones are inevitably in phase, while the two load modes can be decoupled within certain limits with a double actuator machine. Analyzing the literature on fretting-fatigue, the first setup has been really common and is now replaced by better performing double actuator devices. With that said, even with this setup it is difficult to simulate the real in flight loads ratio experienced by the disc/root blade attachment, since it would mean to have extremely long tests with important costs. As a consequence, the effect of the fatigue load will be overestimated.

1.2.4 Slip quantification for transition criteria

As it is already mentioned before, one of the peculiarities of fretting-fatigue is represented by the microdisplacements over part of the interface that can severely damaged the surface. It is necessary to quantify the “micro” displacement in order to separate the different slip regimes that have a direct effect on the damage mode.

A first distinction can be made between fretting regime, characterized by a central zone which is never exposed to the external environment, and reciprocal sliding. A simple way to formalize the transition between these two conditions is obtained using the ratio of the displacement amplitude, δ^* , to the contact semi width, a_c , [Fouvry et al., 1996]. For values of the ratio higher than 1, the contacting parts are in total slip condition otherwise fretting regime is established (Figure 1.16).

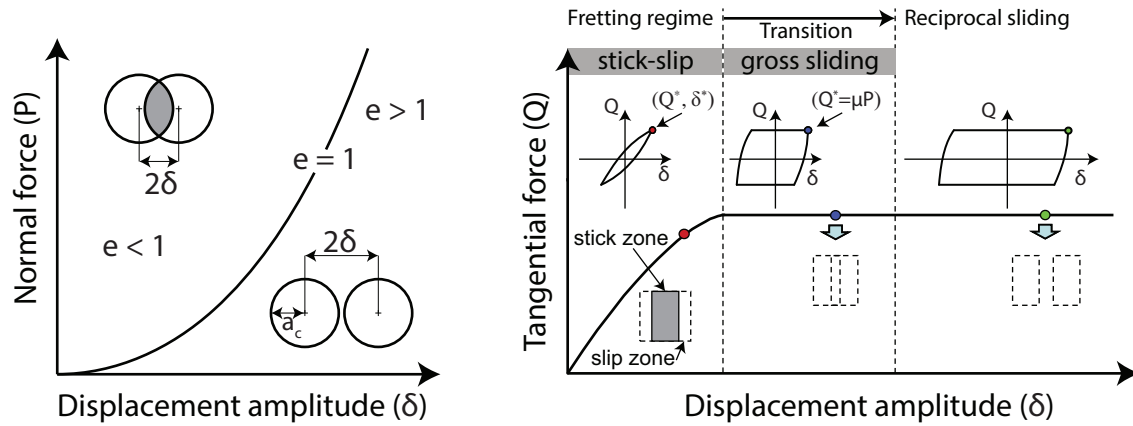


Figure 1.16: Transition between fretting regime and reciprocal sliding, [Meriaux, 2010, Mary, 2009].

In this manuscript we focus on the fretting regime since is the situation experienced at the attachment between disc and blade root. With that said, by analyzing the contact behavior through the evolution of the tangential force, Q , as a function of the displacement, δ , a subdivision of the fretting regime can be made. Three different slip conditions are observed, as described in [Vingsbo and Söderberg, 1988]:

- **Stick condition:** in this case the tangential force at the contact interface, $q(x)$, is lower than the Coulomb limit, $\mu p(x)$, where μ is the Coulomb’s coefficient and $p(x)$ is the local normal force. The displacement registered is therefore exclusively produced by the elastic deformation of the parts;
- **Stick-slip condition:** locally the Coulomb’s slip limit is reached, $q(x) > \mu p(x)$ and, as a consequence, a slip zone is created that is located at the extremity of the contact surface. The macroscopic response of the assembly, $Q(\delta)$, has an elliptic shape. The nonlinear evolution of $Q(\delta)$ is related to the friction at the contact interface that can be coupled with plasticity if the local stresses are high enough;

- **Gross slip condition:** the Coulomb's slip limit is reached on the whole contact surface and the response of the assembly, $Q(\delta)$, is characterized by a plateau where the tangential force, Q , remains constant with the increase of the displacement.

Among the three fretting regimes, the stick-slip condition is the one which causes more damage as it is explained in Section 1.3. It is therefore important during experimental tests to be able to recognize precisely the transition between stick-slip and gross-slip regime. In [Fouvry et al., 1996] three transition criteria for the sphere/plane contact configuration are presented: the energy ratio criterion, $A = E_d/E_t$, the aperture ratio criterion, $B = \delta_g/\delta^*$, and the system free ratio, $C = E_d/E_0$, (Figure 1.17). By comparing the three criteria to the respective constants, A_t , B_t , C_t , that represents the theoretical value at the transition from partial slip to gross slip, it is possible to estimate correctly the stick-slip limit.

To sum up, the damaging process in fretting-fatigue is highly dependent on the fretting regime experienced by the specimen. As a consequence, a good knowledge of this parameter is needed to perform representative test campaigns. The criteria presented by Fouvry and his colleagues, [Fouvry et al., 1996], are an effective way to control the transition from stick-slip to gross slip condition.

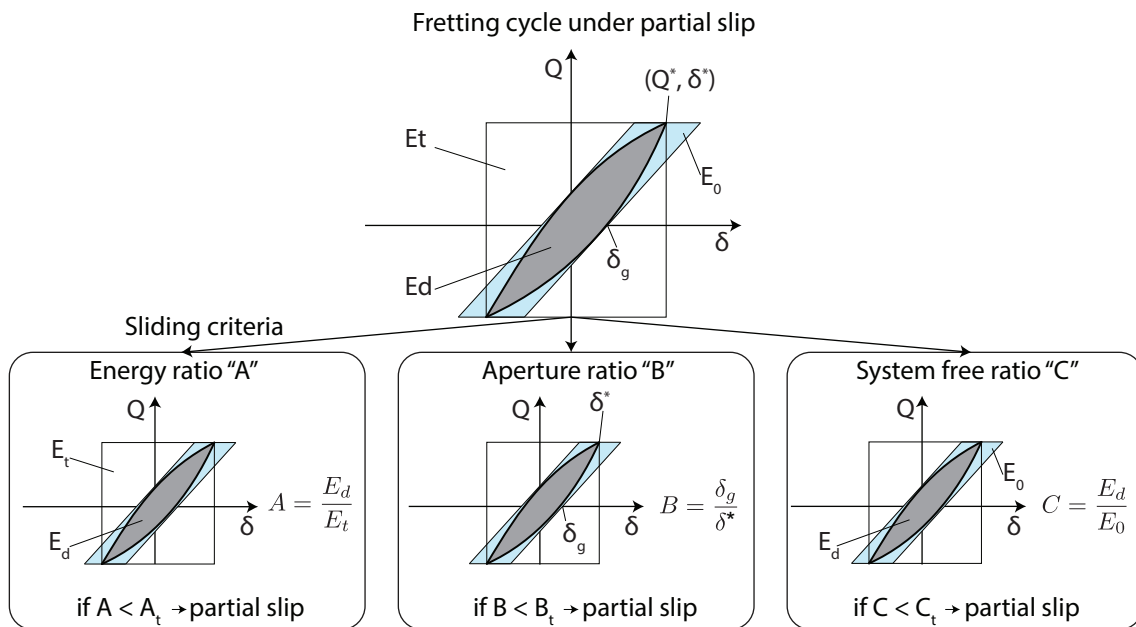


Figure 1.17: Transition criteria in fretting regimes, [Fouvry et al., 1996].

1.3 Damaging mechanisms in fretting-fatigue

In the previous sections the words fretting and fretting-fatigue have been used sometimes as synonyms. Of course the distinction is clear and the use of one term to replace the other was only related to the fact that, with respect to the arguments discussed, this simplification was acceptable. Conversely, speaking about the damaging process, a precise distinction is needed.

The diagram presented in Figure 1.18 describes the effects of a given combination of fretting and fatigue loads. If the example of the cylinder/plane fretting-fatigue test apparatus is considered, when the fatigue component, σ_B , is small, then the damaging process is mainly driven by the fretting loads, P and Q (Figure 1.14). By increasing the values of the tangential and normal force experienced at the interface between the specimen and the pad, it is likely that crack initiation will occur very early in the life of the part, followed by a long crack propagation phase which may end with the arrest of the crack if the fatigue load is not big enough. Following the same reasoning, if the bulk load becomes important cracks propagate faster and therefore the initiation phase becomes the dominant part in the life of the specimen. A further simplification leads to decouple the two components of fretting-fatigue, assuming that the crack initiation is controlled only by the fretting damaging process while the crack propagation depends mainly on the bulk loads. Surely, this is not completely true. For instance, in [Meriaux, 2010] an effect of the fatigue load on the initiation phase is observed, and, on the other hand, the fretting load influence the propagation phase even if their impact rapidly decreases far from the contact surface.

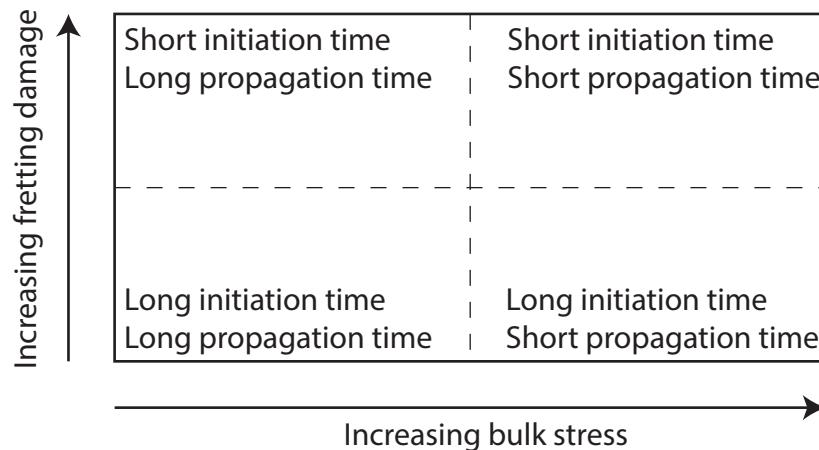


Figure 1.18: Loading conditions described by the term fretting-fatigue, [Hills and Nowell, 1994].

For the sake of simplicity, in the next paragraphs, the aforementioned simplification is done, i.e., the effects of the damage caused by fretting-fatigue are described

as if the fretting component (P, Q) could be perfectly decoupled from the fatigue one (σ_B).

1.3.1 Fretting map

Nishioka and Hirakawa, [Nishioka et al., 1968] were among the first, in 1969, to observe a direct effect of the slip magnitude on the life of specimens subjected to fretting loading. This was confirmed some years later by Vingsbo and Söderberg, [Vingsbo and Söderberg, 1988], that precisely quantify this dependence.

Regarding the three fretting regimes introduced in Section 1.2.4, here the relation with the wear rate and the effect on the fatigue life of the specimen are investigated. Wear is produced as a consequence of the interactions between surfaces and consists in the removal and deformation of material on the interface, which can be caused by fretting, corrosion, oxidation, abrasion, etc. In Figure 1.19a a plot presenting the variation of wear produced during fretting cycles as a function of the slip amplitude is shown. For low slip amplitudes, corresponding to a stick or stick-slip condition, the wear rate is extremely small. Conversely, a sharp increase in the wear rate is observed as soon as the slip amplitude approaches the value where the contact surface experiences gross slip. A plateau is reached when the contacting parts are in reciprocal sliding. The evolution of the fatigue life as a function of the slip amplitude is presented in Figure 1.19a. The curve has an inverted bell shape with a minimum located at the transition between partial slip and gross slip.

The increase of the slip amplitude leads to higher shear stresses at the surface, which in turn, accelerates crack initiation, reducing the fatigue life of the part, as demonstrated in [Nishioka et al., 1968]. However this trend is inverted for slip amplitude corresponding to gross slip since the increase of the wear rate eliminates the nucleated cracks, slowing down the crack initiation process. To sum up, depending on the fretting regime in which the specimen operates, a different damage mode will be observed: crack initiation followed by crack propagation for partial slip condition or surface wear for gross slip (Figure 1.19b).

The work presented in this manuscript focuses on crack initiation and propagation mechanisms; the partial slip regime is the condition in which the totality of the results reported, are obtained.

1.3.2 Crack initiation

Crack initiation is a process involving the gradual accumulation of damage, which takes place even if the macroscopic load applied to the structure is lower than the material elastic limit. Inclusions, surface or subsurface flaws, manufacturing defects or geometric singularities work as stress concentration factors creating cyclic small plastic deformations. This behavior results in an increase of the number of dislocations, which organize themselves in characteristic patterns, the slip bands, in order to minimize the total energy of the system. The cyclic nature of the loading

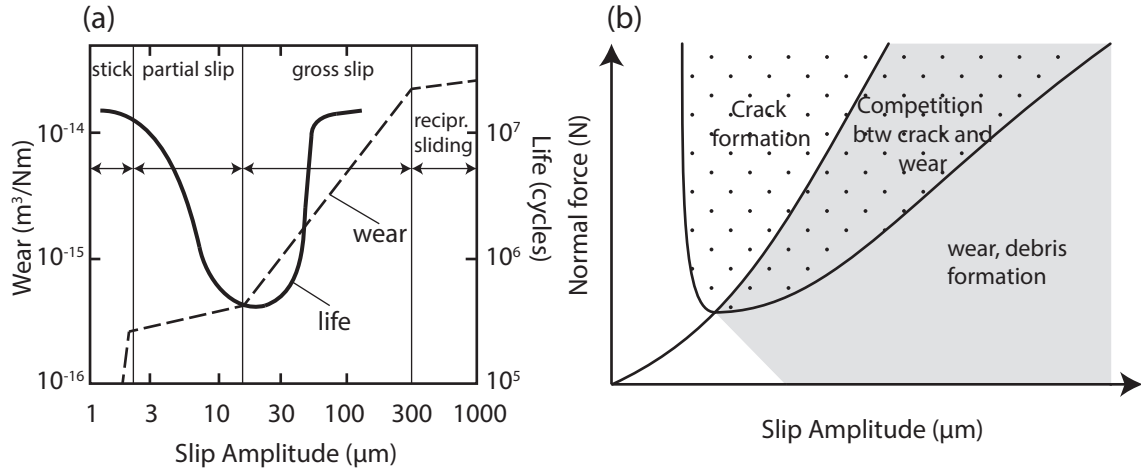


Figure 1.19: (a) Relation between slip amplitude and wear rate, [Vingsbo and Söderberg, 1988]; (b) material response fretting map, [Fouvry et al., 1996].

feeds this process and, as the cycles accumulates more crystals display sign of slip bands and ultimately some of them develop into small cracks.

The aforementioned description of the initiation mechanism applies to crack initiation in general. Fretting, however, introduces some peculiarities that are not present in plain fatigue. In particular the strong stress concentration at the contact surface is so localized that the location of the crack initiation site can be predicted. The shear stress reaches its peak at the transition between stick and partial slip zone, that corresponds to the usual crack nucleation site as it is shown in Figure 1.20 where the stress distribution at the contact surface for a cylinder/plane contact configuration is presented.

Once the crack is nucleated, it will grow following the direction maximizing the shear stress (Figure 1.21), which is usually inclined toward the interior of the contact by an angle close to 45 degrees (Stage I, mode II propagation). Since at this stage the crack length is really small, 10 or 20 μm, the same order of magnitude of the grain size, it is interesting to analyze whether the material microstructure influences the crack path. This is what has been investigated by, Proudhon and his colleagues, [Proudhon et al., 2006], who studied the nucleation and propagation of a crack under fretting wear loading in a 2024 Al alloy, employing X-ray tomography technique. In Figure 1.22 the 3D reconstruction of the fretting crack observed during the experiment is shown. Starting from this data, three angles can be defined: ϑ_i corresponds to the crack path angle with respect to the Y axis at the initiation point, (crack length of around 20 μm), ϑ_p is defined as ϑ_i for a crack length between 20 μm and 200 μm and ϑ_s for a crack length larger than 300 μm.

Concerning the initiation an important feature can be observed, (Figure 1.22). The evolution of ϑ_i as a function of X is pretty scattered confirming the influence of the microstructure on the initiation angle. Nevertheless, a series of plateaus with

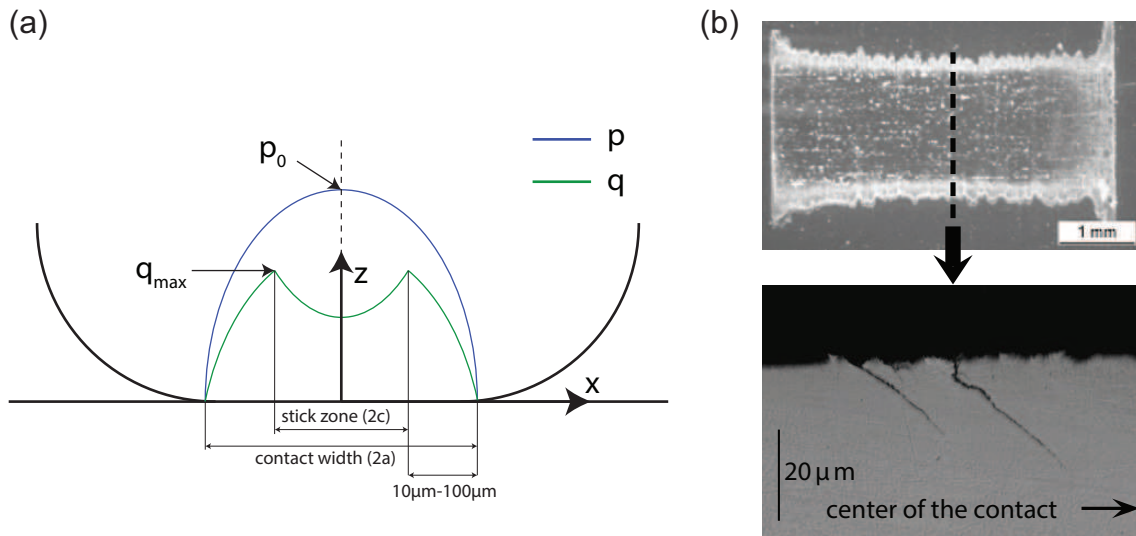


Figure 1.20: (a) Stress concentration at the contact surface; (b) fretting scar and crack initiation, [Proudhon et al., 2006].

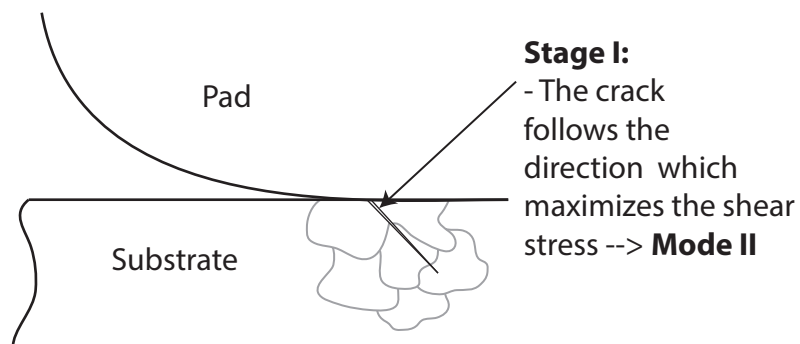


Figure 1.21: Different crack propagation stages under plain fretting.

an inclination close to 45 degrees is observed as well. This is in accordance with the theoretical value maximizing the shear stress at the contact interface.

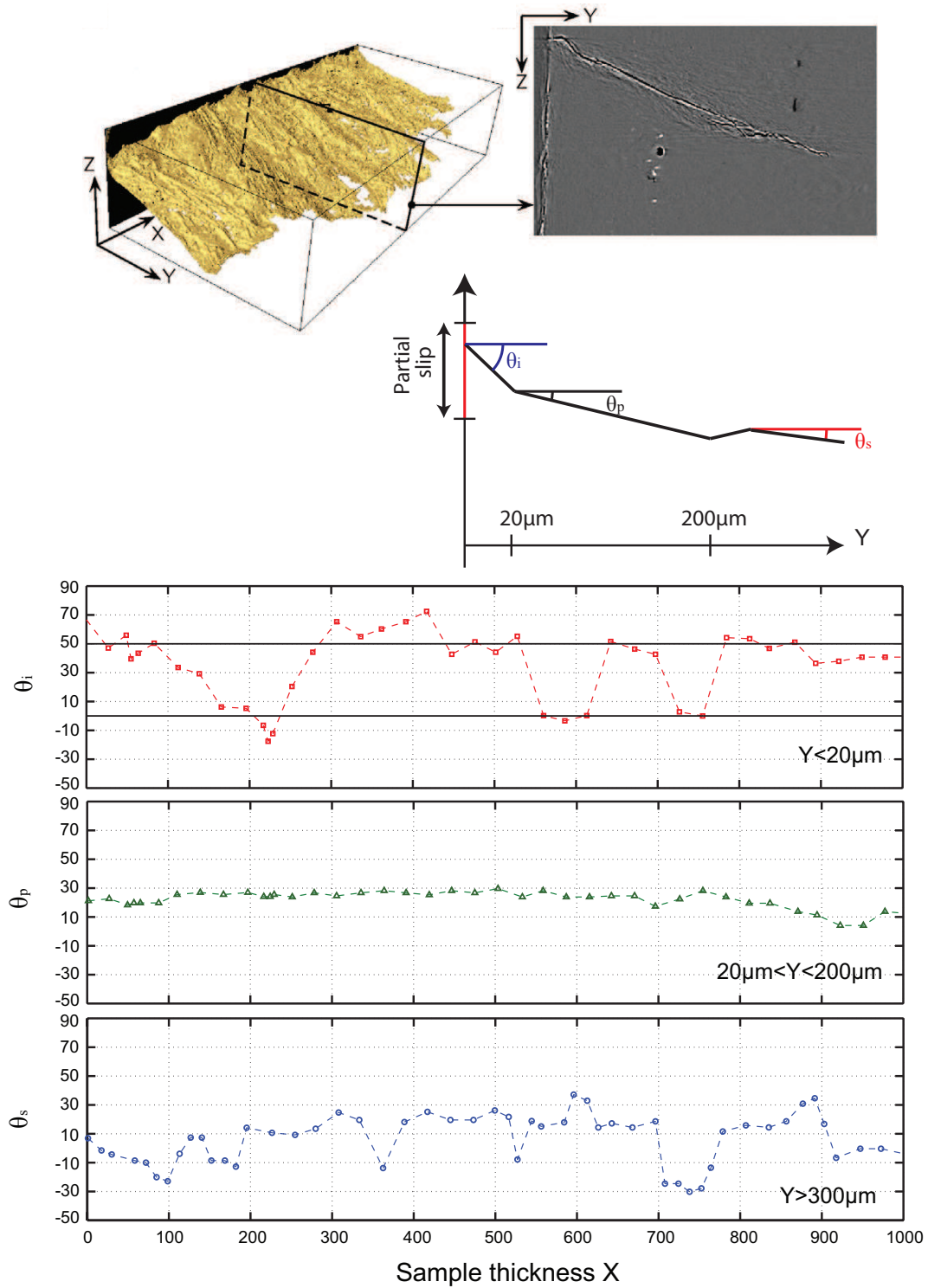


Figure 1.22: Quantitative analysis of a 3D fretting crack morphology by X-ray tomography: evolution of the nucleation and propagation angles ϑ_i , ϑ_p and ϑ_s measured inside the material along the specimen thickness, [Proudhon et al., 2007].

1.3.3 Crack propagation

Once the crack overcomes the first microstructural barriers, the grain distribution has a smaller influence on the path and the mechanical field becomes the dominant mechanism in the crack path definition. This is confirmed by the observations made by Proudhon and his colleagues. In Figure 1.22 it is possible to see how the propagation angle, ϑ_p , describing the crack inclination during the propagation phase (length between 20 μm and 200 μm) is almost constant, ($\vartheta_p \simeq 25^\circ\text{C}$), and it corresponds to the direction maximizing the tensile stress. This behavior reflects the change of propagation mode from mode II to mode I.

1.3.3.1 Linear elastic fracture mechanics

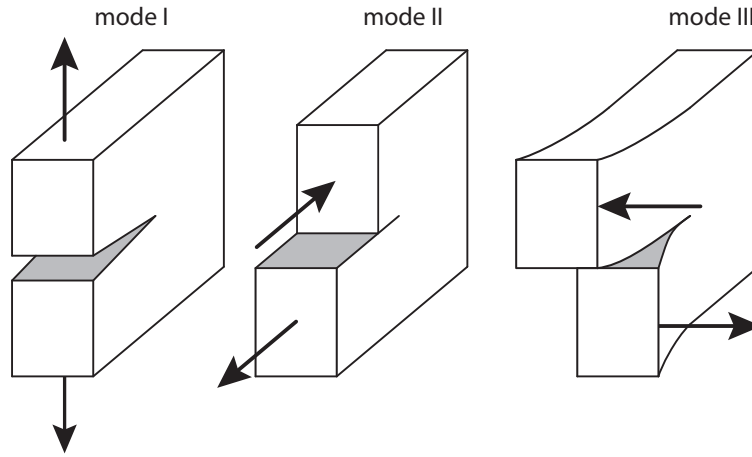


Figure 1.23: Crack loading modes.

Speaking about mode I and mode II, we are implicitly adopting the linear elastic fracture mechanics (LEFM) approach to describe whether the crack will grow or not and its velocity. The assumption behind this approach is to consider that the plastic deformation at the crack tip is negligible with respect to the size of the crack, which is called small-scale yielding condition. If this hypothesis is respected then the stress state around the crack tip can be described as follows:

$$\sigma_{ij}(r, \vartheta) = \frac{K}{\sqrt{2\pi r}} f_{ij}(\vartheta) + \text{higher order terms}, \quad (1.1)$$

as the product between a dimensionless factor depending just on ϑ , and a second one depending on r . By applying the principle of similitude it can be stated that for similar crack geometries the stress evolution with respect to r and ϑ remains the same and therefore only K , the stress intensity factor, is needed to univocally characterize the stress state in the proximity of a crack. This formalism has been introduced by Irwin in 1957, [Irwin, 1957], based on the analytical solution of the

stress and strain displacement ahead of a sharp crack developed by Westergaard some years before, [Westergaard, 1939].

The load experienced by the crack can be decomposed in a combination of three different modes, as Figure 1.23 illustrates. In mode I loading, or opening mode, tensile forces are applied to the body, such that the displacement of the crack surfaces are perpendicular to the crack plane. Conversely in Mode II, shear forces parallel to the direction of propagation promote the sliding of the crack surfaces over each other. Mode III refers to out-of-plane shear.

As a consequence of what has been said above, if one assumes that the material failure is related to a critical combination of stress and strain, then it follows that fracture must occur at a critical value of the stress intensity factor, K_{Ic} . Thus, K_{Ic} is a measure of fracture toughness.

In some engineering applications such as the aircraft engines a damage tolerance approach is applied. It is based on the assumption that flaws can exist in any structure and they can be safely handled by knowing the crack growth process. Inspection intervals are then set in order to replace the damage part before the occurring of a critical failure. Thus, the relation between, K , and the crack growth rate per cycle, da/dN , is needed. For a common alloy, tested in fatigue, this relation is characterized by the trend shown in Figure 1.24.

Three distinct regions are highlighted. In Region I, the damage produced by the cyclic loading at the crack tip is almost zero; for ΔK lower than the threshold value, ΔK_{th} , no macroscopic crack growth is observed. In Region II, instead, the relation between da/dN and ΔK can be approximated with the law introduced by Paris and Erdogan in 1963, [Paris and Erdogan, 1963]. Thus, the two variables are related by a power law dependence. In region III, the crack growth rate increases exponentially up to failure. At this level the K_{max} experienced by the crack is close to the material fracture toughness, K_{Ic} .

1.3.3.2 Short crack

One of the main problems encountered by engineers in the design process against fatigue is that the propagation laws used to predict the crack growth rate are extrapolated from cracks that are relatively long (some millimeters). However for some applications it is necessary to know the growth rate when the crack is extremely short, lower than 500 μm , for instance. Experimental evidence shows that in this case the crack can propagate much faster than what can be inferred from Figure 1.24, even for ΔK values that are lower than ΔK_{th} . The reason of the difference is due to the fact that linear fracture mechanics relies on the principle of similitude. The strain and stress tensor experienced at the crack tip is the same, regardless of the loads applied, if and only if the stress intensity factors are equal. For short cracks this principle is no more valid. To obtain the same ΔK , one should compare a long planar crack, weakly loaded, to a 3D short crack strongly loaded. In addition the small scale yielding approximation is no more valid since the size of the plastic zone

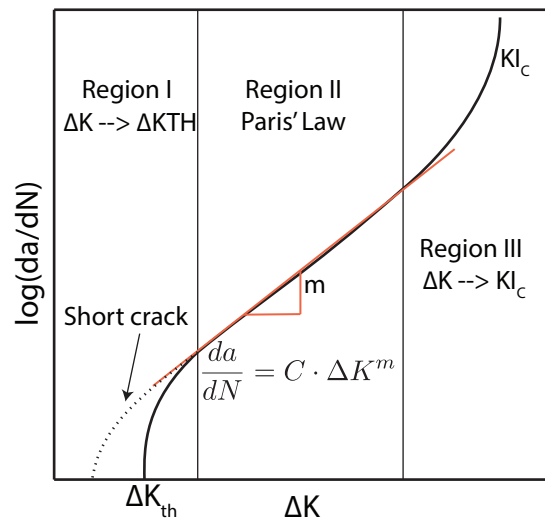


Figure 1.24: Typical fracture mechanics fatigue crack propagation behavior.

at the crack tip becomes not negligible.

This behavior has to be taken into account if a precise estimation of the total fatigue life of the part is needed. With that said, the transition between short and long crack is tricky. Miller [Miller, 1993a] approaches this problem by dividing cracks into three families as a function of their length:

- microstructural short cracks that have a characteristic length close to the grain size;
- mechanically short cracks that have a size varying in range from 50 μm to 500 μm ;
- and long cracks with a length of some millimeters or more, that can be described by the linear elastic fracture mechanics.

This qualitative classification is coupled with a quantitative determination of the frontiers between the three regimes that is based on the Kitagawa-Takahashi diagram, [H. Kitagawa, 1976]. The two authors observed the growth of small cracks initiated from very small surface notches under uniaxial cyclic tension loads. Through this procedure they determined the frontier between propagation and non propagation as a function of the load applied and the crack length. As it is possible to see in Figure 1.25, for cracks smaller than a critical length, a_c , LEFM falls short in predicting the crack arrest frontier. In this way it is possible to discriminate whether the crack is in the short or long regime. Furthermore a_c is a material constant that can be obtained through experimental tests.

As a consequence of what has been presented in this section, it is clear that the crack evolution presented in Figure 1.22 has all the features of short cracks. This

is the typical scenario observed when fretting crack are analyzed. To predict the growth rate an interesting approach is proposed in [Brugier et al., 2013]. LEFM is enriched by including the non-singular terms of the asymptotic developments, the T-stresses, which allow to estimate the crack growth rate of short and long cracks in the near threshold regime.

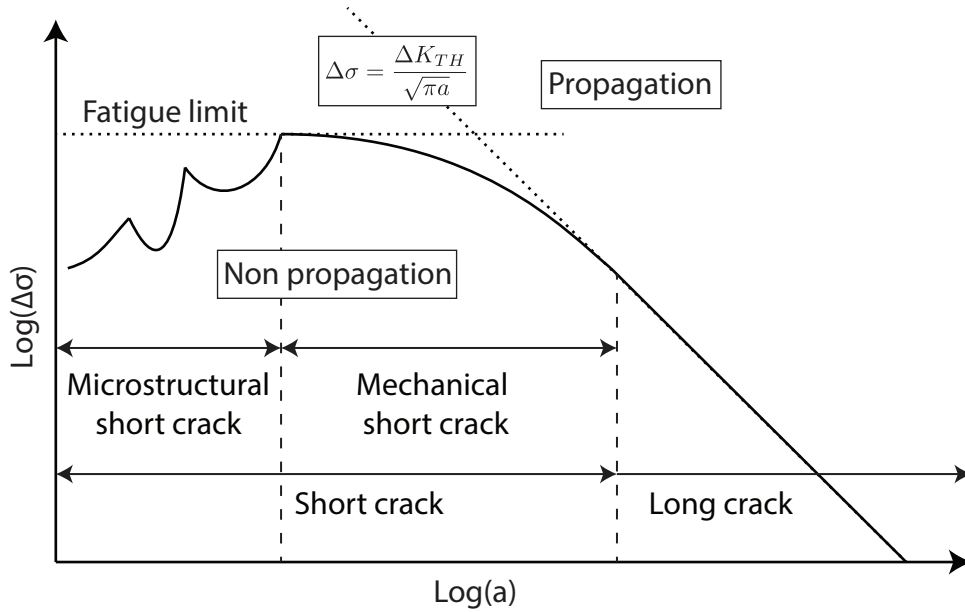


Figure 1.25: Kitagawa-Takahashi diagram, [Miller, 1993b].

1.3.4 Crack arrest

The damaging process under fretting loading is generated by the forces arising at the surface as a result of the interaction between two contacting bodies. Therefore the stress tensor will be characterized by a peak close to the contact edge followed by a decrease in magnitude since, far from the surface, the influence of the superficial loading weakens. Thus, the initiated crack will propagate as long as the stress field is big enough to promote the growth process.

The crack arrest as a result of the decreasing stress field has been observed experimentally by several authors. In Figure 1.26 the test data obtained by Kubiak [Kubiak, 2006], are presented. As it is possible to see, the crack length after 10^5 cycles reaches a plateau, stopping to propagate. In addition, the author investigates the relation between the maximum crack length and the fretting loading applied. In Figure 1.26b the influence of the tangential load, Q , is shown. As expected a bigger tangential force will result in a longer non propagating crack. A similar dependency is observed with respect to the normal force.

Furthermore, an other interesting aspect observed experimentally, [Proudhon et al., 2006], is the fact that, in this phase, the microstructure restarts to have an

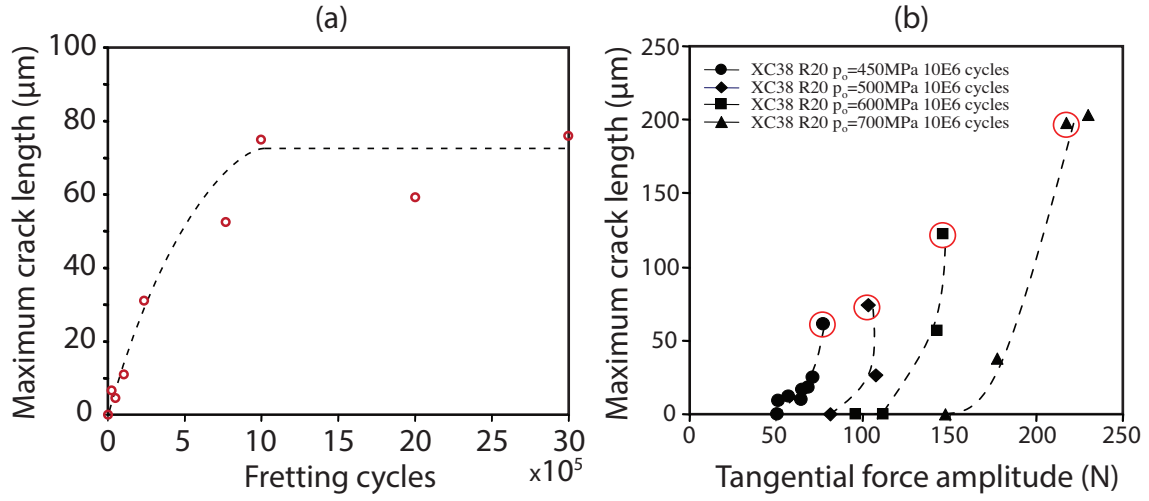


Figure 1.26: (a) Crack length evolution in function of the number of cycles under plain fretting, $P_{0,max} = 700$ MPa, $Q_{max} = 280$ N/mm; (b) maximum crack length in function of Q_{max} , [Kubiak, 2006].

influence on the crack path. This is coherent, since the stresses at the crack tip rapidly decrease far from the contact surface, becoming too small to propagate the crack in mode I. Therefore there must be some points in the material, where the influence of the microstructure ahead of the crack front becomes significant again, and this is exactly what it is shown in Figure 1.22. Analyzing the values of ϑ_s , which represent the crack inclination for a situation where it is close to the maximum reached length before to stop, the trend followed is quite scattered; ϑ_s varies in a range from -30 to 45 degrees.

By analyzing the evolution of the stress intensity factor at the crack tip, and comparing it to the Kitagawa-Takahashi non propagation frontier, it is possible to predict the maximum length that the crack will reach before to stop. In the short crack domain, $a < a_c$, the frontier is defined by the following relation:

$$\Delta K_{th} = \Delta K \sqrt{\frac{a}{a_c}}. \quad (1.2)$$

The aim is therefore to be able to define the evolution of ΔK as a function of the crack length, $\Delta K = f(a)$, and comparing it with the arrest frontier described in equation 1.2, to define whether the crack will stop or not. There are several methods allowing to compute this relation:

- finite element computation and post-treatment analysis of the mechanical field obtained through the use of J integral [Rice, 1968, Proudhon, 2005] to compute the stress intensity factor evolution;
- computation of the stress intensity factors by using the weight function method [Bueckner, 1970, Rice, 1972];

- application of the distributed dislocation method [Nowell and Hills, 1987, Fouvry et al., 2008].

In Figure 1.27, the typical behavior of the fretting crack is presented. It will nucleate due to the peak stress at the contact edge, and it will propagate as long as the influence of the surface load (P, Q) is high enough to promote the growth process. The stress intensity factors at the crack tip will increase during early propagation and then rapidly decrease far from the contact. As a consequence, sooner or later, ΔK value becomes lower than propagation frontier resulting in the arrest of the crack.

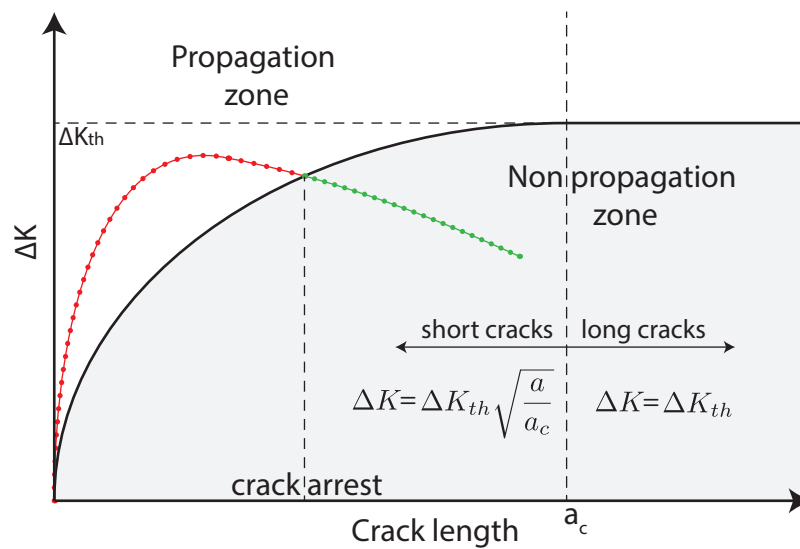


Figure 1.27: Short crack arrest schematic representation [Kubiak, 2006].

1.3.5 Fretting-fatigue peculiarities

In the previous sections, the attention has been focused on the damaging process under fretting loading; the evolution of a crack, from the nucleation to the arrest has been analyzed. Here, we investigate the case in which a cyclic bulk load is present in addition to the fretting loading.

In Figure 1.28, the different stages in the crack propagation process are listed. With respect to fretting a first important difference is shown. The crack initiates at the contact surface due to the high stress concentration factor (stage I) and, in the next 100 - 200 μm , propagates mainly under the influence of the contact loading. As the crack penetrates deeper, the effects of the fretting loading starts to weaken and the cyclic bulk load becomes the dominant propagation driver. The transition from stage II to stage III is characterized by a change in the crack inclination that gradually orients itself perpendicular to the fatigue load. In this stage the growth

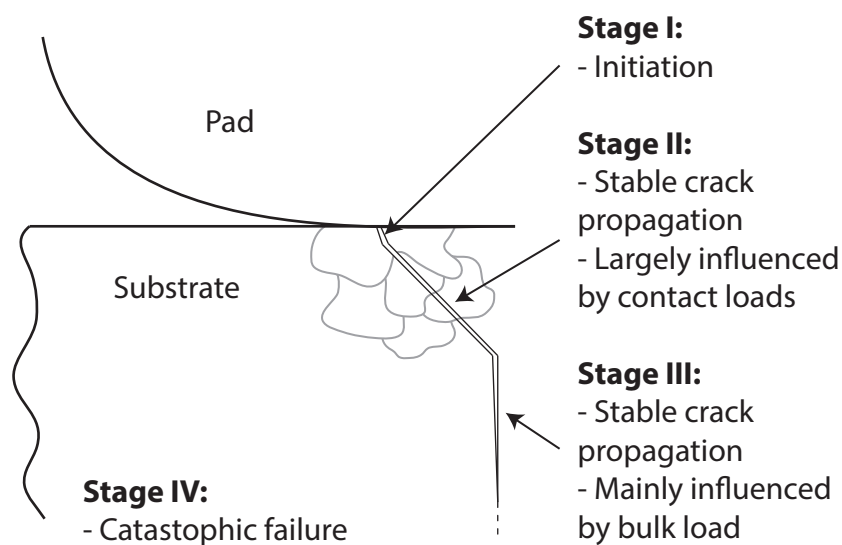


Figure 1.28: Different crack propagation stages under fretting-fatigue.

process is driven by the principal maximum stress, and the crack will propagate in mode I. If the fatigue load is high enough, then the failure of the part will be the inevitable result. In brief, stage I and II are almost the same either for fretting or fretting-fatigue, while stage III and stage IV, being strongly influenced by the bulk load are a peculiarity of fretting-fatigue.

As a consequence of what has been presented, engineers have to deal with three main problems in order to effectively design against fretting-fatigue:

- i) Will the crack initiate or not for a given fretting-fatigue loading combination?
- ii) Will the crack arrest or propagate up to failure?
- iii) Is it possible to estimate the crack growth rate?

Aiming at proposing an integrated tool to answer the questions above, Fouvry and Kubiak [Fouvry and Kubiak, 2009], introduced a fretting-fatigue mapping concept in which three important domains are defined (Figure 1.29):

- the safe crack nucleation domain, where for the given combination of (P, Q, σ_B) , no crack nucleation is experienced,
- the safe crack propagation domain characterized by the fact that the initiated crack propagates and then stops before to reach a critical length,
- the failure domain in which the loading combination provokes the failure of the part after a certain number of cycles.

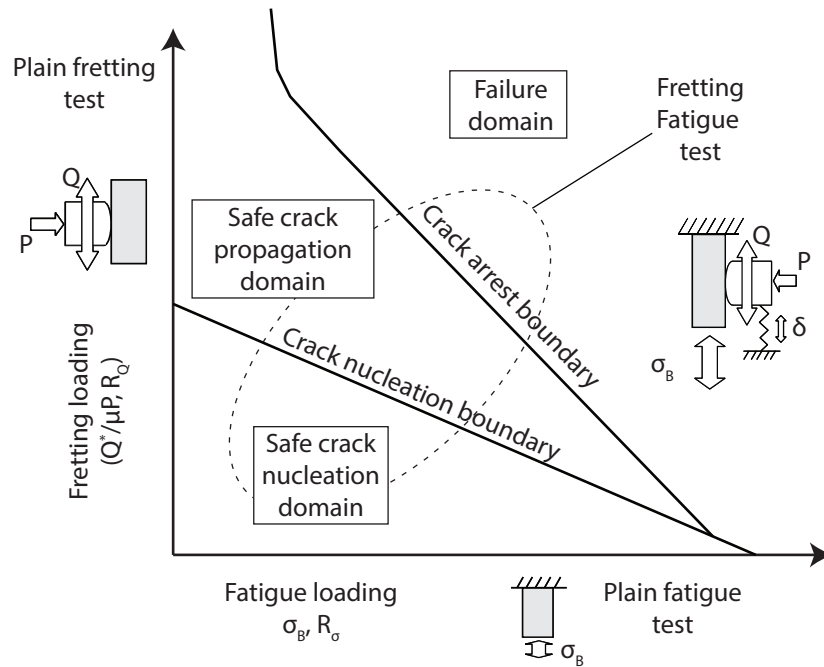


Figure 1.29: Illustration of the fretting-fatigue mapping concept defined for partial slip condition, [Fouvry and Kubiak, 2009].

This type of representations is quite useful since it constitutes a powerful tool to decide which design approach to follow as a function of the material employed.

In Figure 1.30a the fretting-fatigue maps for a low carbon steel alloy, AISI1034, is presented. It is obtained through an experimental campaign using a fretting-fatigue test apparatus. The two crack initiation and arrest frontiers intersect each other in $\sigma_{B.CA_{th}}$, which represents the fatigue value, over which, if crack initiates then it will propagate until fracture occurs. Two scenarios will then be possible:

- if the structure experienced a fatigue load lower than $\sigma_{B.CA_{th}}$, then for the condition characterized by small contact loads a safe crack nucleation approach can be considered while for the other cases a safe crack arrest design is still applicable;
- in the case in which the fatigue load is higher than $\sigma_{B.CA_{th}}$, the only strategy applicable is the one aiming at avoiding crack nucleation.

By comparing Figure 1.30a and Figure 1.30b it is extremely clear that the two materials, a steel alloy and a titanium alloy, have a quite different behavior in terms of crack initiation and propagation. The titanium alloy displays a larger crack initiation domain and a very little crack arrest domain. For this material therefore the optimal

strategy seems to be the one in which the design of the part focuses on avoiding crack initiation.

Concerning the crack growth rate, the idea is to estimate the fatigue life of the part by computing the stress intensity factors evolution and by comparing it with the Kitagawa-Takahashi diagram for the short crack domain and the S-N curve for the long crack domain.

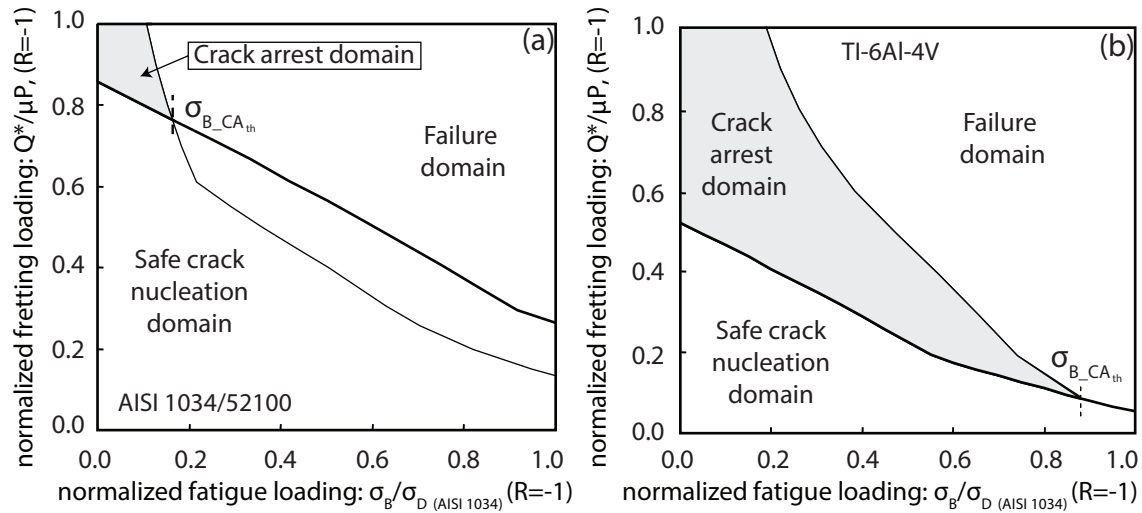


Figure 1.30: Fretting-fatigue Map, ($P = 227 \text{ N/mm}$, $p_0 = 450 \text{ MPa}$) (a): AISI 1034/52100 (Radius pad = 40 mm); (b) Ti-6Al-4V/52100 (Radius pad = 30 mm), [Fouvry and Kubiak, 2009].

1.4 Life prediction criteria

In the previous section a qualitative analysis of the damaging mechanism under fretting-fatigue has been presented. Due to the loads at the contact surface, the crack can initiate and propagate until the failure of the part or stop if the fatigue bulk load is not strong enough to promote the growth process far from the surface.

In the design process against fretting-fatigue, this behavior has to be analyzed. For instance, our industrial partner, Snecma, applies a policy based on the fact that, for aircraft engine components, crack initiation has to be avoided, but at the same time for certification procedures it is necessary to prove that if cracks initiate then they will stop before to reach a critical length. To meet this requirements, two families of fatigue criteria exist: the ones focusing on the crack initiation prediction based on multiaxial fatigue approach, and the others analyzing the stress intensity factor evolution in order to predict whether the crack will stop or not.

1.4.1 Crack initiation prediction criteria

As presented in Section 1.3.2, the accumulation of plastic deformations at the grain boundaries is one of the main mechanisms in the crack initiation process. Experimental evidence shows that a big role is played by the shear stress that is at the origin of the crystallographic slip band formation along preferential slip planes and by the normal stress with respect to these planes promoting the crack opening. This two mechanisms are the basis for some of the most used crack initiation prediction criteria:

- **Critical plane approaches.**

The main components of the critical plane criteria are the normal and shear stresses acting on a selected material plane. Several formulations are presented in the literature, [Papadopoulos et al., 1997]. They differ in the way in which the terms are computed, but the process followed is merely the same. Once the critical plane is determined, it is checked whether the criterion is satisfied on this plane or not. If the criterion is not satisfied, the selected plane can experience crack initiation.

- Findley criterion.

$$\tau_a(\varphi^*, \alpha^*) + \kappa \sigma_{N,max}(\varphi^*, \alpha^*) < \lambda, \quad (1.3)$$

where k and λ are material parameters, τ_a is the shear stress amplitude and σ_N is the normal stress on the critical plane, which is determined as follows:

$$(\varphi^*, \alpha^*) : \max_{(\varphi, \alpha)} [\tau_a(\varphi, \alpha) + \kappa \sigma_{N,max}(\varphi, \alpha)]. \quad (1.4)$$

- Modified Wöhler curve method, [Araújo et al., 2007]

$$\tau_a(\varphi^*, \alpha^*) + \kappa \frac{\sigma_{N,max}(\varphi^*, \alpha^*)}{\tau_a(\varphi^*, \alpha^*)} < \lambda, \quad (1.5)$$

where k and λ are material parameters, τ_a is the equivalent shear stress and σ_N is the normal stress on the critical plane, which is determined as follow:

$$(\varphi^*, \alpha^*) : \max_{(\varphi, \alpha)} [\tau_a(\varphi, \alpha)]. \quad (1.6)$$

- **Approaches based on the stress invariant.**

These criteria are based on a linear combination between hydrostatic stress and the second invariant of the stress deviator tensor. They are well suited for predicting crack initiation for proportional fatigue loading since they do not take into account the possibility that the principal stress plane may vary along the loading cycle. As a consequence the orientation of the potential fatigue crack is by no means specified by these criteria.

- Sines criterion

$$\sqrt{J_{2,a}} + \kappa\sigma_{H,m} < \lambda, \quad (1.7)$$

where k and λ are material parameters, $J_{2,a}$ is the amplitude of the second invariant of the stress tensor and $\sigma_{H,m}$ is the mean value of hydrostatic stress during load history.

- Crossland criterion

$$\sqrt{J_{2,a}} + \kappa\sigma_{H,max} < \lambda, \quad (1.8)$$

where k and λ are material parameters, $J_{2,a}$ is the amplitude of the second invariant of the stress tensor and $\sigma_{H,m}$ is the maximum value of hydrostatic stress during load history.

- **Mesoscopic scale criteria.**

All the criteria presented before try to predict the fatigue behavior of the materials from a macroscopic scale point of view. A different choice consists in focusing on the microscopic phenomena at the dislocation scale while a third possibility is to consider an intermediate scale between the macro and micro levels. This is the mesoscopic scale, which is the scale of the metal grains of a metallic aggregate. The criterion formulated by Dan Vang, [Dang Van et al., 1982] is based on the mesoscopic scale approach. The initiation is experienced in the grains that have slip system orientations compatible with the macroscopic load direction. Those grains will suffer plastic deformation before to reach elastic shakedown condition. Residual stresses, ρ^* , will therefore appear. The local stress tensor, $\hat{\sigma}(t)$, used in the fatigue analysis is defined as the sum of the stresses due to the macroscopic loads, $\Sigma(t)$, and the residual stresses, ρ^* ,

$$\hat{\sigma}(t) = \Sigma(t) + \rho^*. \quad (1.9)$$

Similarly to what is done for the critical plane approaches, the direction which maximizes the resolved shear stress is computed,

$$\max_{(\varphi, \alpha)} \left\{ \max_{(t)} \left[\hat{\tau}(\varphi, \alpha) + \alpha \hat{P}_h(t) \right] \right\} < \lambda. \quad (1.10)$$

- **Incremental criteria.**

These methods are based on the definition of a damage function, D , to account for the material degradation as a function of the experienced mechanical loading. The advantage with respect to the criteria presented above lies in the fact that the computation of the damage evolution can be done in an incremental way, cycle by cycle.

Fatigue damage is usually modeled by means of cyclic damage laws [Chaudonneret, 1993], i.e. laws for damage increment per cycle,

$$\frac{dD}{dN} = G(\sigma_a, \dots) \quad (1.11)$$

expressed in terms of stress amplitude $\sigma_a = \Delta\sigma/2$ and either the mean stress, $\sigma_m = 1/2(\sigma_{min} + \sigma_{max})$, or the stress ratio, $R = \sigma_{min}/\sigma_{max}$, quantities defined over a cycle.

Ruiz criterion, [Ruiz and Chen, 1986], can be included in this family, and it has been developed studying the damage on dovetail joints. According to this criterion, surface damage driving factors are the relative slip, δ , and the contact shear stress at the interface τ_{fric} . As a consequence a fretting damage parameter (FDP) can be defined as the product between these two quantities,

$$FDP = \tau_{fric} \cdot \delta. \quad (1.12)$$

Criteria application to fretting

The application of the criteria presented in the previous section to fretting-fatigue is not straightforward. To understand why, it is interesting to look at the results presented in Figure 1.31 where the experimental crack initiation boundaries founded by Amargier [Amargier et al., 2010] are presented. The experimental tests have been performed employing a cylinder/plane configuration, with different pad radii (further details are presented in Chapter 3). The initiation frontiers are defined with respect to the maximum local quantities at the contact surface, q_{max} and p_0 .

It is clear that this values are not sufficient to univocally characterize the initiation frontiers. A fundamental role is played by the pad radius. By varying the macroscopic loads applied to the pad, it is possible to ensure the same stress distribution at the contact surface no matter which radius is used, still for two different pad radii, different initiation frontiers will be experienced.

To interpret this trend, two different explanations are possible. By keeping the same contact distribution for different radii it follows that the size of the contact varies, as it can be inferred from equation 1.13 where some basics relations between macroscopic load and contact size for cylinder/plane contact configuration are reported.

$$a = \sqrt{\frac{4P_l R}{\pi E^*}}, \quad \frac{a}{c} = \sqrt{1 - \left| \frac{Q}{\mu P} \right|}, \quad p_0 = \sqrt{\frac{P_l E^*}{\pi R}}. \quad (1.13)$$

where P_l is the normal force per unit length. The surface of the zone in stick-slip condition will increase as well. Therefore, the size effect can be reputed to be a possible cause of the behavior observed in Figure 1.31. From a statistical point of view, the increasing of the stick-slip surface will increase the probability to encounter a material defect or a grain with a favorable orientation for initiation. The quantification of this effect is one of the research objectives of the PhD work of Barbara Ferry who is performing experimental tests at the university of Brasilia. With that said, regarding the crack initiation frontiers presented in Figure 1.31, the surface is in the same order of magnitude and does not seem to be sufficient to explicate the difference encountered.

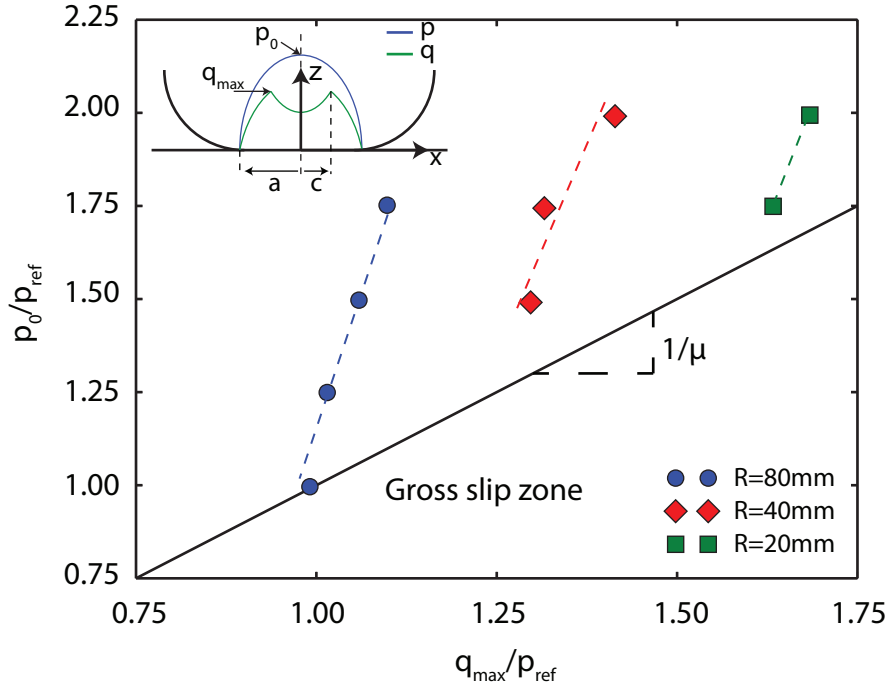


Figure 1.31: Experimental crack initiation boundaries in term of maximum local quantities for Inconel 718 in plain fretting as a function of the pad radius [Amargier et al., 2010].

The second explanation of the crack initiation frontier dependency to the radius used can be attributed to the gradient effect. As it has already been mentioned, fretting is characterized by a stress concentration at the contact surface (at the transition between stick and partial slip zone) followed by a steep gradient. For a simple configuration as the cylinder/plane one, the mutual dependency between radius and stress gradient can be summed up by saying that for a smaller radius a steeper stress gradient is experienced by the specimen. With that said, it is important to notice that two factors influence crack nucleation; (i) the maximum stress at the hot spot and (ii) the material process volume over which the maximum stress operates. The increase in pad dimension extends the influence of contact stress below the surface, and therefore increases the process volume, [Neuber, 1958].

In view of what has been said, it is clear that all the initiation criteria presented in Section 1.4.1 (with the exception of the empirical ones) if applied in a classic way, i.e., using as input the stress values at the hot spots, will underestimate the fatigue life of the part.

To mitigate the effect of the stress concentration or, in other words, to take into account the gradient effect, the multiaxial fatigue criteria are usually coupled with some sort of averaging technique over a critical distance. Fouvry, [Fouvry et al., 2000], shows that by averaging the stress tensor components over a cubic volume,

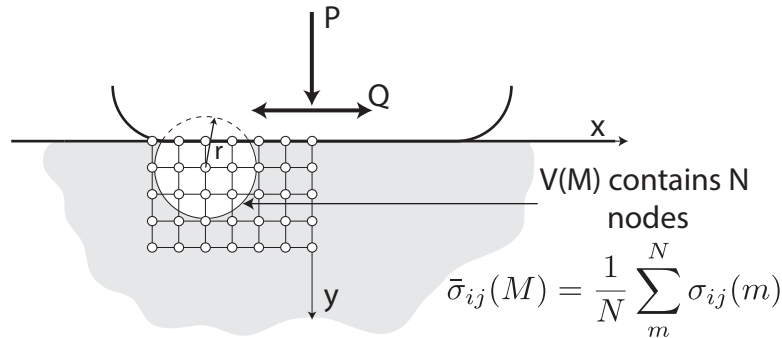


Figure 1.32: Schematic representation of the radial shape process volume, [Proudhon et al., 2005].

the length needed to match the experimental result is close to the grain size of the material, establishing therefore a relation with a characteristic material property. The same approach is applied by Proudhon, [Proudhon et al., 2005], with the only difference that the cubic volume is replaced by a circular surface as presented in the schematic representation of Figure 1.32. Araújo and his colleagues, [Araújo et al., 2007], coupled the modified Wölher curve method with the theory of critical distance. This approach is based on the assumption that the damaging process causing crack initiation is confined within the so-called structural volume. The size of this volume is considered not to be dependent on either the stress concentration feature or the complexity of the stress field damaging the fatigue process zone. It is equal to the value that divides the long crack from the short crack regime, being therefore a material constant.

This approach shows good results being capable of correctly predicting failures with an accuracy of about $\pm 20\%$. With that said, it is important to say that to compute the quantities for applying the above criteria, the stress gradient evolution needs to be accurately determined. Since its value decreases really fast far from the surface, to capture this evolution by means of a FE technique, a really fine mesh is required which makes this criteria difficult to be employed in industrial context.

1.4.2 Life prediction criteria

Two factors play an important role in the crack propagation process under fretting-fatigue: the surfacic stresses ($q(x)$, $p(x)$) have a huge impact in the first part of the growing path weakening far from the contact where the cyclic bulk stress, σ_B , becomes dominant. Depending on the magnitude of the fretting-fatigue loading components (P , Q , σ_b) two different scenarios are then possible as it is presented in Figure 1.33; either the crack will stop or it will propagate until failure if the bulk load is strong enough.

For industrial applications, such as, turbofan engines, it is fundamental to be able to discriminate between these two possible outcomes to achieve a better prediction

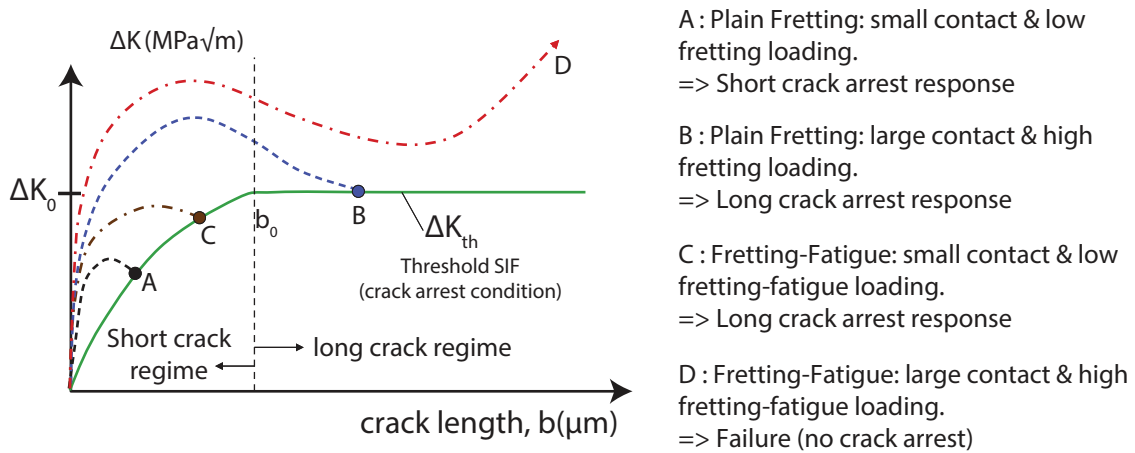


Figure 1.33: Evolution of the crack tip stress intensity factors for plain fretting and fretting-fatigue, [de Pannemaecker et al., 2015].

of the fatigue life of the component. Several criteria have been developed to address this issue. Almost all of them try to model the different stages in the crack growth process (Figure 1.28) to obtain an estimation of the total life of the part. Usually a crack initiation criterion is coupled with a crack propagation model.

This is the case of the research work performed by Chambon [Chambon and Journet, 2006], in which for each different stage, stage I, stage II, stage III and stage IV, (Figure 1.28) a phenomenological model is proposed. By assuming that, from an engineering point of view, cracks nucleate almost immediately when loads are applied, Chambon exploits the crack-analogue approach, [Giannakopoulos et al., 1998], to describe the contact problem through fracture mechanics “tools”. Stress intensity factors are therefore computed and, by applying the Paris’ law, it is possible to quantify the number of cycles needed for the crack to propagate (stage I and stage II). Once the crack penetrates deeper in the specimen a weight function approach for a kinked crack is used. During this stage, the crack propagates in mode I under the effect of the bulk load. Once again, the Paris’ law can be used to predict the crack growth rate; in addition crack arrest can be anticipated by comparing the evolution of the stress intensity factors with the non propagation threshold, (Kitagawa-Takahashi diagram, Figure 1.25). The results obtained with this multi-criteria approach match the experimental total fatigue life with an accuracy rate of $\pm 30\%$.

A powerful tool to accurately predict the crack propagation path and growth rate is represented by the X-FEM technique. Using this approach Baietto and her colleagues, [Baietto et al., 2013] propose a methodology coupling experimental data and numerical simulations in order to predict crack initiation and propagation. In particular a series of fretting-fatigue tests were performed and interrupted after a given number of cycles in order to analyze whether the crack was initiated and its inclination. This data were used as input for the prediction of the crack growth path

computed using X-FEM algorithm, which is a technique where the finite element method (FEM) approach is enriched by using discontinuous shape function bases able to capture the interface discontinuities and the asymptotic behavior close to the crack front. By comparing the results obtained with the outcome from the experimental tests, a very good agreement in terms of crack path and growth rate is observed.

1.5 Scientific challenges

In this first chapter an overview of the industrial challenges introduced by fretting-fatigue have been presented. The damage process caused by this phenomenon can lead to mechanical failures very early in the life of the part. As a consequence, in the last fifty years, important research efforts have been done aiming at improving the design technique against fretting-fatigue.

Undoubtedly, the researchers have made some important progresses. The physical mechanism leading to crack initiation are now much better known than some decades ago, increasing computational power and new numerical algorithms (X-FEM for instance) allow to estimate more accurately the crack propagation phase and finally fatigue criteria adapted to fretting-fatigue have shown to be able to predict well the experimental results in terms of fatigue life.

However some issues remain to be addressed. In Figure 1.31 crack initiation frontiers for a test campaign performed with a plain fretting apparatus are shown. The different frontiers corresponds to the different pad radii employed in the tests. Clearly the geometry plays an important role. In particular, the stress gradient arising as a result of the concentration factor at the surface depends on the contact configuration. In Figure 1.34b, the stress evolution in the specimen, corresponding to cylinder/plane contact, is shown. By varying the macroscopic loads, P and Q , it is possible to ensure the same stress distribution for the two different geometries, nevertheless a different gradient evolution will be experienced and, as a consequence, a different behavior in terms of crack initiation will be observed.

From practical applications, the dependency of the fatigue behavior on the geometry, is a real problem. To understand why, let's consider the case of an engine maker, producing different engines characterized by different size and power. Of course, all the components need to pass the certification procedures to validate the design. In this process, fretting-fatigue poses two main problems.

First, it is impossible to perform laboratory test on simple geometries, like the cylinder/plain one, to infer the effect of fretting-fatigue in terms of life reduction; the size of this setup is not representative of the real industrial part. The use of these simple tests are therefore limited to comparative analysis between different material surface treatments or lubricants.

Secondly, even if a difficult and expensive fretting-fatigue test apparatus is developed in order to test the fatigue life of the compressor blades, for instance, the analysis is valid exclusively for that particular design configuration. In other words, the inability to transfer the experimental results between different geometries represents

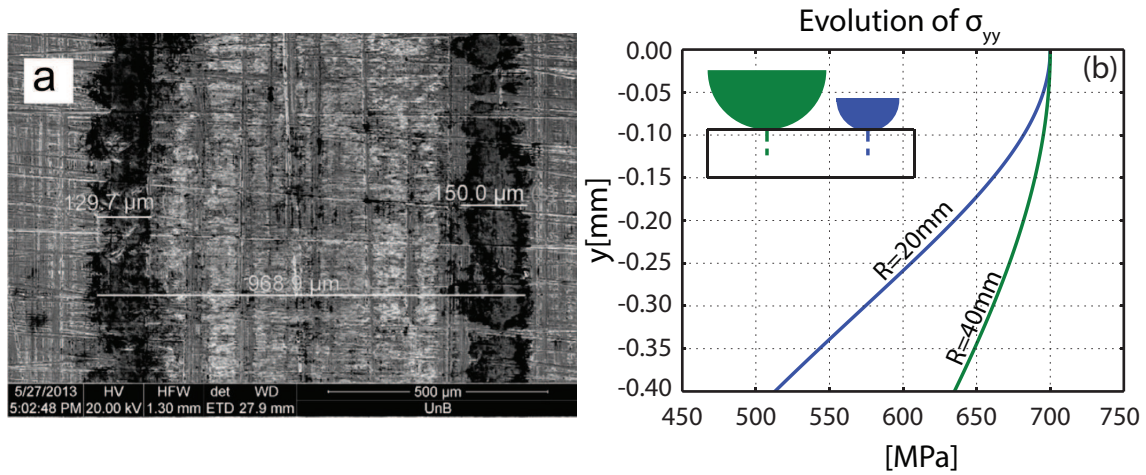


Figure 1.34: (a) Typical fretting-fatigue mark on an unbroken specimen, [Bellecave et al., 2014]; (b) stress gradient evolution for two plain fretting test with different pad radii.

an enormous cost for industrial applications.

To answer this issue a nonlocal description of the mechanical fields arising in the proximity of the contact edges is developed. It is based on nonlocal stress intensity factors (I^s , I^a , I^c) which, as it is proven in the following chapters, are objective quantities. In Linear Elastic Fracture Mechanics (LEFM) the similitude principle states that if two different structures experienced the same stress intensity factor K at the crack tip, then their behavior in term of crack propagation is identical. It is therefore possible to transpose the test results obtained on laboratory setup to the real industrial components, provided that K is the same. By using the nonlocal stress intensity factors (I^s , I^a , I^c) the same approach can be applied to fretting-fatigue problems.

In Section 1.4 several strategies to predict the damaging process have been presented; some of them ensure good results in terms of fatigue life prediction. However the application of these criteria are often limited to academic research. Fretting-fatigue is, in fact, a heavily multiscale phenomenon as it is shown in Figure 1.35. If we consider the blade root/disc attachment, blade dimension is in the order of some centimeters (Figure 1.35a), the scar produced at the contact surface by fretting has a characteristic length of some millimeters (Figure 1.35b) while the stress gradient evolution and the typical crack initiation length is in the order of some micrometers (Figure 1.35c).

The fatigue criteria existing in the literature to deal with fretting-fatigue related problems can be divided in three families:

- The local criteria which are multiaxial fatigue criteria applied by using as input the stress tensor values at the hot-spot zones in the proximity of the contact edges. Since fretting-fatigue is characterized by the presence of a strong stress

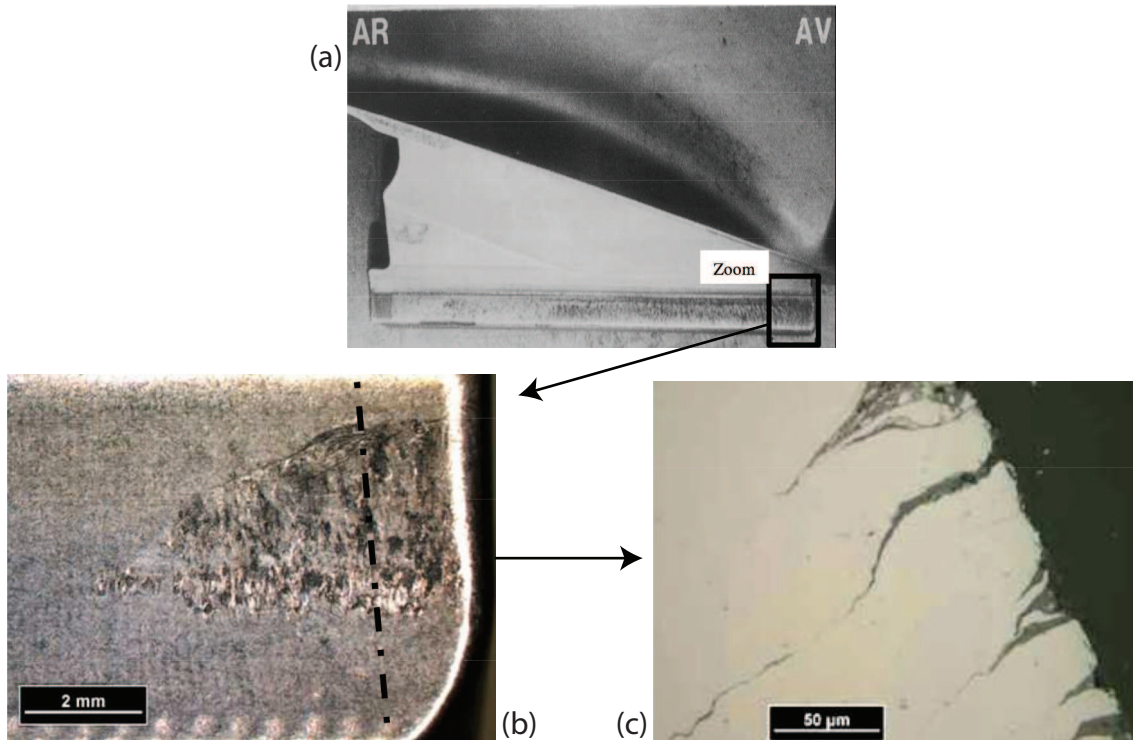


Figure 1.35: (a) Wear on the internal part of a CFM56-3A fan root; (b) fretting-fatigue scar; (c) cracks initiation sites.

gradient, this approach performs poorly and greatly underestimate the fatigue life of the components.

- The nonlocal criteria that differ from the first ones by the fact that they take as input the stress tensor at a specific distance to mitigate the effect of the stress gradient. Acceptable results are obtained. However, a good resolution of the stress variation is needed. To meet this requirement by means of FE computations a micrometric mesh size is necessary which is too small and non compatible with industrial applications due to the excessive computation time.
- The criteria based on fracture mechanics which, by analyzing the evolution of the stress tensors at the crack tip, estimate whether the crack will stop or propagate. The analysis of the K evolution as a function of the crack length implies to set up a computational strategy to determine the crack path resulting from the macroscopic load application. This operation is heavily time-consuming and difficult to implement in industrial procedures.

To sum up, even if different criteria exist, some of them ensuring good estimations of the negative effects related to fretting-fatigue, their industrial applications remain marginal.

The method developed and presented in this manuscript aims at answering this issue. The description of the mechanical fields, arising in fretting-fatigue in the proximity of the contact edges, based on the use of nonlocal stress intensity factors is well suited for a multiscale approach and is non intrusive; two features that make it easily implementable in the industrial context.

Chapter 2

Nonlocal description of the fretting-fatigue problem

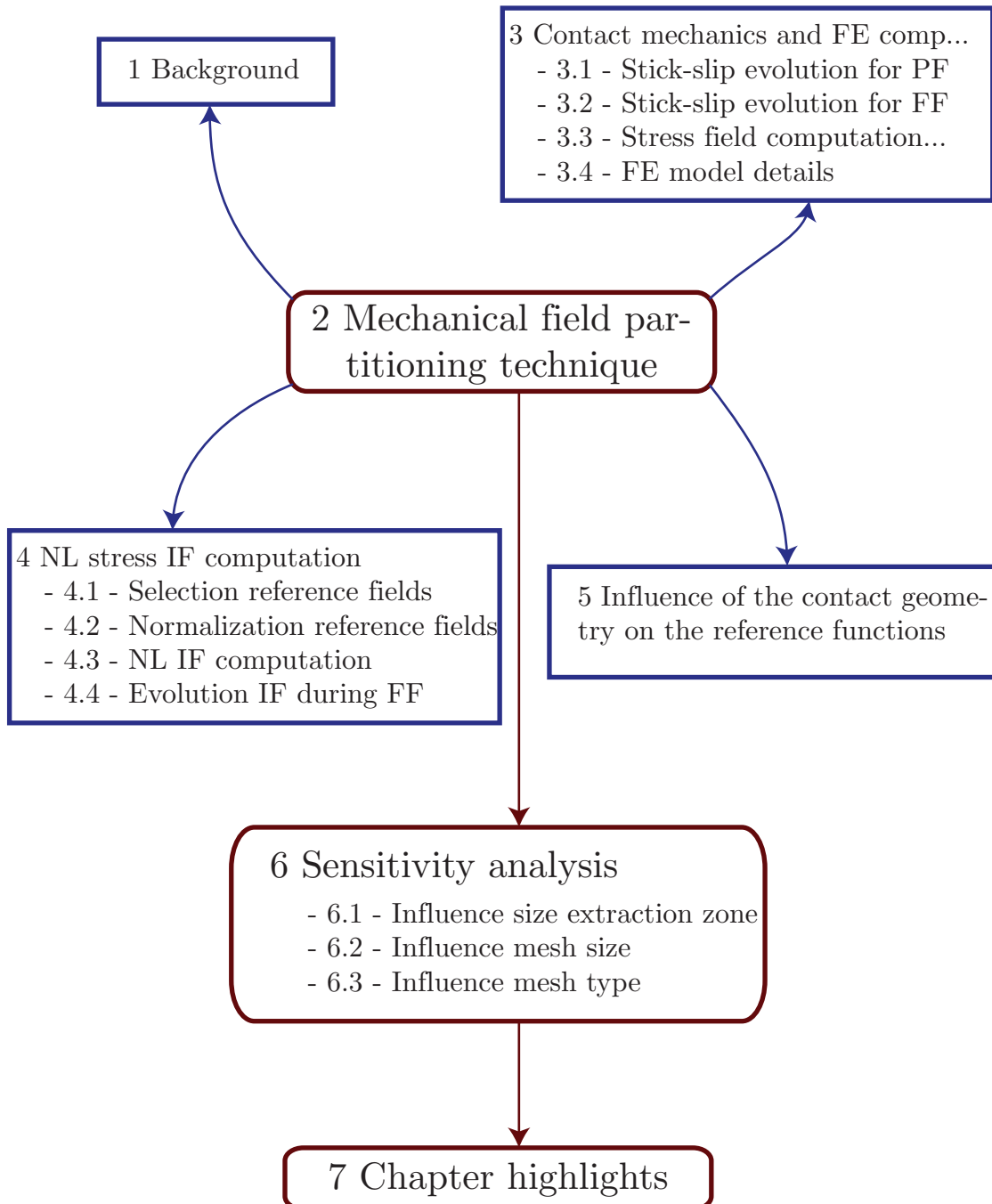
In this chapter a new method to take into account the stress gradient effect in fretting-fatigue is presented.

The approach is applied to the velocity field generated by the interaction between the contacting bodies in the proximity of the contact edges. In particular, \underline{v} , is partitioned into a summation of multiple terms, each one expressed as the product between nonlocal intensity factors, I^s , I^a , I^c , depending on the macroscopic loads applied to the mechanical assembly, and spatial reference fields, \underline{d}^s , \underline{d}^a , \underline{d}^c , depending on the local geometry of the part. The chapter is organized in the following way: in the first section, some insights from the work of Giannakopoulos [Giannakopoulos et al., 1998, Giannakopoulos et al., 2000], and Pommier [Pommier and Hamam, 2007] are introduced. In a sense, these contributions represent the basis for the development of the approach. A description of the analytical tools available to characterize the stress field generated by fretting-fatigue is presented as well.

In the second part of the chapter, the different steps allowing to obtain a nonlocal description of the velocity field are detailed.

The chapter ends with a sensitivity analysis in order to understand the impact that some key parameters have on the final outcome

Chapter 2 - Table of Contents Flowchart



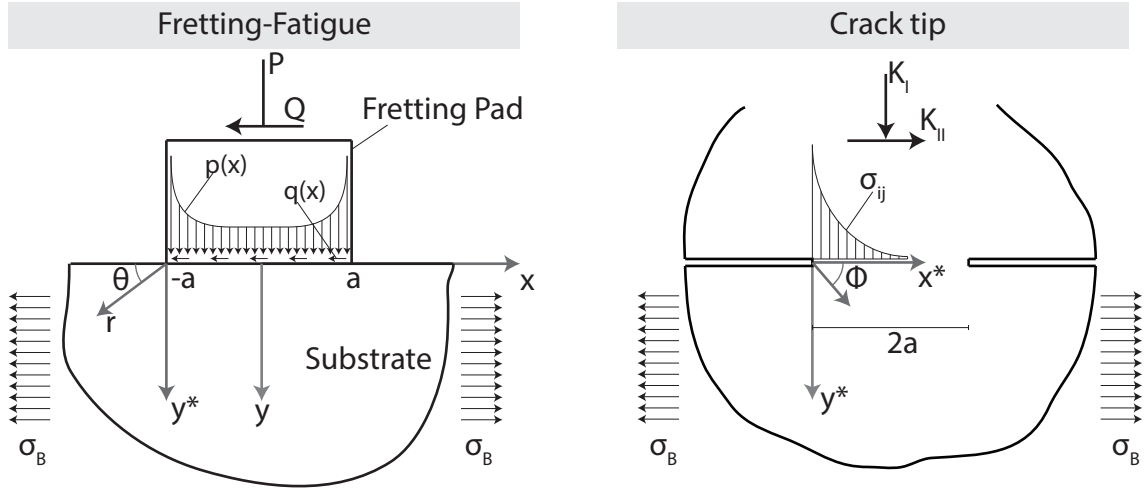


Figure 2.1: Crack analogue approach (flat punch over planar surface), [Giannakopoulos et al., 1998].

2.1 Background

One of the main characteristics of fretting-fatigue is the extremely localized and severe stress gradient generated by the contacting bodies at the interface. This is similar to what is observed close to a crack tip in terms of stress evolution. As a consequence, the mechanical fields arising under fretting-fatigue at the contact edges can be compared with the ones present in the proximity of a crack or a notch as it is shown by Giannakopoulos [Giannakopoulos et al., 1998, Giannakopoulos et al., 2000]. In particular, for a configuration where the contact generates a stress singularity at the contact tip (flat punch over planar surface, Figure 2.1), a crack analogue model [Giannakopoulos et al., 1998] may be used while a notch analogue model [Giannakopoulos et al., 2000] is well suited for a situation where a smooth transition to zero pressure at the contact edges is expected (round punch over planar surface).

For the configuration presented in Figure 2.1, the comparison between the stress evolution at the contact edge and at the crack tip can be performed analytically. In a reference system attached to the contact edge, the stresses generated by a normal force applied to the fretting pad are found to vary as follows:

$$\begin{pmatrix} \sigma_{rr} \\ \sigma_{\vartheta\vartheta} \\ \sigma_{r\vartheta} \end{pmatrix} \propto -\frac{3}{4\sqrt{r}} \begin{pmatrix} \sin \frac{3\vartheta}{2} + 5 \sin \frac{\vartheta}{2} \\ -\sin \frac{3\vartheta}{2} + 3 \sin \frac{\vartheta}{2} \\ \cos \frac{3\vartheta}{2} - \cos \frac{\vartheta}{2} \end{pmatrix}. \quad (2.1)$$

By exploiting the crack analogue transformation, $\phi = \pi - \vartheta$ for $0 \leq \vartheta \leq \pi$, Equation

2.1 becomes:

$$\begin{pmatrix} \sigma_{rr} \\ \sigma_{\phi\phi} \\ \sigma_{r\phi} \end{pmatrix} \propto \frac{1}{\sqrt{r}} \begin{pmatrix} \cos \frac{\phi}{2} (1 + \sin^2 \frac{\phi}{2}) \\ \cos^3 \frac{\phi}{2} \\ \sin \frac{\phi}{2} \cos^2 \frac{\phi}{2} \end{pmatrix}, \quad (2.2)$$

which describes a stress field evolution matching the one experienced at the crack tip. It is therefore possible to define a set of stress intensity factors describing the mechanical field generated by fretting, similarly to what is commonly done in fracture mechanics (K).

The normal force, P , generates a symmetric mechanical field that is analogue to what is observed at the crack tip loaded in mode I while the effect of the tangential force, Q , are comparable to a mode II loading. To notice that, since the analytical equations presented hereunder apply to 2D geometries, from now on, every time that the quantities P and Q appear in the text, the reader should consider them as force per unit length.

Considering a frictionless contact, the pressure distribution can be expressed as follows:

$$\sigma_{yy}(x) = \frac{P}{\pi\sqrt{a^2 - x^2}}, \quad \sigma_{yy}(x \rightarrow -a) = -\frac{P}{\pi\sqrt{2ar}}. \quad (2.3)$$

The effect of the normal pressure is analogue to the opening stress at the crack tip, $K_I = \sigma_{yy}\sqrt{2\pi r}$. By comparing Equation 2.3 with the equation describing K_I at the crack tip, the following relation is found,

$$K_I = -\frac{P}{\sqrt{\pi a}}. \quad (2.4)$$

The same approach is applied to find the relation between Q and K_{II} , obtaining the following result:

$$K_{II} = \frac{Q}{\sqrt{\pi a}}. \quad (2.5)$$

Equation 2.4 and 2.5 establish a connection between contact and fracture mechanics for the simple configuration presented in Figure 2.1. This allows to simplify the analysis of crack initiation and propagation in fretting by exploiting the tools already developed for fracture mechanics.

Despite the really interesting approach, its practical applications are limited by the fact that the analytical expressions developed are valid only for the specific contact geometry presented in Figure 2.1 where the partial slip zone is null.

Concerning the crack tip, an original approach has been proposed by Pommier [Pommier and Hamam, 2007, Pommier et al., 2009] aiming at describing mixed-mode cyclic elastic-plastic behavior of this region at the global scale. The purpose is to

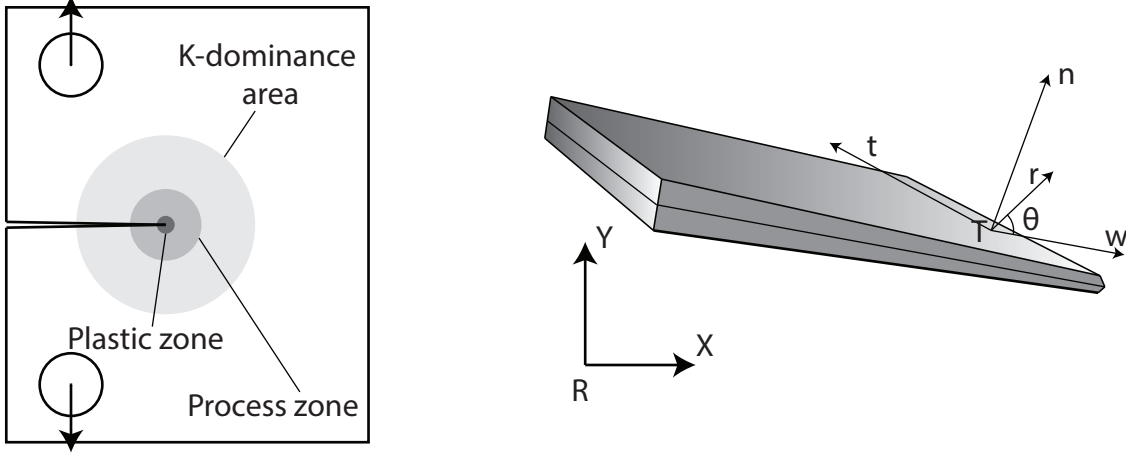


Figure 2.2: (a) Illustration of the different scales in fracture mechanics ;(b) reference frame attached to the crack tip T, [Fremy et al., 2012].

establish a reasonably precise model but condensed into a set of partial differential equations so as to avoid huge elastic-plastic FE computations. For this purpose the kinematics of the crack tip region is defined by a set of condensed variables:

$$\underline{v}_I \simeq \frac{d\tilde{K}_I}{dt} \underline{u}_I^e(P) + \frac{d\rho_I}{dt} \underline{u}_I^c(P), \quad (2.6)$$

$$\underline{v}_{II} \simeq \frac{d\tilde{K}_{II}}{dt} \underline{u}_{II}^e(P) + \frac{d\rho_{II}}{dt} \underline{u}_{II}^c(P). \quad (2.7)$$

Equations 2.6 and 2.7 describe the kinematics of the crack tip region, through a sum of products of spatial reference fields and intensity factor rates. This approach can be seen as a multiscale description of the crack tip behavior allowing to precisely represent what is happening in a confined zone by means of macroscopic quantities.

The two works presented above have been the inspiration for the method proposed in this manuscript. The main idea is to develop a tool capable to describe the stresses arising close to the contact surface under fretting-fatigue via nonlocal macroscopic quantities, transposing what has been proposed by Pommier for fracture mechanics to fretting-fatigue. This approach is justified by the fact that important analogies exist between the two different problems as proved by Giannakopoulos.

2.2 Mechanical field partitioning technique

Experimental evidence in fretting-fatigue [Proudhon et al., 2007] has shown that crack initiation is always experienced at the stick-slip region due to the huge increase in shear stress. This zone is extremely localized considering that its length is some micrometers and, therefore, a time-consuming FE computation (fine mesh) is needed to properly characterize the crack initiation risk. To overcome this limitation, the

idea is to establish a reasonably precise model to describe the stress gradient arising in the proximity of the contact edge, through a set of condensed variables.

In the presence of a strong stress gradient, the local geometry imposes the spatial distribution of the mechanical field while its intensity is determined by the macroscopic loads. Therefore, the solution of the problem can be described through a “fracture mechanics” approach, as the product between intensity factors and spatial reference fields:

$$\underline{v}(\underline{x}, t)_{R'} \simeq \underbrace{\dot{I}^s(t)\underline{d}^s(\underline{x}) + \dot{I}^a(t)\underline{d}^a(\underline{x})}_{\underline{v}^e} + \underbrace{\dot{I}^c(t)\underline{d}^c(\underline{x})}_{\underline{v}^c}. \quad (2.8)$$

This description is valid in a reference frame attached to the contact edge, as shown in Figure 2.3.

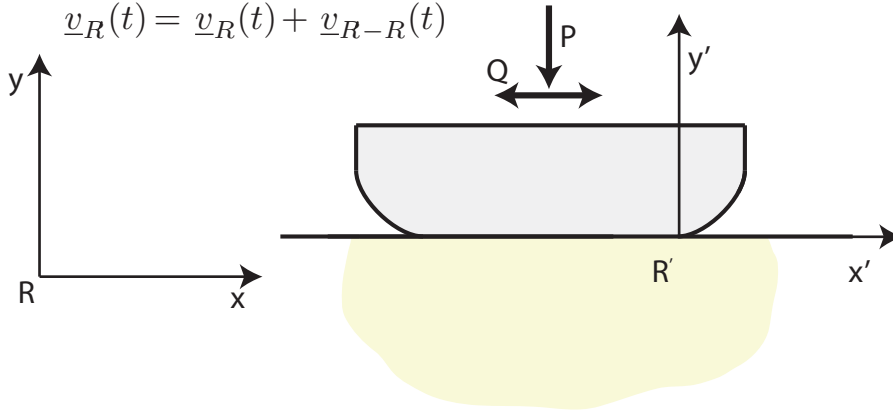


Figure 2.3: Reference frame (R') attached to the contact tip in which the velocity field (Equation 2.8) is defined.

In Equation 2.8, two different contributions to the total velocity field, \underline{v} , are underlined. \underline{v}^e represents the linear elastic response of the structure while \underline{v}^c describes the nonlinear contribution due to the friction in the stick-slip zone. This is the only source of nonlinearity since the material behavior is considered to remain inside the elastic domain. In turn, the elastic velocity field can be divided into a symmetric and antisymmetric part with respect to the contact plane.

The key assumption, behind this type of description, is to consider that there is just one degree of freedom for each term. The reference fields (\underline{d}^s , \underline{d}^a , \underline{d}^c) are defined by the local geometry of the problem and, therefore, only the nonlocal intensity factors (I^s , I^a , I^c) are independent variables. From a different perspective, \underline{d}^s , \underline{d}^a and \underline{d}^c form an orthonormal basis while I^s , I^a and I^c are the coefficients through which univocally characterize $\underline{v}(\underline{x}, t)$ in the proximity of the contact edges.

The partition is done on the velocity field rather than the stress or displacement fields because the velocity is an extensive variable that characterizes properly the nonlinear contribution of friction. In other words, to take into account the effect of

the nonlinearity there is the need to choose a variable that allows one to apply an incremental description of the mechanical field generated by fretting-fatigue loading. The velocity field, by definition $((X_{t+1} - X_t)/\Delta t)$ has this property.

Finally, it is important to remember that the aforementioned partition relies on some precise hypothesis. First, a geometric discontinuity is necessary to create the strong gradient imposing the spatial distribution of the mechanical field, reducing the degrees of freedom necessary to describe the system. Secondly, small deformation condition has to be respected to assure the possibility to decompose the velocity field in independent elastic and nonlinear terms. Lastly, the fact that the algorithm is applied to a self-similar geometry (scale invariant) permits to describe the reference fields as a product of two functions, depending separately on r and ϑ ,

$$\underline{d}^s(\underline{x}) \rightarrow \underline{d}^s(r, \vartheta) \simeq f^s(r)\underline{g}^s(\vartheta), \quad (2.9)$$

$$\underline{d}^a(\underline{x}) \rightarrow \underline{d}^a(r, \vartheta) \simeq f^a(r)\underline{g}^a(\vartheta), \quad (2.10)$$

$$\underline{d}^c(\underline{x}) \rightarrow \underline{d}^c(r, \vartheta) \simeq f^c(r)\underline{g}^c(\vartheta). \quad (2.11)$$

A generic contact configuration does not respect the last hypothesis. However the algorithm is applied to the velocity field inside a circular zone centered at the contact edge where, instead, the local geometry can be approximated as self-similar (Figure 2.9)

In the next section, the details to obtain a nonlocal description of the velocity field are presented. Here, I would like to stress the goal behind this type of approach, which is the extraction of objective quantities in order to apply the similitude principle to the fretting-fatigue problem. This would allow us to transpose the experimental or numerical results to a different scale from the one in which they have been obtained. In addition the approach must be suitable for industrial applications, no matter which contact geometry is analyzed. To meet the requirement, we propose a numerical algorithm based on finite element computations. An analytical approach ([Hills et al., 2012]) could have been chosen as well, but its validity is limited to some particular contact geometries and its introduction in industrial procedures seems to be more difficult.

2.3 Contact mechanics and FE computation

The first step for the application of the algorithm is the computation of the velocity field, that is obtained through finite element analysis. FE computations ensure superior performance with respect to analytical computations, in particular in any situation where the contact geometries cannot be described through a 2D approximation.

In this chapter the method is applied to a cylinder/plane 2D fretting-fatigue configuration. This choice is driven by the fact that for this particular setup numerous experimental results are presented in the literature, [Amargier et al., 2010, Fouvry et al., 2014, Ferré et al., 2013]. This allows one to easily validate the outcomes

of the numerical algorithm. With that said, the methodology has been developed, with the aim to be applicable to any possible contact geometry. This topic will be addressed shortly in the Conclusions where an example studying a 3D fretting-fatigue configuration is presented.

2.3.1 Stick-slip evolution for plain fretting

In this section the analytical development allowing to fully characterize the normal and shear stress distribution at the contact surface for a cylinder/plane contact configuration is presented. These results are important since they are systematically employed to validate the FE models through which the velocity field is computed; the velocity field represents the first step in the application of the approach and this is the reason why it is important to verify it.

As underlined several times in the previous sections, crack initiations are usually experienced at the stick-slip frontier. For this reason, it is important to accurately compute the stress field in this zone as a function of the macroscopic loads applied. For this purpose, the Cattaneo-Mindlin contact solution, [Cattaneo, 1938, Mindlin, 1949], is used.

When the pad and the specimen are pressed together under the action of a normal force, P , the pressure distribution at the interface between the two contacting bodies varies according to the following relation:

$$p(x) = -p_0 \sqrt{1 - \left(\frac{x}{a}\right)^2}, \quad (2.12)$$

where p_0 is the peak pressure

$$p_0 = \frac{2P}{\pi a}, \quad (2.13)$$

a is the semi-contact width

$$a = \sqrt{\frac{4PR}{\pi E^*}}, \quad (2.14)$$

R is an equivalent radius

$$R = \left(\frac{1}{R_1} + \frac{1}{R_2} \right)^{-1}, \quad (2.15)$$

which in the case of the cylinder/plane configuration is equal to the pad radius, and E^* is the equivalent Young's modulus,

$$E^* = \left(\frac{1 - \nu_1^2}{E_1} + \frac{1 - \nu_2^2}{E_2} \right)^{-1}. \quad (2.16)$$

By applying a monotonically increasing tangential force, Q , lower than the total slip limit value, ($Q < \mu P$), a shear stress distribution is generated over the contact surface,

$$q(x) = \frac{Q}{\pi\sqrt{a^2 - x^2}}. \quad (2.17)$$

Equation 2.17 holds true under the hypothesis of stick contact. However, it is immediately evident that $q(x)$ approaches infinity as $x \rightarrow \pm a$ whereas the normal pressure falls to zero. As a consequence, locally, the stick condition, $q(x) < \mu p(x)$, is not fulfilled. Some slip will occur within part of the contact surface even if the tangential force is very small, (Figure 2.4). In absence of a fatigue bulk force, the slip takes place in two symmetrical regions $a > |x| \geq c$ which surround a stick central zone $|x| < c$. To take into account this particular behavior, the shear traction is represented as a linear superposition of the fully sliding solution and a second term accounting for the stick central zone distribution,

$$q(x) = fp_0\sqrt{1 - \left(\frac{x}{a}\right)^2} + q'(x), \quad (2.18)$$

with

$$q'(x) = -fp_0\frac{c}{a}\sqrt{1 - \left(\frac{x}{c}\right)^2}, \quad (2.19)$$

and c equals to

$$c = a\sqrt{1 - \left|\frac{Q}{\mu P}\right|}. \quad (2.20)$$

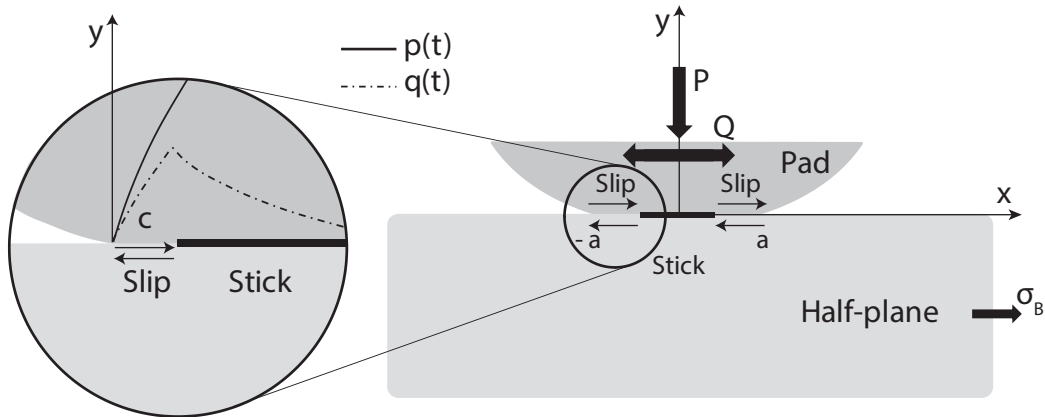


Figure 2.4: Schematic representation of cylinder-plane contact configuration under fretting-fatigue.

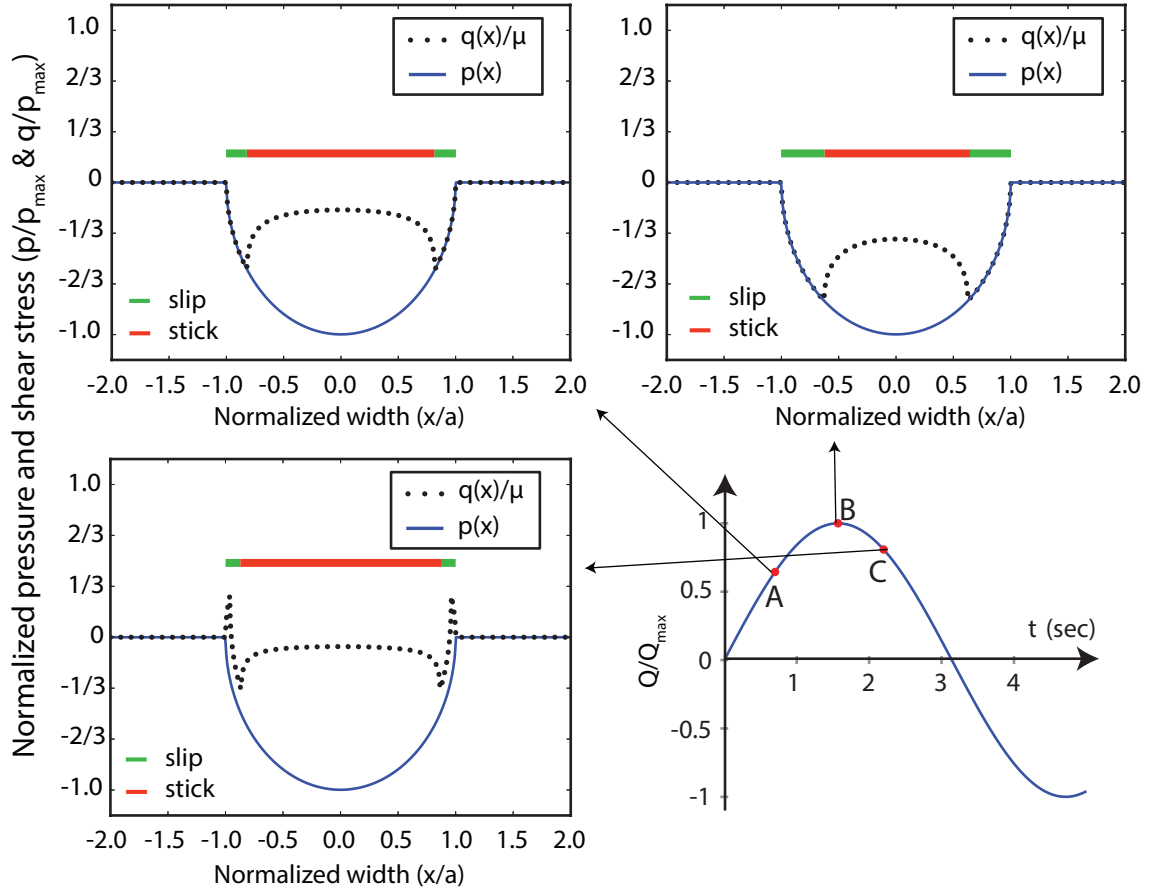


Figure 2.5: Evolution of the stick-slip zone as a function of the tangential force for cylinder plane configuration in plain fretting.

In Figure 2.5 the evolution of the stick-slip zone as a function of the tangential force is shown. With regard to the figure, from point A to point B, the increase of Q leads to the extension of the slip zone, reaching its maximum width where the peak tangential force value is experienced. As soon as the force starts to decrease, a sudden transition to a stick condition on the whole contact surface is observed. Further reducing the value of Q leads to the appearance of a reverse slip zone due to the fact that, locally, the relative displacement direction between the surfaces has been reversed. To take into account this third effect an additional corrective term is added,

$$q''(x) = 2\mu p_0 \frac{c'}{a} \sqrt{1 - \left(\frac{x}{c'}\right)^2}. \quad (2.21)$$

The following shear traction evolution is obtained,

$$\frac{q(x)}{fp_0} = -\sqrt{1 - \left(\frac{x}{a}\right)^2} \quad c' < |x| \leq a, \quad (2.22)$$

$$= -\sqrt{1 - \left(\frac{x}{a}\right)^2} + 2\frac{c'}{a}\sqrt{1 - \left(\frac{x}{c'}\right)^2} \quad c \leq |x| \leq c', \quad (2.23)$$

$$= -\sqrt{1 - \left(\frac{x}{a}\right)^2} + 2\frac{c'}{a}\sqrt{1 - \left(\frac{x}{c'}\right)^2} - \frac{c}{a}\sqrt{1 - \left(\frac{x}{c}\right)^2} \quad |x| \leq c, \quad (2.24)$$

with

$$\frac{c'}{a} = \sqrt{1 - \frac{Q_{max} - Q}{2\mu P}}. \quad (2.25)$$

2.3.2 Stick-slip evolution for fretting-fatigue

Once the bulk force is introduced, this term generates a corresponding bulk strain that is not present in the pad. The Cattaneo-Mindlin contact solution has to be modified in order to take into account this effect. As for the case of plain fretting the solution of the stick-slip evolution can be found by describing $q(x)$ as a variation with respect to the total slip condition,

$$q(x) = \mu p_0 \sqrt{1 - \left(\frac{x}{a}\right)^2} + q'(x), \quad (2.26)$$

where

$$q'(x) = -\mu p_0 \frac{c}{a} \sqrt{1 - \left(\frac{x - e}{c}\right)^2}, \quad (2.27)$$

with

$$e = \frac{\sigma_B a}{4\mu p_0}. \quad (2.28)$$

The shear distribution follows the same evolution as the one obtained for the case in which the bulk stress is equal to zero except for the fact that the center of the stick zone is shifted from the center of the contact, ($|x - e| < c$). Figure 2.6 illustrates what has been said regarding the stick slip zone evolution in presence of a bulk stress.

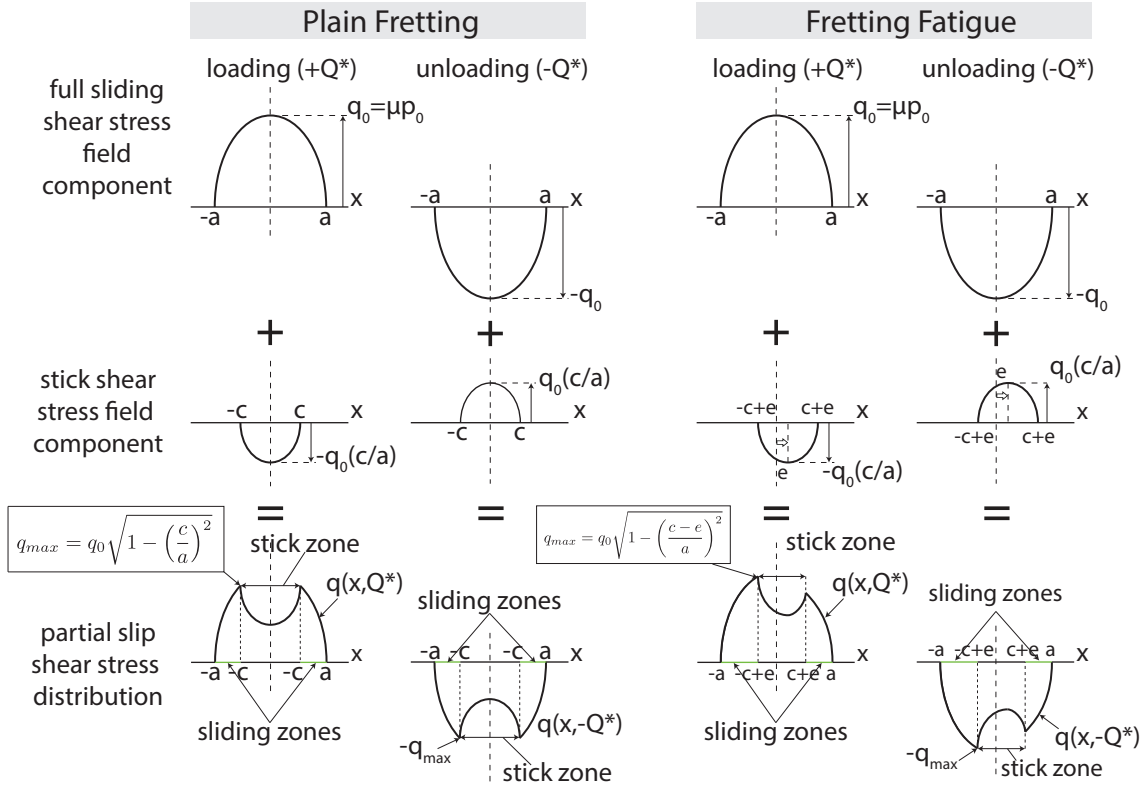


Figure 2.6: Illustration of Mindlin surface shear distributions generated in partial slip cylinder/plane contact under plain fretting and fretting-fatigue loading conditions, [Fouvry et al., 2014].

2.3.3 Stress field computation in the substrate

Once the distribution of the shear and normal force at the contact surface has been computed, it is possible to determine the stress evolution in the substrate. The most efficient way to characterize this field consists in using the complex potentials developed by Muskhelishvili, [Muskhelishvili, 1953], which, for plane elasticity, describe completely the stress field by means of a function of complex variables, $\phi(z)$,

$$\sigma_{xx} + \sigma_{yy} = 2 \left[\phi(z) + \overline{\phi(z)} \right], \quad (2.29)$$

$$\sigma_{yy} - \sigma_{xx} + 2i\tau_{xy} = 2 \left[(\bar{z} - z)\phi'(z) - \overline{\phi(z)} - \phi(z) \right], \quad (2.30)$$

$$\sigma_{zz} = \nu(\sigma_{xx} + \sigma_{yy}), \quad (2.31)$$

$$\tau_{zy} = \tau_{zx} = 0, \quad (2.32)$$

where $z = x + iy$.

For cylinder/plane contact configuration the analytical expressions of the poten-

tials are known,

$$\phi^n(z) = \frac{1}{2\pi i} \int_{-a}^a \frac{p(\xi)}{\xi - z} d\xi, \quad (2.33)$$

$$\phi^s(z) = \frac{1 - if}{2\pi i} \int_{-a}^a \frac{p(\xi)}{\xi - z} d\xi. \quad (2.34)$$

By solving the linear system described by Equations 2.29-2.32, the value of the stress field for each time step is computed. Once again, the complete solution for a cyclic loading is obtained by superposing the different contributions (full slide solution + corrective term for reverse slip + corrective term for eccentricity of the slip zone + bulk load). For instance, for a configuration where the normal load is constant and the tangential load varies sinusoidally, ($P(t) = P$, $Q(t) = Q^* \sin(\omega t)$), σ_{xx} is found to vary as follows:

- $P(t) = P$, and $Q(t) = Q_{max}$:

$$\frac{\sigma_{xx}(x, y)}{p_0} = \left(\frac{\sigma_{xx}^n\left(\frac{x}{a}, \frac{y}{a}\right)}{p_0} \right) + \mu \left(\frac{\sigma_{xx}^t\left(\frac{x}{a}, \frac{y}{a}\right)}{\mu p_0} \right) - \mu \frac{c}{a} \left(\frac{\sigma_{xx}^t\left(\frac{x-e}{c}, \frac{y}{c}\right)}{\mu p_0} \right) + \frac{\sigma_B}{p_0}, \quad (2.35)$$

- $P(t) = P$, and $Q_{min} < Q(t) < Q_{max}$ and $dQ(t)/dt < 0$:

$$\begin{aligned} \frac{\sigma_{xx}(x, y)}{p_0} = & \left(\frac{\sigma_{xx}^n\left(\frac{x}{a}, \frac{y}{a}\right)}{p_0} \right) - \mu \left(\frac{\sigma_{xx}^t\left(\frac{x}{a}, \frac{y}{a}\right)}{\mu p_0} \right) + 2\mu \frac{c'}{a} \left(\frac{\sigma_{xx}^t\left(\frac{x-e'}{c'}, \frac{y}{c'}\right)}{\mu p_0} \right) + \\ & - \mu \frac{c}{a} \left(\frac{\sigma_{xx}^t\left(\frac{x-e}{c}, \frac{y}{c}\right)}{\mu p_0} \right) + \frac{\sigma_B}{p_0}, \end{aligned} \quad (2.36)$$

- $P(t) = P$, and $Q = Q_{min}$:

$$\frac{\sigma_{xx}(x, y)}{p_0} = \left(\frac{\sigma_{xx}^n\left(\frac{x}{a}, \frac{y}{a}\right)}{p_0} \right) - \mu \left(\frac{\sigma_{xx}^t\left(\frac{x}{a}, \frac{y}{a}\right)}{\mu p_0} \right) + \mu \frac{c}{a} \left(\frac{\sigma_{xx}^t\left(\frac{x-e}{c}, \frac{y}{c}\right)}{\mu p_0} \right) + \frac{\sigma_B}{p_0}, \quad (2.37)$$

- $P(t) = P$, $Q_{min} < Q(t) < Q_{max}$ and $dQ(t)/dt > 0$:

$$\begin{aligned} \frac{\sigma_{xx}(x, y)}{p_0} = & \left(\frac{\sigma_{xx}^n\left(\frac{x}{a}, \frac{y}{a}\right)}{p_0} \right) + \mu \left(\frac{\sigma_{xx}^t\left(\frac{x}{a}, \frac{y}{a}\right)}{\mu p_0} \right) - 2\mu \frac{c'}{a} \left(\frac{\sigma_{xx}^t\left(\frac{x-e'}{c'}, \frac{y}{c'}\right)}{\mu p_0} \right) + \\ & + \mu \frac{c}{a} \left(\frac{\sigma_{xx}^t\left(\frac{x-e}{c}, \frac{y}{c}\right)}{\mu p_0} \right) + \frac{\sigma_B}{p_0}, \end{aligned} \quad (2.38)$$

where c is the stick zone half width, e and e' are equal to,

$$\frac{e}{a} = \frac{\sigma_B^{max}}{4\mu P}, \quad \frac{e'}{a} = \frac{\sigma_B^{max} - \sigma_B(t)}{8\mu P}, \quad (2.39)$$

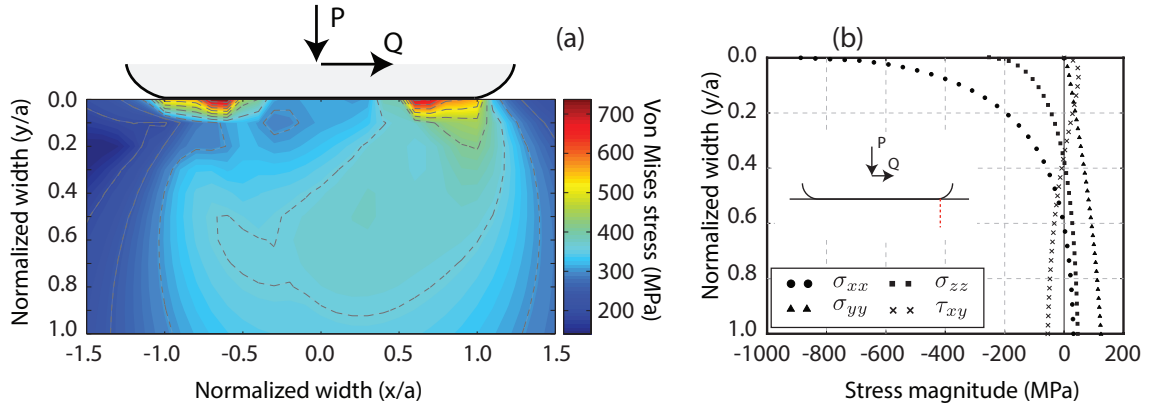


Figure 2.7: (a) Von Mises stress distribution in the substrate; (b) Stress tensor evolution as a function of the normalized depth.

$\sigma_{xx}^n, \sigma_{xx}^t, \sigma^B$ are the components of the stress tensor generated by normal, tangential and bulk load, and the other terms take into account the reverse slip.

The evaluation of the stress tensor in the substrate is therefore straightforward. In Figure 2.7 a simple example of the application of the procedure described above is presented. The geometry used is a cylinder/plane contact configuration characterized by the following parameters: Pad radius = 20 mm, friction coefficient = 0.8, Young's modulus = 119 400 MPa, Poisson's ratio = 0.3, $P = 347 \text{ N mm}^{-1}$ and $Q^* = 237 \text{ N mm}^{-1}$.

2.3.4 FE model details

Figure 2.8 presents the basic features of the finite element model employed in the fretting-fatigue simulations. It consists in an elastic quasi-static computation and plane strain linear elastic quadrilateral elements are employed. The elastic simulation is justified by the fact that, for the loading combinations tested, the stresses do not overcome the yield limit. In addition, the particular contact configuration chosen allows one to reproduce an initial 3D experimental setup with a 2D model via the plane strain assumption.

To model the contact, the Lagrange multipliers technique is chosen. Some benchmarks have been performed comparing this technique to the others proposed by the FEM software used, (ABAQUS), and Lagrange multipliers have shown to be the algorithm that assures the best accuracy. To handle the relative slip between the two contacting bodies Coulomb's friction law is employed. Close to the surface, a region with a structured finer mesh permits to well describe the stress gradient evolution. The typical length of the elements composing this zone varies in a range of 5 to 10 μm in order to ensure a good convergence between the FE stress tensor value at the contact surface and the analytical solution presented in Section 2.3.3. Linear quadrilateral element, CPE4, are employed assuring the best trade-off between

accuracy and performance in terms of computational cost.

Concerning the loading, constant normal load (P) and cyclic tangential load (Q) are applied at the top of the pad in order to simulate fretting while a cyclic bulk load (σ_B) is applied on the specimen, in phase with the tangential load, to reproduce the fatigue effect.

With regards to the geometrical and material parameters employed in the FE model, they depend on the experimental tests that one wish to numerically reproduce. Chapter 3 focuses on the application of the method developed to experimental results and therefore further details are given. Here it is sufficient to say that a fully parametric FE model is employed allowing an easy switch from one configuration to another.

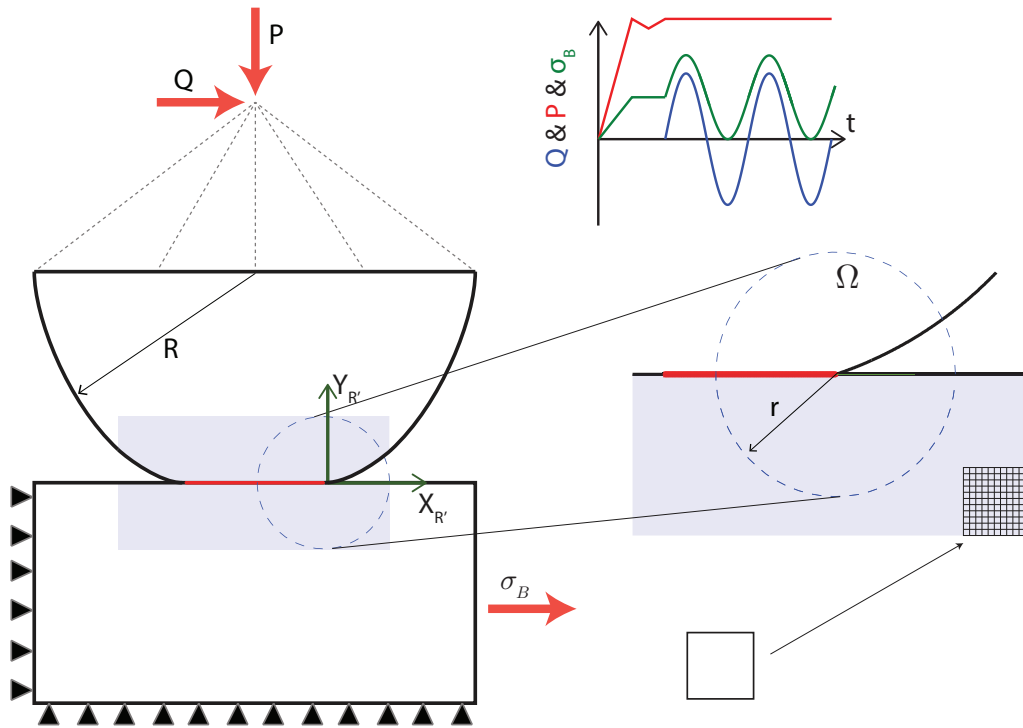


Figure 2.8: FEM parameters and loading evolution used.

2.4 Nonlocal stress intensity factor computation

In the previous section the FE model to compute the velocity field generated during a fretting-fatigue simulation has been presented in detail. Once the requested field is obtained, the next step is represented by the post-treatment of the information gathered in order to extract the nonlocal intensity factors.

Since the aim is to describe the mechanical fields arising around the contact edges by exploiting the crack analogue approach, only the values inside the circular region,

Ω , of radius r , centered at the contact tip, are analyzed (Figure 2.9),

$$\underline{v}(\underline{x}, t) \rightarrow \underline{v}_{i,t} \quad i \in \Omega, \quad t \in T, \quad (2.40)$$

where T is the total time length of the fretting-fatigue simulation. The value of r is chosen in order to obtain a ratio $r/R < 0.05$. Since R is determined by the geometry of the problem, the variation of the ratio has the consequence to increase or reduce the zone, around the contact edge, where the analysis is performed. The selected value reflects the idea that the crack analogue approach can be employed with the hypothesis to be sufficiently close to the contact edge so as to work with a self-similar geometry. Inside this range no particular sensitivity with respect to r has been experienced; nevertheless in Section 2.6.1 further details are given concerning this topic.

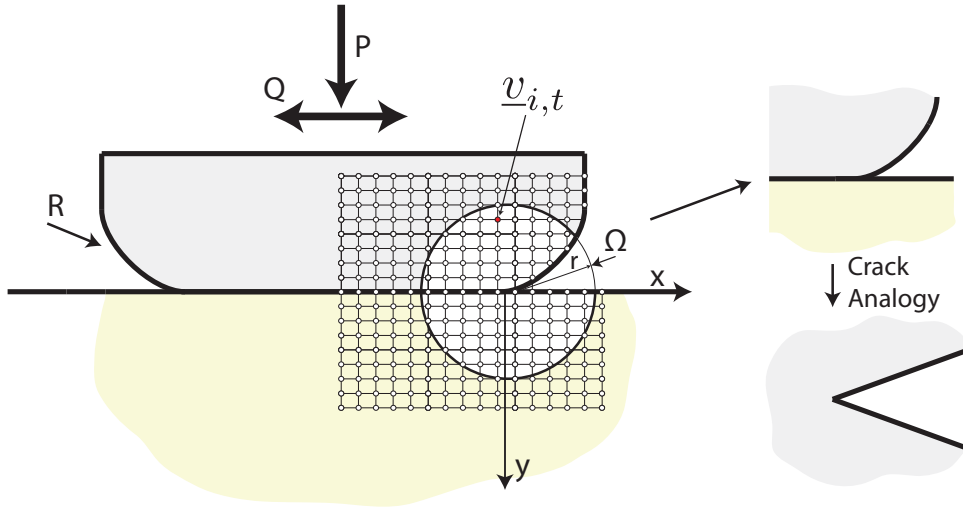


Figure 2.9: Extraction of the velocity field over a circular zone centered at the contact edge.

2.4.1 Selection of the reference fields

To perform the partition of the velocity field, as presented in Equation 2.8, the first step consists in the selection of the spatial reference fields. The velocity field at the contact tip is considered to be comparable to the one originated at the crack tip. In 2D LEFM, it is a common approach to describe the resultant displacement field close to the crack tip as a product between intensity factors and spatial reference fields corresponding to the symmetric (mode I) and antisymmetric (mode II) parts of the displacement field.

For fretting-fatigue the same approach can be employed, considering that the geometry is self similar in the proximity of the contact edges. The symmetric and antisymmetric reference fields are generated respectively by normal and tangential

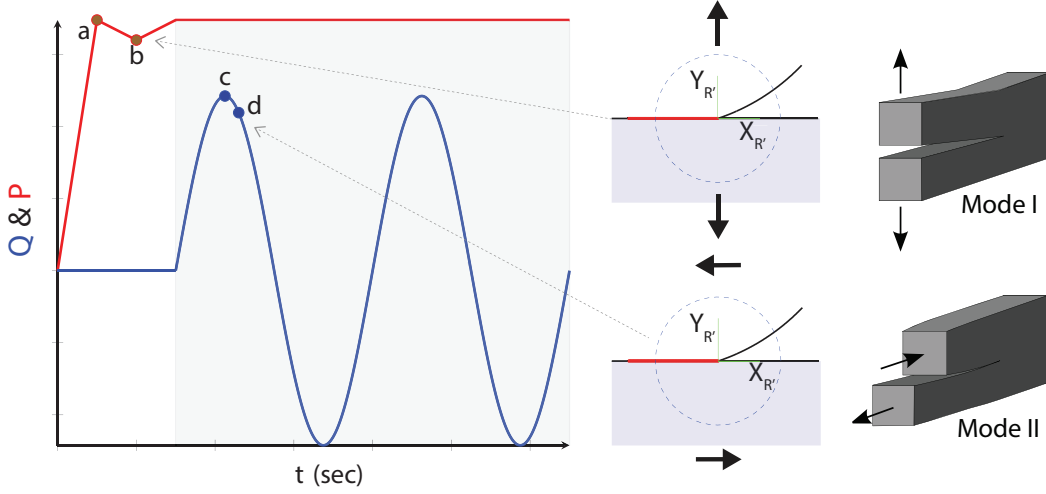


Figure 2.10: Different steps in the FE computation to extract the reference fields.

forces (P, Q) . In particular $\underline{d}^s(\underline{x})$ is selected as the reference field generated by a ΔP , while $\underline{d}^a(\underline{x})$ as the one produced by a ΔQ in a situation where all the contact surface is in a stick condition in order to separate the elastic response from the nonlinear contribution of the friction arising in the slip zone.

In Figure 2.10 an example of a possible loading path, suitable to extract the intensity factors, is shown. The normal load reaches its peak value followed by an unloading step which allows to extract the symmetric reference field. Bearing in mind the analogy with a crack, this specific loading history reproduces, a mode I analogue velocity field close to the contact edge

$$\underline{d}^s(\underline{x}) = \frac{\underline{x}(t_B) - \underline{x}(t_A)}{t_B - t_A}. \quad (2.41)$$

Concerning the tangential load, the same procedure is applied, and a mode II analogue velocity field is computed. As specified before, the asymmetric reference field is extracted in a situation where all the contact surface is in stick condition; the assumption of no slip requires the two bodies to behave as one. For a simple sinusoidal tangential load this condition is respected every time its derivative changes sign (In Figure 2.13b a typical evolution of the slip zone is shown). This justifies the extraction point selection made in Figure 2.10,

$$\underline{d}^a(\underline{x}) = \frac{\underline{x}(t_D) - \underline{x}(t_C)}{t_D - t_C}. \quad (2.42)$$

2.4.2 Normalization of the reference fields

By expressing the reference fields in polar coordinates, their radial and tangential evolution with respect to the contact tip are obtained, under the form of a product between two functions depending separately on r and ϑ . For this purpose the

Karhunen-Loève decomposition [Loève, 1955] is employed (further details concerning the algorithm are presented in Appendix A),

$$\underline{d}^s(\underline{x}) \rightarrow \underline{d}^s(r, \vartheta) \simeq f^s(r) \underline{g}^s(\vartheta), \quad (2.43)$$

$$\underline{d}^a(\underline{x}) \rightarrow \underline{d}^a(r, \vartheta) \simeq f^a(r) \underline{g}^a(\vartheta). \quad (2.44)$$

In Figures 2.11 and 2.12 the outcomes from a plain fretting simulation characterized by the following parameters, Pad radius = 20 mm, friction coefficient = 0.8, Young's modulus = 119 400 MPa, Poisson's ratio = 0.3, $P = 347 \text{ N mm}^{-1}$ and $Q^* = 237 \text{ N mm}^{-1}$, are presented. Both the tangential and radial evolution of \underline{d}^s and \underline{d}^a show a good accordance with what is observed, in terms of displacement field, at the crack tip (mode I and mode II), validating the crack analogue approach. It is worth mentioning that both reference fields are normalized in order to correspond to the displacement field obtained at the crack tip during an elastic loading phase with either $\Delta K_I^\infty = 1 \text{ MPa}\sqrt{\text{m}}$ or $\Delta K_{II}^\infty = 1 \text{ MPa}\sqrt{\text{m}}$.

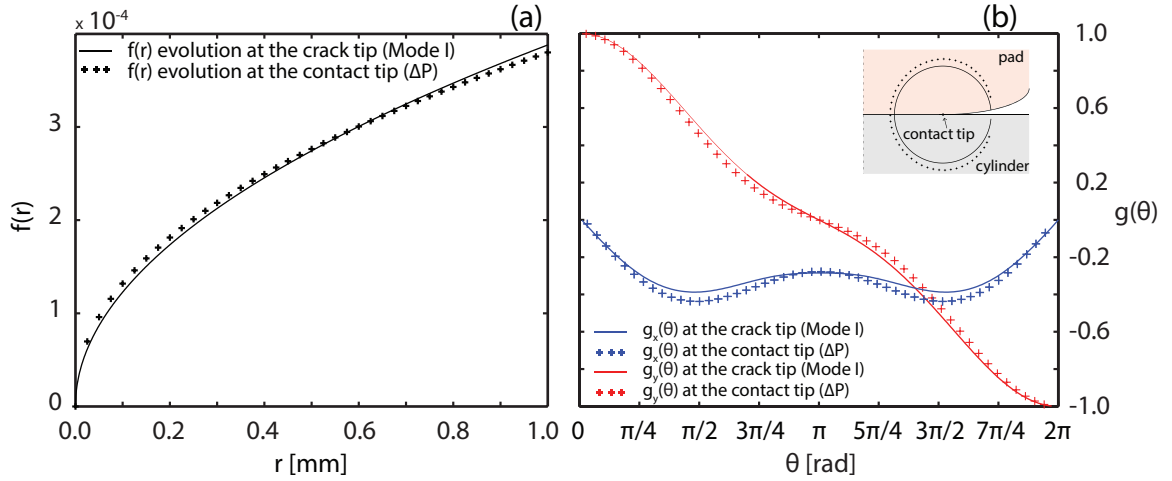


Figure 2.11: (a) Comparison between radial evolution of \underline{d}^s and radial evolution of the displacement field at the crack tip (mode I); (b) Comparison between tangential evolution of \underline{d}^s and tangential evolution of the displacement field at the crack tip (mode I).

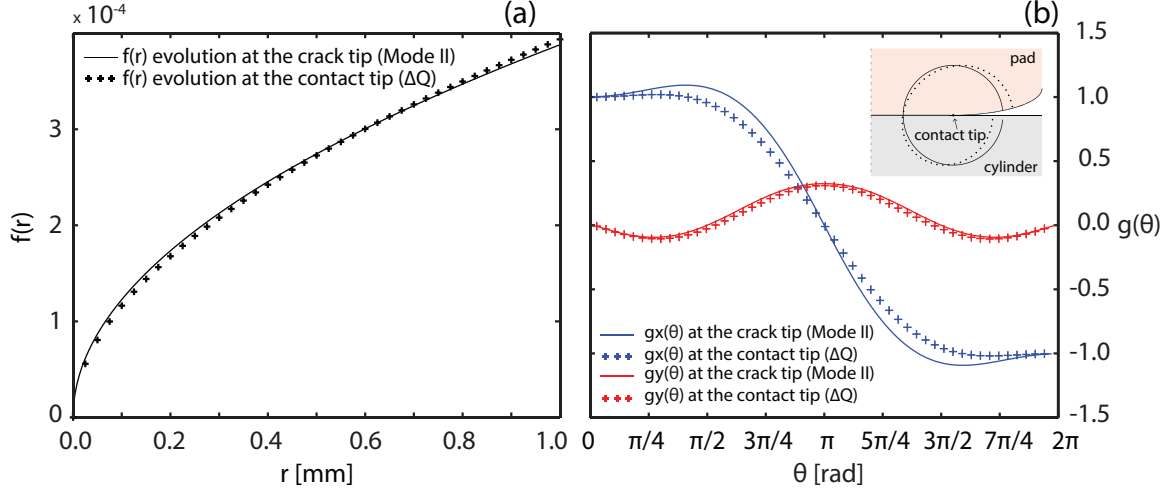


Figure 2.12: (a) Comparison between radial evolution of \underline{d}^a and radial evolution of the displacement field at the crack tip (mode II); (b) Comparison between tangential evolution of \underline{d}^a and tangential evolution of the displacement field at the crack tip (mode II).

2.4.3 Nonlocal intensity factor computation

By projecting the reference fields on the velocity field, outcome of the finite element computation, the relative intensity factor rates are computed:

$$\dot{I}^s(t) = \frac{\int_{\Omega} \underline{v} \cdot \underline{d}^s}{\int_{\Omega} \underline{d}^s \cdot \underline{d}^s} \rightarrow \dot{I}_t^s = \frac{\sum_i^N \underline{v}_{i,t} \cdot \underline{d}_i^s}{\sum_i^N \underline{d}_i^s \cdot \underline{d}_i^s}, \quad (2.45)$$

$$\dot{I}^a(t) = \frac{\int_{\Omega} \underline{v} \cdot \underline{d}^a}{\int_{\Omega} \underline{d}^a \cdot \underline{d}^a} \rightarrow \dot{I}_t^a = \frac{\sum_i^N \underline{v}_{i,t} \cdot \underline{d}_i^a}{\sum_i^N \underline{d}_i^a \cdot \underline{d}_i^a}. \quad (2.46)$$

$\dot{I}^s(t)$, $\dot{I}^a(t)$ highlight the contribution of each reference field with respect to the initial velocity field. A first approximation of $\underline{v}(\underline{x}, t)$ is therefore obtained:

$$\underline{v}(\underline{x}, t) \simeq \dot{I}^s(t) \underline{d}^s(\underline{x}) + \dot{I}^a(t) \underline{d}^a(\underline{x}), \quad (2.47)$$

where

$$\underline{v}^e(\underline{x}, t) = \dot{I}^s(t) \underline{d}^s(\underline{x}) + \dot{I}^a(t) \underline{d}^a(\underline{x}). \quad (2.48)$$

This description includes just the elastic response of the assembly to the macroscopic loads (in a reference frame attached to the contact edge), neglecting the effects of friction in the stick-slip zone, which constitute a source of nonlinearity.

To evaluate the accuracy of the approximation described by Equation 2.47, the “elastic” error is computed:

$$\xi_e(t) = \sqrt{\frac{\int_{\Omega} [\underline{v}(\underline{x}, t) - \underline{v}^e(\underline{x}, t)]^2}{\int_{\Omega} \underline{v}(\underline{x}, t)^2}}. \quad (2.49)$$

In Figure 2.13, its evolution during the fretting-fatigue cycle is presented. With

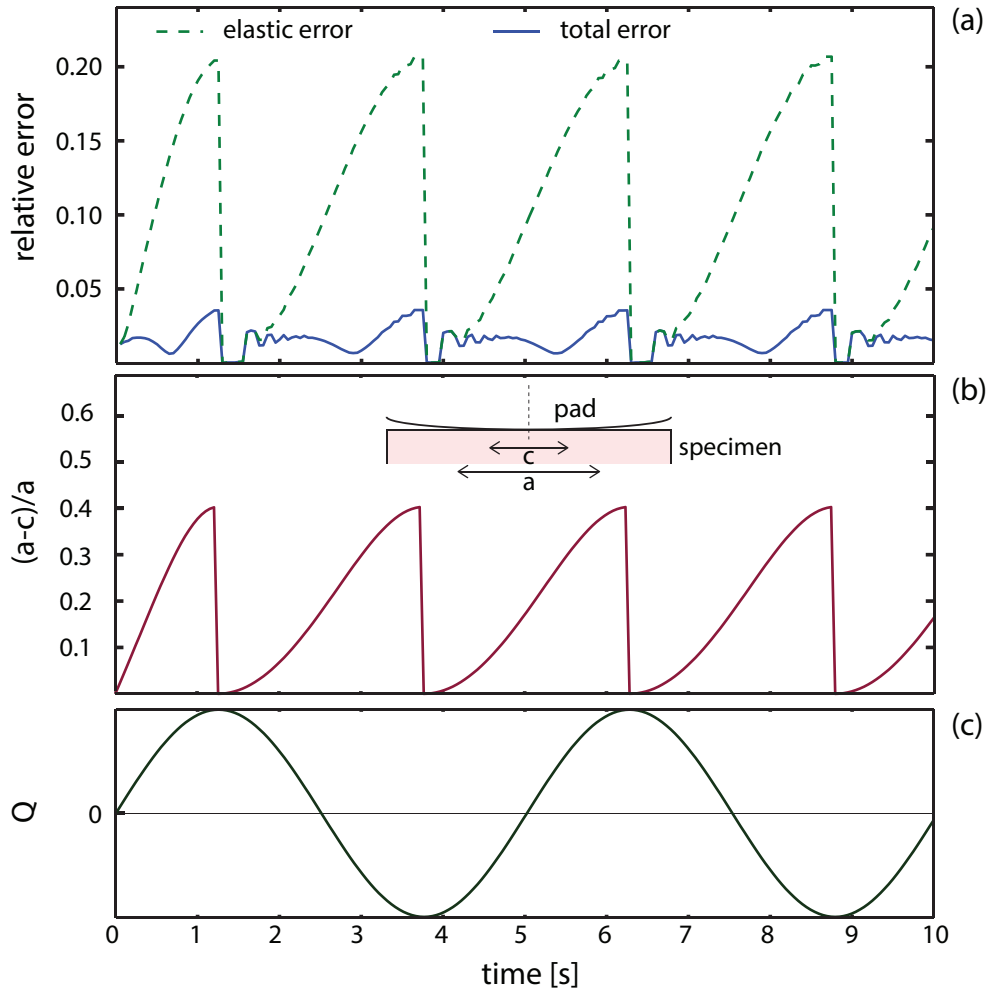


Figure 2.13: (a) Error evolution introduced by the approximation; (b) evolution of the stick-slip region during fretting-fatigue cycle; (c) cyclic tangential load, Q .

the variation of Q , the percentage of contact surface, being in a stick-slip condition, varies. In particular, with the increase of the slip zone, the nonlinear term becomes more important and, as a consequence, the “elastic” approximation is no more representative of the initial velocity field. At the same time this behavior can be seen as a confirmation of the importance of the nonlinear effect of friction. An additional

term is therefore added to the approximation,

$$\underline{v}^c(\underline{x}, t) = \underline{v}(\underline{x}, t) - \underline{v}^e(\underline{x}, t). \quad (2.50)$$

In this case, The Karhunen-Loeve decomposition is used twice, the first time to partition the field in a product between two functions depending separately on time and space:

$$\underline{v}^c(\underline{x}, t) \simeq \dot{I}^c(t)\underline{d}^c(\underline{x}), \quad (2.51)$$

and the second time to express the complementary reference field as a function of r and ϑ ,

$$\underline{d}^c(\underline{x}) \rightarrow \underline{d}^c(r, \vartheta) \simeq f^c(r)\underline{g}^c(\vartheta). \quad (2.52)$$

The intensity of $\underline{d}^c(\underline{x})$ decreases quickly (Figure 2.14) confirming the very localized effect of the friction in the stick-slip region. In addition, the fact that the complementary field is “confined” and its influence vanishes rapidly allows us to suppose that the elastic nonlocal intensity factors, I^s and I^a , are sufficient to univocally characterize the contact edge stress condition. This is exactly the same approach adopted in fracture mechanics where the hypothesis of small scale yielding permits to use the linear elastic stress intensity factor, K , to describe the mechanical field close to the crack tip.

In Figure 2.14, the radial and tangential evolution of the complementary reference field is shown. In this case the normalization rule applied is such that $f^c(r = 0) = 1$.

The new approximation of the initial velocity field (output from the FE computation) is eventually obtained (Equation 2.8) and the error associated is expressed as follows:

$$\xi_{tot}(t) = \sqrt{\frac{\int_{\Omega} [\underline{v}(\underline{x}, t) - \underline{v}^e(\underline{x}, t) - \underline{v}^c(\underline{x}, t)]^2}{\int_{\Omega} \underline{v}(\underline{x}, t)^2}}. \quad (2.53)$$

It is worth noting that, with the introduction of the nonlinear term in the approximation, the error falls below 5 %, (Figure 2.13a). Moreover, in the definition of the error (Equations 2.49 and 2.53) each node, where the velocity field is extracted, is considered to have the same weight equally contributing to the final error. This is due to the fact that the mesh is structured and uniform, thus, every node has the same support volume.

2.4.4 Evolution of the intensity factors during fretting-fatigue

By integrating, I^a , I^s and I^c , the evolution of the nonlocal intensity factors is obtained.

$$I = \int_{t=0}^T \dot{I}(\tau) d\tau. \quad (2.54)$$

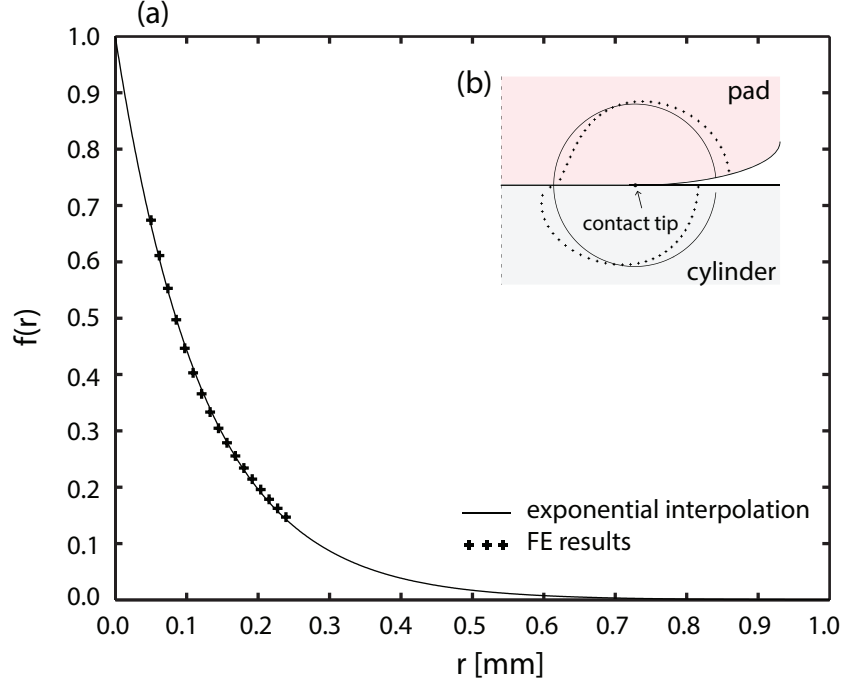


Figure 2.14: (a) Radial evolution of \underline{d}^c ; (b) $(++)$ evolution of $\underline{g}^c(\vartheta)$ applied on a circle around the contact tip.

In Figures 2.15 and 2.16 the variation of I^a , I^s and I^c during a plain fretting simulation is investigated. The test case is, once again, characterized by the following parameters, Pad radius = 20 mm, friction coefficient = 0.8, Young's modulus = 119 400 MPa, Poisson's ratio = 0.3, $P = 347 \text{ N mm}^{-1}$ and $Q^* = 237 \text{ N mm}^{-1}$.

Two interesting points are highlighted. First, the evolution of I^a and I^s (Figure 2.15) confirms that the effect of the normal force, P , and tangential force, Q , are independent. Furthermore, considering the loading evolution used to extract the velocity field, (Figure 2.15), characterized by a sinusoidal tangential force, Q , a sinusoidal bulk load, σ_B , and a constant normal force, P , it is clear that

$$\int_T \dot{I}^s(t) dt = 0, \quad I^s(t) = 0,$$

since a constant force has no effect on the velocity field that takes into account only the incremental changes. This is the reason why it is important to include in the loading history a small variation of the normal force, ΔP , which allows to compute the effect of P ,

$$I^s = I_{\Delta P}^s \frac{P}{\Delta P}, \quad (2.55)$$

where $I_{\Delta P}^s$ is computed for a very small ΔP in order to consider negligible the variation of the contact area resulting from the change in the normal force. This

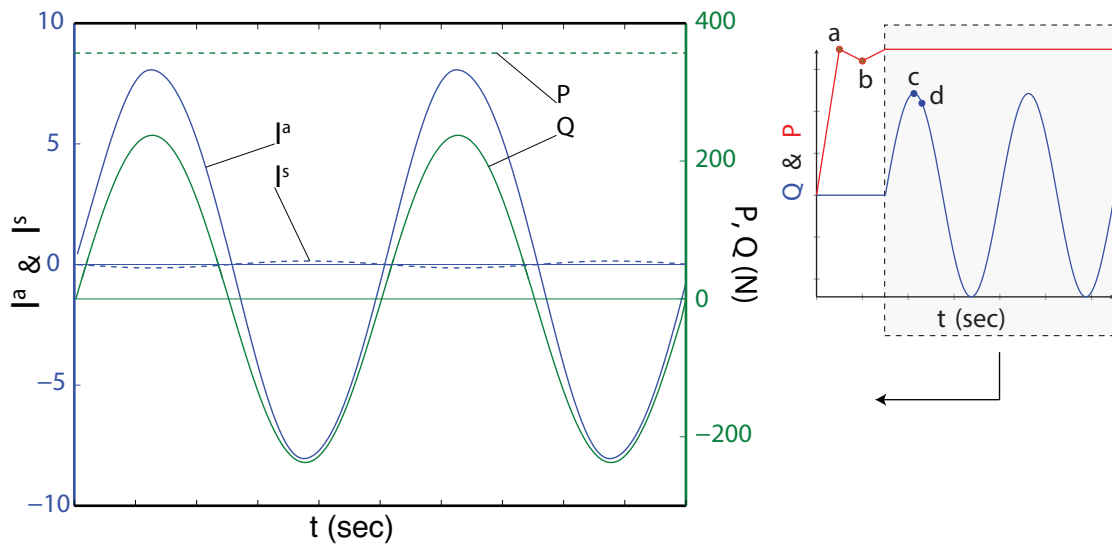


Figure 2.15: Evolution of I^a and I^s during a plain fretting FE simulation.

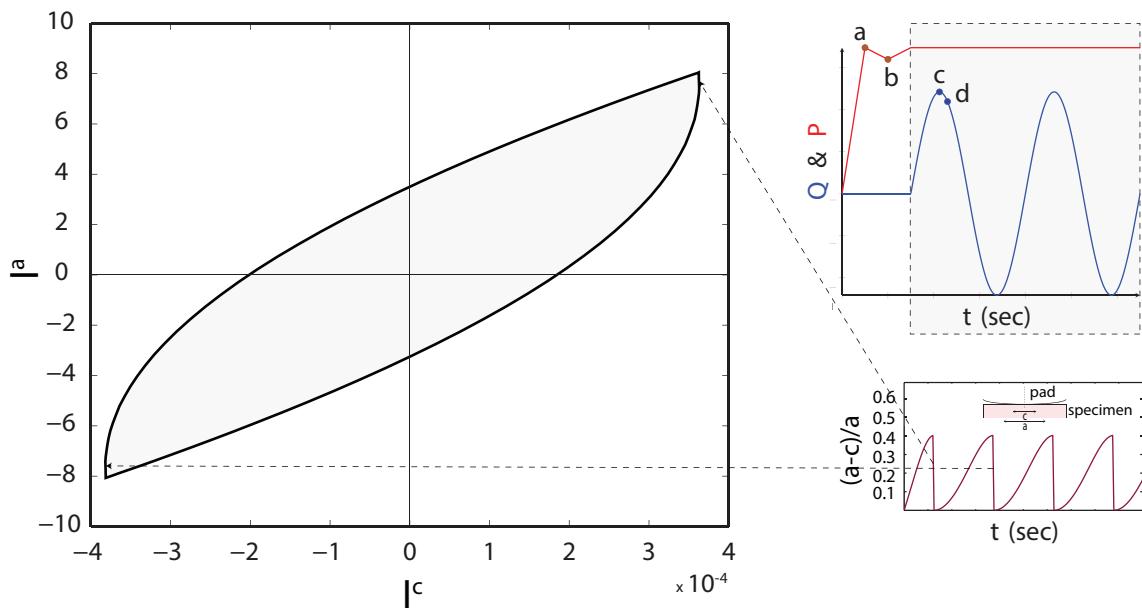


Figure 2.16: Evolution of I^a and I^c during a plain fretting FE simulation.

assumption implies that in the case where the normal force, P varies over the cycles, the partition technique has to be applied in an incremental way since the current formulation does not take into account the displacement of the contact front (to remember that for a constant normal force, no matter which tangential force is applied, the contact surface remains unchanged while the size of the partial slip zone will change).

By contrast, I^a varies in phase with the tangential load Q .

Concerning I^c , term that takes into account the nonlinear contribution introduced by the friction coefficient, it is interesting to look at the hysteresis loop presented in Figure 2.16. The area below the curve represents the energy dissipated by friction. Once again, the trend shown confirms the independence of the different mechanisms intervening in the definitions of the velocity field. For instance, when the slip zone becomes null, I^c does not vary and vice versa.

To sum up, the partition permits to reduce the degrees of freedom needed to characterize the velocity field. As a matter of fact, for any given macroscopic load combination (P, Q, σ_B) , I^s , I^a and I^c give a portrait of the severity of the stresses arising close to the contact edges during a fretting-fatigue simulation. These nonlocal quantities are computed studying the evolution of the mechanical fields and therefore the gradient effect is taken into account. The main steps in order to partition the velocity field are listed hereunder:

- step 1: for any given macroscopic load combination and geometry, a FE computation is performed to obtain the velocity field close to the contact edges,
- step 2: the spatial reference fields, $\underline{d}^s(\underline{x})$, $\underline{d}^a(\underline{x})$ are selected,
- step 3: the intensity factor rates, \dot{I}^s , \dot{I}^a , are computed (elastic approximation),
- step 4: an additional term, $\underline{v}^c(\underline{x}, t)$, is introduced to take into account the nonlinearity linked to the effect of friction at the contact interfaces
- step 5: $\underline{v}^c(\underline{x}, t)$ is partitioned to obtain $\underline{d}^c(\underline{x})$ and \dot{I}^c ,
- step 6: the integration of the intensity factor rates is performed to get, I^s , I^a and I^c .

The following relation is therefore established,

$$(P, Q, \sigma_B) \Leftrightarrow (I^s, I^a, I^c). \quad (2.56)$$

2.5 Influence of the contact geometry on the reference functions

One of the most interesting aspects of the partition technique applied to the velocity field described in this chapter, relies on the possibility to describe $\underline{v}(\underline{x}, t)$ by means of

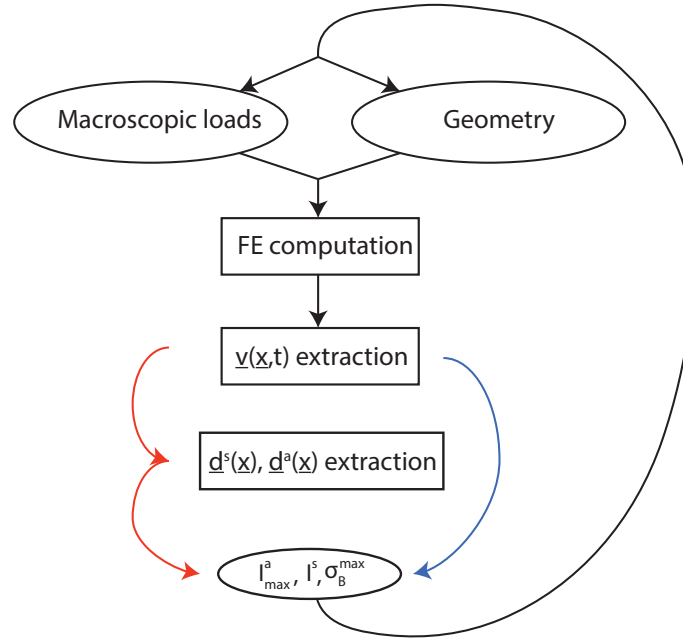


Figure 2.17: Schematic representations of the steps of the algorithm: (\rightarrow) classic path, (\dashrightarrow) the re-computation of the reference fields is skipped.

a summation of different terms, each one expressed as the product between nonlocal intensity factors, depending on the macroscopic loads applied to the mechanical assembly, and reference functions depending on the local geometry of the part.

The fact that the reference functions depend just on the contact geometry is really important because for a given configuration, it allows to compute them once and then, if other computations are needed, only the intensity factors are extracted thanks to the information gathered in the previous step. This can reduce the computation time (no need to extract and normalize the reference fields, Figure 2.17) in situations where, for instance, for a given geometry, a lot of different load combinations are tested in order to verify which one is the most dangerous for the structure.

As a results of what has been said, one would expect to be compelled to recompute the reference functions each time the contact geometry changes. Fortunately, it is not the case. It is important to recall the initial hypothesis in order to apply the velocity field partition:

- a self-similar geometry,
- a geometric discontinuity,
- small deformations / infinitesimal strain,
- analysis performed in a reference system attached to the contact tip.

If these hypothesis hold true for a different contact configuration from the one for which the reference functions have been computed, there is no need to perform this computation a second time.

In Figures 2.18, 2.19 and 2.20, the evolution of $\underline{d}^s(\underline{x})$, $\underline{d}^a(\underline{x})$ and $\underline{d}^c(\underline{x})$, as a function of the pad radius, is analyzed. Here, the variation of the pad size is used to simulate a change in geometry, in particular the biggest radius tested is 4 times the smallest one. The results clearly show that no matter which radius is used the reference functions do not change.

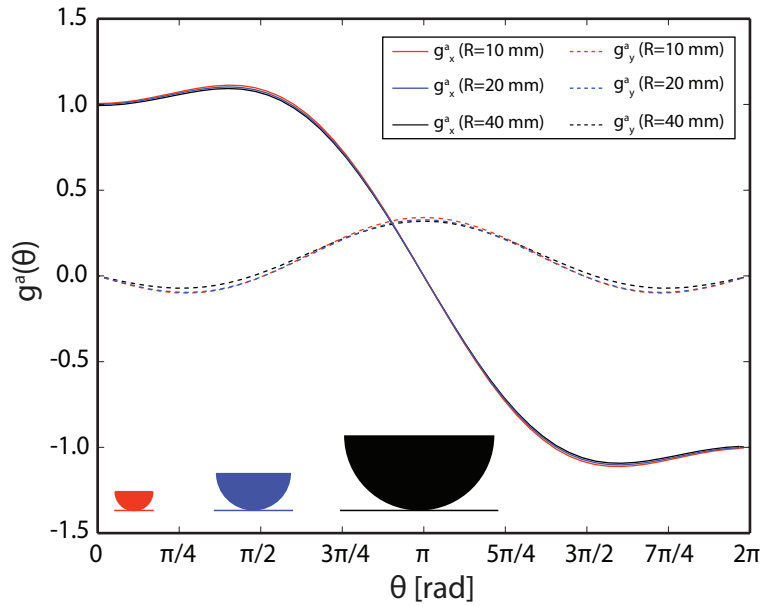


Figure 2.18: Comparison of $\underline{g}^a(\vartheta)$ for different geometries characterize by a change in pad radius.

These results are meaningful. The industrial applications are characterized by contact configurations different from the simple cylinder/plane contact. For instance, in the case of a disc/blade root attachment the contact geometry is more similar to plane/plane contact with rounded edges. Nevertheless, close to the contact tip, where the partition technique is applied, the aforementioned hypothesis are respected, since as shown in Figure 2.21, locally the contact geometry is self-similar. In other words, the fact that the reference functions remain unchanged gives to the algorithm the flexibility needed to be easily applicable in the industrial context.

2.6 Sensitivity analysis

In the previous sections the details on how to partition the velocity field to extract nonlocal intensity factors characterizing the stress field close to the contact tip have been presented. Hereunder a sensitivity analysis is carried out in order to study

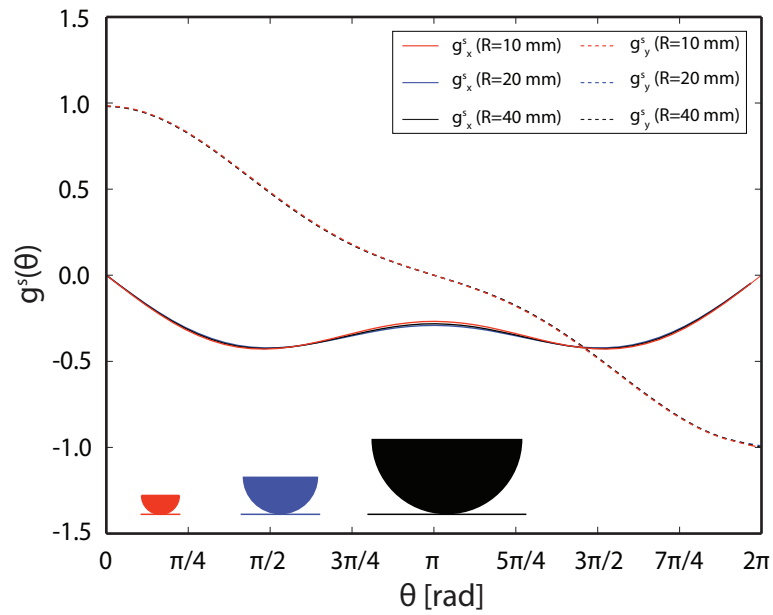


Figure 2.19: Comparison of $\underline{g}^s(\vartheta)$ for different geometries characterize by a change in pad radius.

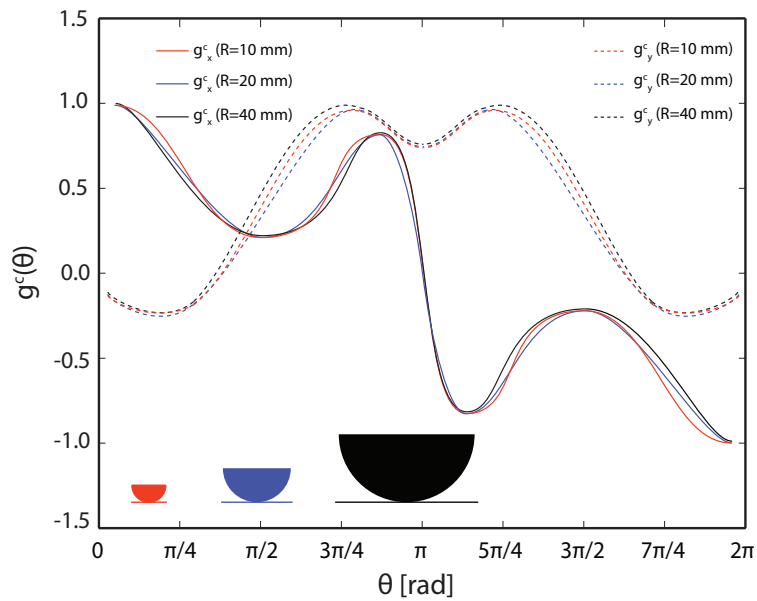


Figure 2.20: Comparison of $\underline{g}^c(\vartheta)$ for different geometries characterize by a change in pad radius.

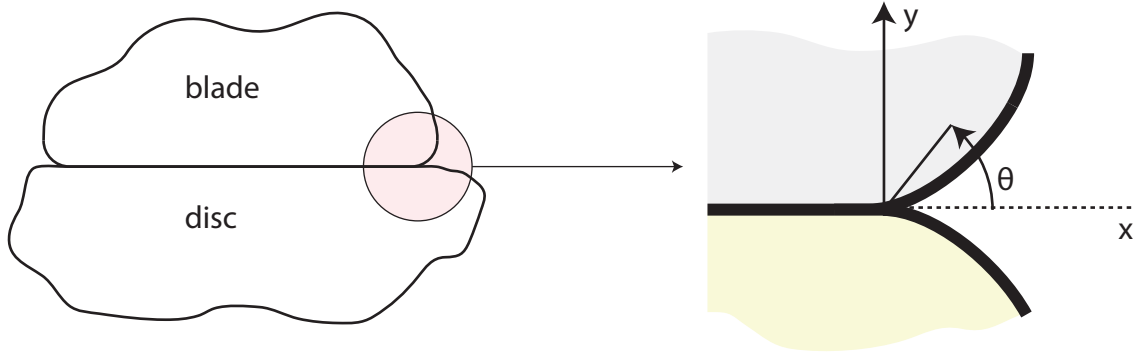


Figure 2.21: Plane/plane contact configuration with rounded edges.

the influence of several parameters on the extraction of the nonlocal stress intensity factors:

- the influence of the size of the extraction zone (circular region centered at the contact tip, Figure 2.9),
- the influence of the mesh size.
- the influence of the mesh type (structured mesh vs non structured one).

The study is carried out by recording the evolution of I_{max}^a and I^s as a function of the aforementioned parameters. To notice that, the analysis is limited to the elastic nonlocal intensity factors, I^s and I^a since it is assumed that they are sufficient to univocally characterize the contact edge stress condition. In addition, considering that the value of I^a varies during the simulation, only its maximum value, I_{max}^a , is used for the study.

2.6.1 Influence of the size of the extraction zone

In Section 2.4 it has been explained that only the velocity field values in a circular region, Ω , of radius, r , centered at the contact edge, are retained for the partition. The value of r is chosen in order to obtain a ratio, $r/R < 0.05$, condition that ensure the applicability of the approach. This assumption permits to set an upper boundary for the value of r , while the lower boundary is determined such as to obtain a circular zone large enough to include at the same time the stick and the slip zone. A radius too small will overestimate the effect of the friction in the slip zone.

Nevertheless, it is important to analyze the influence of the radius of the extraction zone on the outputs of the numerical algorithm (Figure 2.22). The analysis has been carried out on a reference contact configuration characterized by the following parameters: plain fretting analysis, Pad radius = 20 mm, friction coefficient = 1.0, Young's modulus = 119 400 MPa, Poisson's ratio = 0.3, $P = 347 \text{ N mm}^{-1}$ and Q^*

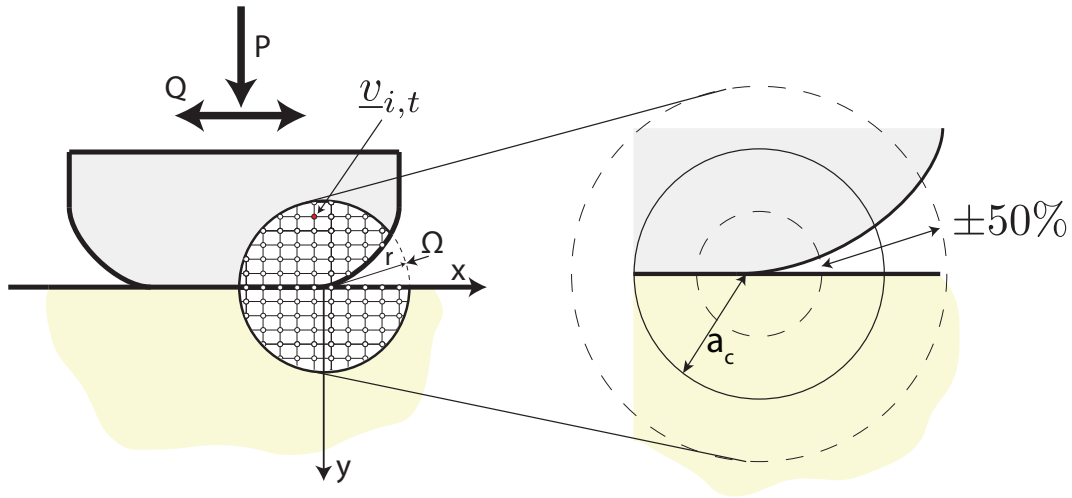


Figure 2.22: Schematic representation of the sensitivity analysis concerning the effect of the variation of the size of the extraction zone, Ω .

$= 237 \text{ N mm}^{-1}$. The contact zone half width is equal to 0.37 mm and the slip zone accounts for 32 percent of the total contact surface.

Different computations of the nonlocal intensity factors are performed, varying the value of r employed.

In Figures 2.23 and 2.24, the results of the sensitivity analysis are presented. Starting from an initial reference situation where the values of r is considered equal to the contact half width, a_c , the size of the extraction zone has been forced to vary in a range of $0.5a_c$ to $1.5a_c$. The outcome of the analysis shows that the procedure is robust with respect to a change in the value of r . In Figure 2.24 the relative error with respect to the reference situation, $r = a_c$, is displayed. A remarkable low difference in the computation of the nonlocal intensity factors is observed in particular for values of r higher than a_c . The worst case in term of relative errors (close to 10 per cent) is when r approaches $0.5a_c$; this condition corresponds to a situation close to the lower boundary of the acceptable r variation and this explains the observable but still reasonable error.

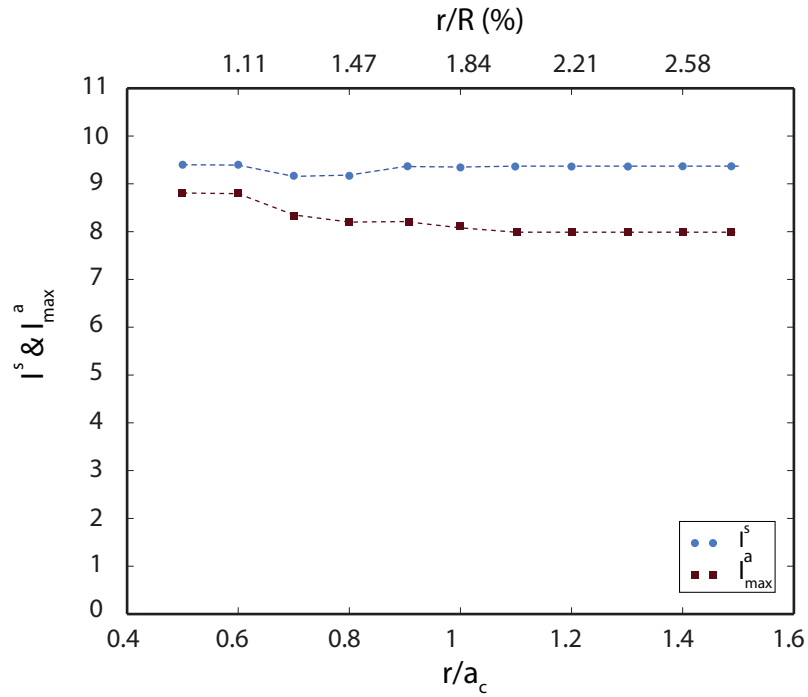


Figure 2.23: Nonlocal intensity factor as a function of radius.

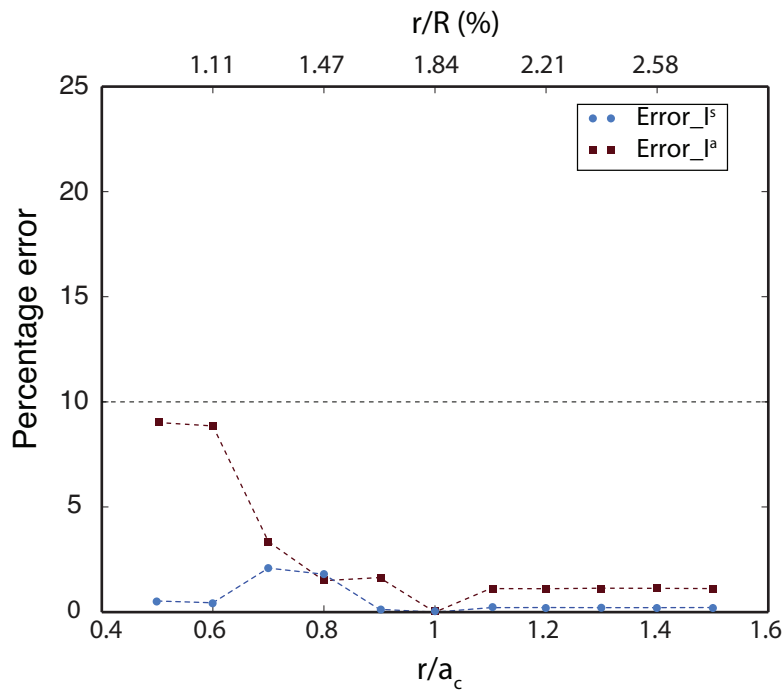


Figure 2.24: Error evolution as a function of radius.

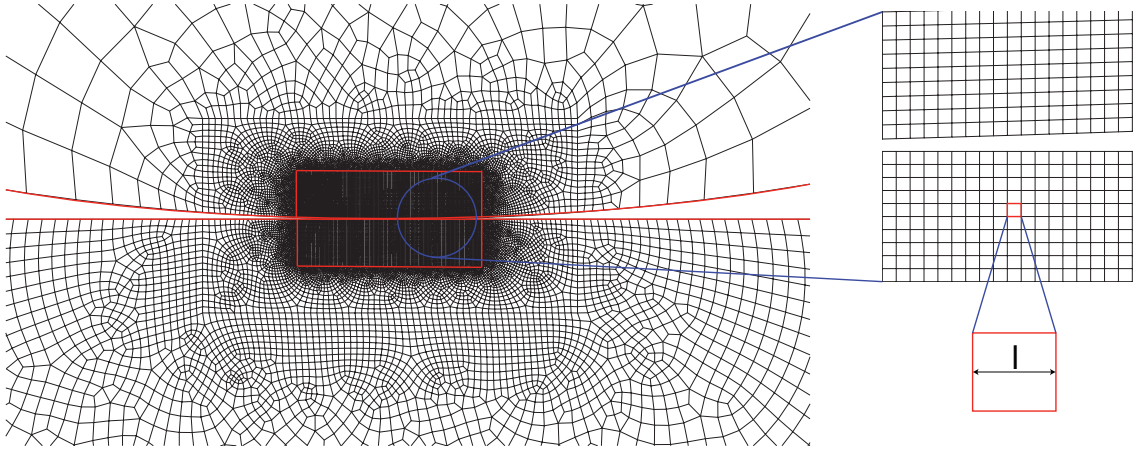


Figure 2.25: Mesh employed in the FE computations.

2.6.2 Influence of the mesh size

One of the key points of the research work presented in this manuscript is the possibility to apply the algorithm developed to extract nonlocal intensity factors from industrial size FE models. For this purpose it is necessary to verify how the value of I_{max}^a and I^s are modified by a change in the mesh size or in the type of elements used in the simulation. The analysis is carried out on a reference contact configuration characterized by the following parameters: plain fretting analysis, Pad radius = 20 mm, friction coefficient = 1.0, Young's modulus = 119 400 MPa, Poisson's ratio = 0.3, $P = 347 \text{ N mm}^{-1}$ and $Q^* = 237 \text{ N mm}^{-1}$. Close to the surface, a region characterized by a structured finer mesh of linear quadrilateral elements CPE4R (Figure 2.25) permits to well describe the stress gradient evolution. Step by step, the size of the quadrilateral elements, l , is increased diminishing the number of elements needed to cover the contact surface. The variation of the nonlocal intensity factors as a function of the mesh size is recorded.

The results, presented in Figure 2.26, show a good stability. Different computations are performed, varying the mesh size, l , in a range from $5 \mu\text{m}$ to $70 \mu\text{m}$. Considering that for the configuration used to perform the analysis the half contact width is equal to 0.37 mm, this means that the number of elements needed to cover all the contact surface passes from around 140 to 10. Despite the big variation in the mesh size, the nonlocal intensity factor values are sufficiently stable.

A quantitative evaluation confirming the last statement is presented in Figure 2.26 which displays the evolution of different relative percentage errors defined as follows:

- Error on the shear force computation

$$\xi_r = 100 \frac{|q_{max}^{FE} - q_{max}^{th}|}{q_{max}^{th}},$$

where q_{max}^{th} is the maximum shear stress at the contact surface computed using Cattaneo-Mindlin relation, and q_{max}^{FE} is the value computed through FE computation.

- Error on the symmetric nonlocal intensity factor

$$\xi_{I^s} = 100 \frac{|I^s - I_{\infty}^s|}{I_{\infty}^s},$$

where I_{∞}^s is the converged value extracted, in this case, with a mesh characterized by a size equal to 5 μm .

- Error on the antisymmetric nonlocal intensity factor

$$\xi_{I^a} = 100 \frac{|I_{max}^a - I_{max,\infty}^a|}{I_{max,\infty}^a}.$$

- Total error

$$\xi_{tot} = \max_{t \in T} \left(100 \sqrt{\frac{\int_{\Omega} [\underline{v}(\underline{x}, t) - \underline{v}^e(\underline{x}, t) - \underline{v}^c(\underline{x}, t)]^2}{\int_{\Omega} \underline{v}(\underline{x}, t)^2}} \right).$$

- Elastic error

$$\xi_e = \max_{t \in T} \left(100 \sqrt{\frac{\int_{\Omega} [\underline{v}(\underline{x}, t) - \underline{v}^e(\underline{x}, t)]^2}{\int_{\Omega} \underline{v}(\underline{x}, t)^2}} \right).$$

To notice that the definition of ξ_{tot} and ξ_e differs from the one given in Section 2.4.3 since, in this case instead of studying their evolution during the simulation, the maximum value is recorded and compared to other computations characterized by a different mesh size.

By comparing the evolution of the different errors displayed in Figure 2.27, it is clear that the algorithm developed to extract the nonlocal intensity factors by post-processing the velocity field has a satisfactory precision even with rough meshes. In particular, it is worth noting that, despite an increasing error in the computation of the contact stress distribution overcoming 40 percent for rougher meshes, the values of I_{max}^a and I^s are just marginally perturbed with a percentage error which does not cross the 5 % line.

The highlighted square in the Figure 2.27, (bottom left hand corner) represents the “industrial domain”, meaning that if it is possible to assure good precision, and a reasonable number of elements to cover the whole contact zone, than the methodology can be applied to industrial size FE models. This requirement is met. Furthermore, as a bonus, by reducing the number of elements in the analyzed zone the computation time is reduced as well. In the test case employed to perform the

computations displayed above, passing from a mesh size of $5\ \mu\text{m}$ to one of $50\ \mu\text{m}$ will reduce the number of extraction points from more than fifteen thousand to less than two hundred. By comparing these two situations in term of time to perform all the procedure (FE computation + post-treatment of the velocity field to extract the intensity factors) in the first case it takes more than 5 hours while in the second case only 4 minutes are sufficient. This benchmark has been performed on a computer equipped with a Intel Xeon X5660 processor, 12GB RAM and a clock frequency equal to 2.8 GHz.

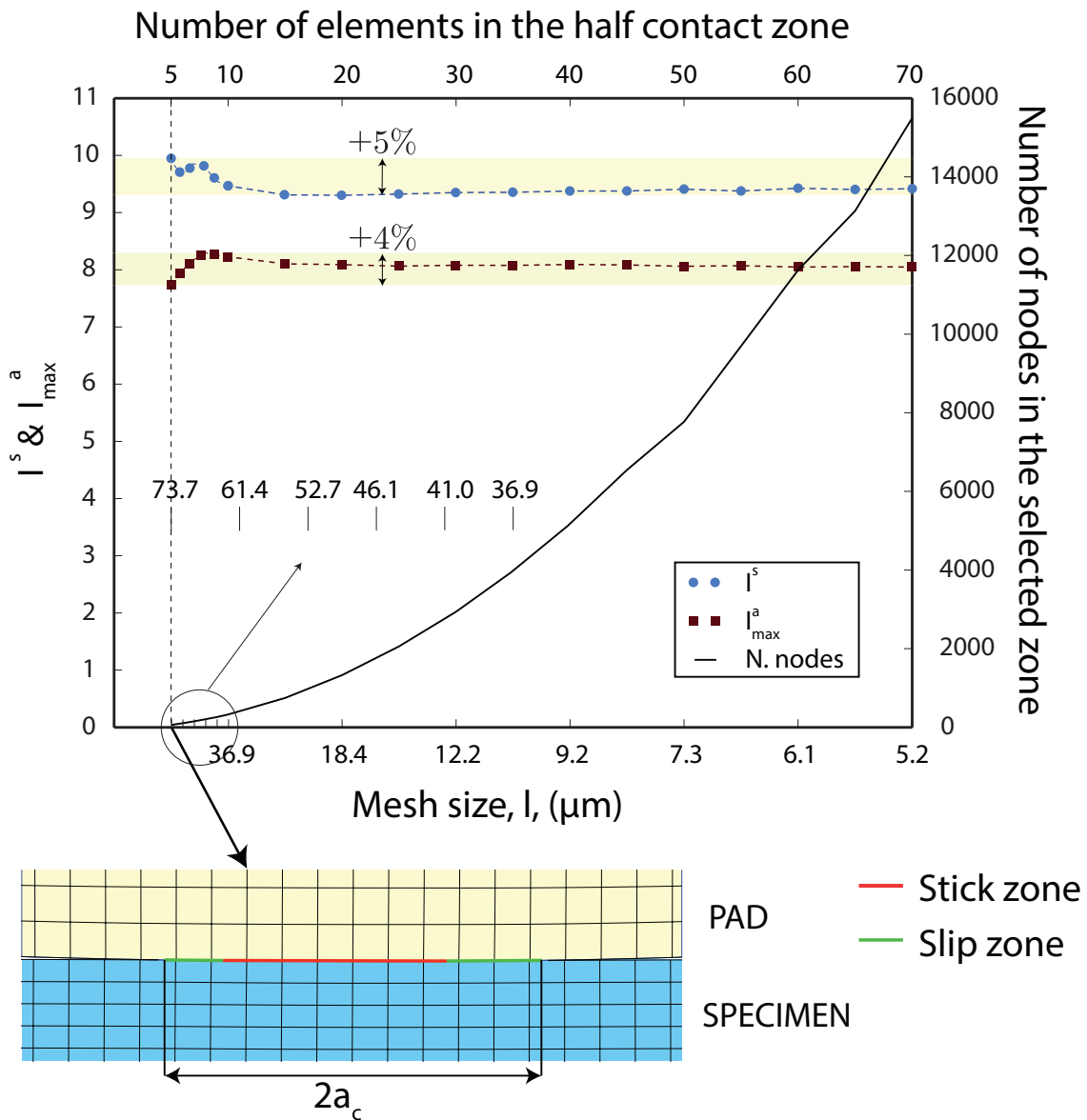


Figure 2.26: Nonlocal intensity factor as a function of the mesh size.

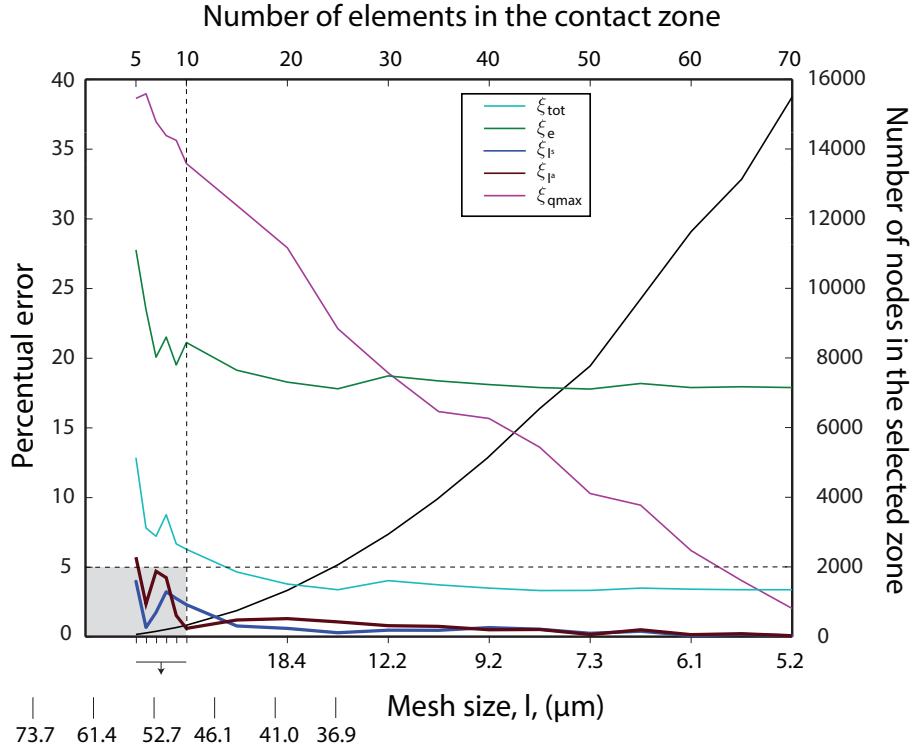


Figure 2.27: Error evolution as a function of the mesh size.

2.6.3 Influence of the mesh type

In the previous section the influence of the mesh size on the nonlocal intensity factor value has been investigated. Here the analysis is repeated but instead of working with structured meshes, different possibilities have been tested such as triangular nonstructured mesh exploiting linear and quadratic elements, CPE3 and CP6M, and quadrilateral nonstructured mesh, CPE4R and CPE8R.

The aim is to verify whether it is possible or not to get rid off the structured mesh constraint which can be interesting for industrial applications since a nonstructured mesh is usually easier to put in place via automated mesh generators.

The reference contact configuration is the same of the one introduced in the previous section with the exception of the mesh definition.

The results of the analysis are presented in Figures 2.28 and 2.29. The highlighted error bar is defined with respect to the reference value obtained for a structured mesh composed by linear quadrilateral elements with a size of around $5\ \mu\text{m}$. For a nonstructured mesh composed by linear elements the error increases faster compared to the reference case, especially when the number of elements is drastically reduced. Nevertheless, a possible solution is to use quadratic elements which show a much better stability on the whole range.

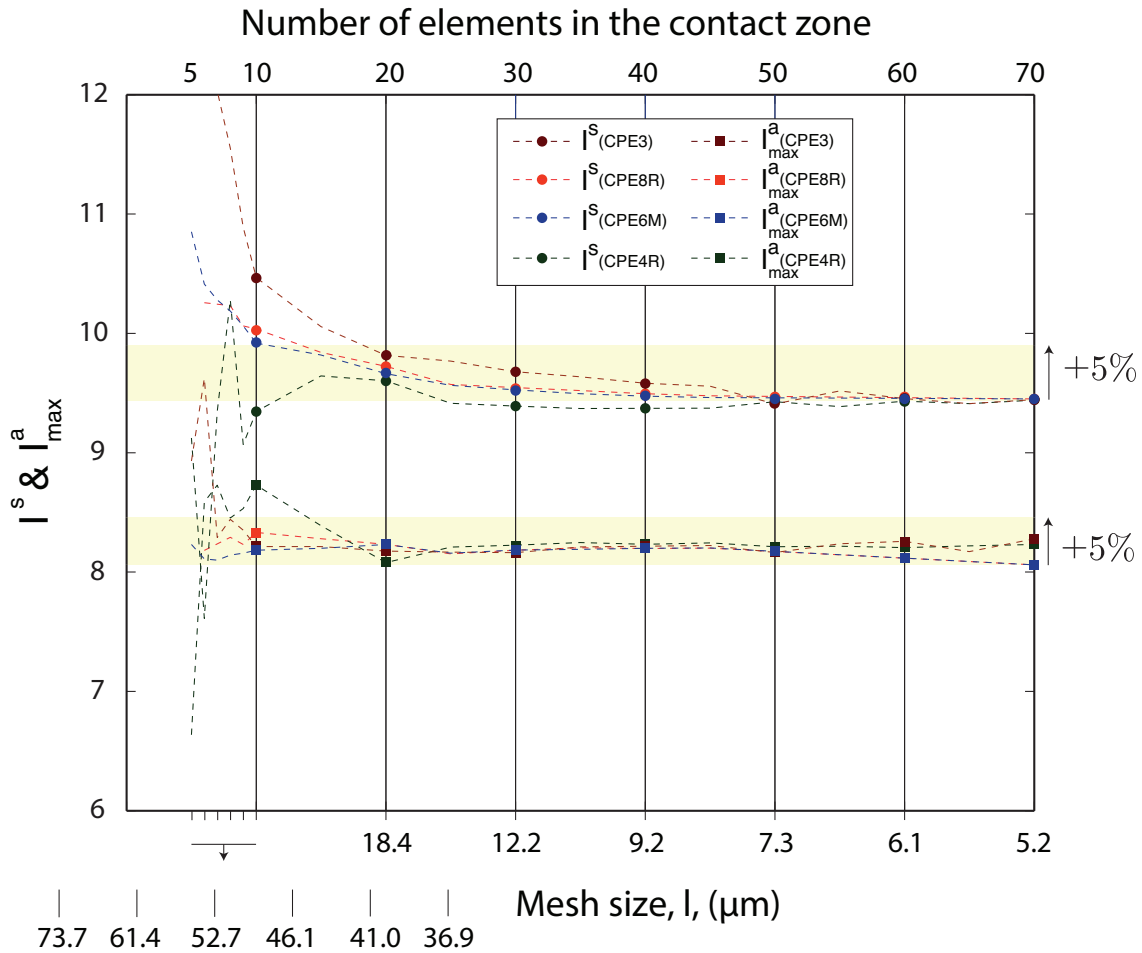


Figure 2.28: Nonlocal intensity factor as a function of the mesh size and element type: CPE3 (linear triangular element), CPE4R (linear quadrilateral element), CPE6M (quadratic triangular element) CPE8R (quadratic quadrilateral element).

2.7 Chapter highlights

In this chapter a new method to describe the velocity field produced by fretting-fatigue close to the contact edges has been introduced.

In the presence of a strong gradient, the local geometry imposes the spatial distribution of the mechanical field while its intensity is determined by the macroscopic loads. Therefore, the solution of the problem can be described through a “fracture mechanics” approach, as the product between intensity factors and spatial reference fields. These quantities are defined in a frame attached to the contact edge. The mathematical details to perform this decomposition have been presented, as well as a practical example on a test case.

The nonlocal intensity factors are extracted by analyzing the velocity field close to the contact edges and therefore they include the information on the stress gradient

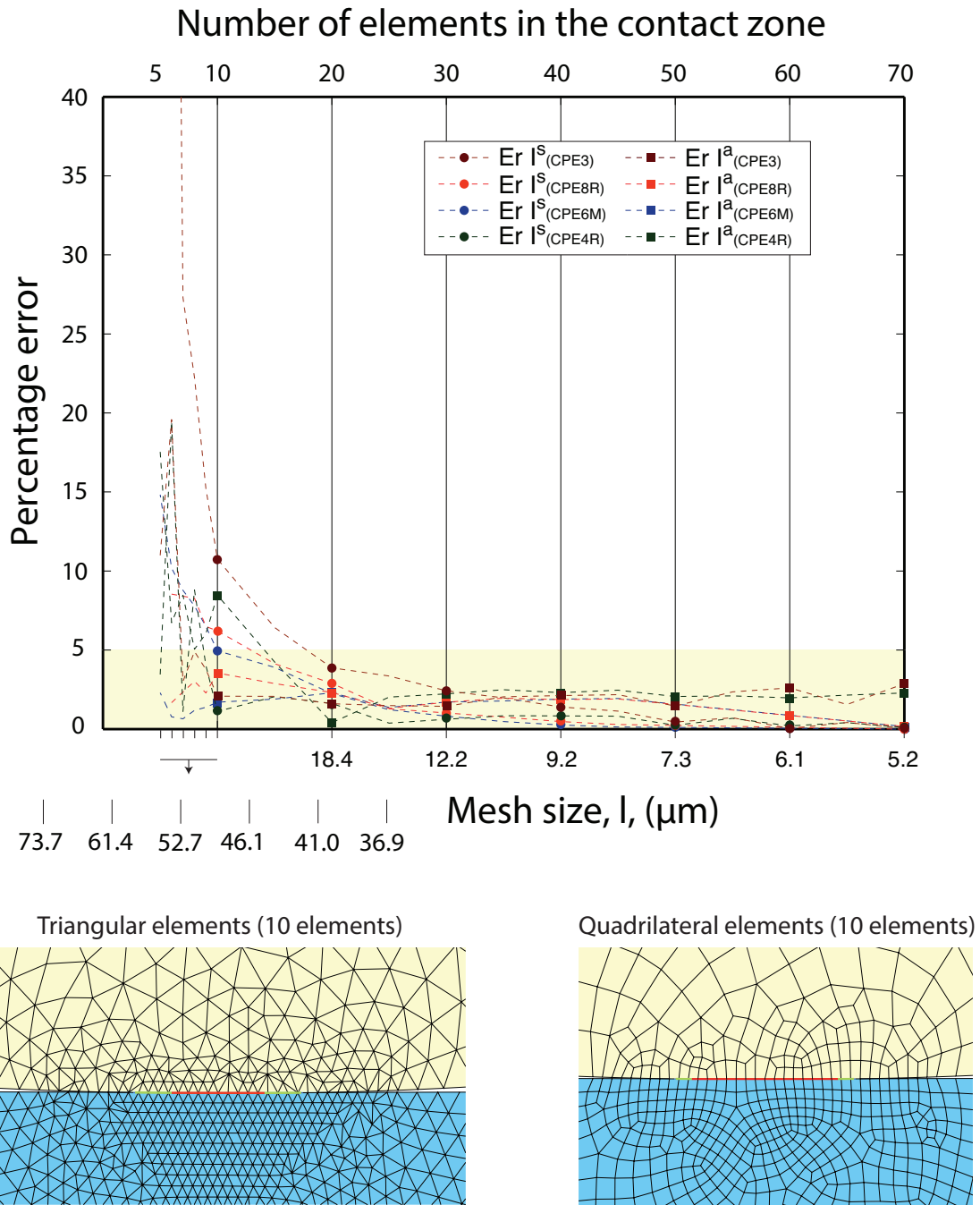


Figure 2.29: Error evolution as a function of the mesh size and element type: CPE3 (linear triangular element), CPE4R (linear quadrilateral element), CPE6M (quadratic triangular element) CPE8R (quadratic quadrilateral element). Example of triangular and quadrilateral meshes for a configuration corresponding to 10 elements for half-contact width.

evolution produced by fretting-fatigue.

In the second part of the chapter, a sensitivity analysis is carried out, aiming at investigating the influence of the variation of some key parameters on the algorithm outcome. Two main results have been obtained:

- The fact that the reference functions remain unchanged with the variation of the contact geometry (provided that some hypothesis are respected) is important because it allows one to compare different attachment configurations just by looking at the value of the nonlocal intensity factors.
- It is shown that the values of I^a and I^s are only marginally influenced by the change of mesh size and type, which is a key point to introduce the approach inside the industrial applications.

Chapter 3

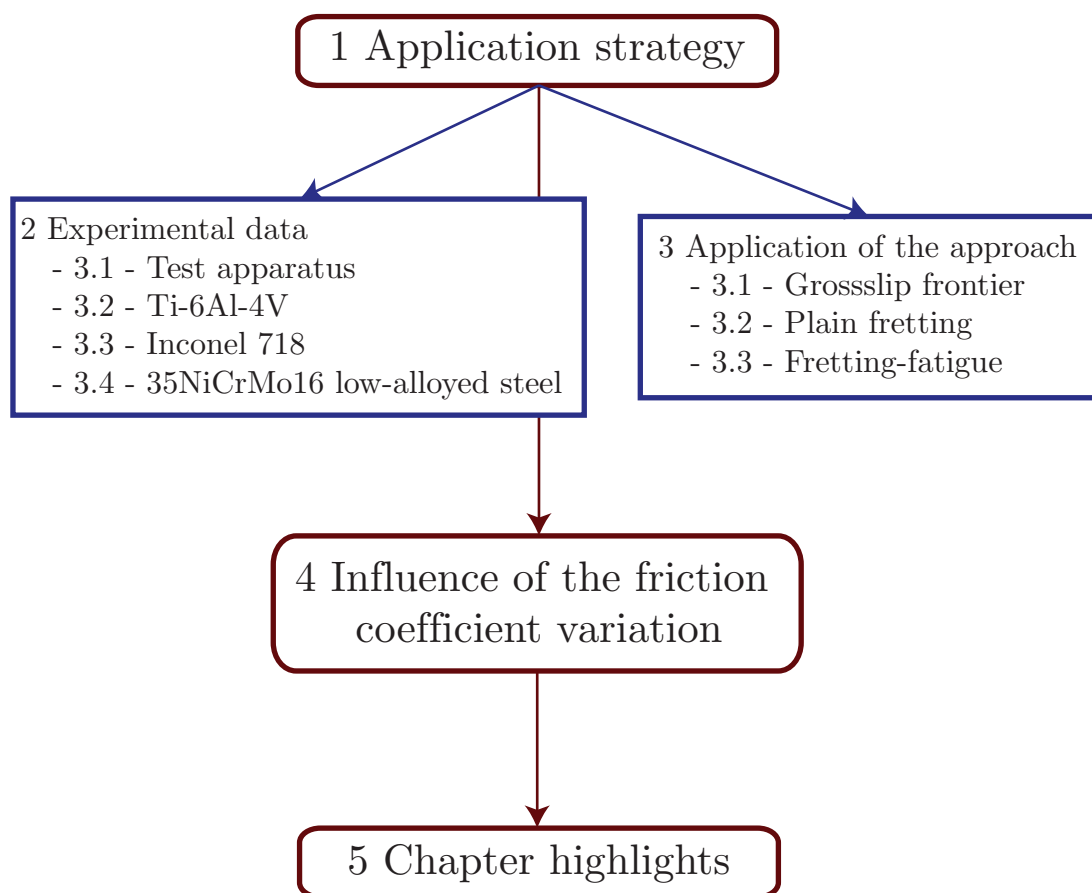
Application of the approach to fretting-fatigue test data

In the previous chapter the details to extract the nonlocal stress intensity factors have been presented. They are computed analyzing the velocity field close to the contact edges and they are defined with the objective to take into account the gradient effect. Here, this statement is verified by comparing the numerical results with experimental data coming from the works of Amargier, [Amargier et al., 2010], Ferré [Ferré et al., 2013] and Fouvry, [Fouvry et al., 2014]. The aim is to confirm the transferability of the experimental fretting-fatigue data to different geometries from the one in which they have been obtained

In particular, it is shown how a common crack initiation map expressed in $(q_{max} - p_0)$ coordinates, characterized by different initiation frontiers depending on the geometry employed, is transformed if the nonlocal intensity factors, $(I_{max}^a - I^s)$, are used as reference quantities.

In the first part of the chapter, the experimental data used to validate the algorithm are presented while in the second part, the steps to obtain the nonlocal crack initiation map are detailed. A sensitivity analysis is performed in order to understand the impact that some key parameters have on the final outcome.

Chapter 3 - Table of Contents Flowchart



3.1 Application strategy

In Chapter 2 the velocity field generated close to the contact edges during a fretting-fatigue simulation is partitioned into a summation of multiple terms, each one expressed as the product between nonlocal intensity factors, I^s , I^a , I^c , depending on the macroscopic loads applied to the mechanical assembly, and spatial reference fields, \underline{d}^s , \underline{d}^a , \underline{d}^c , depending on the local geometry of the part. In this approach, the nonlocal stress intensity factors play the same role of K_I and K_{II} in fracture mechanics. In other words, I^s , I^a , I^c , are an index of the severity of the stresses arising close to the contact edges. Their values vary all along the simulation as a results of the evolution of the macroscopic loads. In presence of a complex loading spectrum, only the maximum values of the nonlocal stress intensity factors are retained which represent the worst condition the material will encountered. In particular, in this chapter the loading evolution used to reproduce the experimental tests is such that the resultant nonlocal intensity factors are characterized by the following evolution (analogue to what it has been shown in Section 2.4.4):

$$I^a(t) = I_{max}^a \sin(\omega t) \quad (3.1)$$

$$I^c(t) = I_{max}^c \sin(\omega t) \quad (3.2)$$

$$I^s(t) = I^s \quad (3.3)$$

$$\sigma_B(t) = \sigma_B^{max} \sin(\omega t) \quad (3.4)$$

To univocally characterize the loading condition the following set of values are sufficient: $(I^s, I_{max}^a, I_{max}^c)$.

The test results presented in [Amargier et al., 2010, Ferré et al., 2013, Fouvry et al., 2014], describe different crack initiation frontiers as a function of the pad radius employed. The data are obtained on a cylinder/plane configuration from plain fretting and fretting-fatigue test campaigns. The frontiers are expressed in local coordinates, $(q_{max} - p_0)$.

Knowing the values at which crack initiation is experienced, FE simulations are run in order to reconstruct the velocity field corresponding to these loading conditions. By applying the algorithm developed, the nonlocal stress intensity factors are eventually computed.

To sum up, starting from the experimental points describing the initiation frontiers in plain fretting, the method presented in Chapter 2 is applied and a set of nonlocal stress intensity factors is extracted. This process is repeated for each experimental point and a new initiation curve based on $I_{max}^a - I^s$ is defined, (Figure 3.1).

It is worth noting that only the elastic non local stress intensity factors are used in the description of the crack initiation frontiers. The first reason why I^c is neglected relies on the fact that this term describes the nonlinear effect of friction which is extremely localized as confirmed in Figure 2.14. As a consequence, the elastic nonlocal intensity factors, I^s and I^a , are sufficient to univocally characterized the contact edge stress evolution. This approach is analogue to the one followed in

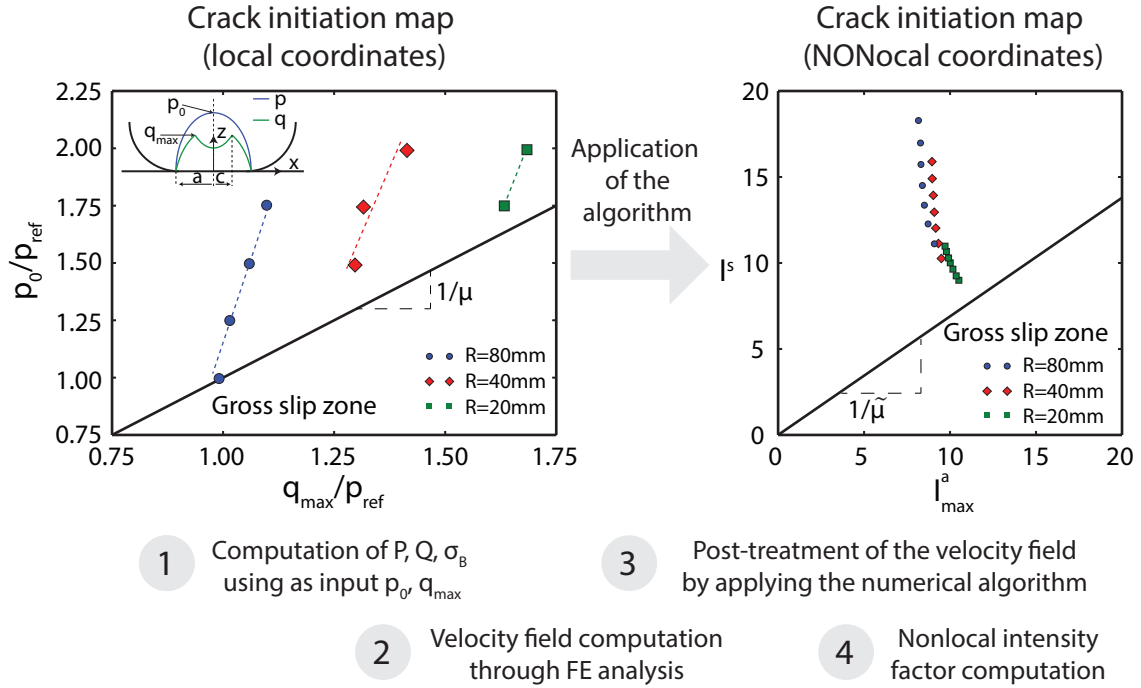


Figure 3.1: Different steps in the application of the methodology developed in Chapter 2.

fracture mechanics where the hypothesis of small scale yielding permits to use an elastic stress intensity factor, K , to describe the mechanical field close to the crack tip. Secondly, all the test data are obtained assuring that the contact was in partial slip regime. As Vingsbo and Sodernberg [Vingsbo and Söderberg, 1988] pointed out, in this condition the wear rate due to friction is negligible which justifies the choice to neglect I^c .

The process is generalized to fretting-fatigue, where a nonlocal initiation surface, $(I_{\max}^a, I^s, \sigma_B^{\max})$ is built.

In the following sections a detailed description of the experimental data used for the application of the procedure, as well as the test conditions in which the data have been obtained, are presented.

3.2 Experimental data

The main idea behind the application process is based on the description of the crack initiation frontiers, which are heavily influenced by the gradient effect, through the use of nonlocal intensity factors. The aim is to verify whether these quantities are objective quantities able to take into account the gradient effect.

Concerning the experimental data, the selection has been driven by the need to test different materials in order to verify that the outcomes are not influenced by

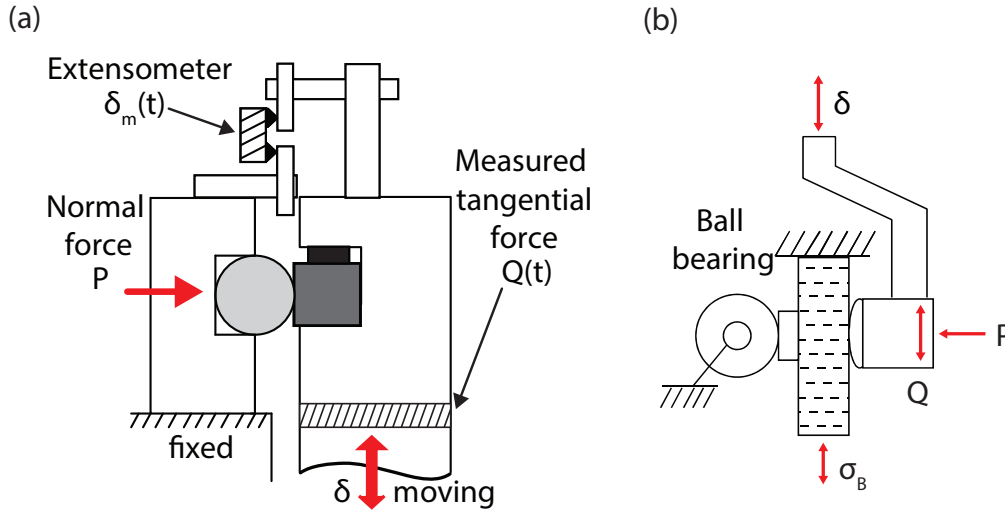


Figure 3.2: (a) Plain fretting; (b) fretting-fatigue test apparatus.

the material chosen.

3.2.1 Test apparatus

Plain fretting tests are carried out using a tension-compression MTS hydraulic system [Fouvry et al., 1996]. A schematic representation of the machine is shown in Figure 3.2a. The normal force (P) is kept constant, while a purely alternating cyclic displacement (δ) is imposed. As a consequence, a cyclic tangential load (Q) is generated at the contact surface. After a certain number of cycles, usually 10^5 or 10^6 , the test is stopped and the specimen is cut along the median axis of the fretting scar in order to verify whether the crack is initiated or not. This procedure is repeated several times to find the tangential load amplitude (Q^*) that provokes crack initiation for a given normal load.

The same procedure is repeated for fretting-fatigue, as well. In this case, experiments are performed using a dual actuator device [Meriaux et al., 2010] that allows to separate the application of fretting and fatigue loading, Figure 3.2b. The analysis focuses on how the crack initiation frontiers, previously found for plain fretting, move with the introduction of a fatigue force in phase with the fretting loading.

3.2.2 Ti-6Al-4V

Ferré [Ferré et al., 2013] performed plain fretting and fretting-fatigue tests with specimens made of Ti-6Al-4V, which is a two phase titanium based alloy. An hexagonal close-packed alpha phase (60 %) in coexistence with a body-centered cubic beta phase (40 %) is observed. The main mechanical properties are presented in Table 3.1.

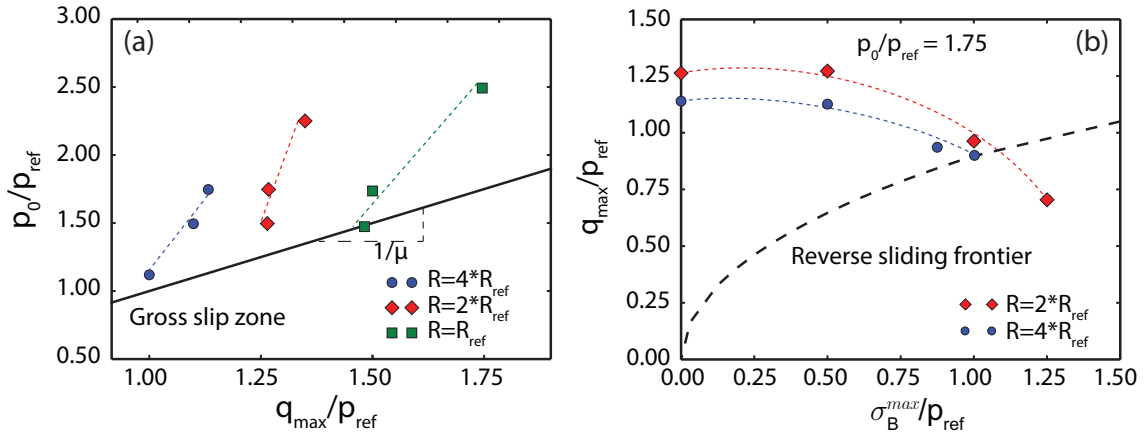


Figure 3.3: (a) Crack initiation frontiers in plain fretting for different contact configurations; (b) evolution of the crack initiation frontiers in fretting-fatigue for two different radii ($\sigma_B(R = 0.01)$), Ti-6Al-4V.

Elastic modulus	119.4 (GPa)
Poisson's ratio	0.29
Coulomb's friction coefficient	1.0
Yield stress	970 (MPa)
$\sigma_{R=-1}(10^5)$	$0.97 \cdot p_{ref}$ (MPa)
$\tau_{R=-1}(10^5)$	$0.65 \cdot p_{ref}$ (MPa)
ΔK_{th}	5.5 (MPa \sqrt{m})

Table 3.1: Mechanical properties of Ti-6Al-4V used in [Ferré et al., 2013].

The reference values for traction-compression fatigue limit and full torsion fatigue limit are extracted for a load ratio equal to -1. This choice is driven by the fact that in fretting, close to the contact edges, where the crack initiation probability is the highest, a fully reversed loading is experienced. Moreover the targeted crack initiation life in the experimental tests corresponds to 10^5 cycles. σ_{-1} and τ_{-1} are identified by applying the staircase method.

Due to confidentiality issues, the obtained fatigue values and the following crack initiation map are normalized with respect to a reference maximum Hertzian peak pressure (p_{ref}) used to standardize the analysis of the crack nucleation process.

By following the procedure described in section 3.2.1 the crack initiation map presented in Figure 3.3 is obtained. The results clearly show the effects of the stress gradient. The lowest is the pad radius the highest is the threshold value for crack initiation, keeping the normal pressure constant. As already explained in Chapter 1, it is important to notice that two factors influence crack nucleation; (i) the maximum

stress at the stick-slip frontier and (ii) the material process volume over which the maximum stress operates. The increase in pad dimension extends the influence of the contact stress below the surface, and therefore augments the process volume, [Neuber, 1958].

All the results have been obtained considering a crack initiation length threshold equal to 70 μm .

Figure 3.3 shows the effect of the introduction of a fatigue force in phase with the fretting tangential load, on the initiation frontiers. Little or no effect is experienced for small values of σ_B^{max} up to $0.5 \sigma_B^{max}/p_{ref}$, followed by an observable reduction in the initiation threshold for bigger values.

3.2.3 Inconel 718

Here the reference data come from the research performed by Amargier, [Amargier et al., 2010]. The author carried out some tests in plain fretting employing a cylinder/plane contact configuration, where both the pad and the flat specimen are made of Inconel 718. This nickel based alloy is annealed at about 1000 $^{\circ}\text{C}$, and then heated to an intermediate temperature, 8 hours at 720 $^{\circ}\text{C}$ followed by a second step at 620 $^{\circ}\text{C}$ for 10 hours, so as to induce precipitation hardening. The heat treatment ends with air cooling. In Table 3.2 some material data are listed.

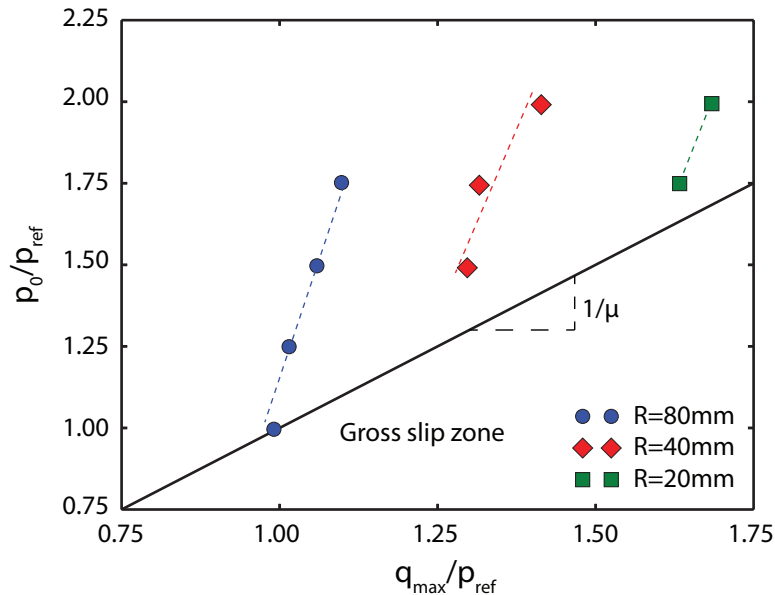


Figure 3.4: (a) Crack initiation frontiers in plain fretting for different contact configurations, Inconel 718.

Elastic modulus	203 (GPa)
Poisson's ratio	0.29
Coulomb's friction coefficient	1.0
Yield stress	>1000 (MPa)
Ultimate tensile strength	>1300 (MPa)
$\tau_{R=-1}/\sigma_{R=-1}(10^5)$	0.85
ΔK_{th}	5.0 (MPa \sqrt{m})

Table 3.2: Mechanical properties of Inconel 718 used in [Amargier et al., 2010].

To quantify the effect of the stress gradient on crack initiation frontiers, the author performs several tests varying the cylinder radius employed; three pad radii are used: 80 mm, 40 mm and 20 mm. In Figure 3.4 the results are displayed. It is important to add that the threshold length to determine whether a crack is initiated or not is equal to 10 μm .

Once again the gradient effect is evident confirming what has already been presented for TI-6Al-4V.

3.2.4 35NiCrMo16 low-alloyed steel

Fouvry [Fouvry et al., 2014], performed plain fretting and fretting-fatigue tests with specimens made of 35NiCrMo16 low-alloyed steel displaying a tempered martensitic structure. The key properties for the material employed are listed in Table 3.3

Elastic modulus	205 (GPa)
Poisson's ratio	0.3
Coulomb's friction coefficient	0.8
Yield stress	950 (MPa)
Ultimate tensile strength	1130 (MPa)
$\sigma_{R=-1}(10^7)$	575 (MPa)
$\tau_{R=-1}(10^7)$	386 (MPa)
Long crack threshold, ΔK_0	3.2 (MPa \sqrt{m})

Table 3.3: Mechanical properties of 35NiCrMo16 low-alloyed steel.

Once again the results obtained by the author, presented in Table 3.4 and displayed in Figure 3.5, underline the effect of the stress gradient on the crack initiation frontiers. The analysis is analogue to the one already presented for the previous materials. The crack initiation length threshold is equal to 10 micrometers and the

Experimental data

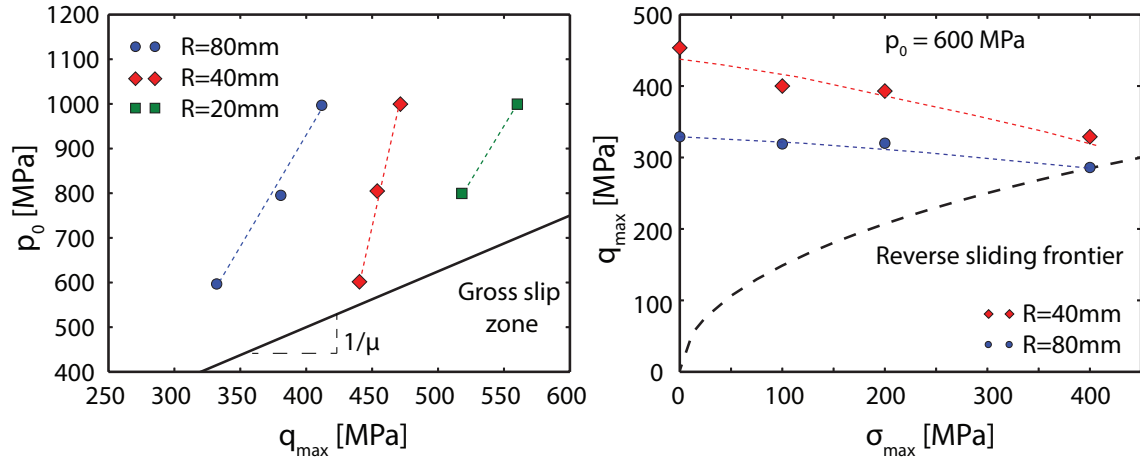


Figure 3.5: (a) Crack initiation frontiers in plain fretting for different contact configurations; (b) evolution of the crack initiation frontiers in fretting-fatigue for two different radii, 35NiCrMo16 low-alloyed steel.

number of cycles, after which the specimen surface is inspected to verify whether a crack is initiated or not, is equal to 10^6 .

	R (mm)	μ	P (N/mm)	Q^* (N/mm)	σ_B^{max} (MPa)	R_B	p_0 (MPa)	q_{max} (MPa)
PF ₁	20	0.8	353	186	0	-	800	517
PF ₂	20	0.8	552	218	0	-	1000	559
PF ₃	40	0.85	398	271	0	-	600	454
PF ₄	40	0.85	707	287	0	-	800	468
PF ₅	40	0.75	1100	310	0	-	1000	471
PF ₆	80	0.79	795	305	0	-	600	329
PF ₇	80	0.78	1414	399	0	-	800	374
PF ₈	80	0.74	2209	470	0	-	1000	395
FF ₉	40	0.85	398	210	100	0.1	600	400
FF ₁₀	40	0.85	398	192	200	0.1	600	393
FF ₁₁	40	0.85	398	100	400	0.1	600	329
FF ₁₂	80	0.79	795	273	100	0.1	600	319
FF ₁₃	80	0.79	795	261	200	0.1	600	320
FF ₁₄	80	0.79	795	137	400	0.1	600	286

Table 3.4: Test data for 35NiCrMo16 low-alloyed steel presented in [Fouvry et al., 2014] (PF: plain fretting, FF: fretting-fatigue), number of cycles = 10^6 .

3.3 Application of the approach

Referring to what has been already introduced in Section 3.1, hereunder the procedure is explained in detail.

The different steps to build a nonlocal representation of the crack initiation frontiers based on I^a and I^s are listed in Figure 3.1. The starting point is represented by the experimental data expressed in a $(p_0, q_{max}, \sigma_B^{max})$ reference system, (Figures 3.3, 3.4, 3.5). To reproduce the velocity field corresponding to this local values a FE computation is needed.

In Figure 2.8 a standard FE model used to perform this type of computation is presented. As it is possible to see, the input quantities to load the structures are the normal and tangential force, (P and Q), applied at the pad surface to simulate fretting and σ_B , applied to the specimen to reproduce the fatigue effect.

Therefore for a given point, P, of coordinates, $(p_0, q_{max}, \sigma_B^{max})$, the following relation,

$$P(p_0, q_{max}, \sigma_B^{max}) \Rightarrow P(P, Q, \sigma_B^{max}), \quad (3.5)$$

needs to be determined in order to compute the loading forces to use in the FE model. For this purpose, the equations describing the cylinder/plane contact problem are used.

The peak pressure, p_0 , at the contact surface is equal to:

$$p_0 = \sqrt{\frac{PE^*}{\pi R}}, \quad P = p_0^2 \frac{\pi R}{E^*}, \quad (3.6)$$

where R and E^* have already been defined in Equations 2.15 and 2.16.

Concerning q_{max} , its computation is more complicated. The distribution of the shear load at the contact surface writes as follows:

$$q(x) = \mu p_0 \left(\sqrt{1 - \left(\frac{x}{a}\right)^2} - \frac{c}{a} \sqrt{1 - \left(\frac{x-e}{c}\right)^2} \right), \quad (3.7)$$

where

$$c = a \sqrt{1 - \left| \frac{Q}{\mu P} \right|}, \quad (3.8)$$

and

$$e = \frac{\sigma_B a}{4\mu p_0}. \quad (3.9)$$

By replacing Equations 3.8 and 3.9 in 3.5, the following relation is obtained:

$$q_{max} = \mu p_0 \sqrt{1 - \left(\sqrt{1 - \frac{Q}{\mu P}} - \frac{\sigma_B^{max}}{4\mu p_0} \right)^2}. \quad (3.10)$$

By solving Equation 3.10 with respect to Q , it follows,

$$Q^* = \frac{\pi R q_{max}^2}{\mu E^*} - \frac{1}{2} \frac{\pi R \sigma_B^{max}}{\mu E^*} \left(\frac{\sigma_B^{max}}{8} + \sqrt{(\mu p_0)^2 - q_{max}^2} \right). \quad (3.11)$$

It is worth noting that in plain fretting σ_B^{max} is equal to zero, and as a consequence,

$$Q^* = \frac{\pi R q_{max}^2}{\mu E^*}. \quad (3.12)$$

To sum up, by exploiting the Mindlin-Cattaneo solutions for cylinder/plane contact, it is possible to express Q and P as a function of p_0 and q_{max} . In other words, for a given point expressed in $(q_{max}, p_0, \sigma_B^{max})$ coordinates, Equations 3.6 and 3.10 describe the transformation rules to obtain the same point in a (P, Q^*, σ_B^{max}) reference system. This step is necessary since allows one to determine the macroscopic loads to apply as input in the FE model to compute the velocity field generated by the interaction between the two contacting bodies during a fretting-fatigue simulation.

Thanks to the relations developed in the previous paragraphs it is now possible to tackle the two following problems: (i) how the crack initiation frontiers will be transposed by using nonlocal intensity factors as reference quantities and (ii) similarly, how the gross slip frontier will be transformed in this new reference system.

3.3.1 Gross slip frontier

To transpose the crack initiation frontier, (Figure 3.4a), expressed as a function of q_{max} and p_0 , in a nonlocal representation, the first question to be addressed is how the gross slip frontier will be transformed by the change of reference quantities.

For this purpose, for a given Coulomb friction coefficient, different points laying on the corresponding gross slip limit are transposed on $(I_{max}^a - I^s)$ crack initiation map and a nonlocal gross slip frontier is defined ($I_{max}^a / I^s = \tilde{\mu}$). Different pad radii are tested in order to verify whether the geometry has an influence or not.

In more detail, provided that the interactions between the contacting bodies is handled by using the Coulomb's friction law, the gross slip frontier expressed in a $(q_{max} - p_0)$ reference system, is a straight line passing through the origin with a slope equal to the friction coefficient, ($q_{max}/p_0 = \mu$). Similar results are obtained if the frontier is described as a function of the macroscopic loads, P and Q^* , ($Q^*/P = \mu$).

For a given point, P, of coordinates $(Q^*, Q^*/\mu)$, a finite element computation is performed using as loading: $Q = Q^* \sin(\omega t)$ and $P = Q^*/\mu$. The velocity field is then extracted and post-processed to extract I_{max}^a and I^s . A description of the gross slip limit as a functions of nonlocal coordinates is eventually obtained.

In Table 3.5 the outcomes of the application of the aforementioned procedure to the configuration presented in [Fouvry et al., 2014], are displayed. Three different radii have been tested to analyze the influence of the change in geometry on the slip frontiers. Similarly, three different coulomb friction coefficients are analyzed to determine how these values are transformed.

q_{max} (MPa)	p_0 (MPa)	μ	R=20mm		R=40mm		R=80mm	
			I_{max}^a	I^s	I_{max}^a	I^s	I_{max}^a	I^s
300	600	0.5	5.4	7.0	7.4	10.2	10.0	14.5
400	800	0.5	8.2	11.0	11.2	15.9	14.9	21.9
500	1000	0.5	11.3	15.5	15.5	22.1	19.8	30.4
300	429	0.7	4.6	4.2	6.3	6.1	8.7	8.8
400	571	0.7	7.0	6.5	9.6	9.5	13.1	13.5
500	714	0.7	9.7	9.2	13.3	13.3	17.9	18.7
300	333	0.9	4.1	2.8	5.6	4.1	7.7	6.0
400	444	0.9	6.2	4.4	8.6	6.5	11.8	9.3
500	555	0.9	8.6	6.3	11.9	9.1	16.2	12.9

Table 3.5: Gross slip frontier evolution in nonlocal quantities for 35NiCrMo16 low-alloyed steel.

In Figure 3.6 a graphical representation of the information gathered in Table 3.5 is presented. Two conclusions can be drawn. First, there is a linear relation between local (μ) and nonlocal ($\tilde{\mu}$) Coulomb's friction coefficients,

$$I_{max}^a/I^s = \tilde{\mu} \quad \text{where} \quad \tilde{\mu} = \alpha\mu. \quad (3.13)$$

Secondly, the geometry has no important effect. Regardless of the pad radius, for a given μ , all the points that represent the outcome of the transposition from local to nonlocal coordinates lay on the same line, (Figure 3.6a).

A similar behavior is observed for the two other materials tested, Ti-6Al-4V and Inconel 718.

In Figures 3.7 and 3.8 the results are displayed and in Table 3.6 a summary of the computed linear parameters, α , linking the local friction coefficients to the nonlocal ones, is presented.

Material	E (GPa)	ν	μ	$\alpha \rightarrow \tilde{\mu} = \alpha\mu$
35NiCrMo16 low-alloyed steel	205	0.3	0.8	1.48
Inconel 718	203	0.29	1.0	1.47
Ti-6Al-4V	119	0.29	1.0	1.45

Table 3.6: Variation of the ratio between local and nonlocal friction coefficient as a function of the material considered.

The definition of a nonlocal friction coefficient is particularly interesting since in fretting-fatigue the definition of a local μ is tricky due to the different contact conditions experienced at the interface, i.e stick and partial slip. The difficulties

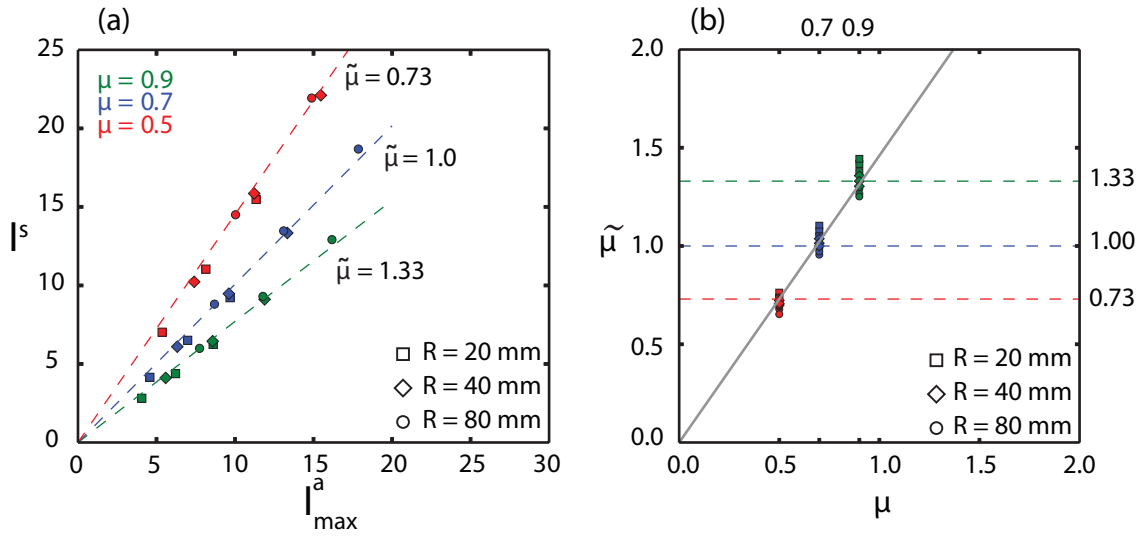


Figure 3.6: (a) Evolution of the gross slip limit in nonlocal coordinates for different Coulomb's friction coefficients and different geometries (Table 3.5); (b) relation between local and nonlocal friction coefficient (35NiCrMo16 low-alloyed steel).

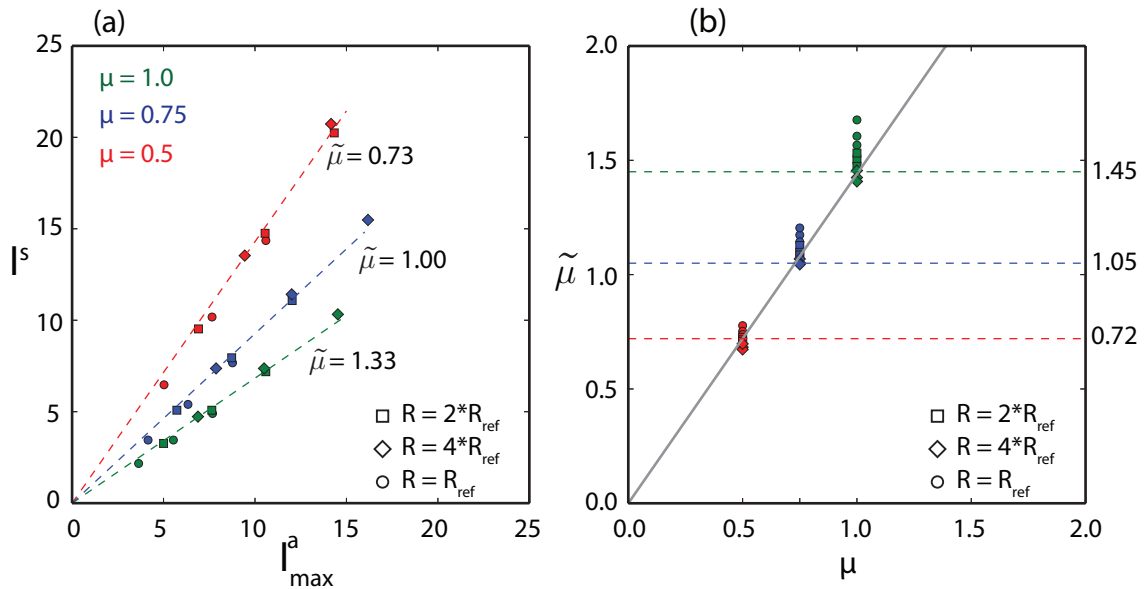


Figure 3.7: (a) Evolution of the gross slip limit in nonlocal coordinates for different Coulomb's friction coefficients and different geometries; (b) relation between local and nonlocal friction coefficient (TI-6Al-4V).

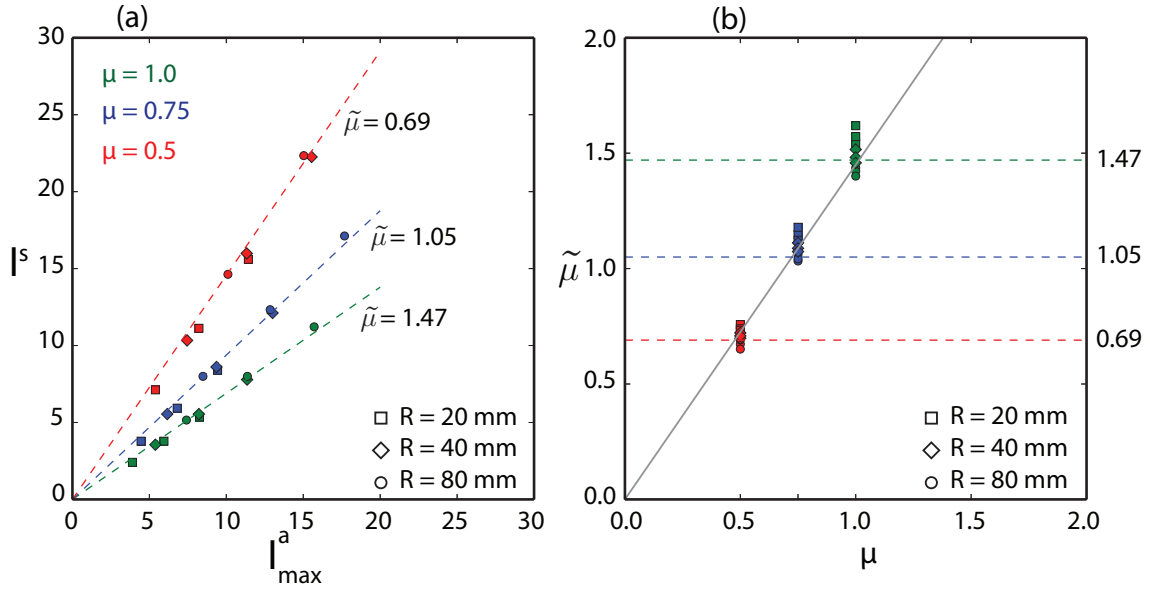


Figure 3.8: (a) Evolution of the gross slip limit in nonlocal coordinates for different Coulomb's friction coefficients and different geometries; (b) relation between local and nonlocal friction coefficient (Inconel 718).

encountered in the experimental identification of this parameter are proved by the fact that different procedures exist ([Hills and Nowell, 1994, Proudhon et al., 2005]) which give sometimes pretty different results.

For these reasons, the nonlocal friction coefficient, $\tilde{\mu}$, seems to be better suited for fretting-fatigue contact problems.

3.3.2 Plain fretting

Knowing how the gross slip frontier changes, the procedure is repeated to verify how the crack initiation thresholds are transformed.

For plain fretting, the steps followed are listed hereunder.

1. The experimental works highlight some crack initiation frontiers expressed in $(q_{max}-p_0)$ coordinates (Figures 3.4a, 3.3a, 3.5). For each point on these frontiers the relative macroscopic loads (P, Q^*) are computed by exploiting Equations 3.6 and 3.10.
2. A FE computation is performed to obtain the velocity field close to the contact edges. P and Q^* , computed in the previous step, are used here to load the structure.
3. The nonlocal intensity factors are obtained, following the steps listed in Section 2.4.4.

4. A crack initiation map based on nonlocal quantities is built.

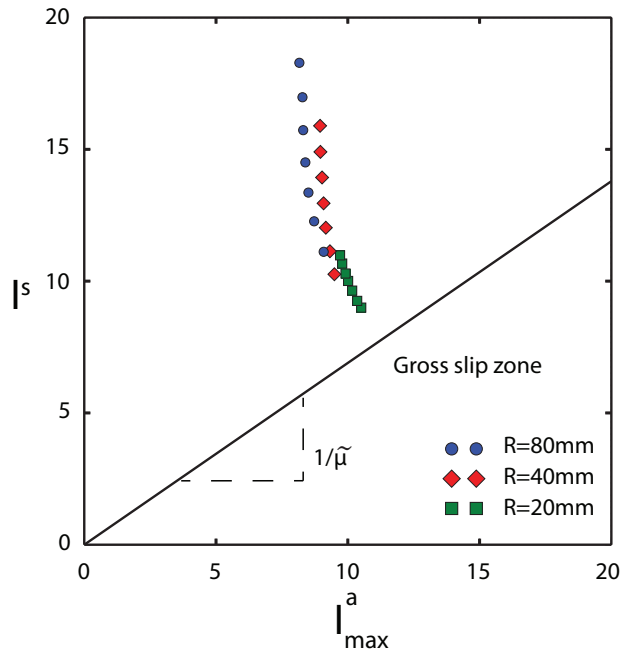


Figure 3.9: Nonlocal crack initiation boundaries for Inconel 718 in plain fretting.

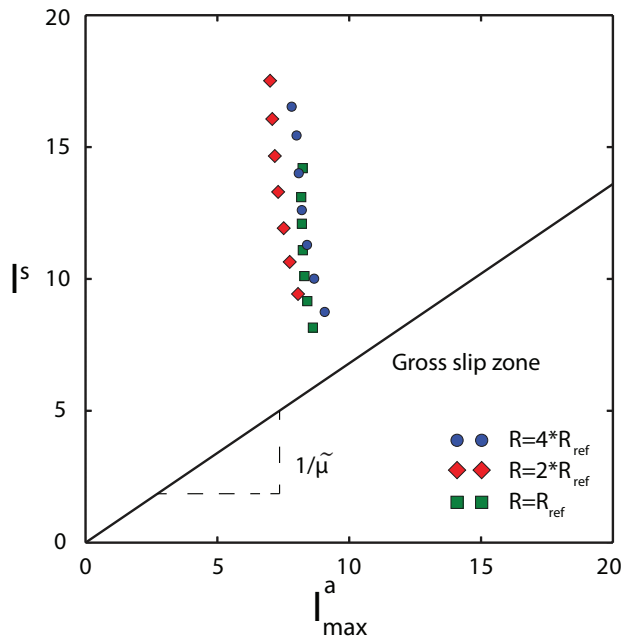


Figure 3.10: Nonlocal crack initiation boundaries for Ti-6Al-4V in plain fretting.

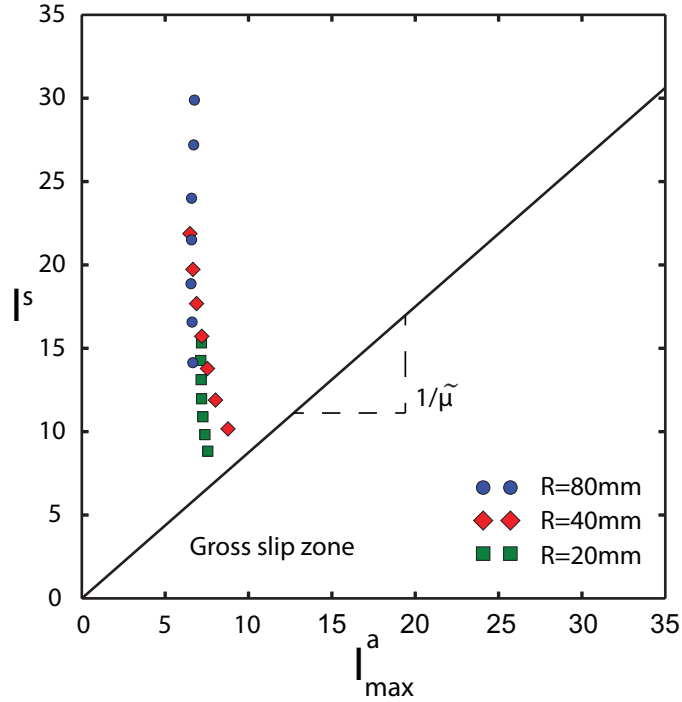


Figure 3.11: Nonlocal crack initiation boundaries for 35NiCrMo16 low-alloyed steel in plain fretting.

It is worth mentioning that, in order to have a better understanding of how crack initiation frontiers are transformed, the experimental data are enriched; a linear interpolation of the experimental points is done and this permits to apply the steps listed above on a more complete set of data.

Figures 3.9, 3.10 and 3.11 present the outcome of the procedure described above.

The interest in adopting a nonlocal representation of the crack initiation frontiers is evident. The classic crack initiation frontiers, expressed either in $(q_{max}-p_0)$ or (Q^*-P) coordinates, clearly show the influence of the gradient since, for different geometries tested, different frontiers are obtained. If the same map is represented through nonlocal quantities, the gradient effect disappears and all the curves merge into a single one.

3.3.3 Fretting-fatigue

In [Ferré, 2013] and [Fouvry et al., 2014] some experimental tests have been carried out aiming at analyzing the evolution of the crack initiation frontiers when a cyclic bulk load, (σ_B) , in phase with the tangential force, Q , is introduced. More precisely, for a given pressure level (p_0 fixed), different tests are performed varying the magnitude of σ_B^{max} and recording each time the value of q_{max} leading to crack initiation after a certain number of cycles. The results of these test campaigns are displayed in

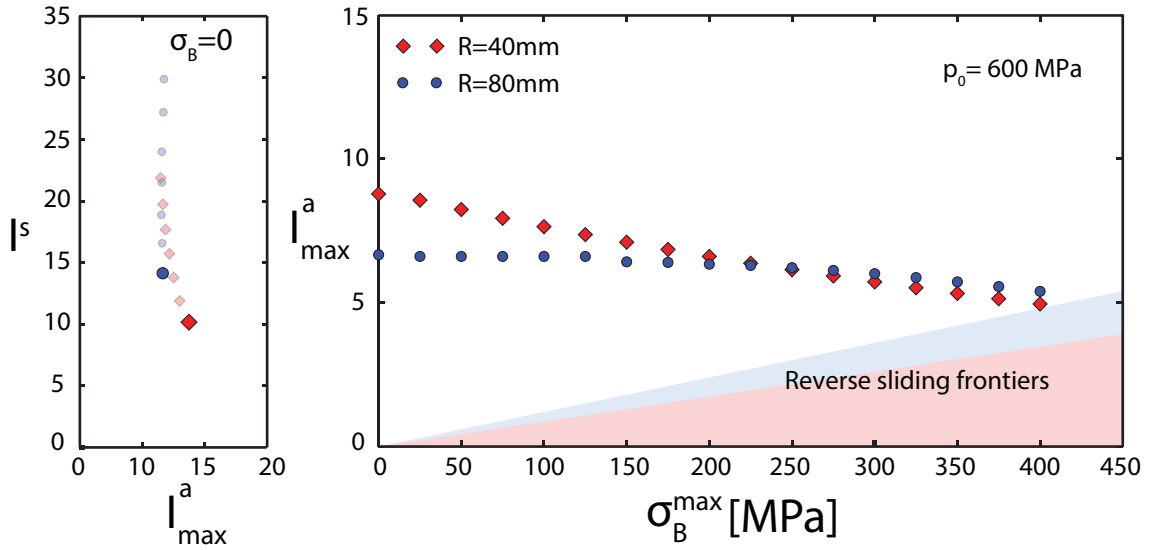


Figure 3.12: Nonlocal crack initiation boundaries evolution with the introduction of a cyclic bulk load, σ_B , for 35NiCrMo16 low-alloyed steel in fretting-fatigue.

Figures 3.3b and 3.5b; for small values of the cyclic bulk load little or no effect on the initiation frontiers are experienced. A reduction in the q_{max} amplitude, needed to initiated cracks, starts to be observable when σ_B^{max} overcomes 200 MPa.

The data, collected by the authors cited above, allow us to study how the nonlocal crack initiation frontiers is modified by the introduction of a cyclic bulk force. As a matter of fact, a third dimension is added to the initiation map introduced in the previous paragraph. The evolution of q_{max} as a function of σ_B^{max} , transposed in nonlocal quantities, becomes the evolution of I_{max}^a as a function of σ_B^{max} (I^s is fixed since it depends on P which does not vary).

The steps followed to obtain the new representation are the same of the ones presented in Section 3.3.2 except that the macroscopic loads, applied as input in the FE computation, include the fatigue force, as well. As for plain fretting, the available data are enriched by interpolating the experimental points.

The outcomes of the transposition are presented in Figures 3.12 and 3.13. The introduction of a cyclic bulk force does not change the trend already observed in Figures 3.3b and 3.5b. No matter which reference system is used, large values of σ_B have a negative effect on the initiation frontiers.

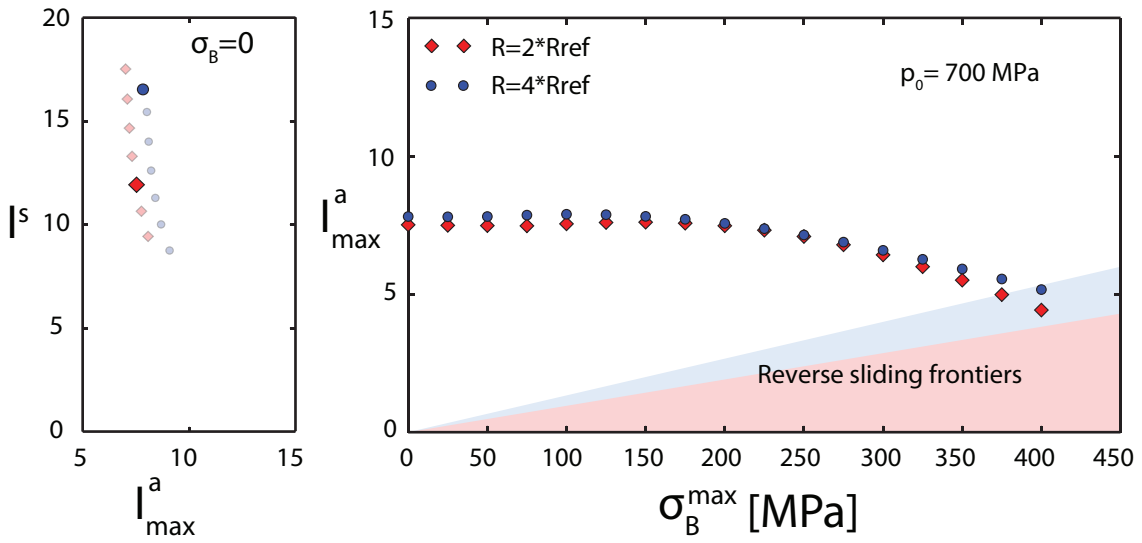


Figure 3.13: Nonlocal crack initiation boundaries evolution with the introduction of a cyclic bulk load, σ_B , for Ti-6Al-4V in fretting-fatigue.

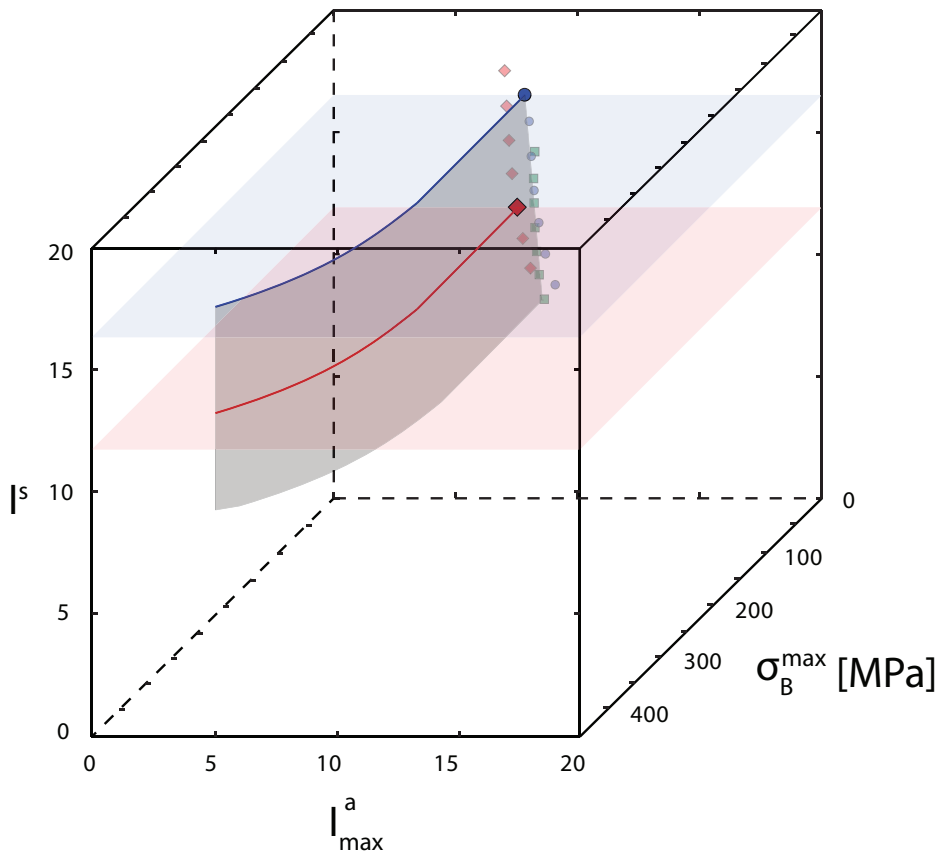


Figure 3.14: Nonlocal crack initiation frontier in fretting-fatigue for Ti-6Al-4V.

Since the experimental data available have been obtained for a fixed pressure, (\bar{p}_0) , only the evolution of a specific point of coordinates (q_{max}, \bar{p}_0) on the crack initiation frontier is analyzed. Basically, what is possible to infer from the data is how this point evolves inside a three-dimensional space where the third dimension is represented by σ_B^{max} . Assuming that the frontier moves together with the analyzed point, then a local crack initiation surface, S , that depends on p_0, q_{max} and σ_B^{max} can be defined. By applying the approach described in Chapter 2 the correspondent nonlocal intensity factors are extracted, which permit to define a tridimensional nonlocal crack initiation map $(I_{max}^a, I^s$ and $\sigma_B^{max})$ as presented in Figure 3.14.

To sum up, using the results coming from the plain fretting experimental campaign and the ones obtained in fretting-fatigue a tridimensional crack initiation map is defined. By expressing this map in nonlocal quantities it is possible to eliminate the gradient effect and, therefore, a single frontier is obtained no matter which geometry is used.

The results obtained here are important for several reasons.

First it has been proven that the nonlocal intensity factors represent a set of objective quantities allowing to describe the crack initiation frontiers eliminating the dependency on the contact geometry caused by the gradient.

This could allow to reduce the number of experimental tests in order to certify components characterized by different contact configurations.

The nonlocal intensity factors represents in fact a powerful tool to transpose the results from a geometry to another.

Here the limitation remains the fact that experimental tests are still needed to build the initiation frontier for a given material. This is the reason why in the next chapter we focus in finding a multiaxial criterion in order to predict the initiation frontier just by using simple material fatigue data. This should permit us to get rid of the experimental tests, which will represent a big saving for industrial applications.

3.4 Influence of the friction coefficient variation

Usually one of the first step during a plain fretting or fretting-fatigue test campaign is to evaluate the friction coefficient for the given materials (pad and specimen) employed. Two main procedures allow one to compute this parameter.

The first possibility to determine the friction coefficient for a cylinder plane contact configuration under condition of plane deformation is the technique described by Hills and Nowell in [Hills and Nowell, 1994]. The authors point out that the different slip and stick zone presented in fretting are characterized by different friction coefficients. Furthermore this value evolves with the number of cycles. It can be useful therefore to define an average friction coefficient on the entire contact surface:

$$\bar{\mu} = \frac{\int_{-a}^a q(x)dx}{\int_{-a}^a p(x)dx}. \quad (3.14)$$

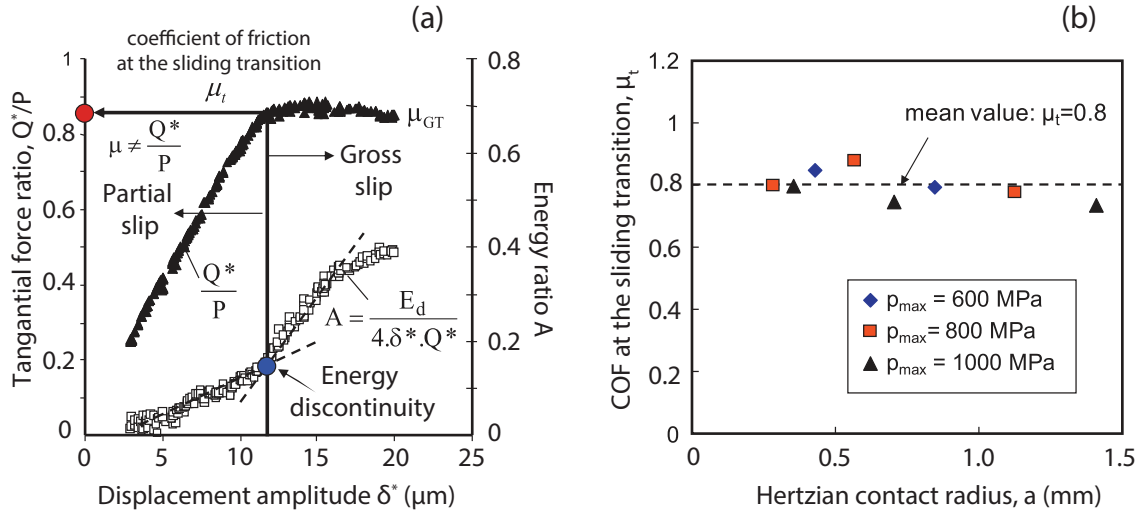


Figure 3.15: (a) Variable displacement method to compute the friction coefficient (b) evolution of the friction coefficient as a function of contact radius and maximum Hertzian pressure, [Fouvry et al., 2014].

Starting from this macroscopic value it is then possible to go back to the friction coefficient in the slip zone by exploiting the Mindlin-Cattaneo calculation:

$$\bar{\mu} = \mu_s - \frac{2}{\pi} \int_{\mu_0}^{\mu_s} \left(\frac{Q}{\mu_s P} \sqrt{1 - \frac{Q}{\mu_s P}} + \sin^{-1} \sqrt{1 - \frac{Q}{\mu_s P}} \right) d\mu_s, \quad (3.15)$$

where μ_0 is the coefficient of friction at the beginning of the experiments where its value is still constant over the entire contact surface, and μ_s is the coefficient of friction in the slip zone.

A second technique for estimating μ is based on the assumption that the friction coefficient measured at the transition between partial and gross slip regimes (μ_t) provides a representative value of the friction under partial slip condition (i.e. $\mu_t \approx \mu_s$), [Proudhon et al., 2005]. A variable displacement method is employed to determine the transition value. The procedure consists in keeping the normal load (P) constant whereas the relative displacement amplitude (δ^*) is progressively increased. For cylinder plane configuration the transition point is identified as the point where the tangential force ratio (Q/P) and the friction energy ratio ($A = E_d/4Q^*\delta^*$) show a discontinuity.

No matter which technique is used to evaluate the friction coefficient, large variation in the computed value of μ is usually experienced. In this context, it is fundamental to test the sensitivity of the numerical algorithm developed with respect to the value of the friction coefficient employed. The study is carried out by investigating how the nonlocal crack initiation map is influenced by a change on the nominal μ . More precisely starting from the crack initiation frontiers obtained by

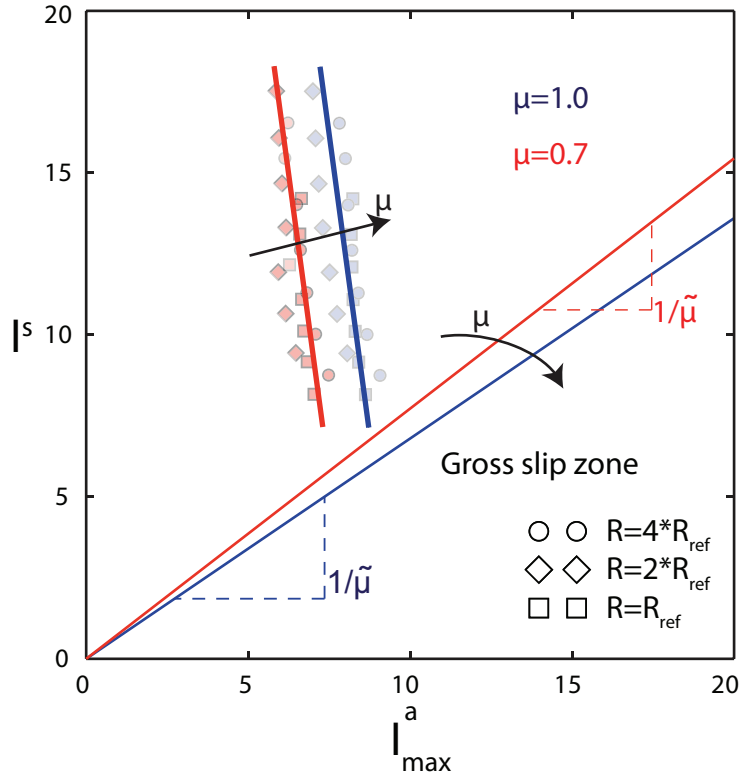


Figure 3.16: Variation of the crack initiation frontiers as a function of the friction coefficient for TI-6Al-4V.

Ferré [Ferré et al., 2013] (Figure 3.3a), the macroscopic forces (P , Q) are computed and then the FE computation is run to obtain the velocity field. The friction coefficient used in the FE model has been varied with respect to the experimental value found by Ferré to simulate an uncertainty.

In Figure 3.16 the results of the analysis are presented. In particular the nonlocal initiation curve obtained with the original Coulomb's friction coefficient ($\mu = 1$) is compared with a second curve, output of a computation in which the friction coefficient is intentionally lowered to 0.7. The lower friction coefficient makes the frontier move toward the left and this is coherent. The macroscopic loads leading to crack initiation are kept constant, and therefore the reduction of μ will result in lower shear stresses at the contact interface and as a consequence lower values of I^a , as well.

Nevertheless the results clearly show that no matter which value of the friction coefficient is used, the behavior already observed does not change. The crack initiation frontiers keep superposing one on the other if the nonlocal intensity factors are employed as coordinates.

We can, therefore, conclude that the procedure to describe fretting-fatigue through nonlocal quantities is robust with respect to an uncertainty on the friction coefficient.

3.5 Chapter highlights

In this chapter the algorithm developed has been applied to experimental data coming from plain fretting and fretting-fatigue test campaigns. Several local crack initiation maps expressed in $(q_{max} - p_0)$ coordinates are transposed by using I_{max}^a and I^s as reference quantities.

The application of the procedure has several important advantages.

First, the nonlocal intensity factors are geometry independent. This is an important point because experimental data, expressed either in $(Q^* - P)$ or $(q_{max}-p_0)$ coordinates, clearly show that for different geometries various crack initiation frontiers are observed. This represents a limitation for industrial applications since it is difficult to transpose the results obtained on laboratory test machines to real-scale industrial components. On the contrary, if the crack initiation map is expressed in nonlocal quantities $(I_{max}^a-I^s)$, that take into account the gradient effect, all the different crack initiation frontiers merge into a single one. As a consequence, the nonlocal intensity factors can be considered objective quantities through which it is possible to compare different fretting-fatigue experimental or numerical results.

Secondly, the good stability shown by the method allows one to apply it to more complex contact configurations, such as, the disc-blade root attachment in a turbofan engine. The spatial reference fields depend only on the local geometry of the parts and therefore for a given configuration they can be pre-computed through the use of a fine mesh as it is presented in Section 2.3. Then, for any given macroscopic load combination a rough mesh FE computation will be performed aiming at extracting directly the nonlocal intensity factors thanks to the information already stocked on the shape of the reference fields. Neither the methods based on the theory of critical distances, nor the ones based on stress intensity factor computation have this peculiarity obliging to adopt very fine meshes (micrometer size).

Chapter 4

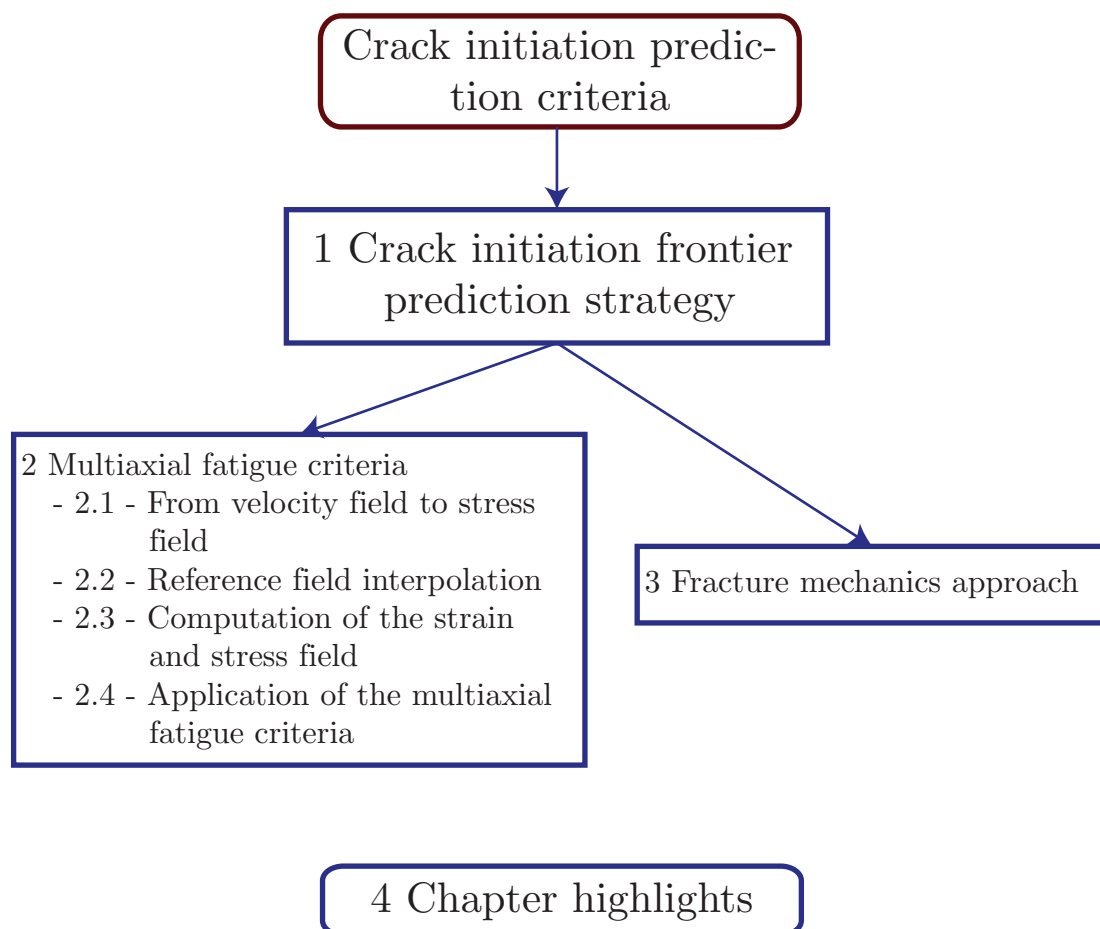
Crack initiation prediction criteria

In the previous chapter it has been shown how, by describing the crack initiation map with nonlocal stress intensity factors as reference quantities, it is possible to define an initiation frontier, which is independent of the geometry of the contacting bodies.

Here, the goal is to predict the location of the frontier by using simple material data, such as the fatigue limit or the crack initiation threshold. For this purpose, several multiaxial fatigue criteria are coupled to the description of fretting-fatigue through nonlocal intensity factors which allow to obtain a numerical crack initiation frontier as a function of I_{max}^a , I^s and σ_B^{max} .

An attempt to link the nonlocal stress intensity factors, corresponding to the crack initiation frontiers, with a ΔK threshold is done as well.

Chapter 4 - Table of Contents Flowchart



4.1 Crack initiation frontier prediction strategy

The nonlocal stress intensity factors employed to univocally characterized the velocity field close to the contact edges under fretting-fatigue are used here to predict the fatigue behavior of the contacting bodies. For this purpose two main approaches are investigated.

The first one consists in applying different multiaxial fatigue criteria using as input the stress field associated to the nonlocal intensity factors previously computed. More precisely, since there is a direct relation between $(I^s, I_{max}^a, \sigma_B^{max})$ and the magnitude of the velocity field generated at the contact tip, by exploiting the Hooke's law, it is possible to compute the stress field, so that a link between the nonlocal stress intensity factors and the stress field arising close to the contact edge is established.

The second approach aims at correlating directly the nonlocal stress intensity factors corresponding to the crack initiation frontier with a ΔK threshold as it is usually done in fracture mechanics.

4.2 Multiaxial fatigue criteria

4.2.1 From velocity field to stress field

By applying the partition technique detailed in Chapter 2, it is possible to describe the velocity field generated close to the contact tip under fretting-fatigue through a set of nonlocal quantities. Thus, for a given set of macroscopic loads, P , Q and σ_B^{max} the following relation is determined:

$$(P, Q, \sigma_B) \Leftrightarrow (I^s, I^a, I^c). \quad (4.1)$$

The velocity field can be described as follows (in a reference system attached to the contact front),

$$\underline{v}(\underline{x}, t) \simeq \underbrace{\dot{I}^s(t)\underline{d}^s(\underline{x}) + \dot{I}^a(t)\underline{d}^a(\underline{x})}_{v^e} + \underbrace{\dot{I}^c(t)\underline{d}^c(\underline{x})}_{v^c}. \quad (4.2)$$

Since the third term, v^c , describing the nonlinear effect of friction, is extremely localized (Figure 2.14), it is assumed that its effect on the velocity field can be neglected, provided that the analyzed zone is large enough. This approach is analogue to the one followed in fracture mechanics where the hypothesis of small scale yielding permits to use an elastic stress intensity factor, K , to describe the mechanical field close to the crack tip.

The steps to pass from the velocity field to the stress field are listed hereunder,

$$\underline{u}(\underline{x}, t) = \int \dot{I}^a(t)\underline{d}^a(\underline{x})dt + \int \dot{I}^s(t)\underline{d}^s(\underline{x})dt, \quad (4.3)$$

$$= \underline{d}^a(\underline{x}) \int \dot{I}^a(t)dt + \underline{d}^s(\underline{x}) \int \dot{I}^s(t)dt. \quad (4.4)$$

Once the displacement field is obtained, the strain tensor is derived,

$$\varepsilon_{ij} = I^a \varepsilon_{ij}^a + I^s \varepsilon_{ij}^s, \quad (4.5)$$

where

$$\varepsilon_{ij}^a = \left[\frac{1}{2} \left(\frac{\partial d_i^a}{\partial x_j} + \frac{\partial d_j^a}{\partial x_i} \right) \right], \quad \varepsilon_{ij}^s = \left[\frac{1}{2} \left(\frac{\partial d_i^s}{\partial x_j} + \frac{\partial d_j^s}{\partial x_i} \right) \right]. \quad (4.6)$$

The stress tensor is eventually computed by exploiting Hooke's equation

$$\sigma_{ij} = I^a \sigma_{ij}^a + I^s \sigma_{ij}^s, \quad (4.7)$$

where

$$\sigma_{ij}^a = C_{ijkl} \varepsilon_{kl}^a, \quad \sigma_{ij}^s = C_{ijkl} \varepsilon_{kl}^s. \quad (4.8)$$

Here the general idea on how to obtain the stress tensor using as input the nonlocal intensity factors has been introduced. In the next sections the mathematical details are presented.

It is worth mentioning that by deriving the strain tensor as described above, an approximation is made since the displacement field is defined in a reference system attached to the contact front the strain is defined in a reference system attached to the deformed material.

4.2.2 Reference field interpolation

In order to perform the derivative of the reference functions, $\underline{d}^a(\underline{x})$ and $\underline{d}^s(\underline{x})$, as described in Equation 4.6, two possibilities can be considered. A numerical technique such as the central difference method can be used. On the other hand, a second option consists in interpolating the reference field with derivable functions allowing to obtain an analytical expression of the strain tensor.

The second strategy has been chosen since by looking at the characteristic shape of $\underline{d}^a(\underline{x})$ and $\underline{d}^s(\underline{x})$ the analogy with the displacement field at the crack tip is evident, which allows one to use the equations already developed for fracture mechanics to describe the evolution of the reference fields in fretting-fatigue.

In more detail, the velocity field at the crack tip for Mode I and Mode II, in the reference frame presented in Figure 4.1, is described by the following relations,

$$\underline{v}_x^I = \dot{K}_I f^I(r) g_x^I(\vartheta), \quad (4.9)$$

$$f^I(r) = \frac{4(1-\nu^2)}{E} \sqrt{\frac{r}{2\pi}} \quad g_x^I(\vartheta) = \frac{1}{4\nu-4} \cos(\vartheta) \sin(\vartheta/2) + \frac{3-4\nu}{4\nu-4} \sin(\vartheta/2),$$

$$\underline{v}_y^I = \dot{K}_I f^I(r) g_y^I(\vartheta), \quad (4.10)$$

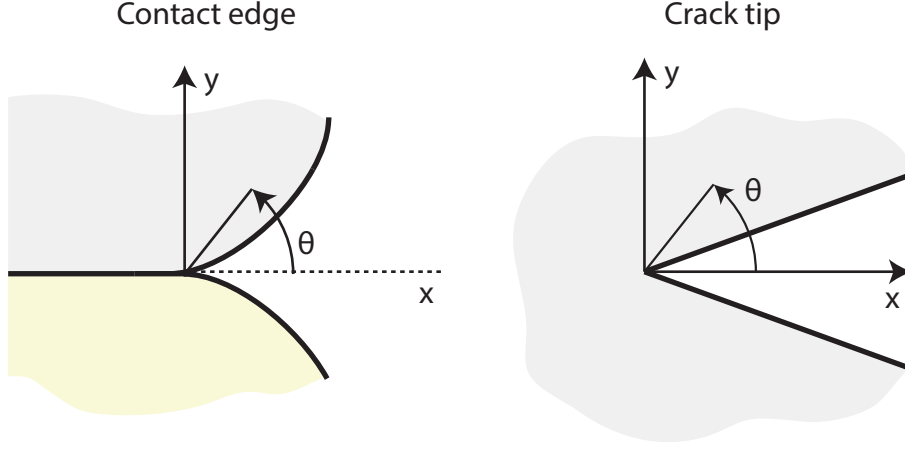


Figure 4.1: Crack analogue approach, $0 \leq \vartheta \leq 2\pi$.

$$f^I(r) = \frac{4(1-\nu^2)}{E} \sqrt{\frac{r}{2\pi}} \quad g_y^I(\vartheta) = \frac{1}{4-4\nu} \cos(\vartheta) \cos(\vartheta/2) + \frac{3-4\nu}{4-4\nu} \cos(\vartheta/2),$$

$$\underline{v}_x^{II} = \dot{K}_{II} f^{II}(r) g_x^{II}(\vartheta), \quad (4.11)$$

$$f^{II}(r) = \frac{4(1-\nu^2)}{E} \sqrt{\frac{r}{2\pi}} \quad g_x^{II}(\vartheta) = \frac{1}{4\nu-4} \cos(\vartheta) \cos(\vartheta/2) + \frac{4\nu-5}{4\nu-4} \cos(\vartheta/2),$$

$$\underline{v}_y^{II} = \dot{K}_{II} f(r)^{II} g_y^{II}(\vartheta), \quad (4.12)$$

$$f^{II}(r) = \frac{4(1-\nu^2)}{E} \sqrt{\frac{r}{2\pi}} \quad g_y^{II}(\vartheta) = \frac{1}{4\nu-4} \cos(\vartheta) \sin(\vartheta/2) + \frac{4\nu-1}{4\nu-4} \sin(\vartheta/2).$$

The above equations are valid for plain strain, and they are slightly different from the ones that can be found in the literature, [Anderson, 2005], due to the reference system (Figure 4.1) chosen and the normalization rules applied,

$$g^I(\vartheta) \rightarrow \frac{g_y^I(0) - g_y^I(2\pi)}{2} = 1, \quad (4.13)$$

$$g^{II}(\vartheta) \rightarrow \frac{g_x^{II}(0) - g_x^{II}(2\pi)}{2} = 1. \quad (4.14)$$

Concerning the symmetric and antisymmetric reference field in fretting-fatigue, their evolution with respect to the analogue field at the crack tip are displayed in Figures 4.2 and 4.3 (the details on how these fields and their evolution have been obtained are presented in Chapter 2). Both the reference fields are normalized in

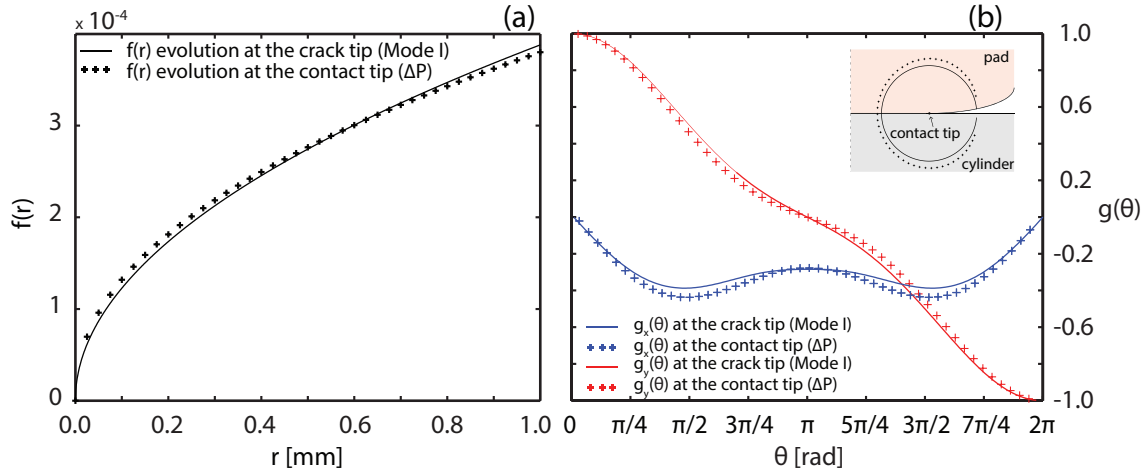


Figure 4.2: (a) Comparison between radial evolution of \underline{d}^s and radial evolution of the displacement field at the crack tip (mode I); (b) Comparison between tangential evolution of \underline{d}^s and tangential evolution of the displacement field at the crack tip (mode I).

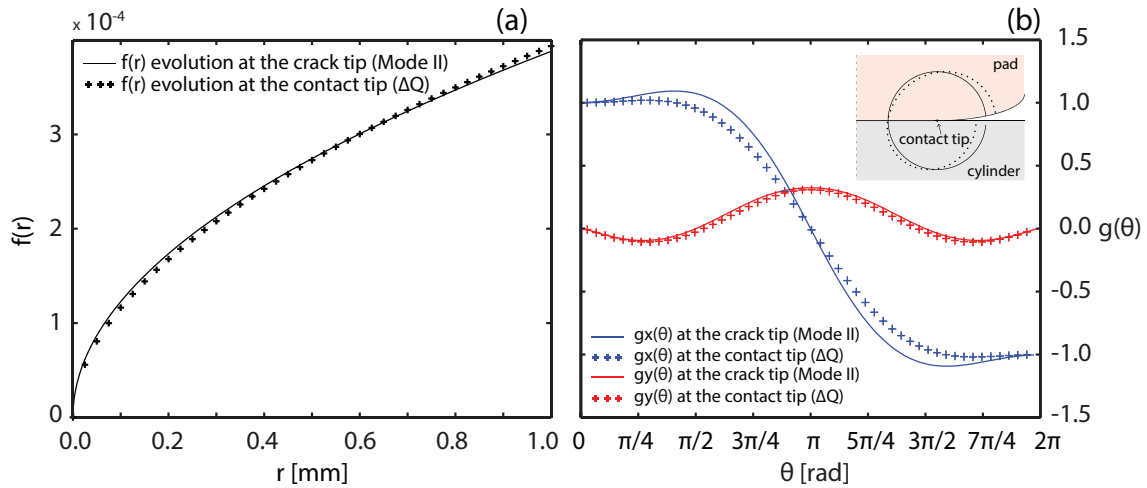


Figure 4.3: (a) Comparison between radial evolution of \underline{d}^a and radial evolution of the displacement field at the crack tip (mode II); (b) Comparison between tangential evolution of \underline{d}^a and tangential evolution of the displacement field at the crack tip (mode II).

order to correspond to the velocity field obtained at the crack tip during an elastic loading phase with a unitary K_I and K_{II} .

As a result of what has been shown above, the following relation can be used to obtain an analytical description of the antisymmetric and symmetric reference field. In particular, comparing the radial evolution at the crack tip and at the contact edge, they are almost identical which justifies the following simplification,

$$f^s(r) = f^a(r) = \frac{4(1 - \nu^2)}{E} \sqrt{\frac{r}{2\pi}}, \quad (4.15)$$

where f^s and f^a are the radial evolution of $\underline{d}^s(\underline{x})$ and $\underline{d}^a(\underline{x})$.

In regard to $\underline{g}^s(\vartheta)$ and $\underline{g}^a(\vartheta)$, either they are described through the functions coming from the fracture mechanics or by using an interpolation technique. The first choice introduces an approximation, since as it shown in Figures 4.2 and 4.3, little but not negligible differences are present between the tangential evolution observed at the crack tip and the one experienced at the contact edge.

The analytical expression of $\underline{g}^s(\vartheta)$ and $\underline{g}^a(\vartheta)$ are therefore obtained by interpolating their evolution with derivable functions. A wise selection of the interpolation functions consists in exploiting the crack analogue approach by using the same equations describing the kinetics field around the crack tip, and adapting them by means of a least square approach. In more detail, the interpolation functions chosen are the followings ones,

$$\hat{g}_x^s(\vartheta) = \alpha \cos(\vartheta) \sin(\vartheta/2) + \beta \sin(\vartheta/2), \quad (4.16)$$

$$\hat{g}_y^s(\vartheta) = \gamma \cos(\vartheta) \cos(\vartheta/2) + \delta \cos(\vartheta/2), \quad (4.17)$$

$$\hat{g}_x^a(\vartheta) = \epsilon \cos(\vartheta) \cos(\vartheta/2) + \zeta \cos(\vartheta/2), \quad (4.18)$$

$$\hat{g}_y^a(\vartheta) = \eta \cos(\vartheta) \sin(\vartheta/2) + \lambda \sin(\vartheta/2). \quad (4.19)$$

The values of the coefficients are computed by minimizing the difference between the output of the velocity field partition and the interpolating functions.

For instance, for a reference configuration characterized by the following parameters – plain fretting analysis, Pad radius = 20 mm, friction coefficient = 1.0, Young's modulus = 119 400 MPa, Poisson's ratio = 0.3, $P = 347 \text{ N mm}^{-1}$ and $Q^* = 237 \text{ N mm}^{-1}$ – once the velocity field is partitioned, $\underline{d}^s(\underline{x})$ and $\underline{d}^a(\underline{x})$ can be computed and $\underline{g}^s(\vartheta)$ and $\underline{g}^a(\vartheta)$ are determined. The analytical expression of these fields is eventually obtained in the following way,

$$\text{Symmetric field:} \quad \alpha, \beta \rightarrow \min \|g_x^s - \hat{g}_x^s\|, \quad \gamma, \delta \rightarrow \min \|g_y^s - \hat{g}_y^s\|, \quad (4.20)$$

$$\text{Antisymmetric field:} \quad \epsilon, \zeta \rightarrow \min \|g_x^a - \hat{g}_x^a\|, \quad \eta, \lambda \rightarrow \min \|g_y^a - \hat{g}_y^a\|. \quad (4.21)$$

By replacing the computed coefficient values in Equations 4.16-4.19 a satisfactory interpolation of the reference fields is obtained.

In Table 4.1 the values of the coefficients, outcome of the minimization procedure, are displayed.

	Fretting-fatigue	Fracture mechanics
α	-0.3199	$1/(4\nu - 4) = -0.3501$
β	-0.6021	$(3 - 4\nu)/(4\nu - 4) = -0.6499$
γ	0.3004	$1/(4 - 4\nu) = 0.3501$
δ	0.6829	$(3 - 4\nu)/(4 - 4\nu) = 0.6499$
ϵ	-0.5244	$1/(4\nu - 4) = -0.3501$
ζ	1.5244	$(4\nu - 5)/(4\nu - 4) = 1.3501$
η	-0.3377	$1/(4\nu - 4) - 0.3501$
λ	-0.0104	$(4\nu - 1)/(4\nu - 4) = -0.0504$

Table 4.1: Coefficient values allowing to interpolate $\underline{g}^s(\vartheta)$ and $\underline{g}^a(\vartheta)$ and the ones obtained for crack-tip displacement field in mode I and mode II.

The value of the coefficients describing mode I and mode II velocity field in fracture mechanics are displayed as well, which allows to have a quantitative estimation of the error introduced by applying the crack analogue approach.

In Figures 4.5 and 4.4 the results of the interpolation are presented. The functions used allow to reproduce the variation of the symmetric and antisymmetric reference field accurately.

4.2.3 Computation of the strain and stress field

Once that the analytical description of $\underline{d}^s(\underline{x})$ and $\underline{d}^a(\underline{x})$ is obtained, the corresponding strain field can be computed as described in Equation 4.6. To notice that by using Equations 4.15-4.19, the reference fields are implicitly described in polar coordinates. This has to be taken into account in order to perform the derivatives to compute the strain field,

$$\varepsilon_{xx}^a(r, \vartheta) = \left(\frac{\partial d_x^a(r, \vartheta)}{\partial r} \frac{\partial r}{\partial x} + \frac{\partial d_x^a(r, \vartheta)}{\partial \vartheta} \frac{\partial \vartheta}{\partial x} \right), \quad (4.22)$$

$$\varepsilon_{yy}^a(r, \vartheta) = \left(\frac{\partial d_y^a(r, \vartheta)}{\partial r} \frac{\partial r}{\partial y} + \frac{\partial d_y^a(r, \vartheta)}{\partial \vartheta} \frac{\partial \vartheta}{\partial y} \right), \quad (4.23)$$

$$\varepsilon_{xy}^a(r, \vartheta) = \left(\frac{\partial d_y^a(r, \vartheta)}{\partial r} \frac{\partial r}{\partial x} + \frac{\partial d_y^a(r, \vartheta)}{\partial \vartheta} \frac{\partial \vartheta}{\partial x} + \frac{\partial d_x^a(r, \vartheta)}{\partial r} \frac{\partial r}{\partial y} + \frac{\partial d_x^a(r, \vartheta)}{\partial \vartheta} \frac{\partial \vartheta}{\partial y} \right). \quad (4.24)$$

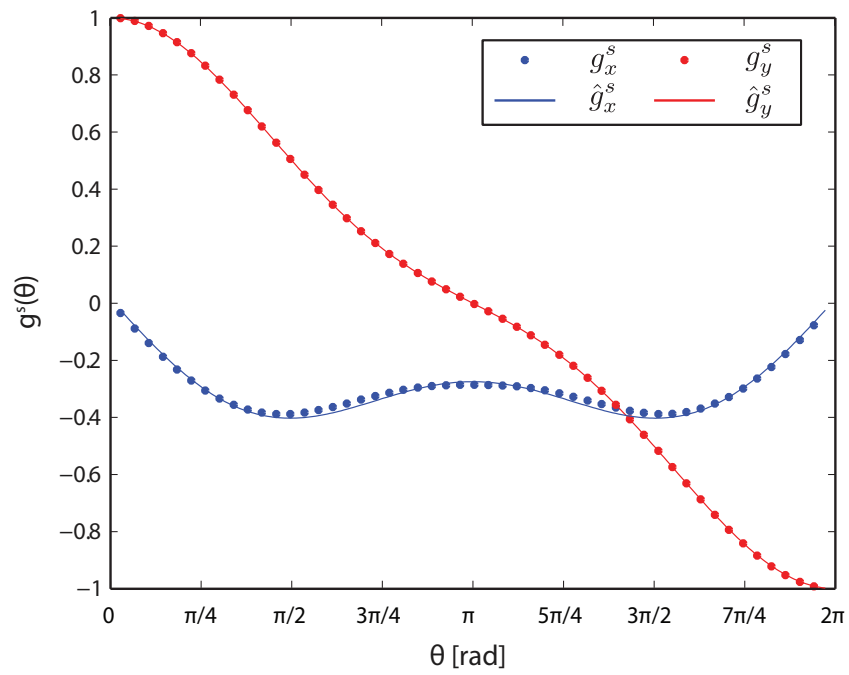


Figure 4.4: Interpolation of $g^s(\vartheta)$.

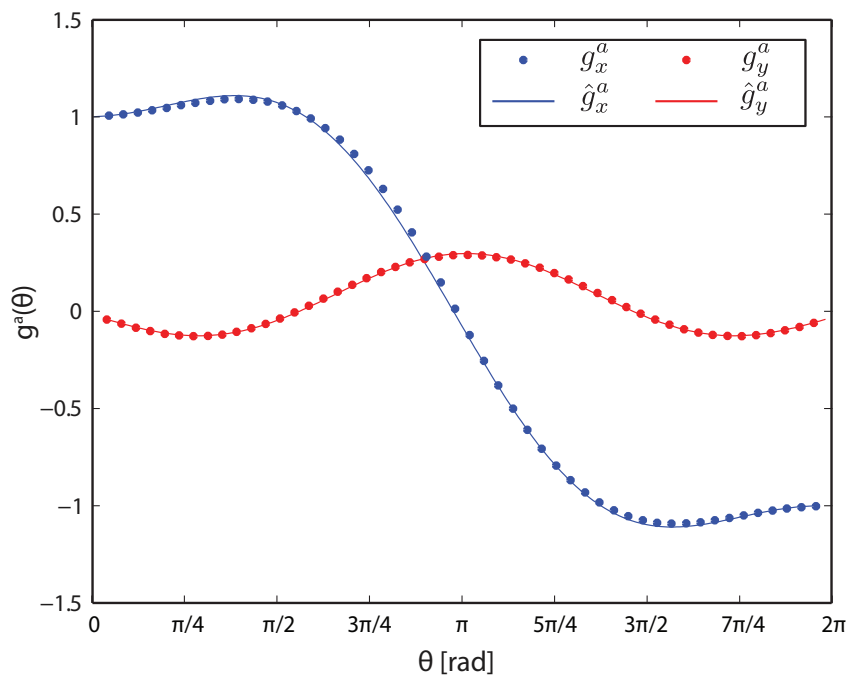


Figure 4.5: Interpolation of $g^a(\vartheta)$.

The same process is repeated for ϵ_{xx}^s , ϵ_{yy}^s and ϵ_{xy}^s . Knowing the expression of $\underline{d}^s(\underline{x})$ and $\underline{d}^a(\underline{x})$, the computation of the strain field is straightforward,

$$\epsilon_{xx}^s = K \sqrt{\frac{2}{\pi r}} \frac{(\nu^2 - 1)}{E} \sin(\vartheta/2) (-\alpha + \beta + \alpha \cos(\vartheta) + \alpha \cos(2\vartheta)), \quad (4.25)$$

$$\epsilon_{yy}^s = K \sqrt{\frac{2}{\pi r}} \frac{(\nu^2 - 1)}{E} \sin(\vartheta/2) (\gamma - \delta + \gamma \cos(\vartheta) + \gamma \cos(2\vartheta)), \quad (4.26)$$

$$\epsilon_{xy}^s = K \sqrt{\frac{1}{2\pi r}} \frac{(1 - \nu^2)}{E} \cos(\vartheta/2) (\alpha + \beta + \gamma + \delta + (\gamma - \alpha)(\cos(\vartheta) - \cos(2\vartheta))), \quad (4.27)$$

$$\epsilon_{xx}^a = K \sqrt{\frac{2}{\pi r}} \frac{(1 - \nu^2)}{E} \cos(\vartheta/2) (\epsilon + \zeta + \epsilon \cos(\vartheta) - \epsilon \cos(2\vartheta)), \quad (4.28)$$

$$\epsilon_{yy}^a = K \sqrt{\frac{2}{\pi r}} \frac{(1 - \nu^2)}{E} \cos(\vartheta/2) (\eta + \lambda - \eta \cos(\vartheta) + \eta \cos(2\vartheta)), \quad (4.29)$$

$$\epsilon_{xy}^a = K \sqrt{\frac{1}{2\pi r}} \frac{(\nu^2 - 1)}{E} \sin(\vartheta/2) (\epsilon - \zeta - \eta + \lambda + (\zeta + \eta)(\cos(\vartheta) + \cos(2\vartheta))). \quad (4.30)$$

For the sake of simplicity, in the equations above and in the ones that will follow, $K_I = K_{II} = K = 1 \text{ MPa}\sqrt{\text{m}}$. The unitary value comes from the fact that the reference fields are normalized in order to correspond to the displacement field obtained at the crack tip during an elastic loading phase characterized by a stress intensity factor equal to 1.

By exploiting Hooke's law, the stress field corresponding to $\underline{d}^s(\underline{x})$ and $\underline{d}^a(\underline{x})$ is eventually obtained,

$$\begin{aligned} \sigma_{xx}^s = K \frac{1}{\sqrt{2\pi r}} \frac{\nu - 1}{2\nu - 1} & ((-3(\nu - 1)\alpha - 2\beta + 2\nu\beta - \nu\gamma + 2\nu\delta) \sin(\vartheta/2) + \\ & + ((\nu - 1)\alpha - \nu\gamma) \sin(5\vartheta/2)), \end{aligned} \quad (4.31)$$

$$\begin{aligned} \sigma_{yy}^s = K \frac{1}{\sqrt{2\pi r}} \frac{\nu - 1}{2\nu - 1} & ((-\gamma + \nu(3\alpha - 2\beta + \gamma - 2\delta) + 2\delta) \sin(\vartheta/2) + \\ & - (\nu(\alpha - \gamma) + \gamma) \sin(5\vartheta/2)), \end{aligned} \quad (4.32)$$

$$\tau_{xy}^s = K \frac{1}{\sqrt{2\pi r}} (1 - \nu) \cos(\vartheta/2) (\alpha + \beta + \gamma + \delta - (\alpha - \gamma)(\cos(\vartheta) - \cos(2\vartheta))), \quad (4.33)$$

$$\sigma_{zz}^s = \nu(\sigma_{xx}^s + \sigma_{yy}^s), \quad (4.34)$$

$$\begin{aligned} \sigma_{xx}^a = K \frac{1}{\sqrt{2\pi r}} \frac{2\nu - 2}{2\nu - 1} & \cos(\vartheta/2) (\epsilon - \nu\epsilon + \zeta + \nu(-\zeta + \eta + \lambda) + \\ & - ((\nu - 1)\epsilon + \nu\eta)(\cos(\vartheta) - \cos(2\vartheta))), \end{aligned} \quad (4.35)$$

$$\sigma_{yy}^a = K \frac{1}{\sqrt{2\pi r}} \frac{\nu - 1}{2\nu - 1} ((\eta + \nu(3\epsilon + 2\zeta - \eta - 2\lambda) + 2\lambda) \cos(\vartheta/2) + (\eta - \nu(\epsilon + \eta)) \cos(5\vartheta/2)), \quad (4.36)$$

$$\tau_{xy}^a = K \frac{1}{\sqrt{2\pi r}} (\nu - 1)(\epsilon - \zeta - \eta + \lambda + (\epsilon + \eta)(\cos(\vartheta) + \cos(2\vartheta))) \sin(\vartheta/2), \quad (4.37)$$

$$\sigma_{zz}^a = \nu(\sigma_{xx}^a + \sigma_{yy}^a). \quad (4.38)$$

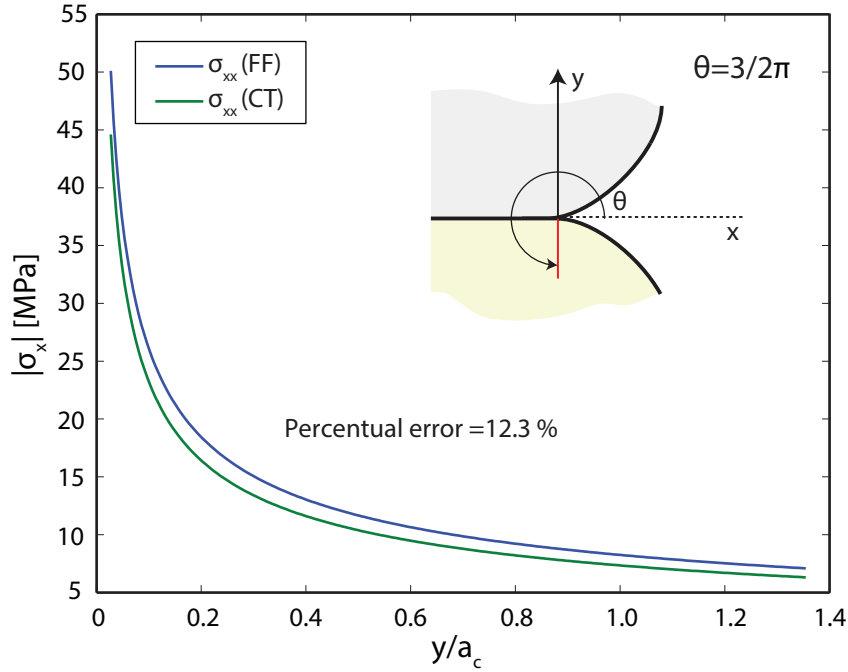


Figure 4.6: Comparison between the evolution of $\sigma_{xx,FF}$ at the contact front and $\sigma_{xx,CT}$ at the crack tip (FF: fretting fatigue, CT: crack tip).

The derivation of the stress field, corresponding to \underline{d}^s and \underline{d}^a , permits to compare them with the corresponding fields produced by a mode I and mode II loading at the crack tip. The comparison is carried out, for a given value of ϑ . The value chosen corresponds to the normal to the specimen surface (Figure 4.6) that is the zone where crack initiation is usually experienced.

A percentage error is defined as follows,

$$\xi_{\sigma_{ij}}^s = \frac{|\sigma_{ij,FF}^s - \sigma_{ij,CT}^s|}{\sigma_{ij,CT}^s}, \quad \xi_{\sigma_{ij}}^a = \frac{|\sigma_{ij,FF}^a - \sigma_{ij,CT}^a|}{\sigma_{ij,CT}^a}, \quad (4.39)$$

where $\sigma_{ij,FF}$ is the stress component at the contact edge, while $\sigma_{ij,CT}$ is the stress component at the crack tip.

In Table 4.2 the relative percentage error corresponding to the different components of the stress tensor are reported.

In Figure 4.6 a visual comparison between σ_{xx} at the crack tip and at the contact tip is displayed. The difference observed remains quite small for all the components.

	$\xi_{\sigma_{xx}}$	$\xi_{\sigma_{yy}}$	$\xi_{\sigma_{zz}}$	$\xi_{\tau_{xy}}$
Symmetric field	12.3	6.1	2.7	7.6
Antisymmetric field	16.8	15.1	10.0	15.5

Table 4.2: Percentage relative error between the stress tensor at the contact edge and at the crack tip for $\vartheta = 3/2\pi$.

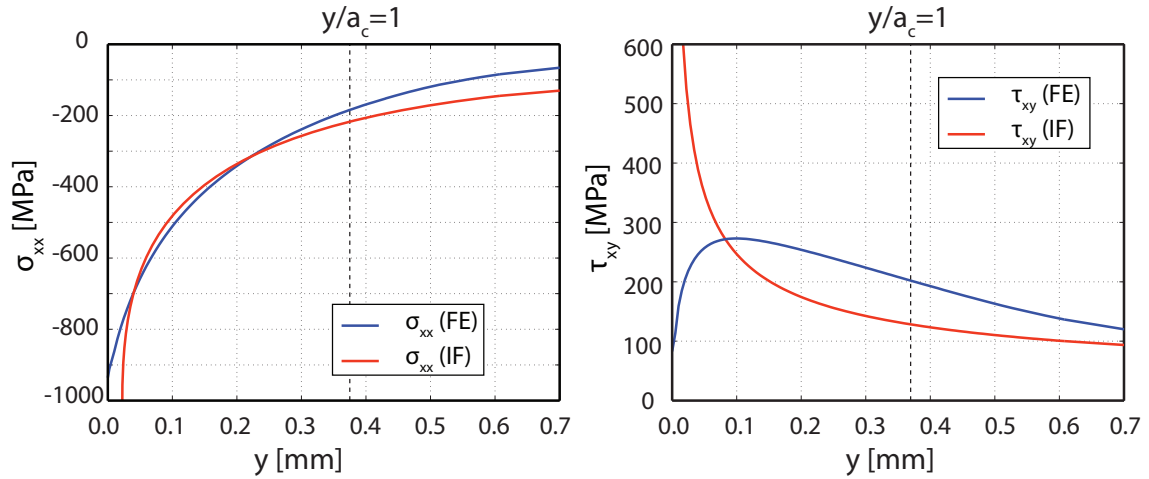


Figure 4.7: Stress field re-construction by using the nonlocal intensity factors (FE parameters: plain-fretting analysis, Pad radius = 20 mm, friction coefficient = 1.0, Young's modulus = 119 400 MPa, Poisson's ratio = 0.3, $P = 347 \text{ N mm}^{-1}$ and $Q^* = 237 \text{ N mm}^{-1}$), IF: intensity factors, FE: finite elements.

The evolution of the stress field around the contact edge, during a fretting-fatigue simulation as a function of the macroscopic loads applied, can be described by superposing the effect of the symmetric and antisymmetric field as follows,

$$\sigma_{ij}(\underline{x}, t) = I^a(t)\sigma_{ij}^a(\underline{x}) + I^s\sigma_{ij}^s(\underline{x}). \quad (4.40)$$

In Figure 4.7 the stress tensor obtained by applying the equation above, has been compared to the output from a FE computation. With respect to σ_{xx} a good match

is observed close to the contact surface. Concerning τ_{xy} , instead, Equation 4.40 overestimates its value. This is due to the fact that, by describing the stress field corresponding to \underline{d}^s and \underline{d}^a with a crack analogue formalism, a stress singularity is introduced for r equal to zero.

To sum up, starting with the computation of the velocity field close to the contact edge generated by fretting-fatigue it is possible to extract nonlocal intensity factors, univocally characterizing the mechanical field. In this section, the steps in order to compute the stress field associated to the nonlocal intensity factors have been detailed.

4.2.4 Application of the multiaxial fatigue criteria

The relation between the nonlocal intensity factors and the stress field, as a function of the macroscopic loads applied to the structure, has been determined. Here, this knowledge is exploited to adapt several common multiaxial fatigue criteria to the formalism developed. In regards to crack initiation, experimental evidence shows that a big role is played by the shear stress that is at the origin of the slip band formation along preferential slip planes and by the normal stress with respect to these planes that promotes the crack opening. These two mechanisms are the basis for several crack initiation prediction criteria, that, in the more general form, can be described as follows,

$$\alpha\tau_e + \beta P < \lambda, \quad (4.41)$$

where τ_e is a quantity that takes into account the effective shear stress playing the role of initiating the crack. Since the stress tensor evolution can be nonproportional, depending on the criterion chosen, different formulations to compute τ_e are presented. P is the term that quantifies the crack opening mechanism and once again, depending on the criterion chosen, it can be equal to the maximum value of the hydrostatic pressure over the cycles or to the normal stress corresponding to the plane maximizing τ_e , etc.

α and β are material factors defining which of the two mechanisms prevails. They are usually obtained with simple fatigue tests such as, push-pull and pure torsion. λ , as well, is a material parameter and the domain respecting the inequality presented in Equation 4.41 represents a safe crack initiation zone in a $(\tau_e - P)$ reference system.

Since in the previous section the stress tensor around the contact edge is obtained as a function of the nonlocal intensity factors, Equation 4.41 can be rewritten as follows,

$$\alpha\tau_e(I_{max}^a, I^s, \sigma_B^{max}) + \beta P(I_{max}^a, I^s, \sigma_B^{max}) < \lambda, \quad (4.42)$$

so that, by computing the different terms as a function of I^s , I^a and σ_B the following equation is obtained,

$$f(I_{max}^a, I^s, \sigma_B^{max}) < \lambda. \quad (4.43)$$

This permits to translate the no-crack initiation domain from the $(\tau_e - P)$ reference system to the $(I_{max}^a, I^s, \sigma_B^{max})$ one, allowing to apply the multiaxial criterion chosen directly on the nonlocal crack initiation map developed in Chapter 3.

The details of this procedure are described in the following sections where the Crossland criterion, [Crossland, 1956] and the modified Wöhler curve method, [Araújo et al., 2007], are used to predict the crack initiation threshold in nonlocal coordinates. The plain fretting case is handled at first and then the approach is generalized to fretting-fatigue.

4.2.4.1 Modified Wöhler curve method - plain fretting

The use of the Modified Wöhler Curve Method (MWCM) in conjunction with the Theory of Critical Distances (TCD) relies on the assumption that all the physical mechanisms leading to crack initiation can be confined within the so-called structural volume. Furthermore the size of this volume is assumed not to be dependent on either the stress concentration feature weakening the component or the complexity of the stress field damaging the fatigue process zone and it can be defined as follows,

$$L = \frac{1}{\pi} \left(\frac{\Delta K_{th}}{\Delta \sigma_{-1}} \right)^2. \quad (4.44)$$

The idea behind this approach is to consider that, if Kitagawa-Takahashi curve is approximated with two straight asymptotic lines (Figure 1.25), cracks can grow up to a length equal to $L/2$, without reducing the nominal fatigue limit of the material.

The principal mechanisms leading to crack initiation for the modified Wöhler curve method are τ_a , the equivalent shear stress, and the ratio between σ_N , the normal stress on the critical plane, and τ_a

$$\tau_a(\varphi^*, \alpha^*, l) + \kappa \frac{\sigma_{N,max}(\varphi^*, \alpha^*, l)}{\tau_a(\varphi^*, \alpha^*, l)} < \lambda, \quad (4.45)$$

where k and λ are material parameters calibrated using, for instance, push-pull and torsional fatigue limits for a load ratio, R , equals to -1,

$$\kappa = \tau_{-1} - \frac{\sigma_{-1}}{2} \quad \lambda = \tau_{-1}, \quad (4.46)$$

and l is the distance from the surface where the stress tensor is computed (Figure 4.8). The critical plane is determined as follows:

$$(\varphi^*, \alpha^*) : \max_{(\varphi, \alpha, l)} [\tau_a(\varphi, \alpha, l)]. \quad (4.47)$$

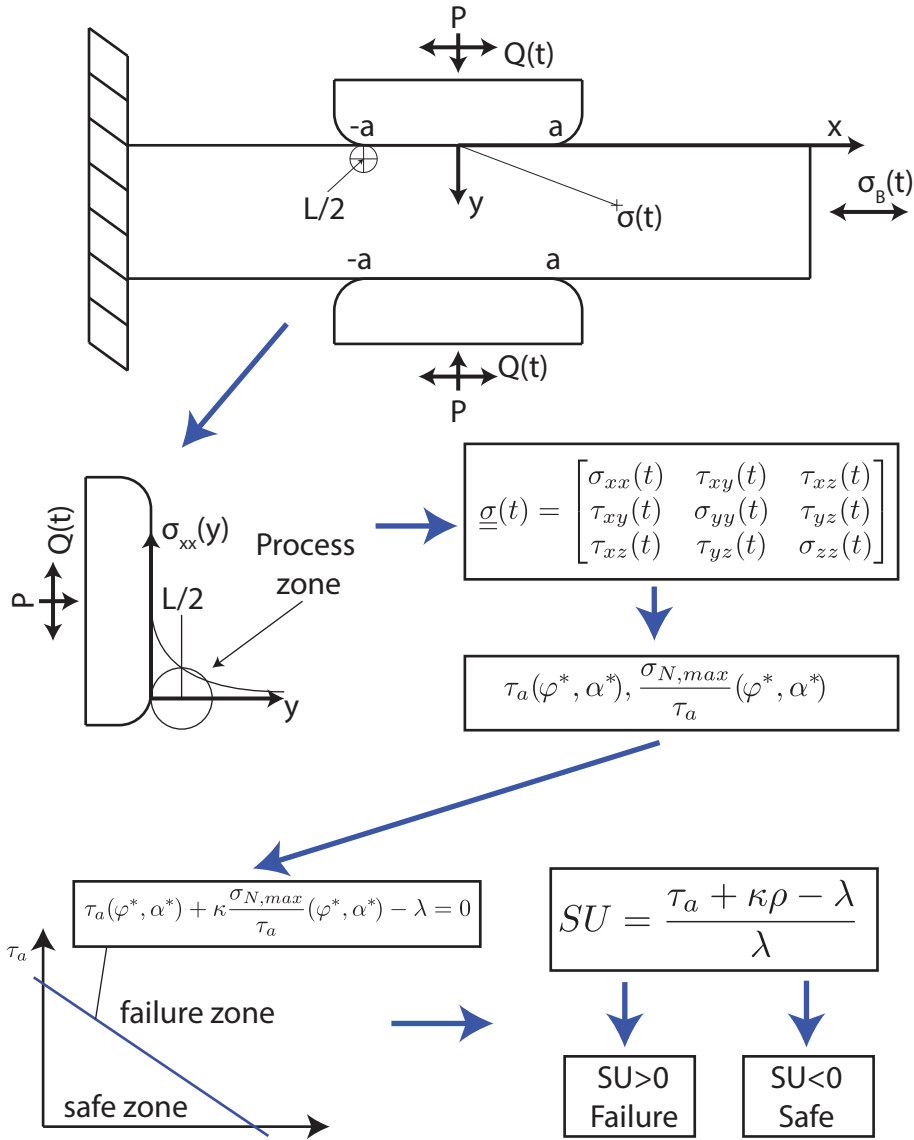


Figure 4.8: Schematic view of the different steps in the application of the modified Wöhler Curve Method, [Araújo et al., 2007].

Using the above equation a “damage” index, D , can be defined:

$$D(l) = \tau_a(\varphi^*, \alpha^*, l) + \kappa \frac{\sigma_{N,max}(\varphi^*, \alpha^*)}{\tau_a(\varphi^*, \alpha^*, l)} - \lambda. \quad (4.48)$$

If D at $l = L/2$ is negative, this criterion predicts no crack initiation, or, if an initiation occurs, the crack size will not exceed the short crack regime.

To compute the different terms in Equation 4.45, for a given material point in the specimen, it is convenient to define a plane Δ , passing through the point under consideration, identified by the normal, \underline{n} . The normal stress with respect to Δ will

be written as follows,

$$\underline{\sigma}_N(t) = (\underline{n} \cdot \underline{\sigma}(t) \cdot \underline{n})\underline{n}, \quad (4.49)$$

and its magnitude is equal to:

$$\sigma_N(t) = (\underline{n} \cdot \underline{\sigma}(t) \cdot \underline{n}). \quad (4.50)$$

Its amplitude, $\sigma_{N,a}$, and mean value, $\sigma_{N,m}$, are easily computed, as well as, its maximum value with respect to a given plane,

$$\sigma_{N,a} = \frac{1}{2} \left(\max_{t \in T} \sigma_N(t) - \min_{t \in T} \sigma_N(t) \right), \quad (4.51)$$

$$\sigma_{N,m} = \frac{1}{2} \left(\max_{t \in T} \sigma_N(t) + \min_{t \in T} \sigma_N(t) \right), \quad (4.52)$$

$$\sigma_{N,max} = \sigma_{N,a} + \sigma_{N,m}. \quad (4.53)$$

To compute the equivalent shear stress, the procedure is a little bit more complicated if the loading are not proportional since $\underline{\tau}$, the projection of $\underline{\sigma} \cdot \underline{n}$ over the plane Δ , acts tangentially to the plane but non necessarily always in the same direction, (Figure 4.9a),

$$\underline{\tau}(t) = \underline{\sigma}(t) \cdot \underline{n} - (\underline{n} \cdot \underline{\sigma}(t) \cdot \underline{n})\underline{n}. \quad (4.54)$$

Here a simple method to compute τ_a , proposed by Araújo and his colleagues, [Araújo et al., 2011], is employed. They claim that the equivalent shear stress amplitude, which correctly characterizes the fatigue damage under multiaxial loading, is given by the Maximum Rectangular Hull (MRH) of the shear stress vector path, ψ , in a material plane Δ (Figure 4.9b) as follows,

$$a_i(\phi) = \frac{1}{2} \left(\max_{t \in T} \tau_i(\phi, t) - \min_{t \in T} \tau_i(\phi, t) \right) \quad i = 1, 2. \quad (4.55)$$

For each rectangular hull defined by the angle, ϕ , the shear stress amplitude is computed,

$$\tau_a(\phi) = \sqrt{a_1^2(\phi) + a_2^2(\phi)}. \quad (4.56)$$

The equivalent shear stress is the one corresponding to the angle, ϕ , maximizing the above equation,

$$\tau_a = \max_{\phi} \sqrt{a_1^2(\phi) + a_2^2(\phi)}. \quad (4.57)$$

As shown in the previous section, where the stress field arising around the contact tip is obtained, in plain fretting the stress tensor depends only on I^a and I^s ,

$$\underline{\sigma}(t) = f(I^a, I^s). \quad (4.58)$$

This represents the input in the application of the modified Wöhler curve method. For a sinusoidal fretting load, $Q = Q^* \sin(\omega t)$,

$$I^a(t) = I_{max}^a \sin(\omega t), \quad (4.59)$$

as it is shown in Chapter 2. The tensor, S , will be written as follows,

$$\sigma_{ij}(\underline{x}, t) = -(I_{max}^a \sin(\omega t) \sigma_{ij}^a(\underline{x}) + I^s \sigma_{ij}^s(\underline{x})), \quad (4.60)$$

where the minus sign is due to the convention used in the normalization of the reference fields. Furthermore, the zone where the criterion is applied is along a perpendicular line with respect to the specimen surface starting at the contact tip as shown in Figure 4.6. In polar coordinates,

$$\sigma_{ij}(3\pi/2, r, t) = -(I_{max}^a \sin(\omega t) \sigma_{ij}^a(3\pi/2, r) + I^s \sigma_{ij}^s(3\pi/2, r)). \quad (4.61)$$

Since the comparison between the stress field at the crack tip and the one at the contact tip performed in Section 4.2.3 has shown that the differences are small, here the following approximation is done,

$$\sigma_{ij}^a = \sigma_{ij}^{II}, \quad \sigma_{ij}^s = \sigma_{ij}^I, \quad (4.62)$$

which allows to obtain equations, describing the stress tensor, that are easier to manipulate.

By replacing Equations 4.9-4.12 in Equation 4.61 the stress tensor is defined as follows,

$$\underline{\sigma}(t) = -\frac{K}{4\sqrt{\pi r}} \begin{bmatrix} I^s + 3I_{max}^a \sin(\omega t) & -(I^s + I_{max}^a \sin(\omega t)) & 0 \\ -(I^s + I_{max}^a \sin(\omega t)) & 3I^s + I_{max}^a \sin(\omega t) & 0 \\ 0 & 0 & 4(I^s + I_{max}^a \sin(\omega t)) \end{bmatrix}. \quad (4.63)$$

To compute the equivalent tangential stress, let us define the frame $O.uvn$ (Figure 4.9a), where \underline{n} is the axis directed along the normal to the plane Δ and $(\underline{u}, \underline{v})$ are the axes lying on it. Their coordinates with respect to the $O.xyz$ reference system are the following ones:

$$\underline{n} = \begin{bmatrix} n_x \\ n_y \\ n_z \end{bmatrix} = \begin{bmatrix} \cos(\alpha) \sin(\varphi) \\ \sin(\alpha) \\ \cos(\alpha) \cos(\varphi) \end{bmatrix} \quad \underline{v} = \begin{bmatrix} v_x \\ v_y \\ v_z \end{bmatrix} = \begin{bmatrix} -\sin(\alpha) \sin(\varphi) \\ \cos(\alpha) \\ -\sin(\alpha) \cos(\varphi) \end{bmatrix} \quad \underline{u} = \begin{bmatrix} u_x \\ u_y \\ u_z \end{bmatrix} = \begin{bmatrix} \cos(\varphi) \\ 0 \\ -\sin(\varphi) \end{bmatrix}. \quad (4.64)$$

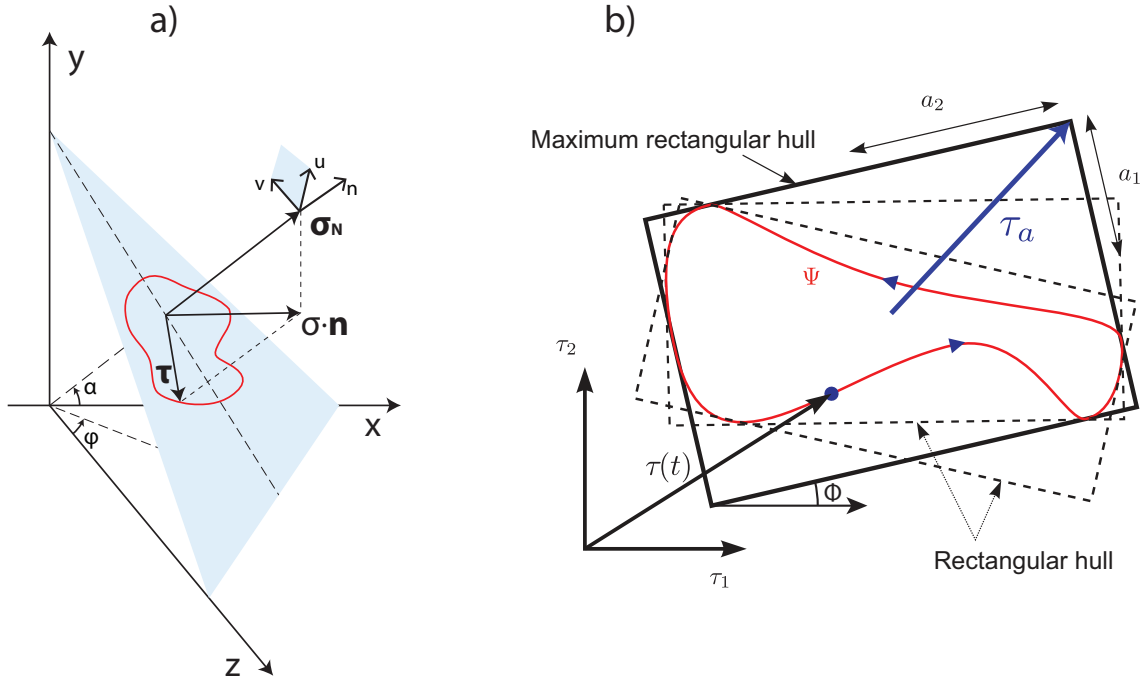


Figure 4.9: (a) Material plane and normal and tangential components of the stress tensor projection; (b) rectangular hull with orientation bounding the shear stress path ψ , [Araújo et al., 2011].

By replacing $\underline{\sigma}$ defined in Equation 4.63 in Equation 4.54, $\underline{\tau}$ is computed and, by projecting it on \underline{u} and \underline{v} , the following result is obtained,

$$\tau_u = \underline{u} \cdot \underline{\tau} \Leftrightarrow \tau_u = u_x \tau_x + u_y \tau_y + u_z \tau_z = a(\alpha, \varphi) + b(\alpha, \varphi) \sin(\omega t), \quad (4.65)$$

$$\tau_v = \underline{v} \cdot \underline{\tau} \Leftrightarrow \tau_v = v_x \tau_x + v_y \tau_y + v_z \tau_z = c(\alpha, \varphi) + d(\alpha, \varphi) \sin(\omega t), \quad (4.66)$$

where a, b, c, d are equal to,

$$a = K \frac{I^s}{4\sqrt{\pi r}} \cos(\varphi) 4\sqrt{\pi r} (\sin(\alpha) + (4\nu - 1) \cos(\alpha) \sin(\varphi)), \quad (4.67)$$

$$b = K \frac{I_{max}^a}{4\sqrt{\pi r}} \cos(\varphi) 4\sqrt{\pi r} (\sin(\alpha) + (4\nu - 3) \cos(\alpha) \sin(\varphi)), \quad (4.68)$$

$$c = K \frac{I^s}{16\sqrt{\pi r}} ((-5 + 4\nu + (4\nu - 1) \cos(2\varphi)) \sin(2\alpha) + 4 \cos(2\alpha) \sin(\varphi)), \quad (4.69)$$

$$d = K \frac{I_{max}^a}{16\sqrt{\pi r}} ((1 + 4\nu + (4\nu - 3) \cos(2\varphi)) \sin(2\alpha) + 4 \cos(2\alpha) \sin(\varphi)). \quad (4.70)$$

Equations 4.65-4.66 are the parametric equations of the curve Ψ described by the tip of the shear stress vector $\underline{\tau}$ on the plane Δ during a loading cycle. The curve Ψ is a line with a slope equal to d/b intercepting the y axis in $y = c - d(a/b)$.

The maximum rectangular hull is easy to compute being Ψ a line,

$$\tau_1 = K \frac{I_{max}^a}{4\sqrt{\pi r}} \cos(\varphi) (\sin(\alpha) + (-3 + 4\nu) \cos(\alpha) \sin(\varphi)), \quad (4.71)$$

$$\tau_2 = K \frac{I_{max}^a}{16\sqrt{\pi r}} ((1 + 4\nu + (-3 + 4\nu) \cos(2\varphi)) \sin(2\alpha) + 4 \cos(2\alpha) \sin(\varphi)), \quad (4.72)$$

$$\tau_a(\alpha, \varphi) = \sqrt{\tau_1^2 + \tau_2^2}. \quad (4.73)$$

The plane Δ is computed by finding the value of α and φ , which maximize Equation 4.73,

$$\varphi^* = \frac{\pi}{2}, \quad \alpha^* = \frac{9}{8}\pi. \quad (4.74)$$

The values found seem to be reasonable since the computed value of α^* describes a crack that initiates in a direction inclined of 22.5 degrees towards the interior of the contact which is coherent with what has been observed experimentally by Proudhon, [Proudhon et al., 2006], (Figure 1.20).

The maximum equivalent shear stress is eventually computed as well as the corresponding normal stress,

$$\tau_a(\alpha^*, \psi^*) = \frac{I_{max}^a K}{2\sqrt{2\pi r}}, \quad (4.75)$$

$$\sigma_{N,max}(\alpha^*, \psi^*) = K \frac{(-2 + \sqrt{2})I^s + 2I_{max}^a}{4\sqrt{\pi r}}. \quad (4.76)$$

The crack initiation frontier, outcome of the application of modified Wöhler curve method, is described by the following relation,

$$\frac{I_{max}^a K}{2\sqrt{2\pi r}} + \kappa \left(K \frac{(-2 + \sqrt{2})I^s + 2I_{max}^a}{4\sqrt{\pi r}} \right) = \lambda. \quad (4.77)$$

The frontier depends on I_{max}^a , I^s and r . By exploiting the critical distance approach, r is replaced by $L/2$ (Equation 4.44).

To apply this approach to the experimental data an assumption is made; it is considered that the normal stress does not play an important role in the crack initiation which seems to be confirmed by the fact that the initiation frontiers in nonlocal coordinates show little dependency on the value of pressure applied. In other words, κ , is considered to be equal to zero and therefore, by solving Equation 4.77 with respect to I_{max}^a , the following relation is obtained:

$$I_{max}^a = 2 \left(\frac{\tau_{-1}}{\sigma_{-1}} \right) \frac{\Delta K_{th}}{K}. \quad (4.78)$$

To remember that K is equal to $1 \text{ MPa}\sqrt{\text{m}}$. This result describes a vertical frontiers which is used to predict the experimental crack initiation threshold in nonlocal coordinates.

Figures 4.10-4.12, display how this approach performs in predicting the crack initiation threshold. It is possible to see that good results are obtained in particular for Inconel 718 and Ti-6Al-4V, while for the steel alloy the frontier is a little bit too conservative. Overall, the outcomes are satisfying because they allow to have a good idea of where to place the frontier without the need to perform experimental analysis, since all the material data used in Equation 4.78, are already available in the literature or can be easily obtained by means of classic fatigue tests.

On the other hand, if experimental tests are necessary, for instance due to certification procedures, the analytical expression of the frontier can be used to wisely plan the test campaign knowing where the initiation threshold will be placed.

To sum up, the coupling of the nonlocal technique to describe the crack initiation map with the modified Wöhler curve method allows to get rid of the gradient effect and at the same time permits to predict the initiation frontier with acceptable accuracy without the need to perform experimental tests.

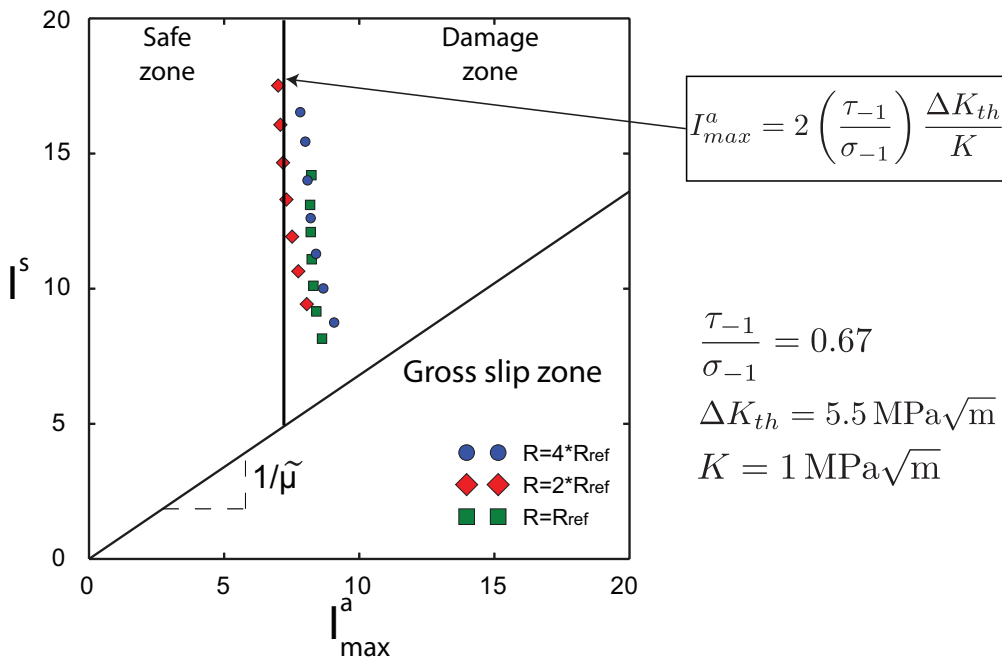


Figure 4.10: Crack initiation frontier obtained by applying the modified Wöhler curve method to the nonlocal crack initiation map for Ti-6Al-4V.

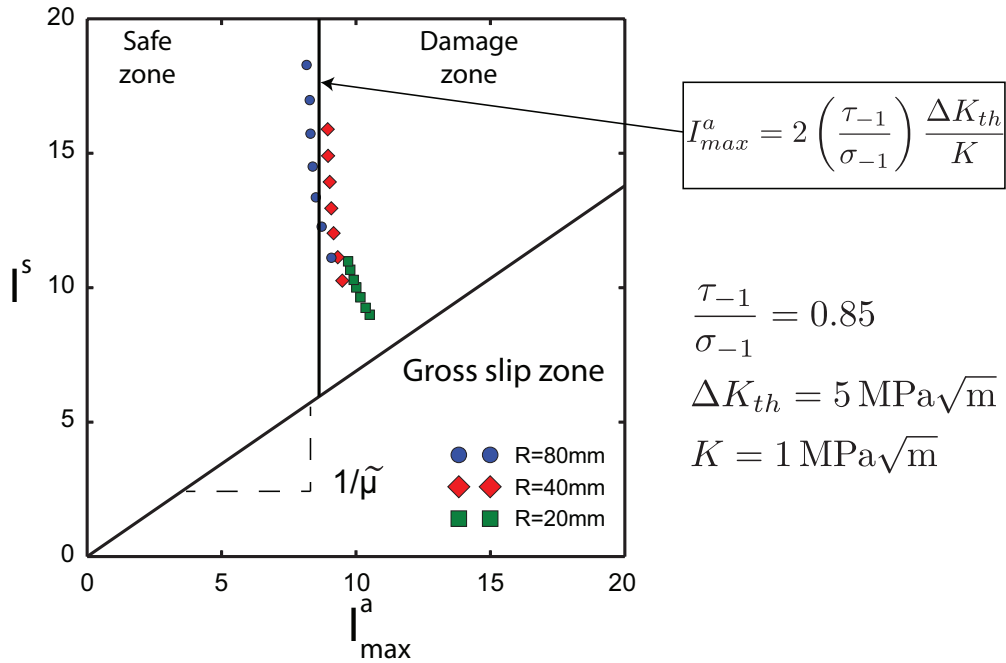


Figure 4.11: Crack initiation frontier obtained by applying the modified Wöhler curve method to the nonlocal crack initiation map for Inconel 718.

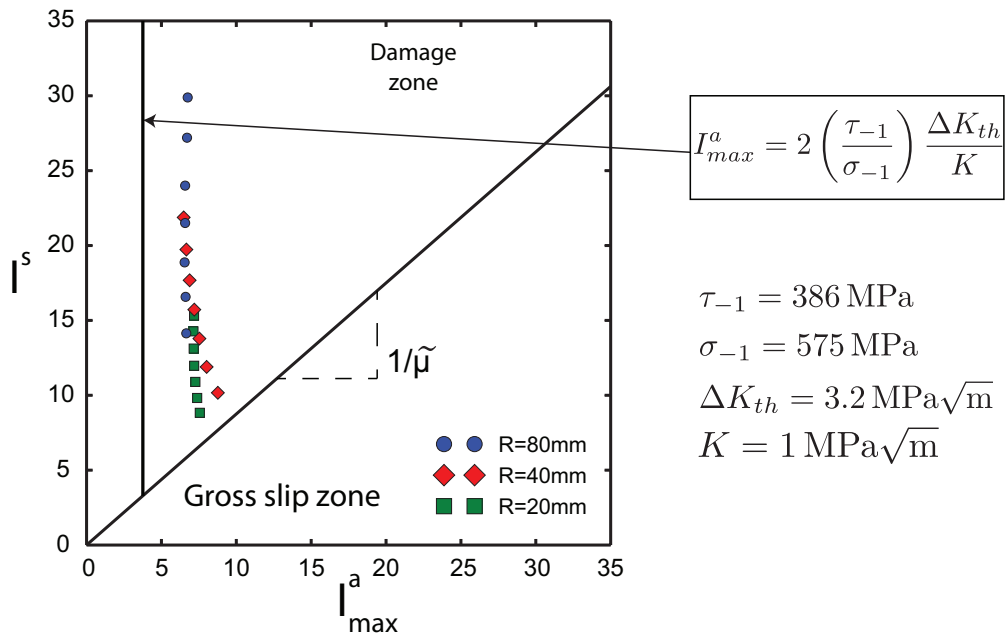


Figure 4.12: Crack initiation frontier obtained by applying the modified Wöhler curve method to the nonlocal crack initiation map for 35NiCrMo16 low-alloyed steel.

4.2.4.2 Crossland criterion - plain fretting

The procedure described in the previous section, which allows one to apply the modified Wöhler curve method to the nonlocal description of crack initiation, is repeated using the Crossland criterion, [Crossland, 1956]. Crossland proposed that the second invariant of the deviatoric stress tensor and the hydrostatic pressure are the variables governing the crack initiation problem,

$$\sqrt{J_{2,a}} + \kappa P_{H,max} < \lambda, \quad (4.79)$$

where κ and λ are defined as follows,

$$\kappa = 3 \frac{\tau_{-1}}{\sigma_{-1}} - \sqrt{3}, \quad \lambda = \tau_{-1}. \quad (4.80)$$

The stress tensor as a function of the nonlocal stress intensity factors has been detailed in Equation 4.63. Here, this knowledge is used to compute the different terms of the Crossland criterion.

Concerning the second invariant of the deviatoric stress tensors, it is defined as follows,

$$\sqrt{J_{2,a}} = \frac{1}{2} \max_{t_0 \in T} \left(\max_{t \in T} \left[\frac{1}{2} (\underline{\underline{S}}(t) - \underline{\underline{S}}(t_0)) : (\underline{\underline{S}}(t) - \underline{\underline{S}}(t_0)) \right]^{(1/2)} \right), \quad (4.81)$$

where $\underline{\underline{S}}$ is the deviatoric part of the stress tensor, $\underline{\underline{\sigma}}(t)$. By performing the computations, the following expression is obtained,

$$J_{2,a} = \frac{5I_{max}^a}{384\pi r} K^2 (16I^s(1-2\nu)^2 + 3I_{max}^a(5+8(\nu-1)\nu)). \quad (4.82)$$

With regard to the hydrostatic pressure, it is computed as follows,

$$P_{H,max} = \max_{0 \leq t \leq T} \left(\frac{1}{3} \text{Tr} [\underline{\underline{\sigma}}(t)] \right) = \frac{(I_{max}^a - I^s)}{3\sqrt{\pi r}} K(1+\nu). \quad (4.83)$$

By replacing Equations 4.82 and 4.83 in Equation 4.79, the following relation is obtained,

$$\left[\frac{5I_{max}^a}{384\pi r} K^2 (16I^s(1-2\nu)^2 + 3I_{max}^a(5+8(\nu-1)\nu)) \right]^{1/2} + \kappa \frac{(I_{max}^a - I^s)}{3\sqrt{\pi r}} K(1+\nu) \leq \lambda. \quad (4.84)$$

For the values of I_{max}^a and I^s coming from the experimental tests, the hydrostatic pressure is negative. For this reason, it is assumed that this term can be neglected,

$$\left[\frac{5I_{max}^a}{384\pi r} K^2 (16I^s(1-2\nu)^2 + 3I_{max}^a(5+8(\nu-1)\nu)) \right]^{1/2} = \tau_{-1}. \quad (4.85)$$

The above equation describes the crack initiation frontier, outcome of the application of the Croosland criterion.

This frontier depends on I_{max}^a , I^s and r . This last value has been calibrated thanks to the experimental data. In this case therefore some of them are needed for the calibration process. Nevertheless an interesting trend is observed. The value of r assuring the best fit between numerical and experimental data, is constant for the three different materials studied as shown in Table 4.3.

	Modified Wöhler curve method	Crossland criterion
	$r = \frac{1}{2\pi} \left(\frac{\Delta K_{th}}{\Delta \sigma_{-1}} \right)^2$	r (calibrated)
Ti-6Al-4V	$10 \cdot l_{ref}$	22 μm
35NiCrMo16 low-alloyed steel	4.93 μm	22 μm
Inconel 718	14.17 μm	22 μm

Table 4.3: Calibration values used for the modified Wöhler curve method and the Crossland criterion, l_{ref} : normalization length for confidentiality issue.

Figures 4.13, 4.14 and 4.15 show how this approach performs in predicting crack threshold. The results are encouraging, confirming that the coupling between the Crossland criterion and the nonlocal description of crack initiation can be used to predict the crack initiation frontier.

Having said that, it is worth saying that the calibration distances obtained do not overcome 22 μm . In this range, the reconstruction of the stress tensor evolution using as input the nonlocal intensity factors leads to an overestimation of the shear stress as presented in Figure 4.7, which in turns influences the crack initiation frontier computation. This aspect is clearly a point where further research is needed.

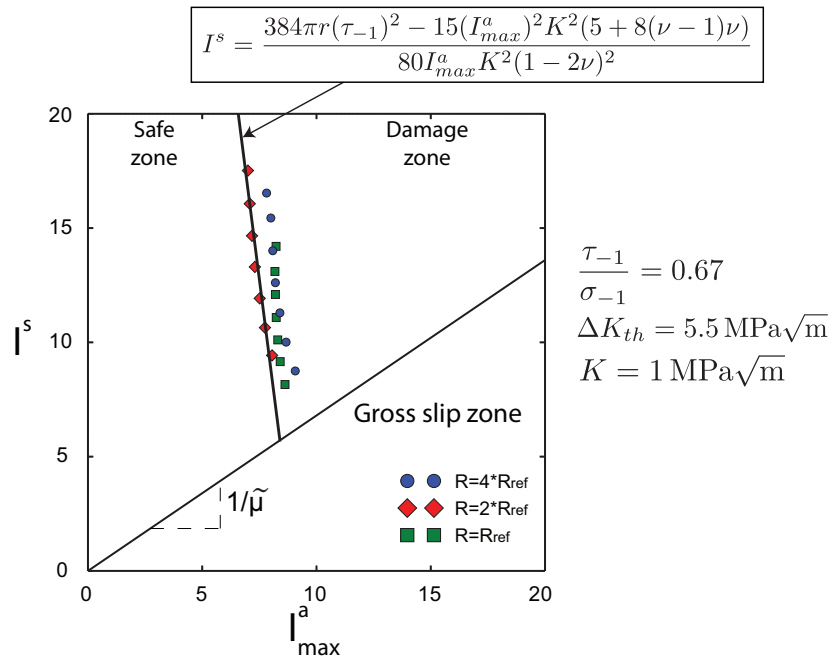


Figure 4.13: Crack initiation frontier obtained by applying the Crossland criterion to the nonlocal crack initiation map for Ti-6Al-4V.

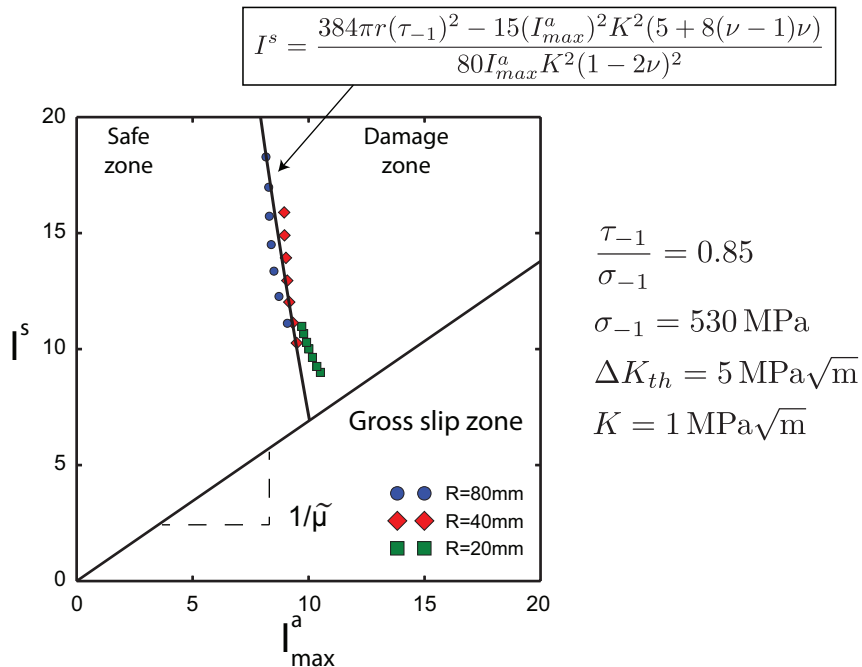


Figure 4.14: Crack initiation frontier obtained by applying the Crossland criterion to the nonlocal crack initiation map for Inconel 718.

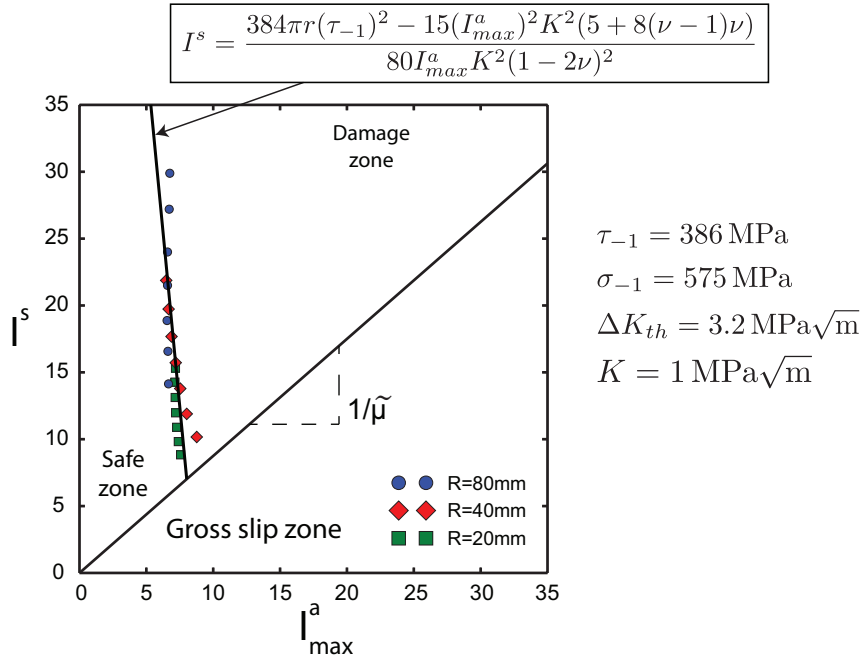


Figure 4.15: Crack initiation frontier obtained by applying the Crossland criterion to the nonlocal crack initiation map for 35NiCrMo16 low-alloyed steel.

4.2.4.3 Critical distance approach - fretting-fatigue

Experimental evidence shows that the introduction of a cyclic bulk load, σ_B , in phase with the fretting force, Q , has a negative impact on the crack initiation frontiers, (Figures 3.3b, 3.5b).

On the other hand, in the previous sections two multiaxial criteria are coupled with the nonlocal description of the crack initiation map, showing that it is possible to predict accurately the crack initiation frontier in plain fretting. The objective is therefore, to generalize this approach to fretting-fatigue.

For this purpose the relation between I_{max}^a and σ_B^{max} is determined. It is assumed that it is possible to decouple the plain fretting loading from the application of the cyclic bulk force, as it is shown in Figure 4.16. The introduction of σ_B in a situation where the contact between the pad and the specimen is assured by the application of the normal load, P , generates an antisymmetric velocity field in the proximity of the contact edges,

$$I^a(Q, \sigma_B) = I^a(Q) + I^a(\sigma_B). \quad (4.86)$$

By looking at the equation above, the first term, $I^a(Q)$, corresponds to the plain fretting situation. Concerning the second term, $I^a(\sigma_B)$, to investigate its evolution as a function of σ_B , it is possible to apply the extraction algorithm presented in Chapter 2 to the situation described in Figure 4.16b.

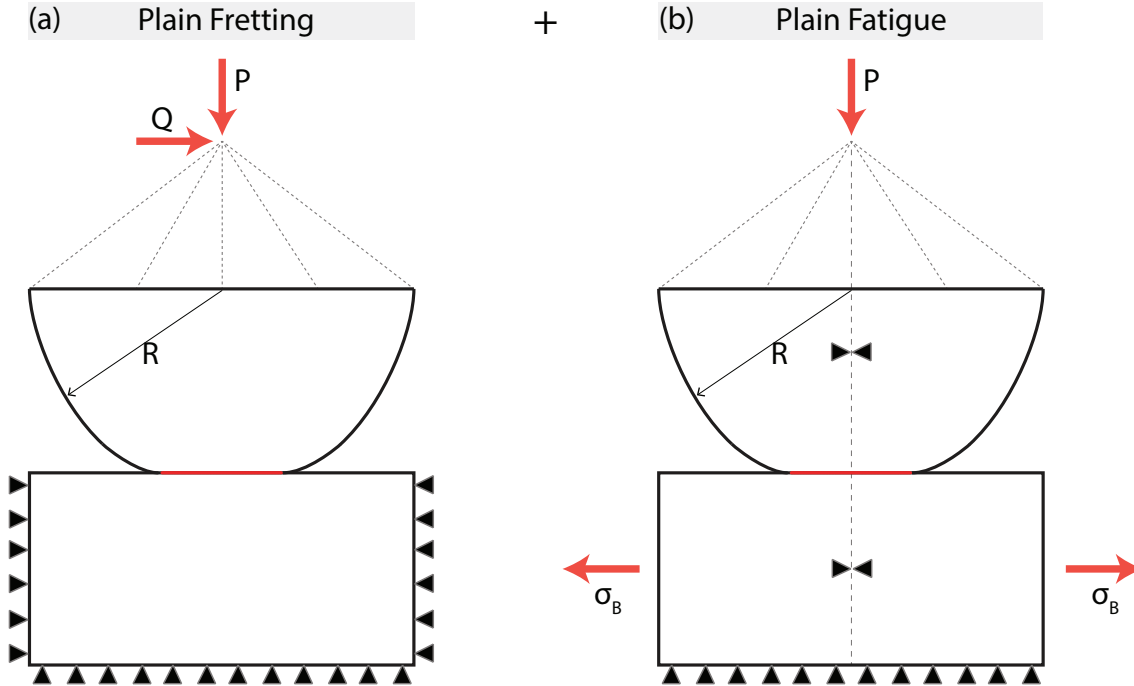


Figure 4.16: Schematic representation of the assumption made to decouple the effect of the plain fretting loading to the cyclic bulk force.

The result of the application of this procedure, shown in Figure 4.17a, describes a linear relation between $I_{max}^a(\sigma_B)$ and σ_B^{max} . As a consequence, Equation 4.86 can be written as follows,

$$I_{max}^a(Q, \sigma_B) = I_{max}^a(Q) - \chi \sigma_B^{max}, \quad (4.87)$$

where $I_{max}^a(Q)$ is the value of I_{max}^a in plain fretting. The minus sign reflects the fact that the velocity field computed by decoupling the fretting and fatigue loading has an opposite direction with respect to the case where the two effects are coupled.

By repeating exactly the same computations already performed in Section 4.2.4.1, exploiting the relation described by Equation 4.86, the following crack initiation frontier definition is obtained:

$$I_{max}^a = 2 \left(\frac{\tau_{-1}}{\sigma_{-1}} \right)^2 \frac{\Delta K_{th}}{K} - \chi \sigma_B^{max}. \quad (4.88)$$

The value of χ is equal to 0.0052 MPa^{-1} and it is computed through FE computations (Figure 4.17).

The above equation describes a surface in a tridimensional space $(I_{max}^a, I^s, \sigma_B^{max})$ which divides the non-initiation zone from the damage one.

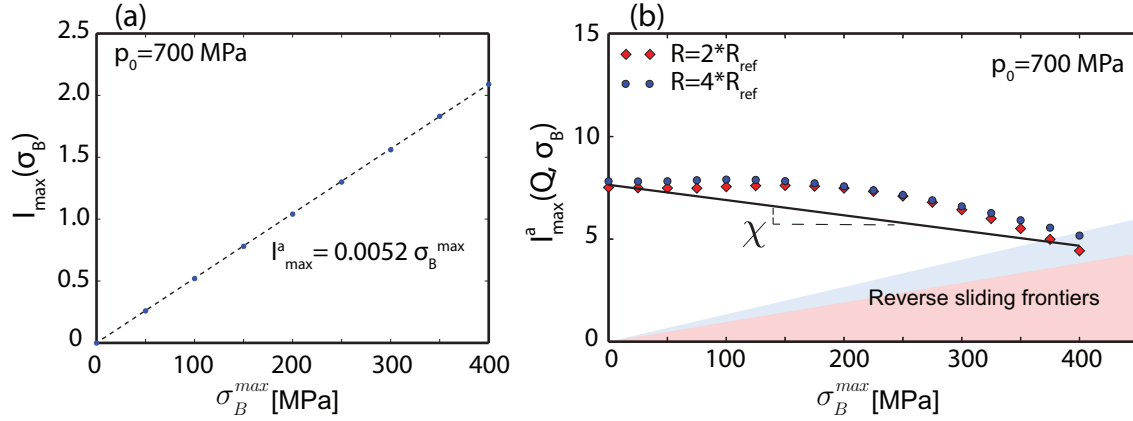


Figure 4.17: (a) Evolution of I_{max}^a as a function of σ_B in a situation where no tangential force, Q , is applied as described in Figure 4.16b; (b) Prediction of the experimental data by applying the assumption presented in Equation 4.86.

4.2.4.4 Crossland criterion - fretting-fatigue

The crack initiation frontier equation obtained by applying the Crossland criterion to plain fretting nonlocal map, is extended to fretting-fatigue following the same approach detailed in the previous section. It is assumed that the dependency of I_{max}^a at the initiation frontier on the cyclic bulk load, σ_B^{max} , can be described with a liner relationship according to Equation 4.87.

The following frontier definition is therefore obtained:

$$\left[\frac{5I_{max}^a + \chi\sigma_B}{384\pi r} K^2 (16I^s(1 - 2\nu)^2 + 3(I_{max}^a + \chi\sigma_B)(5 + 8(\nu - 1)\nu)) \right]^{1/2} = \tau_{-1}. \quad (4.89)$$

where the value of χ is computed by FE computations and, for the experimental results obtained by Ferré for Ti-6Al-4V, is equal to 0.0052 MPa^{-1} .

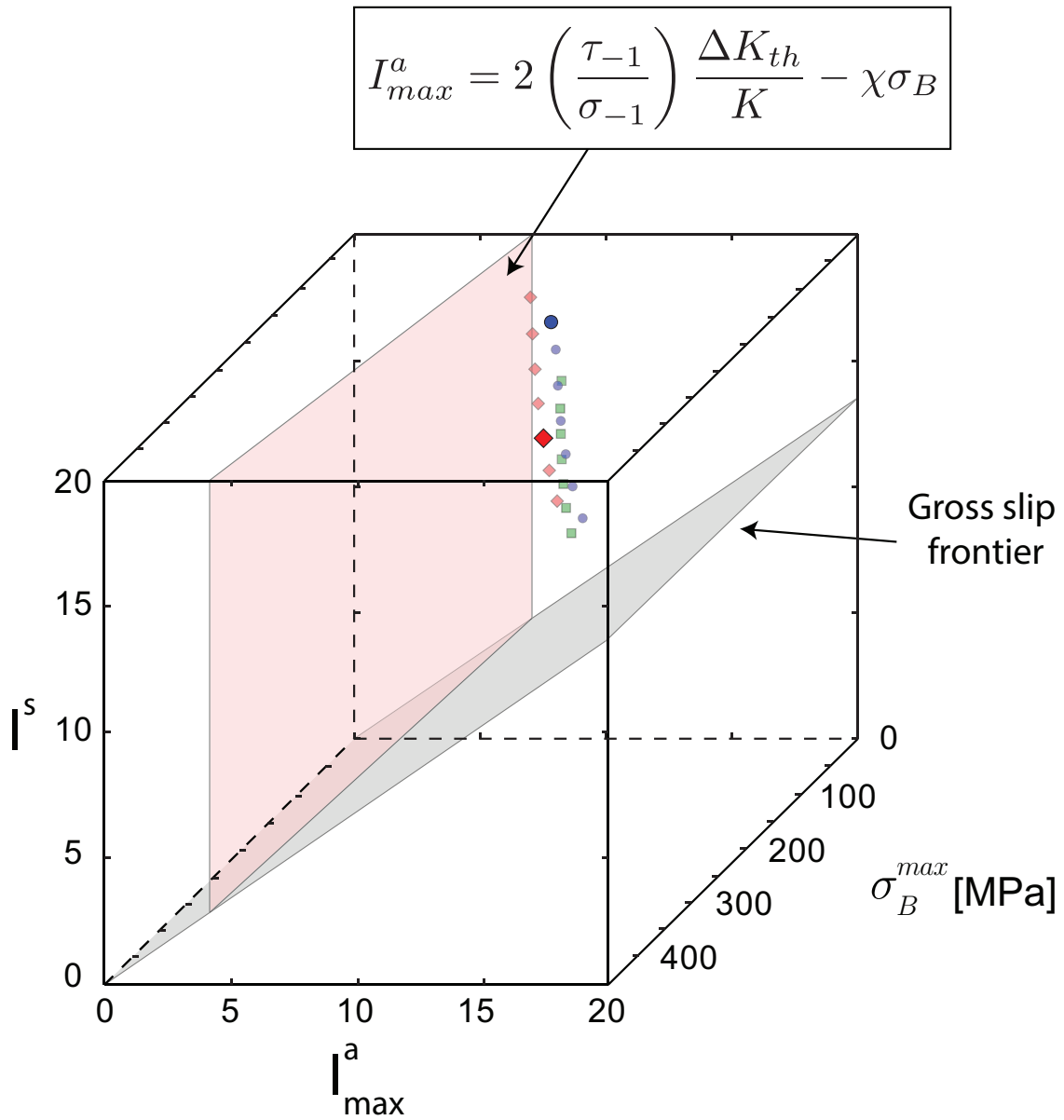


Figure 4.18: Tridimensional crack initiation frontier obtained by applying the modified Wöhler curve method to the nonlocal crack initiation map for Ti-6Al-4V.

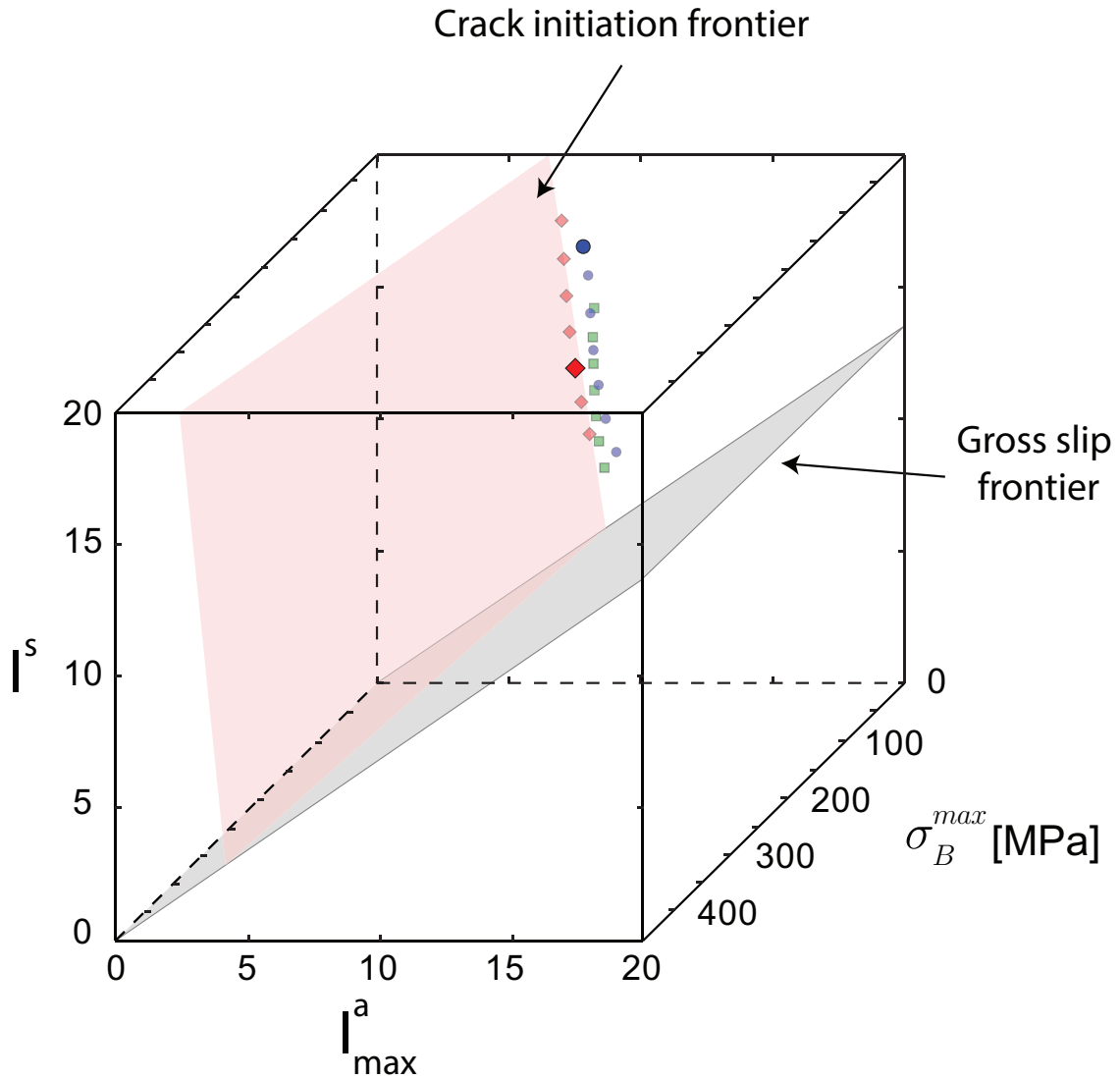


Figure 4.19: Tridimensional crack initiation frontier obtained by applying the Cross-land criterion to the nonlocal crack initiation map for Ti-6Al-4V.

4.3 Fracture mechanics approach

In this section, an attempt to link the nonlocal stress intensity factors, corresponding to the crack initiation frontiers, with a ΔK threshold is done.

The initiation frontiers have been obtained experimentally, considering that the crack was initiated for a length bigger than a threshold value (for Ti-6Al-4V and 35NiCrMo16 low-alloyed steel this value is equal to $70\ \mu\text{m}$ and for Inconel 718 is $10\ \mu\text{m}$).

Coming back to the crack analogue approach, it is like if we were applying a

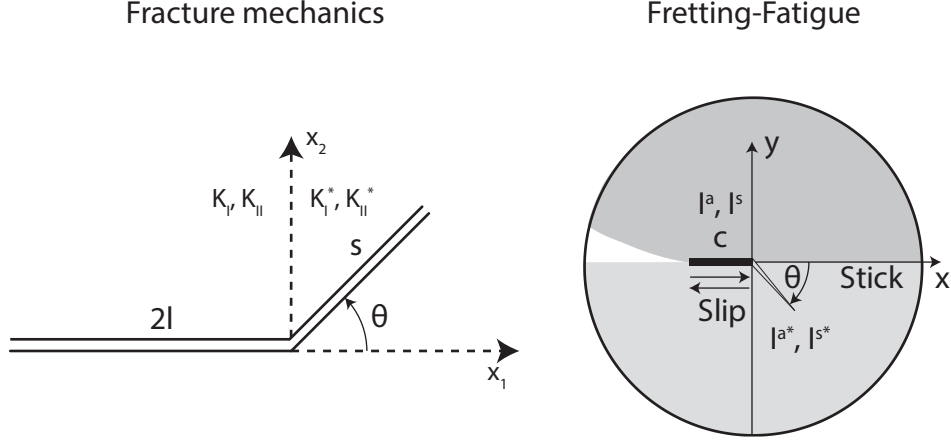


Figure 4.20: (a) Kinked crack; (b) Fretting-fatigue analogue problem.

criterion based on a ΔK threshold at the tip of a kinked crack (Figure 4.20). For a 2D plane crack of length equals to $2l$, the solutions obtained in [Leblond, 1989, Amestoy and Leblond, 1992] describe how the intensity factors, K_I and K_{II} vary after a deviation of the crack of an angle ϑ with respect to the principle plane. For $s \rightarrow 0$ the intensity factors, K_I^* and K_{II}^* , just after the crack direction variation depend only on the K_I and K_{II} before the variation and on the angle, ϑ , of the kinked crack:

$$\begin{bmatrix} K_I^* \\ K_{II}^* \end{bmatrix} = \begin{bmatrix} F_{11}(\vartheta) & F_{12}(\vartheta) \\ F_{21}(\vartheta) & F_{11}(\vartheta) \end{bmatrix} \begin{bmatrix} K_I \\ K_{II} \end{bmatrix}, \quad (4.90)$$

where

$$F_{11}(\vartheta) = \cos^3(\vartheta/2), \quad (4.91)$$

$$F_{12}(\vartheta) = -3 \cos^2(\vartheta/2) \sin(\vartheta/2), \quad (4.92)$$

$$F_{21}(\vartheta) = \frac{1}{2} \sin(\vartheta) \cos(\vartheta/2), \quad (4.93)$$

$$F_{22}(\vartheta) = \frac{1}{2} (3 \cos(\vartheta) - 1) \cos(\vartheta/2). \quad (4.94)$$

By adapting Equation 4.90 to the fretting-fatigue problem (Figure 4.20) the following relation is obtained:

$$\begin{bmatrix} I^{s*} \\ I^{a*} \end{bmatrix} = \begin{bmatrix} F_{11}(\vartheta) & F_{12}(\vartheta) \\ F_{21}(\vartheta) & F_{11}(\vartheta) \end{bmatrix} \begin{bmatrix} I^s \\ I^a \end{bmatrix}, \quad (4.95)$$

and in terms of ΔI^a and ΔI^s ,

$$\begin{bmatrix} \Delta I^{s*} \\ \Delta I^{a*} \end{bmatrix} = \begin{bmatrix} F_{11}(\vartheta) & F_{12}(\vartheta) \\ F_{21}(\vartheta) & F_{11}(\vartheta) \end{bmatrix} \begin{bmatrix} 0 \\ \Delta I^a \end{bmatrix}, \quad (4.96)$$

where ΔI^s is equal to zero and $\Delta I^a = 2I_{max}^a$ for the loading evolution studied.

The following relation is therefore obtained,

$$\Delta I^{s*} = F_{12}(\vartheta)2I_{max}^a = -6 \cos^2(\vartheta/2) \sin(\vartheta/2) I_{max}^a, \quad (4.97)$$

$$\Delta I^{a*} = F_{22}(\vartheta)2I_{max}^a = (3 \cos(\vartheta) - 1) \cos(\vartheta/2) I_{max}^a. \quad (4.98)$$

The angle ϑ which maximizes ΔI^{s*} or ΔI^{a*} is computed and the only result matching the experimental evidence is the following one,

$$\vartheta^* : \underset{(\vartheta)}{\max}(\Delta I^{s*}) \rightarrow \vartheta^* \simeq 70^\circ \rightarrow \Delta I^{s*}(\vartheta^*) = \frac{4\sqrt{3}}{3} I_{max}^a, \quad (4.99)$$

$$\Delta I^{a*}(\vartheta^*) \simeq 0. \quad (4.100)$$

At the crack arrest, $\Delta I^{s*} = \Delta K_{th}$ and therefore it is possible to compute the value of the nonlocal intensity factors corresponding to this situation,

$$I_{max}^a = \frac{\sqrt{3}}{4} \Delta K_{th}. \quad (4.101)$$

Equation 4.101 represents a vertical frontier in the nonlocal crack initiation map developed in the previous chapter.

The values corresponding to this frontier, for the three materials studied in this manuscript, are reported hereunder:

Material	Frontier location
Ti-6Al-4V	$I_{max}^a = 2.38$
Inconel 718	$I_{max}^a = 2.17$
35NiCrMo16 low-alloyed steel	$I_{max}^a = 1.39$

Table 4.4: Location of the initiation frontier following a fracture mechanics approach.

With respect to the results shown in Figure 4.21 and in Table 4.4, it is clear that the fracture mechanics approach to predict the crack initiation frontier location is too conservative. This could be linked to the fact that, in applying the equations developed by Leblond and Amestoy for kinked cracks, s is supposed to be equal to zero, while in the experimental tests its value varies in a range of 10 μm to 70 μm .

This could be the starting point for future research works. For instance, it would be interesting to show how ΔI^{s*} varies as a function of s . Far from the contact surface, the stress tensor decreases in magnitude and therefore, the intensity factor experienced at the tip of the kinked crack should be smaller as well,

$$\Delta I^{s*}(\vartheta^*) = f(s) \frac{4\sqrt{3}}{3} I_{max}^a \quad (4.102)$$

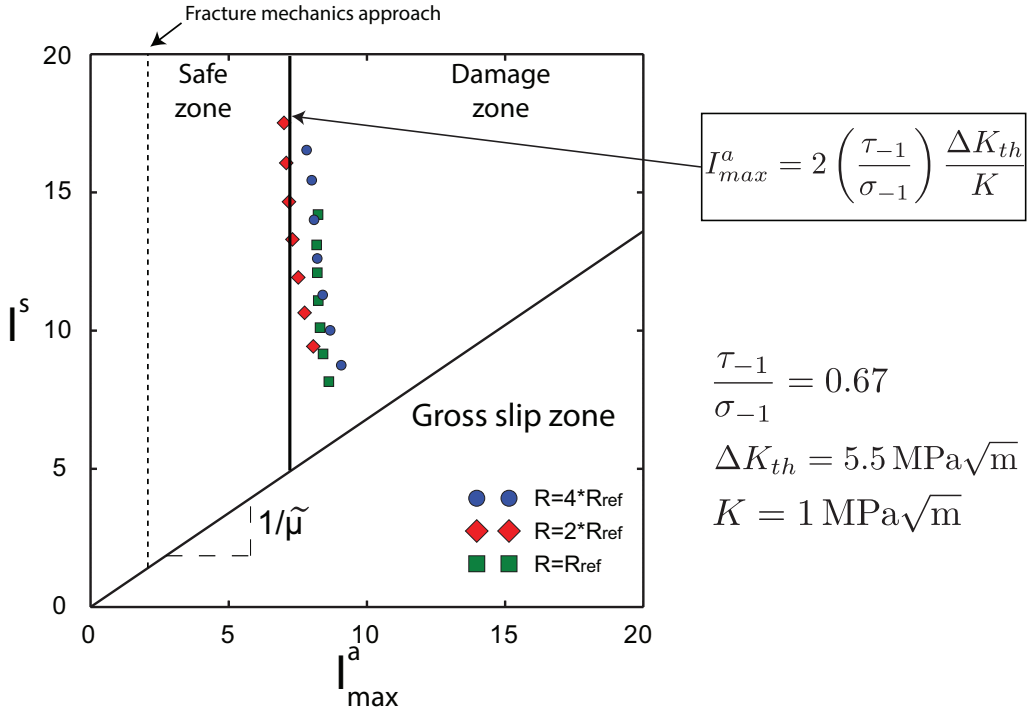


Figure 4.21: Comparison between different strategies to predict the crack initiation frontier location.

where $f(s)$ varies in a range of 0 (for $s \rightarrow \infty$) to 1 (for $s = 0$) in order to take into account the stress gradient evolution. If this relation is confirmed, this would have the effect to move the frontier previously computed to the right for positive values of s which will make the crack initiation frontier prediction less conservative and more precise.

4.4 Chapter highlights

The goal of this chapter was to present two different strategies to predict the crack initiation frontier location expressed in nonlocal quantities by means of simple material data.

For this purpose in the first part of the chapter, an approach based on the coupling between classic multiaxial fatigue criteria and the description of fretting-fatigue through nonlocal intensity factors, has been developed. More in detail, from the velocity field described as a product between intensity factors and reference fields, the corresponding stress field has been computed. To do that, the reference fields have been interpolated with derivable functions allowing to obtain an analytical description of the stress field, which is used as input for the multiaxial fatigue criteria. The modified Wöhler curve method coupled with a critical distance approach and

the Crossland criterion have been tested. The results are encouraging since a good prediction of the crack initiation frontier location has been obtained.

An attempt to link the nonlocal stress intensity factors, corresponding to the crack initiation frontiers, with a ΔK threshold is done as well. In this case, by using the solutions developed by Leblond and Amestoy [Leblond, 1989, Amestoy and Leblond, 1992], it has been possible to compute the nonlocal stress intensity factors corresponding to a kinked crack, and compare their value to a ΔK_{th} . The results are too conservative and this is probably related to the assumption to consider the length of the kinked crack equals to zero.

The development of criteria to predict the crack initiation location by using the nonlocal description of fretting-fatigue, is clearly a domain in which there is much to be done and it could be the subject of future research works. At this time, the level of maturity of these criteria are not yet sufficient to get rid of experimental tests completely, but is a first step toward that direction. The criteria developed in the manuscript can be used as a support in the experimental tests to locate the initiation frontier rapidly.

Conclusion and perspectives

This thesis focuses on the study of the gradient effect in fretting-fatigue aiming at proposing a method that, by taking into account this effect, will allow to apply the similitude principle to contact problems. Furthermore, the procedure is developed in order to be easily implementable for industrial applications.

For this purpose, a new method to describe the velocity field produced by the interaction between the contacting bodies close to the contact edges under fretting-fatigue has been introduced (Chapter 2).

In the presence of a strong gradient, the local geometry imposes the spatial distribution of the mechanical field while its intensity is determined by the macroscopic loads. Therefore, the solution of the problem can be described through a fracture mechanics approach, as the product between intensity factors and spatial reference fields.

In particular, v , is partitioned into a summation of multiple terms, each one expressed as the product between nonlocal intensity factors, I^s , I^a , I^c , depending on the macroscopic loads applied to the mechanical assembly, and spatial reference fields, d^s , d^a , d^c , depending on the local geometry of the part.

The nonlocal intensity factors are extracted by analyzing the velocity field close to the contact edges and therefore they include the information on the stress gradient evolution produced by fretting-fatigue.

To understand the influence of the variation of some key parameters on the nonlocal intensity factor extraction process, a sensitivity analysis is carried out. The results show that the values of the nonlocal intensity factors are only marginally influenced by the change of mesh size and type, which is a key point to introduce the approach inside the industrial applications. Furthermore, the fact that the reference functions remain unchanged with the variation of the contact geometry allows one to compare different attachment configurations just by looking at the value of the nonlocal intensity factors.

In Chapter 3, the procedure developed has been applied to experimental data coming from plain fretting and fretting-fatigue test campaigns. The aim was to confirm the transferability of the experimental fretting-fatigue data to different geometries from the one in which they have been obtained. For this purpose a nonlocal representation of the crack initiation map is built by using the nonlocal

intensity factors, $(I_{max}^a - I^s)$, as reference quantities.

The outcomes confirmed that the nonlocal intensity factors are geometry independent. This is an important point because experimental data, expressed either in $(Q^* - P)$ or $(q_{max}-p_0)$ coordinates, clearly show that for different geometries various crack initiation frontiers are observed. This represents a limitation for industrial applications since it is difficult to transpose the results obtained on laboratory test machines to real-scale industrial components. On the contrary, if the crack initiation map is expressed in nonlocal quantities $(I_{max}^a-I^s)$, that take into account the gradient effect, all the different crack initiation frontiers merge into a single one. As a consequence, the nonlocal intensity factors can be considered objective quantities through which it is possible to compare different fretting-fatigue experimental or numerical results.

The good stability shown by the method allows one to apply it to more complex contact configurations, such as, the disc-blade root attachment in a turbofan engine. The spatial reference fields depend only on the local geometry of the parts and therefore for a given configuration they can be pre-computed through the use of a fine mesh as it is presented in Section 2.3. Then, for any given macroscopic load combination a rough mesh FE computation will be performed aiming at extracting directly the nonlocal intensity factors thanks to the information already stocked on the shape of the reference fields.

In Chapter 4 different crack initiation prediction criteria have been adapted to the nonlocal description of fretting-fatigue. The objective is to predict the location of the initiation frontier by using simple material data, such as the fatigue limit or the crack initiation threshold. To achieve the goal different strategies have been investigated.

Several multiaxial fatigue criteria are coupled to the description of fretting-fatigue through nonlocal intensity factors in order to obtain a numerical crack initiation frontier as a function of I_{max}^a , I^s and σ_B^{max} .

An attempt to link the nonlocal stress intensity factors, corresponding to the crack initiation frontiers, with a ΔK threshold is done as well.

The results are encouraging. In particular, by applying the modified Wöhler curve method coupled with a critical distance approach, [Araújo et al., 2007], it has been possible to accurately predict the experimental crack initiation frontiers obtained for Ti-6Al-4V and Inconel-718, whereas a conservative result has been obtained for 35NiCrMo16 low-alloyed steel.

Even if the level of maturity of these crack initiation prediction criteria are not yet sufficient to get rid of experimental tests completely, I believe that it is a first step toward that direction. The criteria developed in the manuscript can be used as a support in the experimental tests to locate the initiation frontier rapidly.

This work opens up perspectives for future research.

It has been shown, that the procedure developed in this manuscript works well in taking into account the gradient effect for academic fretting-fatigue geometries such as the cylinder-plane contact configuration. With that said, the algorithm has been conceived to be applicable to more complex geometries like the disc-blade root attachment. Therefore, the natural continuation of this research would be the use of the nonlocal intensity factors to transfer the experimental results obtained on laboratory test machine to real industrial components (Figure 5.3).

With this in mind a first feasibility study has already been performed on a 3D cylinder-plane contact configuration (Figure 5.1), characterized by the following parameters: Pad radius = 40 mm, friction coefficient = 1.0, Young's modulus = 119 400 MPa, Poisson's ratio = 0.286, $P = 391$ N and $Q^* = 317$ N.

Considering that for tridimensional components the contact front is a line the extraction process is repeated over the entire contact front, slice by slice. In Figure 5.2 the results of the extraction process are presented. In particular it is interesting to observe the variation of the computed I_{max}^a, I^s as a function of the specimen width, d . The difference is due to the fact that at the center of the contact zone the plain strain assumption is respected almost perfectly (Figure 5.2a), whereas close to the specimen and pad external surfaces a plane stress condition is experienced.

The effect linked to the triaxiality of the stress tensor becomes important for 3D applications and it needs to be analyzed in more detail in future works.

Another interesting perspective consists in the development of new computation approaches for the simulation of fretting fatigue. Actually, this is the objective of Raphael Araújo Cardoso, who starts his PhD research recently under the supervision of David Neron and Sylvie Pommier at the LMT-ENS Cachan and Alex Araújo at the University of Brasilia. The goal is to develop an offline/online multiscale approach allowing to mix local fretting-fatigue models (crack analogue approach extension described in my thesis) and global structural computations. This will be done by using Proper Generalized Decomposition (PDG) reduced modeling [Ladeve ze, 1999]. The offline computations will try to catch the local fretting-fatigue phenomena close to the contact edges, i.e. the stress gradient evolution, using FE computations characterized by very fine mesh. This information will then be reintroduced in the global structure computation (disc + blades) characterized by a coarse mesh. Here the importance of the definition of a nonlocal friction coefficient is clear since it will pilot the position of the contact front where the pre-computed solutions are employed.

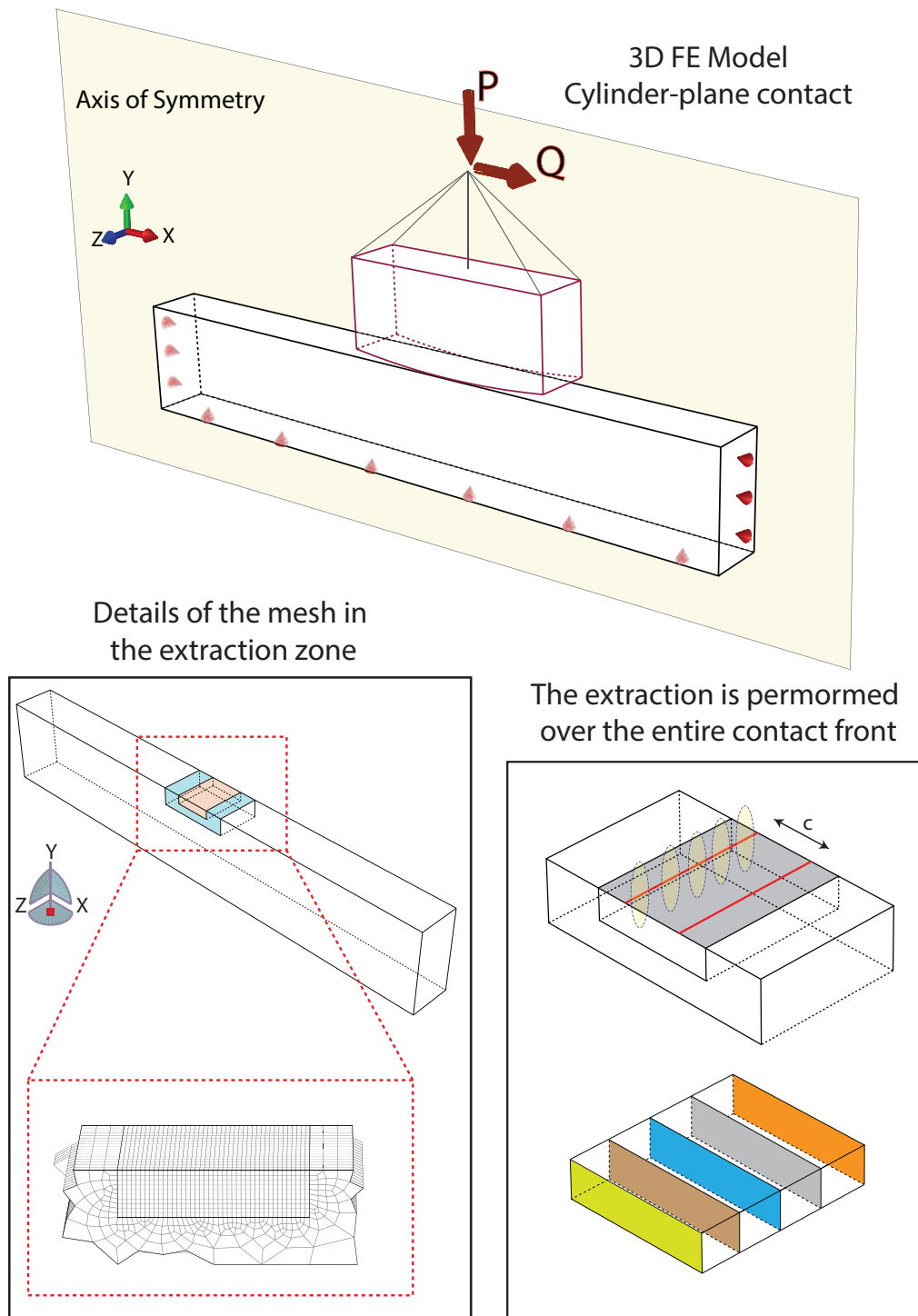


Figure 5.1: Details of a 3D cylinder-plane contact FE model, used to extract the nonlocal intensity factors.

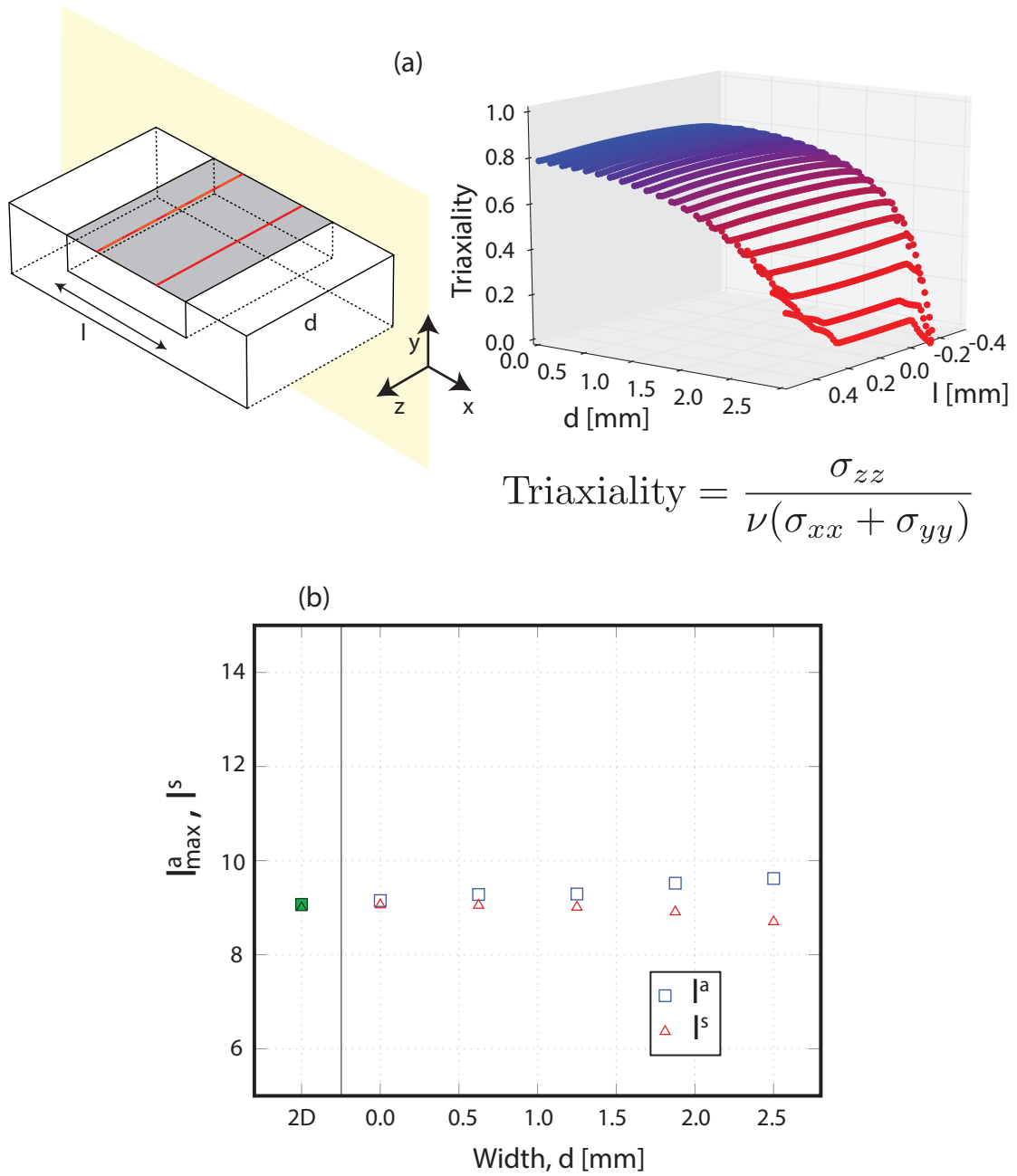


Figure 5.2: (a) Triaxiality variation as a function of the specimen width, d ; (b) Nonlocal intensity factor variation as a function of the specimen width.

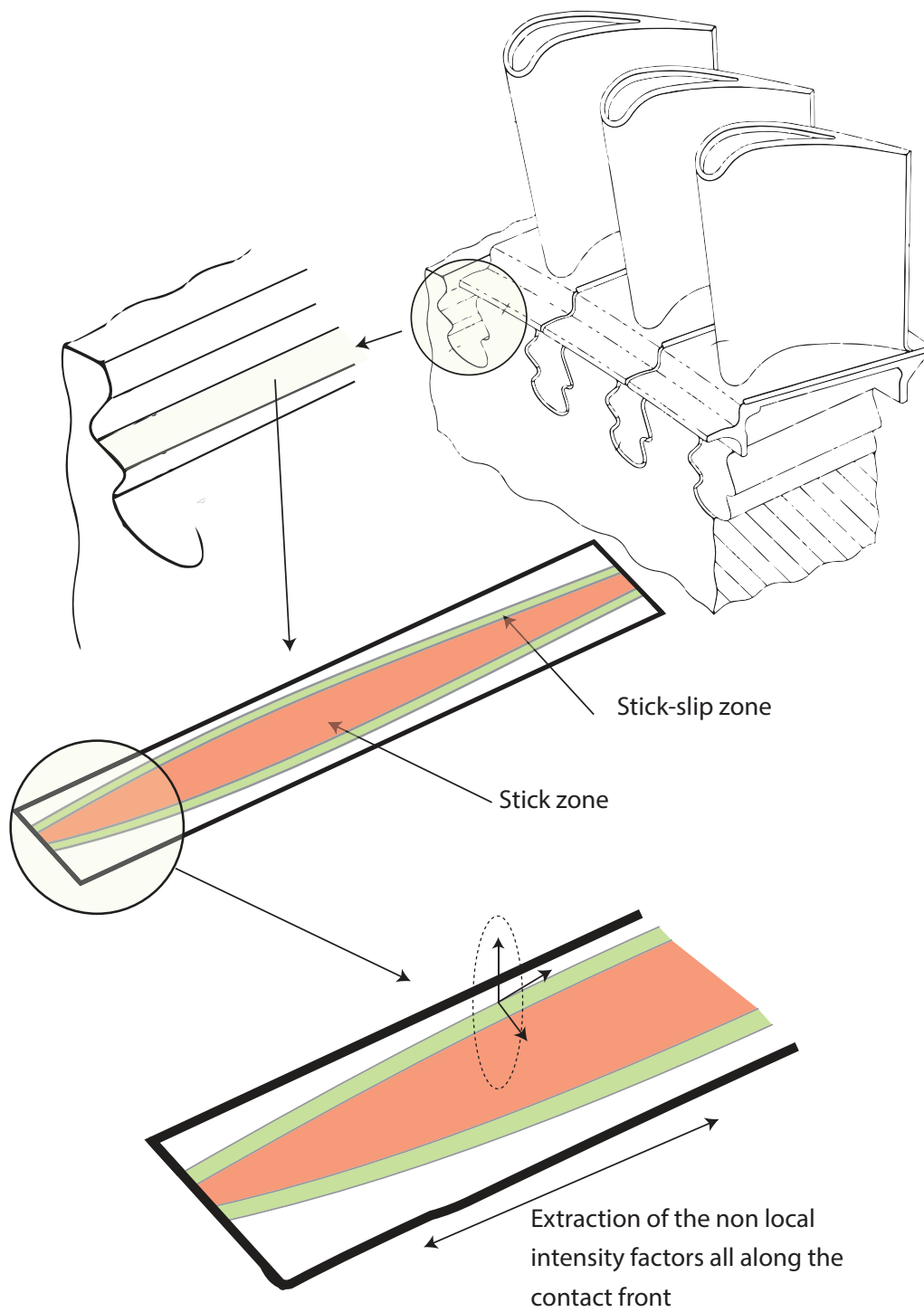


Figure 5.3: Schematic representation of the nonlocal intensity factor extraction process applied to an industrial component.

Appendix A

Karhunen-Loeve transform

The Karhunen-Loeve decomposition [Loève, 1955] has been used in Chapter 2 to partition an initial field depending on several variables into a series of terms, function of a single variable. Here, The mathematical details to apply this technique are described. Some practical examples of the application are given, as well.

Analytical details

The Karhunen-Loeve transform (KLT), also known as Proper Orthogonal Decomposition (POD), is a model reduction technique for approximating a set of vectors or images by a low dimensional subspace.

The KL transform has found many applications in several different fields such as statistics, communication, and computer vision, where it was used for a variety of tasks like face recognition, object recognition, motion estimation, visual learning and object tracking, [Levey and Lindenbaum, 2000].

In this manuscript the technique is applied to fretting-fatigue for the first time (to the author's best knowledge), following the procedure already described in [Pommier et al., 2009].

Let's suppose that we want to approximate a function $v(x, t)$ over a given domain as a finite summation of terms,

$$v(x, t) \simeq \sum_{k=1}^N a_k(t)\phi_k(x), \quad (\text{A.1})$$

with the hypothesis that for $k \rightarrow N$, the error introduced by the approximation tends to zero. If the POD is used to determine ϕ_k the following hypothesis are respected:

- the functions constituting the basis are orthogonal,

$$\int_{\Omega} \delta_{kj} \phi_k(x) \phi_j(x) dx = 0 \quad \text{if } k \neq j \quad \delta_{kj} = \text{delta di Kronecker}, \quad (\text{A.2})$$

- ϕ_k are computed in order to minimize the total mean square error or in other words, maximize the average projection of $v(x, t)$ on the chosen basis,

$$\max \left(\frac{\langle v \cdot \phi \rangle}{\phi \cdot \phi} \right). \quad (\text{A.3})$$

This is a constrained optimization problem and its solution is obtained by solving a Fredholm integral equation,

$$\int_{\Omega} \langle v(x, t) \cdot v'(x, t) \rangle \phi'_k dx = \lambda_k \phi_k, \quad (\text{A.4})$$

$$R(x, t) = \langle v(x, t) \cdot v'(x, t) \rangle, \quad (\text{A.5})$$

where R is the correlation function. The components, ϕ_k , of the basis are the outcome of the eigenvalue problem,

$$R\underline{\phi} = \lambda\underline{\phi}. \quad (\text{A.6})$$

From a practical point of view, to partition the initial function, $v(x, t)$, into two terms depending separately on time and space, the following steps are performed:

1. $v(x, t)$ is rewritten in a matrix form, $\underline{\underline{V}} \in \mathbb{R}^{N \times T}$,

$$\underline{\underline{V}} = \begin{bmatrix} v(x=1, t=1) & \cdots & v(x=1, t=T) \\ \vdots & & \vdots \\ v(x=N, t=1) & \cdots & v(x=N, t=T) \end{bmatrix}, \quad (\text{A.7})$$

2. the correlation matrix, $\underline{\underline{C}}$, is computed,

$$\underline{\underline{C}} = \underline{\underline{V}} \cdot \underline{\underline{V}}^T, \quad (\text{A.8})$$

3. diagonalization of $\underline{\underline{C}}$ by solving the eigenvalues problem,

$$\underline{\underline{C}} \cdot \underline{\underline{\phi}}_k = \lambda_k \underline{\underline{\phi}}_k, \quad k = 1 \dots N, \quad (\text{A.9})$$

4. computation of the temporal coefficients, $\underline{\underline{a}}_k$,

$$\underline{\underline{a}}_k = \underline{\underline{V}}^T \cdot \underline{\underline{\phi}}_k, \quad k = 1 \dots N, \quad (\text{A.10})$$

5. approximation of the initial function,

$$\underline{\underline{V}} \simeq \tilde{\underline{\underline{V}}} = \sum_{k=1}^N \underline{\underline{\phi}}_k \cdot \underline{\underline{a}}_k^T. \quad (\text{A.11})$$

For $k = N$ it is easy to verify that the error introduced by the approximation is equal to zero since,

$$\tilde{\underline{\underline{V}}} = \underline{\underline{\phi}} \cdot \underline{\underline{a}}^T = \underline{\underline{\phi}} \cdot \left(\underline{\underline{V}}^T \cdot \underline{\underline{\phi}} \right)^T = \overbrace{\underline{\underline{\phi}} \cdot \underline{\underline{\phi}}^T}^{\mathbb{I}} \cdot \underline{\underline{V}} = \underline{\underline{V}}. \quad (\text{A.12})$$

Usually the objective is to reduce the complexity of the initial model, and therefore only the first n terms of the development are kept. In this process the eigenvalues (and the correspondent eigenvectors) are ranged in descending order. The eigenvectors associated to the biggest eigenvalues are the ones that contain the majority of the “energy” of the original system. The approximated solution and the error introduced can be computed as follows,

$$\tilde{\underline{\underline{V}}} = \sum_{k=1}^{n < N} \underline{\underline{\phi}}_k \cdot \underline{\underline{a}}_k^T, \quad \xi = \sqrt{\frac{\sum_{i,k} (V_{ik} - \tilde{V}_{ik})^2}{\sum_{i,k} V_{ik}^2}} \quad (\text{A.13})$$

The powerful aspect of this technique relies on the fact that it can be applied to a vectorial field allowing to approximate it through its orthogonal decomposition, $v(\underline{x}, t) = a(t)f(\underline{x})$. Since the vectors are orthogonal with respect to the spatial correlation matrix, C , this means that they constitute a basis where each component is kinematics independent.

Application examples

In Figures A.1 and A.2 an example of the application of the POD is shown. The technique is employed to reduce the size of an image that it can be represented in a matrix form where each element represents the the gray level of a pixel.

For this “particular field”, 50 eigenvectors are sufficient to represent the initial data with a relative error lower than 10% (Figure A.2).

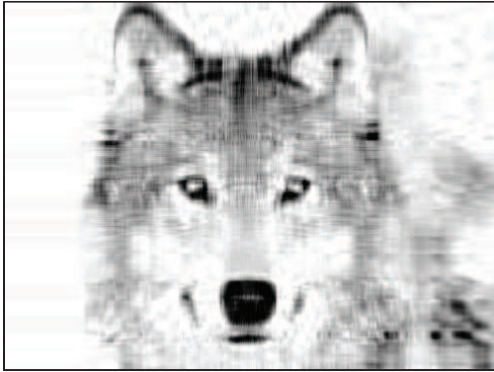
Size reduction with POD technique



Original image (450 eigenvectors)



Reconstruction with 7 eigenvectors



Reconstruction with 15 eigenvectors



Reconstruction with 50 eigenvectors

Figure A.1: Example of the utilization of the POD technique to reduce the image size.

With respect to the way in which the POD is employed in Chapter 2, a single term in the development described in Equation A.1 ($k = 1$) is retained,

$$\underline{d}^s(\underline{x}) \rightarrow \underline{d}^s(r, \vartheta) \simeq f^s(r) \underline{g}^s(\vartheta), \quad (\text{A.14})$$

$$\underline{d}^a(\underline{x}) \rightarrow \underline{d}^a(r, \vartheta) \simeq f^a(r) \underline{g}^a(\vartheta). \quad (\text{A.15})$$

A self-similar geometry assures that it is possible to decompose the reference fields as described above or from a different point of view, it guaranties that a single term

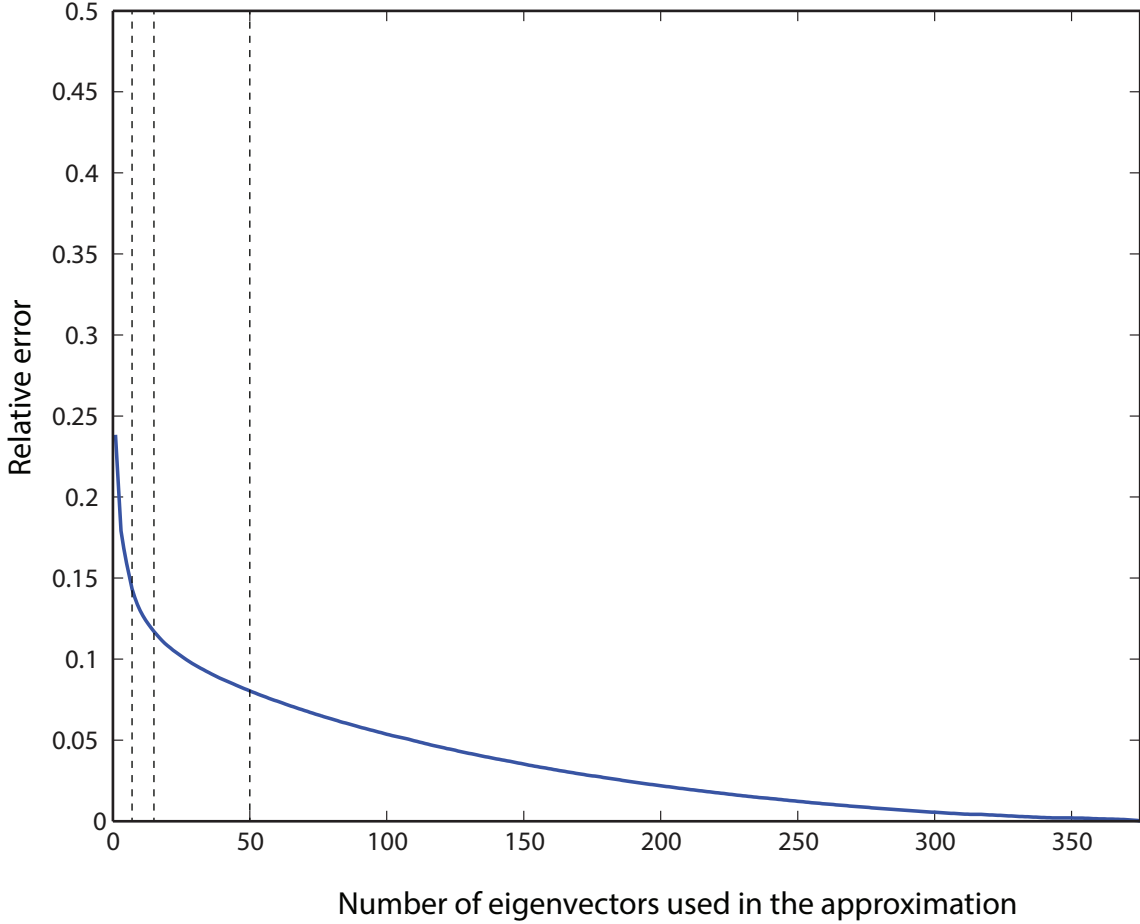


Figure A.2: Evolution of the error in the POD approximation as a function of the number of terms used.

in the POD development is sufficient to completely describe the field. For instance, let's imagine to have the following self-similar field,

$$d(r, \vartheta) = e^{(r+\vartheta)}. \quad (\text{A.16})$$

By applying the POD decomposition and retaining just the first term, it is possible to fully describe $d(r, \vartheta)$,

$$d(r, \vartheta) = f(r)g(\vartheta) = e^r \cdot e^\vartheta. \quad (\text{A.17})$$

The reference fields extracted following the procedure described in Chapter 2 are really close to be self-similar and this is certified by the fact that the error, introduced by the partition technique to obtain the radial and tangential evolution, is close to zero.

Bibliography

- [Almen, 1937] Almen, J. O. (1937). Lubricants and false brinelling of ball and roller bearings. *Mechanical Engineering*, 59:415.
- [Amargier et al., 2010] Amargier, R., Fouvry, S., Chambon, L., Schwob, C., and Poupon, C. (2010). Stress gradient effect on crack initiation in fretting using a multiaxial fatigue framework. *International Journal of Fatigue*, 32(12):1904 – 1912.
- [Amestoy and Leblond, 1992] Amestoy, M. and Leblond, J. (1992). Crack paths inplane situation -ii. detail form of the expansion of the stress intensity factors. *International Journal of Solids and Structures*, 29:465 – 501.
- [Anderson, 2005] Anderson, T. L. (2005). *Fracture Mechanics: Fundamentals and Applications*. CRC Press.
- [Araújo and Castro, 2012] Araújo, J. and Castro, F. (2012). A comparative analysis between multiaxial stress and ΔK -based short crack arrest models in fretting fatigue. *Engineering Fracture Mechanics*, 93(0):34 – 47.
- [Araújo et al., 2011] Araújo, J., Dantas, A., Castro, F., Mamiya, E., and Ferreira, J. (2011). On the characterization of the critical plane with a simple and fast alternative measure of the shear stress amplitude in multiaxial fatigue. *International Journal of Fatigue*, 33(8):1092 – 1100. Multiaxial Fatigue Models.
- [Araújo et al., 2007] Araújo, J., Susmel, L., Taylor, D., Ferro, J., and Mamiya, E. (2007). On the use of the theory of critical distances and the modified Wöhler curve method to estimate fretting fatigue strength of cylindrical contacts. *International Journal of Fatigue*, 29(1):95 – 107.
- [ATSB, 2002] ATSB (2002). Examination of a failed fan blade. Technical report.
- [ATSB, 2010] ATSB (2010). In-flight uncontained engine failure airbus A380-842, VH-0QA. Technical report.
- [Baietto et al., 2013] Baietto, M., Pierres, E., Gravouil, A., Berthel, B., Fouvry, S., and Trolle, B. (2013). Fretting fatigue crack growth simulation based on a combined experimental and XFEM strategy. *International Journal of Fatigue*, 47(0):31 – 43.

- [Bellecave et al., 2014] Bellecave, J., Pommier, S., Nadot, Y., Meriaux, J., and Araújo, J. (2014). T-stress based short crack growth model for fretting fatigue. *Tribology International*, 76(0):23 – 34. Proceedings of the Seventh International Symposium on Fretting Fatigue.
- [Brugier et al., 2013] Brugier, F., Pommier, S., De Moura Pinho, R., and Soria, D. (2013). A novel approach to predict the growth rate of short cracks under multiaxial loadings. The Tenth International Conference on Multiaxial Fatigue & Fracture.
- [Bueckner, 1970] Bueckner, H. F. (1970). A novel principle for the computation of stress intensity factors. *Z. Angew. Math. Mech*, 50:529 – 546.
- [Cattaneo, 1938] Cattaneo, C. (1938). Sul contatto di due corpi elastici: distribuzione locale degli sforzi. *Rendiconti dell'Accademia nazionale dei Lincei*, 27:342 – 348.
- [Chambon and Journet, 2006] Chambon, L. and Journet, B. (2006). Modelling of fretting fatigue in a fracture-mechanics framework. *Tribology International*, 39(10):1220 – 1226. The Fourth International Symposium on Fretting Fatigue The Fourth International Symposium on Fretting Fatigue.
- [Chaudonneret, 1993] Chaudonneret, M. (1993). A simple and efficient multiaxial fatigue damage model for engineering applications of macro-crack initiation. *Journal of Engineering Materials and Technology*, 115(4):373 – 379.
- [Ciavarella and Macina, 2003] Ciavarella, M. and Macina, G. (2003). A note on the crack analogue model for fretting fatigue. *International Journal of Solids and Structures*, 40(4):807 – 825.
- [Crossland, 1956] Crossland, R. (1956). Effect of large hydrostatic pressure on the torsional fatigue strength of an alloy steel. *Institution of Mechanical Engineers*, pages 138 – 149. In: Proc. Int. Conf. on Fatigue of Metals.
- [Dang Van et al., 1982] Dang Van, K., Griveau, B., and Message, O. (1982). On a new multiaxial fatigue limit criterion: Theory and application. *Biaxial and multiaxial fatigue*, M. W. Brown and K. Miller, Eds., EGF Publication(3):479 – 496.
- [de Pannemaecker et al., 2015] de Pannemaecker, A., Fouvry, S., and Buffiere, J. (2015). Reverse identification of short-long crack threshold fatigue stress intensity factors from plain fretting crack arrest analysis. *Engineering Fracture Mechanics*, 134(0):267 – 285.
- [Eden et al., 1911] Eden, E. M., Rose, W. N., and Cunningham, F. (1911). The endurance of metals: experiments on rotating beams at university college. *Proceedings of the Institution of Mechanical Engineers*, 1-196:1847 – 1982.

- [Edwards, 1984] Edwards, P. (1984). Fracture mechanics application to fretting in joints. In Valluri, S., Taplin, D., Rao, P. R., Knott, J., and Dubey, R., editors, *Fracture 84*, pages 3813 – 3836. Pergamon.
- [Fellows et al., 1995] Fellows, L., Nowell, D., and Hills, D. (1995). Contact stresses in a moderately thin strip (with particular reference to fretting experiments). *Wear*, 185(1-2):235 – 238.
- [Fenner and Field, 1958] Fenner, A. J. and Field, J. E. (1958). La fatigue dans les conditions de frottement. *Revue de Metallurgie*, 55:475 – 485.
- [Ferré, 2013] Ferré, R. (2013). *Etude expérimentale et modélisation de la durabilité d'un contact aube/disque de soufflante grenailé revêtu soumis à des chargements de Fretting/Fatigue/Usure*. PhD thesis, Ecole Centrale de Lyon.
- [Ferré et al., 2013] Ferré, R., Fouvry, S., Berthel, B., and Ruiz-Sabariégo, J.-A. (2013). Stress gradient effect on the crack nucleation process of a Ti-6Al-4V titanium alloy under fretting loading: Comparison between non-local fatigue approaches. *International Journal of Fatigue*, 54(0):56 – 67.
- [Findlay and Harrison, 2002] Findlay, S. and Harrison, N. (2002). Why aircraft fail. *Materials Today*, 5(11):18 – 25.
- [Fouvry et al., 2014] Fouvry, S., Gallien, H., and Berthel, B. (2014). From uni- to multi-axial fretting-fatigue crack nucleation: Development of a stress-gradient-dependent critical distance approach. *International Journal of Fatigue*, 62(0):194 – 209. 9th Fatigue Damage of Structural Materials Conference.
- [Fouvry et al., 1996] Fouvry, S., Kapsa, P., and Vincent, L. (1996). Quantification of fretting damage. *Wear*, 200(1-2):186 – 205.
- [Fouvry et al., 2000] Fouvry, S., Kapsa, P., and Vincent, L. (2000). Multiaxial fatigue analysis of fretting contact taking into account the size effect. *ASTM Special Technical Publication*, (1367):167 – 182.
- [Fouvry and Kubiak, 2009] Fouvry, S. and Kubiak, K. (2009). Introduction of a fretting-fatigue mapping concept: Development of a dual crack nucleation - crack propagation approach to formalize fretting-fatigue damage. *International Journal of Fatigue*, 31(2):250 – 262.
- [Fouvry et al., 2008] Fouvry, S., Nowell, D., Kubiak, K., and Hills, D. (2008). Prediction of fretting crack propagation based on a short crack methodology. *Engineering Fracture Mechanics*, 75(6):1605 – 1622.
- [Freymy et al., 2012] Freymy, F., Pommier, S., Galenne, E., and Courtin, S. (2012). A scaling approach to model history effects in fatigue crack growth under mixed mode I+II+III loading conditions for a 316L stainless steel. *International Journal of Fatigue*, 42(0):207 – 216. Fatigue Damage of Structural Materials VIII.

- [Fridrici et al., 2003] Fridrici, V., Fouvry, S., and Kapsa, P. (2003). Fretting wear behavior of a Cu-Ni-In plasma coating. *Surface and Coatings Technology*, 163-164(0):429 – 434. Proceedings of the 29th International conference on Metallurgical Coatings and Thin Films.
- [Garrison, 2000] Garrison, B. (2000). *High Cycle Fatigue (HCF) science and technology program 2000 annual report*. Universal Technology Corporation, 1270 North Fairfield Road, Dayton OH 45432-2600.
- [Giannakopoulos et al., 1998] Giannakopoulos, A., Lindley, T., and Suresh, S. (1998). Aspects of equivalence between contact mechanics and fracture mechanics: theoretical connections and a life-prediction methodology for fretting-fatigue. *Acta Materialia*, 46(9):2955 – 2968.
- [Giannakopoulos et al., 2000] Giannakopoulos, A., Suresh, S., and Chenut, C. (2000). Similarities of stress concentrations in contact at round punches and fatigue at notches: implications to fretting fatigue crack initiation. *Fatigue & Fracture of Engineering Materials & Structures*, 23(7):561 – 571.
- [H. Kitagawa, 1976] H. Kitagawa, S. T. (1976). Applicability of fracture mechanics to very small cracks or cracks in the early stage. *ASM*, page 627 – 631. Proceeding of the second international conference on mechanical behavior of materials.
- [Hertz, 1882] Hertz, R. (1882). Über die berührung fester elastischer körper. *Journal für die reine und angewandte Mathematik*, 92:156 – 171.
- [Hills et al., 2012] Hills, D., Thaitirarot, A., Barber, J., and Dini, D. (2012). Correlation of fretting fatigue experimental results using an asymptotic approach. *International Journal of Fatigue*, 43(0):62 – 75.
- [Hills and Nowell, 1994] Hills, D. A. and Nowell, D. (1994). *Mechanics of Fretting Fatigue*. Kluwer Academic Publishers.
- [Hoepfner and Gates, 1981] Hoepfner, D. and Gates, F. (1981). Fretting fatigue considerations in engineering design. *Wear*, 70(2):155 – 164.
- [Irwin, 1957] Irwin, G. R. (1957). Analysis of stresses and strains near the end of crack traversing a plate. *Journal of Applied Mechanics*, 24:361 – 364.
- [Johnson, 1985] Johnson, K. L. (1985). *Contact Mechanics*. Cambridge University Press.
- [Kubiak, 2006] Kubiak, K. (2006). *Quantification de la fissuration d'un contact soumis à des sollicitations complexes en fretting wear et fretting fatigue*. PhD thesis, Ecole Centrale de Lyon.

- [Ladeve ze, 1999] Ladeve ze, P. (1999). *Nonlinear computational structural mechanics - new approaches and non-incremental methods of calculation*. Springer, Berlin.
- [Leblond, 1989] Leblond, J. (1989). Crack paths in plane situation -i. general form of the expansion of the stress intensity factors. *International Journal of Solids and Structures*, 25:1311 – 1325.
- [Lee and Mall, 2004] Lee, H. and Mall, S. (2004). Some observations on frictional force during fretting fatigue. *Tribology Letters*, 17(3):491 – 499. The Fourth International Symposium on Fretting Fatigue The Fourth International Symposium on Fretting Fatigue.
- [Levey and Lindenbaum, 2000] Levey, A. and Lindenbaum, M. (2000). Sequential karhunen-loeve basis extraction and its application to images. *Image Processing, IEEE Transactions on*, 9(8):1371 – 1374.
- [Lindley, 1997] Lindley, T. (1997). Fretting fatigue in engineering alloys. *International Journal of Fatigue*, 19(93):39 – 49.
- [Liu and Hill, 2009] Liu, K. K. and Hill, M. R. (2009). The effects of laser peening and shot peening on fretting fatigue in Ti-6Al-4V coupons. *Tribology International*, 42(9):1250 – 1262. Special Issue: Fifth International Symposium on Fretting Fatigue.
- [Lo ve, 1955] Lo ve, M. (1955). *Probability theory*. New York: Van Nostrand.
- [Mall et al., 2011] Mall, S., Jain, V. K., and Fadag, H. A. (2011). Effects of shot-peening on fretting fatigue crack growth behavior in Ti-6Al-4V. *Strain*, 47:e305 – e318.
- [Mary, 2009] Mary, C. (2009). *Simulation exp rimentale de l’usure du contact aube-disque de compresseur sous sollicitations de fretting*. PhD thesis, Ecole Centrale de Lyon.
- [McDowell, 1952] McDowell, J. R. (1952). Fretting corrosion tendencies of several combinations of materials. *American Society for Testing and Materials*, STP:144.
- [Meriaux, 2010] Meriaux, J. (2010). *Etude exp rimentale et mod lisation de l’endommagement du contact aube-disque de soufflante soumis   des chargements de fretting fatigue*. Theses, Ecole Centrale de Lyon.
- [Meriaux et al., 2010] Meriaux, J., Fouvry, S., Kubiak, K., and Deyber, S. (2010). Characterization of crack nucleation in Ti-6Al-4V under fretting-fatigue loading using the potential drop technique. *International Journal of Fatigue*, 32(10):1658 – 1668.

- [Miller, 1993a] Miller, K. J. (1993a). Materials science perspective of metal fatigue resistance. *Material Science and Technology*, Volume 9, issue 6:453 – 462.
- [Miller, 1993b] Miller, K. J. (1993b). The two thresholds of fatigue behaviour. *Fatigue & Fracture of Engineering Materials & Structures*, 16(9):931 – 939.
- [Mindlin, 1949] Mindlin, R. (1949). Compliance of elastic bodies in contact. *Journal of Applied Mechanics*, 16:259 – 268.
- [Muskhelishvili, 1953] Muskhelishvili, N. (1953). *Some basic problems of the mathematical theory of elasticity*. Springer.
- [Neuber, 1958] Neuber, H. (1958). *Theory of notch stresses*. Berlin: Springer.
- [Nishioka and Hirakawa, 1969a] Nishioka, K. and Hirakawa, K. (1969a). Fundamental investigations of fretting fatigue : Part 2, fretting fatigue testing machine and some test results. *Bulletin of JSME*, 12(50):180 – 187.
- [Nishioka and Hirakawa, 1969b] Nishioka, K. and Hirakawa, K. (1969b). Fundamental investigations of fretting fatigue : Part 3, some phenomena and mechanisms of surface cracks. *Bulletin of JSME*, 12(51):397 – 407.
- [Nishioka and Hirakawa, 1969c] Nishioka, K. and Hirakawa, K. (1969c). Fundamental investigations of fretting fatigue : Part 4, the effect of mean stress. *Bulletin of JSME*, 12(51):408 – 414.
- [Nishioka and Hirakawa, 1969d] Nishioka, K. and Hirakawa, K. (1969d). Fundamental investigations of fretting fatigue : Part 5, the effect of relative slip amplitude. *Bulletin of JSME*, 12(52):692 – 697.
- [Nishioka and Hirakawa, 1972] Nishioka, K. and Hirakawa, K. (1972). Fundamental investigations of fretting fatigue : Part 6, effects of contact pressure and hardness of materials. *Bulletin of JSME*, 15(80):135 – 144.
- [Nishioka et al., 1968] Nishioka, K., Nishimura, S., and Hirakawa, K. (1968). Fundamental investigations of fretting fatigue : Part 1, on the relative slip amplitude of press-fitted axle assemblies. *Bulletin of JSME*, 11(45):437 – 445.
- [Nowell and Hills, 1987] Nowell, D. and Hills, D. A. (1987). Open cracks at or near free edges. *J Strain Anal*, 22(3):77 – 85.
- [Papadopoulos et al., 1997] Papadopoulos, I. V., Davoli, P., Gorla, C., Filippini, M., and Bernasconi, A. (1997). A comparative study of multiaxial high-cycle fatigue criteria for metals. *International Journal of Fatigue*, 19(3):219 – 235.
- [Paris and Erdogan, 1963] Paris, P. and Erdogan, F. (1963). A critical analysis of crack propagation laws. *Journal of Basic Engineering*, Transactions of the American Society of Mechanical Engineers, 24:528 – 534.

- [Pommier and Hamam, 2007] Pommier, S. and Hamam, R. (2007). Incremental model for fatigue crack growth based on a displacement partitioning hypothesis of mode I elastic-plastic displacement fields. *Fatigue & Fracture of Engineering Materials & Structures*, 30(7):582 – 598.
- [Pommier et al., 2009] Pommier, S., Lopez-Crespo, P., and Decreuse, P. (2009). A multi-scale approach to condense the cyclic elastic-plastic behaviour of the crack tip region into an extended constitutive model. *Fatigue & Fracture of Engineering Materials & Structures*, 32(11):899 – 915.
- [Proudhon, 2005] Proudhon, H. (2005). *Identification des mécanismes de fissuration dans un alliage d'aluminium sollicité en fretting et en fatigue*. PhD thesis, Ecole Centrale de Lyon.
- [Proudhon et al., 2007] Proudhon, H., Buffière, J.-Y., and Fouvry, S. (2007). Three-dimensional study of a fretting crack using synchrotron x-ray micro-tomography. *Engineering Fracture Mechanics*, 74(5):782 – 793.
- [Proudhon et al., 2005] Proudhon, H., Fouvry, S., and Buffire, J.-Y. (2005). A fretting crack initiation prediction taking into account the surface roughness and the crack nucleation process volume. *International Journal of Fatigue*, 27(5):569 – 579.
- [Proudhon et al., 2006] Proudhon, H., Fouvry, S., and Yantio, G. (2006). Determination and prediction of the fretting crack initiation: introduction of the (P, Q, N) representation and definition of a variable process volume. *International Journal of Fatigue*, 28(7):707 – 713.
- [Rajasekaran and Nowell, 2006] Rajasekaran, R. and Nowell, D. (2006). Fretting fatigue in dovetail blade roots: Experiment and analysis. *Tribology International*, 39(10):1277 – 1285. The Fourth International Symposium on Fretting Fatigue The Fourth International Symposium on Fretting Fatigue.
- [Rice, 1968] Rice, J. R. (1968). A path independent integral and the approximate analysis of strain concentration by notches and cracks. *Journal of Applied Mechanics*, 35(2):379 – 386.
- [Rice, 1972] Rice, J. R. (1972). Some remarks on elastic crack-tip stress fields. *International Journal of Solids and Structures*, 8(6):751 – 758.
- [Ruiz and Chen, 1986] Ruiz, C. and Chen, K. (1986). Life assessment of dovetail joints between blades and disks in aero-engines. *Fatigue of Engineering Materials and Structures*, Inst. of Mech. Eng.:187 – 194. Proceedings of International Conference on Fatigue.

- [Sharman, 2002] Sharman, R. C. (2002). Warlow-Davies, Eric John (1910-1964). *Australian Dictionary of Biography, National Centre of Biography, Australian National University*, 55:475 – 485.
- [Taylor and Waterhouse, 1972] Taylor, D. and Waterhouse, R. (1972). Sprayed molybdenum coatings as a protection against fretting fatigue. *Wear*, 20(3):401 – 407.
- [Thomson, 1998] Thomson, D. (1998). The national High Cycle Fatigue (HFC) program.
- [Tomlinson, 1927] Tomlinson, G. A. (1927). The rusting of steel surfaces in contact. *Proceedings of the Royal Society A: Mathematical, Physical and Engineering Sciences*, 115:472 – 483.
- [Tomlinson et al., 1939] Tomlinson, G. A., Thorpe, P. L., and Gough, H. J. (1939). An investigation of Fretting Corrosion of closely fitting surfaces. *Institution of Mechanical Engineers*, 4:223 – 249.
- [Vingsbo and Söderberg, 1988] Vingsbo, O. and Söderberg, S. (1988). On fretting maps. *Wear*, 126(2):131 – 147.
- [Warlow-Davies, 1941] Warlow-Davies, E. J. (1941). Fretting corrosion and fatigue strength: brief results of preliminary experiments. *Institution of Mechanical Engineers*, 146:32 – 38.
- [Waterhouse, 1976] Waterhouse, R. (1976). Fretting fatigue. *Materials Science and Engineering*, 25(0):201 – 206.
- [Waterhouse et al., 1962] Waterhouse, R., Brook, P., and Lee, G. (1962). The effect of electrodeposited metals on the fatigue behaviour of mild steel under conditions of fretting corrosion. *Wear*, 5(3):235 – 244.
- [Waterhouse et al., 1983] Waterhouse, R., Noble, B., and Leadbeater, G. (1983). The effect of shot-peening on the fretting-fatigue strength of an age-hardened aluminium alloy (2014A) and an austenitic stainless steel (En 58A). *Journal of Mechanical Working Technology*, 8(2-3):147 – 153.
- [Westergaard, 1939] Westergaard, H. (1939). Bearing pressure and cracks. *Journal of Applied Mechanics*, series A vol. 49:49 – 53.
- [Williams, 1965] Williams, J. (1965). The airworthiness approach to structural fatigue. *4th ICAF Symposium, Munich*, 4(2):91 – 138.
- [Withey, 1997] Withey, P. (1997). Fatigue failure of the de Havilland comet I. *Engineering Failure Analysis*, 4(2):147 – 154.



Title: Analysis of the stress gradient effect in Fretting-Fatigue through a description based on nonlocal intensity factors

Keywords: Fretting-fatigue, Crack analogue, Stress gradient, Model reduction technique

Abstract: In this manuscript a new method to describe the stress gradient effect in fretting-fatigue is proposed.

It is based on the description of the mechanical fields arising close to the contact edges through nonlocal intensity factors.

For this purpose, the kinetic field around the contact ends is partitioned into a summation of multiple terms, each one expressed as the product between intensity factors, I^s , I^a , I^c , depending on the macroscopic loads applied to the mechanical assembly, and spatial reference fields, d^s , d^a , d^c , depending on the local geometry of the part.

This description is obtained through nonintrusive post-processing of FE computation and is conceived in order to be easily implementable in the industrial context.

As a matter of fact, for any given macroscopic load and geometry, a set of nonlocal intensity factors is computed that permits to characterize the mechanical fields close to the contact edges. Such nonlocal description has the advantage of being (i) geometry independent so that the nonlocal intensity factors can be used to compare laboratory test with real-scale industrial assembly, (ii) applicable to industrial FE models usually characterized by rougher meshes compared to the ones used to describe fretting-fatigue in the academic context.

The procedure is applied to fretting-fatigue test data in order to verify whether the nonlocal intensity factors can be used to transpose experimental results to different contact geometries from the one in which they have been obtained.

Titre : Analyse de l'effet du gradient en Fretting-Fatigue à travers l'utilisation de facteurs d'intensité non locaux

Mots clés : Fretting-fatigue, Crack analogue, Gradient des contraintes, Méthode de réduction de modèle

Résumé : Nous proposons dans ce manuscrit une nouvelle méthode pour prendre en compte l'effet du gradient en Fretting-fatigue.

Les champs mécaniques présents à proximité du front de contact sont décrits à travers des facteurs d'intensité non locaux.

L'objectif est d'aboutir à une description du champ de vitesse sous la forme d'une somme de termes exprimés chacun comme le produit d'un facteur d'intensité (I^s , I^a , I^c), qui dépend des chargements macroscopiques appliqués à l'ensemble et d'une fonction de forme (d^s , d^a , d^c), qui est liée à la géométrie locale du contact.

Cette description est obtenue à travers un processus non intrusif de post-processing des résultats obtenus avec des calculs à éléments finis. De plus, elle a été pensée pour être

implémentée dans un contexte industriel.

En pratique, pour chaque chargement macroscopique et pour chaque géométrie, il est possible de calculer un ensemble de facteurs d'intensité non locaux qui permettent de décrire les champs mécaniques locaux près du front de contact.

Cette description non locale a l'avantage d'être (i) indépendante de la géométrie du contact employé et (ii) utilisable dans des modèles à éléments finis utilisés dans l'industrie qui sont caractérisés par des maillages plus grossiers par rapport à ceux utilisés pour étudier le fretting-fatigue dans des milieux académiques.

Une étude est menée pour vérifier que les facteurs d'intensité non locaux peuvent être utilisés pour transposer les résultats expérimentaux d'une géométrie à une autre.

